

T-4679

Measurement and Application of Nuclear Reactions
 ${}^7\text{Li} + \text{d}$, ${}^9\text{Be} + \text{d}$, ${}^{10}\text{B} + \text{d}$, ${}^{11}\text{B} + \text{d}$ and ${}^7\text{Li} + {}^3\text{He}$

by

Jingsheng Yan

ARTHUR LAKES LIBRARY
COLORADO SCHOOL OF MINES
GOLDEN, CO 80401

ProQuest Number: 10796637

All rights reserved

INFORMATION TO ALL USERS

The quality of this reproduction is dependent upon the quality of the copy submitted.

In the unlikely event that the author did not send a complete manuscript and there are missing pages, these will be noted. Also, if material had to be removed, a note will indicate the deletion.



ProQuest 10796637

Published by ProQuest LLC (2019). Copyright of the Dissertation is held by the Author.

All rights reserved.

This work is protected against unauthorized copying under Title 17, United States Code
Microform Edition © ProQuest LLC.


ProQuest LLC.
789 East Eisenhower Parkway
P.O. Box 1346
Ann Arbor, MI 48106 – 1346


T-4679

A thesis submitted to the Faculty and Board of Trustees of the Colorado School of Mines in partial fulfillment of the requirements for the degree of Doctor of Philosophy (Applied Physics).

Golden, Colorado

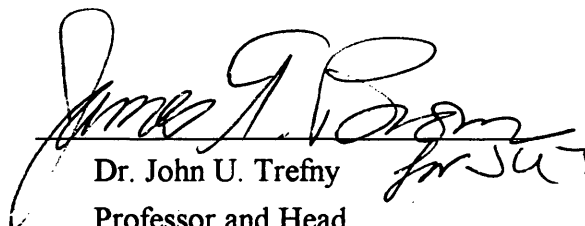
Date 6/26/95

Signed: 
Jingsheng Yan

Approved: 
Dr. F. Edward Cecil
Thesis Advisor

Golden, Colorado

Date 6/26/95


Dr. John U. Trefny
Professor and Head,
Department of Physics

ABSTRACT

In this dissertation, we describe measurements of a class of nuclear reactions, which include the exothermic deuteron-induced reactions, primarily (d,p) and (d, α) reactions, on the nuclei ${}^7\text{Li}$, ${}^9\text{Be}$, ${}^{10}\text{B}$ and ${}^{11}\text{B}$ at deuteron energies from 50 keV to 170 keV and the ${}^7\text{Li}({}^3\text{He}, p_0){}^9\text{Be}(\text{gs})$ reaction at bombarding energies around 160 keV. The angular distributions, cross sections and astrophysical S-factors are presented.

The application of the measured S-factors for the ${}^7\text{Li} + d$ and ${}^7\text{Li}({}^3\text{He}, p_0){}^9\text{Be}(\text{gs})$ reactions has been made to astrophysical nucleosynthesis. It has been proved that the (d, α) reaction on ${}^7\text{Li}$ has a more important contribution to the big-bang ${}^7\text{Li}$ destruction in the present energy region than those from the (d,p) and (d,n) reactions. With the two reaction networks, the ${}^9\text{Be}$ production in big-bang nucleosynthesis has been estimated and the ${}^{12}\text{C}$ production in the sun has been calculated as an example of stellar nucleosynthesis.

The measured cross sections of the ${}^9\text{Be} + d$, ${}^{10}\text{B} + d$ and ${}^{11}\text{B} + d$ reactions have been applied to the plasma diagnostics of the first wall contamination on the JET and TFTR tokamak fusion devices. The beryllium and boron contamination in the JET and TFTR tokamaks, respectively, can be obtained by use of the present cross sections together with γ -ray measurements.

TABLE OF CONTENTS

ABSTRACT	iii
LIST OF FIGURES	vi
LIST OF TABLES	x
ACKNOWLEDGMENTS	xi
Chapter 1. INTRODUCTION	1
1-1 Low-Energy and Light-Nucleus Reactions	1
1-2 Astrophysical Nucleosynthesis	2
1-2-1 Big-Bang Nucleosynthesis	3
1-2-2 Stellar Process	4
1-2-3 Two Alternative Reaction Networks	5
1-3 The Diagnostics of Tokamak Contamination	7
1-4 The Energy Regions	9
1-5 An Overview of the Previous Work	12
1-6 Summary and Organization of the Thesis	14
Chapter 2. EXPERIMENTAL TECHNIQUE	15
2-1 Apparatus	15
2-1-1 The Accelerator and its Beams	15
2-1-2 Setups in the Reaction Chamber	20
2-1-3 The Electronics Setups	22
2-2 Test Experiments	25
2-2-1 The Angular Distribution of ${}^2\text{H}(d,p){}^3\text{H}$	25
2-2-2 Measurements from Infinitely Thick Targets	27
2-2-3 Yield Measurements on the ${}^7\text{Li}(p,\alpha){}^4\text{He}$ Reaction: An Example Without Resonance	29
2-2-4 Yield Measurements on the ${}^{11}\text{B}(p,\alpha_0){}^8\text{Be}(\text{gs})$ Reaction: An Example With Resonance	33

2.3	Experimental Details on the ${}^7\text{Li}({}^3\text{He}, p_0){}^9\text{Be}(\text{gs})$ Reaction	35
2.3.1	The Setups	35
2.3.2	The Beam Contamination	37
2.3.3	The Sequential Reaction	39
2.3.4	The ${}^3\text{He}(\text{d}, p){}^4\text{He}$ Accidental Reaction	40
2.3.5	A Test Experiment	41
Chapter 3.	RESULTS	44
3.1	The ${}^7\text{Li}(\text{d}, \alpha){}^5\text{He}$ Reaction	44
3.2	The Deuteron-Induced Reactions on ${}^9\text{Be}$, ${}^{10}\text{B}$ and ${}^{11}\text{B}$	52
3.2.1	The ${}^9\text{Be} + \text{d}$ Reaction	52
3.2.2	The ${}^{10}\text{B} + \text{d}$ Reaction	74
3.2.3	The ${}^{11}\text{B} + \text{d}$ Reaction	94
3.3	The ${}^7\text{Li}({}^3\text{He}, p_0){}^9\text{Be}(\text{gs})$ Reaction	109
3.3.1	A Simulated 2-D Plot	109
3.3.2	A Measured 2-D Plot and Coincident Spectrum	111
3.3.3	A Measured Anti-Coincident Spectrum	114
3.3.4	The Results	119
Chapter 4.	DISCUSSIONS AND CONCLUSIONS	123
4.1	Applications in Astrophysical Nucleosynthesis	123
4.1.1	${}^9\text{Be}$ Production by ${}^7\text{Li}({}^3\text{He}, p_0){}^9\text{Be}(\text{gs})$ in BBN	123
4.1.2	${}^{12}\text{C}$ Production in the Sun	126
4.1.3	${}^7\text{Li}$ Destruction by ${}^7\text{Li}(\text{d}, 2\alpha)\text{n}$ in BBN	128
4.2	Applications in Tokamaks	130
4.3	Single-Step DWUCK4 Calculations	134
	REFERENCES CITED	140
	APPENDIXES	143
A.1	The Fitting Procedure	143
A.2	The Original Experimental Data	144

LIST OF FIGURES

Fig. 1-1	The CNO cycles	5
Fig. 1-2	The alternative reaction pathways	6
Fig. 1-3	Power from D-T plasma of thermonuclear reaction	8
Fig. 1-4	The Gamow peak	10
Fig. 1-5	The S-factor measured by Boyd and co-workers [Rat90] and the energy regions of the Gamow peaks	13
Fig. 2-1	The CSM accelerator	16
Fig. 2-2	Formation of the α -particle spectrum for $^{11}\text{B} + \text{p}$	18
Fig. 2-3	A spectrum for $^{11}\text{B} + \text{p}$ and the energy calibration of the accelerator	19
Fig. 2-4	Suppression for the secondary electrons	21
Fig. 2-5	The electronics setups for single-detector measurements	23
Fig. 2-6	The electronics setups for ΔE -E measurements	24
Fig. 2-7	A spectrum and the angular distribution for $^2\text{H}(\text{d}, \text{p})^3\text{H}$	25
Fig. 2-8	A spectrum and the yields measured for $^7\text{Li}(\text{p}, \alpha)^4\text{He}$	31
Fig. 2-9	The S-factor and cross section for $^7\text{Li}(\text{p}, \alpha)^4\text{He}$	32
Fig. 2-10	The measured yields for $^{11}\text{B}(\text{p}, \alpha)^8\text{Be}(\text{gs})$	34
Fig. 2-11	The trend in angular distribution for $^{11}\text{B}(\text{p}, \alpha)^8\text{Be}(\text{gs})$	34
Fig. 2-12	A principle schematic diagram of the used electronics	36
Fig. 2-13	The calculated ratio of the number of the sequential reactions to that of the expected reactions	40
Fig. 2-14	A 2-D plot for $^{10}\text{B}(\text{d}, \text{p})^{11}\text{B}$	42
Fig. 2-15	The detected particles	43
Fig. 3-1	Formation of the α -particle spectrum for $^7\text{Li} + \text{d}$	47
Fig. 3-2	Measured and calculated spectra for $^7\text{Li} + \text{d}$	48
Fig. 3-3	Angular distributions for $^7\text{Li} + \text{d}$	49
Fig. 3-4(a)	Cross sections for $^7\text{Li} + \text{d}$	50
Fig. 3-4(b)	S-factors for $^7\text{Li} + \text{d}$	51

Fig. 3-5	A spectrum for ${}^9\text{Be} + d$	57
Fig. 3-6	Angular distribution for ${}^9\text{Be}(d, p_0){}^{10}\text{Be}$ at $E_{\text{cm}} = 90\text{keV}$	58
Fig. 3-7	Angular distribution for ${}^9\text{Be}(d, p_1){}^{10}\text{Be}^*$ at $E_{\text{cm}} = 90\text{keV}$	59
Fig. 3-8	Angular distribution for ${}^9\text{Be}(d, t_0){}^8\text{Be}$ at $E_{\text{cm}} = 90\text{keV}$	60
Fig. 3-9	Angular distribution for ${}^9\text{Be}(d, \alpha_0){}^7\text{Li}$ at $E_{\text{cm}} = 90\text{keV}$	61
Fig. 3-10	Angular distribution for ${}^9\text{Be}(d, \alpha_1){}^7\text{Li}^*$ at $E_{\text{cm}} = 90\text{keV}$	62
Fig. 3-11	Angular distribution for ${}^9\text{Be}(d, p_0){}^{10}\text{Be}$ at $E_{\text{cm}} = 123\text{keV}$	63
Fig. 3-12	Angular distribution for ${}^9\text{Be}(d, p_1){}^{10}\text{Be}^*$ at $E_{\text{cm}} = 123\text{keV}$	64
Fig. 3-13	Angular distribution for ${}^9\text{Be}(d, t_0){}^8\text{Be}$ at $E_{\text{cm}} = 123\text{keV}$	65
Fig. 3-14	Angular distribution for ${}^9\text{Be}(d, \alpha_0){}^7\text{Li}$ at $E_{\text{cm}} = 123\text{keV}$	66
Fig. 3-15	Angular distribution for ${}^9\text{Be}(d, \alpha_1){}^7\text{Li}^*$ at $E_{\text{cm}} = 123\text{keV}$	67
Fig. 3-15(a)	The S-factors from different angular distributions for ${}^9\text{Be} + d$	68
Fig. 3-16	Cross section for ${}^9\text{Be}(d, p_0){}^{10}\text{Be}$	69
Fig. 3-17	Cross section for ${}^9\text{Be}(d, p_1){}^{10}\text{Be}^*$	70
Fig. 3-18	Cross section for ${}^9\text{Be}(d, t_0){}^8\text{Be}$	71
Fig. 3-19	Cross section for ${}^9\text{Be}(d, \alpha_0){}^7\text{Li}$	72
Fig. 3-20	Cross section for ${}^9\text{Be}(d, \alpha_1){}^7\text{Li}^*$	73
Fig. 3-21	A spectrum for ${}^{10}\text{B} + d$	77
Fig. 3-22	Angular distribution for ${}^{10}\text{B}(d, p_0){}^{11}\text{B}$	78
Fig. 3-23	Angular distribution for ${}^{10}\text{B}(d, p_1){}^{11}\text{B}^*$	79
Fig. 3-24	Angular distribution for ${}^{10}\text{B}(d, p_2){}^{11}\text{B}^*$	80
Fig. 3-25	Angular distribution for ${}^{10}\text{B}(d, p_3){}^{11}\text{B}^*$	81
Fig. 3-26	Angular distribution for ${}^{10}\text{B}(d, p_4){}^{11}\text{B}^*$	82
Fig. 3-27	Angular distribution for ${}^{10}\text{B}(d, p_5){}^{11}\text{B}^*$	83
Fig. 3-28	Angular distribution for ${}^{10}\text{B}(d, \alpha_0){}^8\text{Be}$	84
Fig. 3-29	Angular distribution for ${}^{10}\text{B}(d, \alpha_1){}^8\text{Be}^*$	85
Fig. 3-30	Cross section for ${}^{10}\text{B}(d, p_0){}^{11}\text{B}$	86
Fig. 3-31	Cross section for ${}^{10}\text{B}(d, p_1){}^{11}\text{B}^*$	87

Fig. 3-32	Cross section for $^{10}\text{B}(d, p_2)^{11}\text{B}^*$	88
Fig. 3-33	Cross section for $^{10}\text{B}(d, p_3)^{11}\text{B}^*$	89
Fig. 3-34	Cross section for $^{10}\text{B}(d, p_4)^{11}\text{B}^*$	90
Fig. 3-35	Cross section for $^{10}\text{B}(d, p_5)^{11}\text{B}^*$	91
Fig. 3-36	Cross section for $^{10}\text{B}(d, \alpha_0)^8\text{Be}$	92
Fig. 3-37	Cross section for $^{10}\text{B}(d, \alpha_1)^8\text{Be}^*$	93
Fig. 3-38	A spectrum for $^{11}\text{B} + d$	98
Fig. 3-39	Angular distribution for $^{11}\text{B}(d, p_0)^{12}\text{B}$ at $E_{\text{cm}} = 101\text{keV}$	99
Fig. 3-40	Angular distribution for $^{11}\text{B}(d, \alpha_0)^9\text{Be}$ at $E_{\text{cm}} = 101\text{keV}$	100
Fig. 3-41	Angular distribution for $^{11}\text{B}(d, \alpha_2)^9\text{Be}^*$ at $E_{\text{cm}} = 101\text{keV}$	101
Fig. 3-42	Angular distribution for $^{11}\text{B}(d, p_0)^{12}\text{B}$ at $E_{\text{cm}} = 142\text{keV}$	102
Fig. 3-43	Angular distribution for $^{11}\text{B}(d, \alpha_0)^9\text{Be}$ at $E_{\text{cm}} = 142\text{keV}$	103
Fig. 3-44	Angular distribution for $^{11}\text{B}(d, \alpha_2)^9\text{Be}^*$ at $E_{\text{cm}} = 142\text{keV}$	104
Fig. 3-44(a)	The S-factors from different angular distributions for $^{11}\text{B} + d$	105
Fig. 3-45	Cross section for $^{11}\text{B}(d, p_0)^{12}\text{B}$	106
Fig. 3-46	Cross section for $^{11}\text{B}(d, \alpha_0)^9\text{Be}$	107
Fig. 3-47	Cross section for $^{11}\text{B}(d, \alpha_2)^9\text{Be}^*$	108
Fig. 3-48	A simulated 2-D plot for $^7\text{Li}(^3\text{He}, p_0)^9\text{Be}(\text{gs})$	110
Fig. 3-49	A measured 2-D plot for $^7\text{Li}(^3\text{He}, p_0)^9\text{Be}(\text{gs})$	112
Fig. 3-50	A coincident spectrum for $^7\text{Li}(^3\text{He}, p_0)^9\text{Be}(\text{gs})$	113
Fig. 3-51	An anti-coincident spectrum for $^7\text{Li}(^3\text{He}, p_0)^9\text{Be}(\text{gs})$	115
Fig. 3-52	Anti-coincident spectra for $^3\text{He}(d, p)^4\text{He}$	117
Fig. 3-53	Spectra and 2-D plots for $^3\text{He}(d, p)^4\text{He}$	118
Fig. 3-54	S-factor for $^7\text{Li}(^3\text{He}, p_0)^9\text{Be}(\text{gs})$	121
Fig. 3-55	Cross section for $^7\text{Li}(^3\text{He}, p_0)^9\text{Be}(\text{gs})$	122
Fig. 4-1	$^7\text{Li}(^3\text{He}, p_0)^9\text{Be}(\text{gs})$ reaction rate	125
Fig. 4-2	^7Li destruction rate by deuterium	129
Fig. 4-3	γ -ray count rates for the JET and TFTR tokamaks	132

Fig. 4-4	γ -ray count rates for the JET and TFTR tokamaks for injection of neutral beams	133
Fig. 4-5	Formation of the ^{10}Be ground state by single-particle transfer	135
Fig. 4-6	Angular distribution for $^9\text{Be}(d, p_0)^{10}\text{Be}$ by DWUCK4	136
Fig. 4-7	Angular distribution for $^9\text{Be}(d, t_0)^8\text{Be}$ by DWUCK4	137
Fig. 4-8	Angular distribution for $^{10}\text{B}(d, p_0)^{11}\text{B}$ by DWUCK4	138
Fig. 4-9	Angular distribution for $^{11}\text{B}(d, p_0)^{12}\text{B}$ by DWUCK4	139

LIST OF TABLES

Table 1-1	The energy windows of the Gamow peaks for the studied reactions	11
Table 1-2	Summary of the previous work	12
Table 1-3	An overview of the studied reactions	13
Table 2-1	A list of the important accidental reactions	38
Table 3-1	Summary of the angular distributions for the ${}^9\text{Be} + d$ reactions	55
Table 3-1(a)	Summary of the angular distribution parameters for the ${}^9\text{Be} + d$ reactions	55
Table 3-2	Summary of the S-factors with Eq. (3-5) for the ${}^9\text{Be} + d$ reactions	56
Table 3-2(a)	Summary of the S-factors with Eq. (3-5a) for the ${}^9\text{Be} + d$ reactions	56
Table 3-3	Summary of the angular distributions for the ${}^{10}\text{B} + d$ reactions	75
Table 3-4	Summary of the S-factors for the ${}^{10}\text{B} + d$ reactions	76
Table 3-5	Summary of the angular distributions for the ${}^{11}\text{B} + d$ reactions	96
Table 3-5(a)	Summary of the angular distribution parameters for the ${}^{11}\text{B} + d$ reactions	96
Table 3-6	Summary of the S-factors with Eq. (3-5) for the ${}^{11}\text{B} + d$ reactions	97
Table 3-6(a)	Summary of the S-factors with Eq. (3-5a) for the ${}^{11}\text{B} + d$ reactions	97
Table 4-1	Summary of the input parameters to DWUCK4	135
Table 4-2	A standard DWUCK4 input file	135
Table A-1	The original data for the ${}^7\text{Li} + d$ reaction	144
Table A-2	The original data for the ${}^9\text{Be} + d$ reaction	145
Table A-3	The original data for the ${}^{10}\text{B} + d$ reaction	146
Table A-4	The original data for the ${}^{11}\text{B} + d$ reaction	147

ACKNOWLEDGMENT

At first, I wish to thank Prof. F. Edward Cecil, my advisor of this dissertation, for his choosing such an important and challenging dissertation for me, for his leads in my moving in the right direction, for his help and advice in solving all the problems encountered in the dissertation, for his continuous financial support during the last four years, and, particularly, for the truth and encouragement he gave to me during his sabbatical leave to England. In addition to all these, he made every effort to enhance my personal quality and capability to be a qualified scientific researcher. Without his supervision, it would definitely have been impossible for me, a complete stranger to nuclear physics four years ago, to gain so much from this research project.

I would like to acknowledge Prof. R.J. Peterson and Prof. R.A. Ristinen from University of Colorado at Boulder for their helpful suggestions and supervision. Some ideas in this dissertation regarding the ${}^7\text{Li}({}^3\text{He}, p_0){}^9\text{Be}(\text{gs})$ experiment did result from the discussions with them. Prof. R.J. Peterson provided the lithium sample used in the ${}^7\text{Li}({}^3\text{He}, p_0){}^9\text{Be}(\text{gs})$ reaction and he came to my lab in an evening to help to teach me about re-coating the accelerator filament. During the year of Prof. Cecil's sabbatical leave, Prof. R.J. Peterson and Prof. R.A. Ristinen acted as my advisors.

I must express my gratitude to Dr. G.M. Hale and T-2 group at Los Alamos National Laboratory. Dr. Hale provided his computer program "SPECT" to me and did his best to teach me the R-matrix theory and help me in getting familiar with the program. I will not forget his kind hospitality he gave to me during my visit to Los Alamos National Laboratory, which is partially supported by the T-2 group.

I am grateful to Prof. J.A. McNeil for the significant effort and time he devoted which led to my better understanding in all the complicated theoretical calculations with the R-matrix method and DWUCK.

My special thanks also go to Dr. P.D. Kunz at University of Colorado at Boulder for his supplying the DWUCK computer program and his discussions with me.

I would like to thank the CSM Department of Physics and Prof. Don L. Williamson for providing the financial support to me, Jack Kitner, Rex Rideout and Irene

Neighbors for their assistance during these years, and Huizhu Liu and Dave Beddingfield for sharing their experience with me.

I thank J.A. McNeil, J.T. Brown, W.R. Astle, S.A. Pruess, G. Krauss and P. MacCarthy of CSM and R.J. Peterson and R.A. Ristinen of CU-Boulder for serving on my thesis committee.

The financial support from United States Department of Energy through contract No. DE-FG03-93ER40789 is gratefully acknowledged.

Finally, I would like to thank my wife, Hong Chang, for her understanding, support and love during my graduate study at Colorado School of Mines.

T-4679

**I would like to dedicate this dissertation to
the memory of my father, Yü-jing Yan.**

Chapter 1

INTRODUCTION

1-1 LOW-ENERGY AND LIGHT-NUCLEUS REACTIONS

Basic nuclear physics may be divided into two major fields, nuclear structure and nuclear reactions. Applied nuclear physics, on the other hand, has many branches, including astrophysics, medicine, quantitative surface analysis, non-destructive bulk analysis, controlled fusion reactor operation and diagnostics to name a few. One of the goals of basic nuclear reaction physics is the measurement of nuclear reaction cross sections and angular distributions. These measurements, in turn, are the basis for using the reactions in a given area of applied nuclear physics. In this thesis, we describe our measurements of a fairly broad class of nuclear reaction cross sections and angular distributions and discuss two areas of applications of these reactions.

The class of reactions includes the exothermic deuteron-induced reactions, primarily (d, α) and (d,p) reactions, on the nuclei ${}^7\text{Li}$, ${}^9\text{Be}$, ${}^{10}\text{B}$ and ${}^{11}\text{B}$ at low energies as well as the astrophysically interesting reaction ${}^7\text{Li}({}^3\text{He}, p_0){}^9\text{Be}(\text{gs})$. For targets lighter than these, namely ${}^2\text{H}$, ${}^3\text{H}$, ${}^3\text{He}$ and ${}^6\text{Li}$, the (d, α) and (d,p) reactions have been well studied at low energies while for targets heavier than ${}^{11}\text{B}$, the reactions become prohibitively difficult to measure by virtue of the increasing Coulomb barrier between the projectile and the target.

Our measurements of these reactions are then related to two areas of applied nuclear physics:

1) astrophysical nucleosynthesis (both primordial and stellar) of the elements ${}^9\text{Be}$, ${}^{10}\text{B}$, ${}^{11}\text{B}$ and ${}^{12}\text{C}$. Noteworthy is the possible synthesis of ${}^{12}\text{C}$ by a network different from the traditional 3- α process.

2) diagnostics of the first wall contamination of fusion plasmas on the JET and TFTR tokamak fusion devices.

Sections 1-2 and 1-3 will discuss the two areas, respectively, showing what the important reactions of low-energy and light-nucleus are. Section 1-4 will focus on the question "what are the appropriate energy regions for these reactions". Section 1-5 reviews the previous work on these reactions, leading to the final conclusion that the present study on the reactions in the energy regions is of importance.

1-2 ASTROPHYSICAL NUCLEOSYNTHESIS

Astrophysics is the physics of the stars, planets, the galaxies and the cosmos. One area of astrophysics is the study of the origin of the elements. This area of astrophysics is called "astrophysical nucleosynthesis".

The standard view [Ree94] of our current understanding of astrophysical nucleosynthesis is that the light elements ($Z < 6$) are generated by the following three different processes:

1) thermonuclear reactions in the primordial universe, i.e., the so-called big-bang nucleosynthesis (BBN);

2) thermonuclear reactions within stars, i.e., the so-called stellar process (SP);

3) galactic cosmic-ray-induced spallation reactions in cold interstellar atoms. In the process, the interstellar atoms, mostly ${}^{12}\text{C}$, ${}^{14}\text{N}$ and ${}^{16}\text{O}$, as target candidates, are broken up into pieces, the so-called spallation reactions, by galactic cosmic-rays, mostly protons and α -particles, with very high energy from 100MeV up to 1TeV.

Since the energy range of the first two processes matches that of the present work, we will focus onto them.

1.2.1 Big-Bang Nucleosynthesis

There are two kinds of model in primordial BBN, i.e., the standard model (SM) (see, for example, the review papers of Wag67, Sch77 and Ree94) and nonuniform density models (NDM) [Alc87; Ful88; and Mal88]. In SM, which can be dated back to the 1950's, the baryonic density of the primordial universe at the time of BBN (universe lifetime $t \approx 100 \sim 1000$ sec.) is assumed to be homogeneous, leading to the uniform distributions of protons and neutrons, with heavier nuclei then being synthesized in this uniform universe. NDM was brought to light in the mid of 1980's after the theory [Wit84] of the quark-hadron phase transition in the early universe. In NDM, the primordial universe is divided into a high-density proton-rich region (or regions) where the nucleosynthesis involving proton-rich nuclei dominates and a low-density neutron-rich region (or regions) which will favor the nucleosynthesis from neutron-rich nuclei. Consequently, SM and NDM predict different abundances of nuclides, among which ${}^7\text{Li}$ and ${}^9\text{Be}$ are the most important two elements.

Such differences in the ${}^7\text{Li}$ and ${}^9\text{Be}$ abundance provide strong tests for SM and NDM, i.e., comparisons of the SM and NDM predictions with the observed abundances. Since, unfortunately, the cosmologically observed value for the primordial ${}^7\text{Li}$ abundances "is far from clear", as claimed by Boyd [Rat90], people turned to the ${}^9\text{Be}$ abundance as another independent test, which has been suggested by Boyd and Kajino [Boy89; Kaj90; and Yam93].

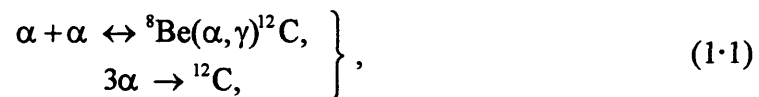
There are two crucial factors regarding the BBN ${}^9\text{Be}$ abundance. First, the production of the ${}^9\text{Be}$ nuclei, which was accomplished by the two reactions ${}^7\text{Li}(t, n_0){}^9\text{Be}(\text{gs})$ and ${}^7\text{Li}({}^3\text{He}, p_0){}^9\text{Be}(\text{gs})$ ¹. For the two reactions, the cross section of ${}^7\text{Li}({}^3\text{He}, p_0){}^9\text{Be}(\text{gs})$ is particularly necessary in the SM and NDM calculations of the primordial ${}^9\text{Be}$ abundance since that of ${}^7\text{Li}(t, n_0){}^9\text{Be}(\text{gs})$ can be inferred from it. Second, the existence of ${}^7\text{Li}$ nuclei, or, in other words, the destruction of ${}^7\text{Li}$ nuclei by proton- and deuteron-induced reactions. Since deuterium can be abundant relatively to protons in the low-density neutron-rich region of NDM and Boyd and Kajino [Boy89; Kaj90; and

¹ Since all the excited states of ${}^9\text{Be}$ are unstable and will decay to $n+{}^8\text{Be}$ [Ajz84], it is only the reactions to the ground state of ${}^9\text{Be}$ that can ultimately produce ${}^9\text{Be}$.

Yam93] claim that the ${}^9\text{Be}$ are mainly produced in this region, the deuteron-induced reaction on ${}^7\text{Li}$ seems to play a role that can not be neglected when considering the NDM ${}^9\text{Be}$ abundance.

1.2.2 Stellar Process

SP is another process of astrophysical nucleosynthesis, particularly for the relatively heavier nuclides ($Z \geq 6$), in which elements are produced in a roughly consecutive way from hydrogen, mostly protons. Stellar nucleosynthesis starts from the three proton-proton (p-p) chains, which can give birth to stable nuclides up to ${}^7\text{Li}$, then, after the burning in the CNO (Carbon-Nitrogen-Oxygen) cycles, where ${}^{12}\text{C}$ is indispensably needed as a catalyst, the famous triple- α process proposed by E.E. Salpeter and F. Hoyle¹ early in 1950's



will be ignited, which enables the whole process of stellar nucleosynthesis to jump over the $A=8$ mass stability gap. Finally some advanced burning stages will follow (for details, see Cla83 and Rol88).

Illustrated in Fig. 1.1, the CNO cycles start from ${}^{12}\text{C}$ and, after a series of reactions, end back in ${}^{12}\text{C}$. The net evolution result of the CNO cycles is the conversion of protons into ${}^4\text{He}$



The rate of the conversion directly depends on the initial number of the ${}^{12}\text{C}$ nuclei. Now, in the consideration of this initial number of the ${}^{12}\text{C}$ nuclei, a question is if ${}^{12}\text{C}$ can be produced by the triple- α process in the burning stage of the p-p chains. The first reaction in Eq. (1.1) involves the formation of ${}^8\text{Be}$, of which the lifetime is as short as $\sim 1 \times 10^{-16}$ second [Ajz84], and the second is a 3- α collision, of which the probability is very small. Though an s-wave resonance of the triple- α process to the 7.654 MeV energy

¹ For details, see the following references: Sal52; Sal53; Sal57; Öpi51; Hoy53; §7.1 in Rol88; and §5.5 in Cla83.

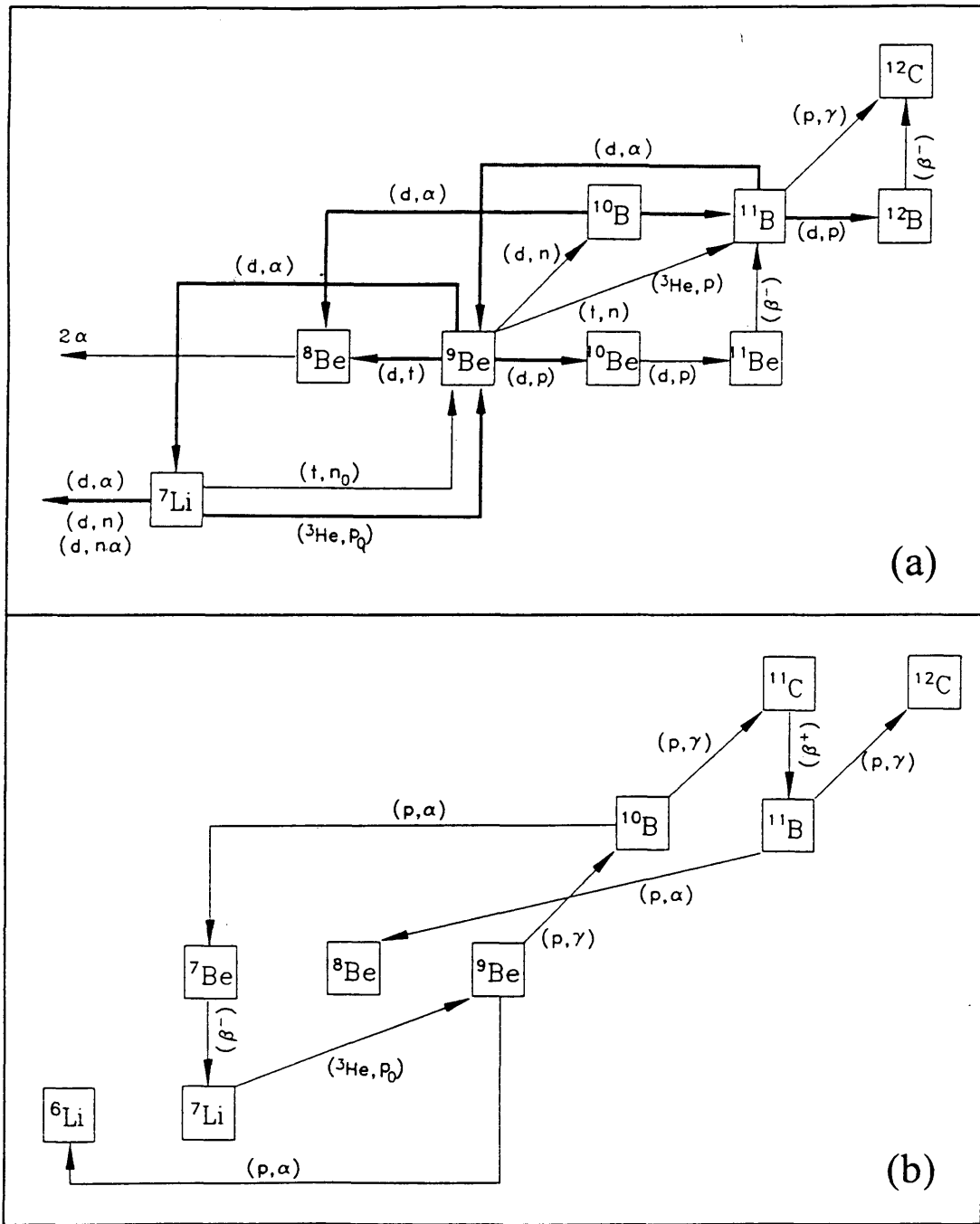


Fig. 1-2. The alternative reaction pathways in big-bang nucleosynthesis (a) and in stellar nucleosynthesis (b). The thicker lines in (a) indicate the reactions studied in this thesis.

hand, since the abundance ratio of deuteron relative to hydrogen in the interior of stars at equilibrium is $10^{-17} \sim 10^{-18}$ [Fig. 6-6 in Rol88], the deuteron-induced reactions on ^9Be , ^{10}B and ^{11}B in the BBN network can be ignored in SP.

1.3 THE DIAGNOSTICS OF TOKAMAK CONTAMINATION

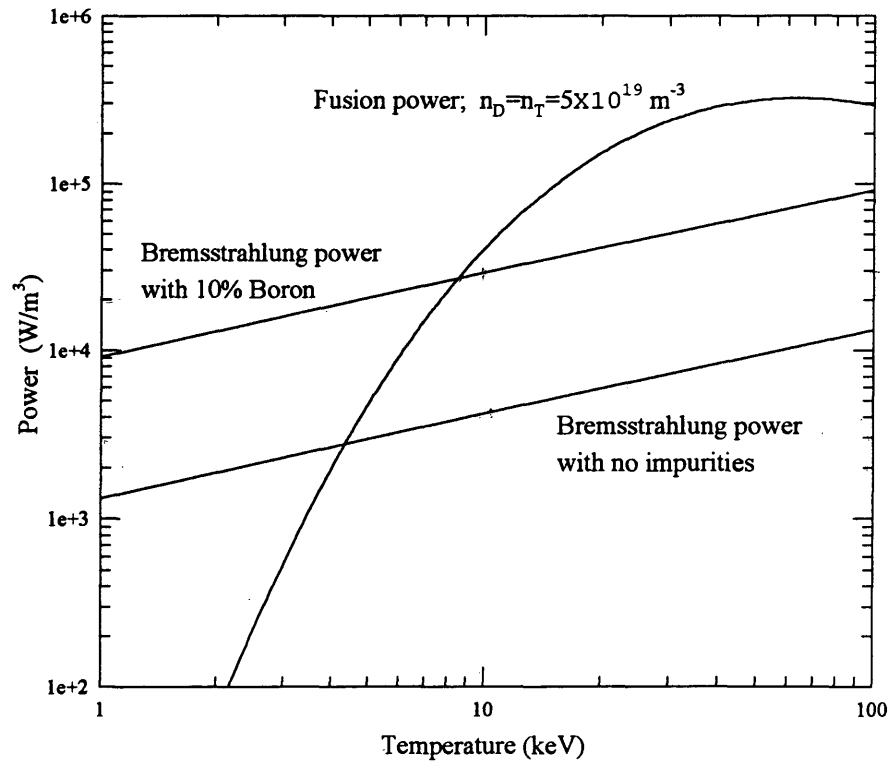
Controlled thermonuclear-fusion reactors, i.e., tokamaks, are thought to be one of the energy sources of the future. The objective of present tokamak research is to produce the plasma conditions under which substantial thermonuclear power will be produced. A more precise description of this aim is to achieve ignition, which requires the plasma to be heated to a temperature of the order of $T = 10$ keV. One of the major obstacles to the achievement of ignition is the energy loss by the bremsstrahlung radiation and other radiative processes from contaminant ions in the plasma. The main source of contamination is the first wall of a tokamak within which the fusion plasma is confined magnetically. The first wall of the JET tokamak (Abingdon, UK) is made of beryllium and that of the TFTR tokamak (Princeton, USA) consists of boron.

The significance of the contaminant radiation in the plasma ignition can be seen by comparing the fusion power from a thermonuclear D-T (Deuterium-Tritium) plasma with and without boron contamination at the 10% level [Wes87; also see Hag77 and Sta84] (see Fig. 1.3). A necessary condition for an ignited plasma is that the fusion power exceed the bremsstrahlung radiative losses. As seen from Fig. 1.3, ignition is possible at a temperature of 4.5 keV for an ideal D-T plasma with no contaminant, whereas with a 10% boron contaminant, the minimum ignition temperature rises to about 9 keV.

Therefore, the diagnostics of first wall contamination becomes very important. One method involves the measurements of γ -rays from sequential decays of the nuclei produced by deuteron-induced reactions, for example, γ -rays of 3.4 MeV can be emitted from the JET tokamak through the reactions $^9\text{Be}(d, p)^{10}\text{Be}^*(3.3680\text{MeV})(\gamma)^{10}\text{Be}(\text{gs})$. With the cross sections of the deuteron-induced reactions on ^9Be , ^{10}B and ^{11}B , the

contamination from the first walls of the two tokamaks can be evaluated from the γ -ray measurements. Hence comes the conclusion of this Section that the deuteron-induced reactions on ^9Be , ^{10}B and ^{11}B are of importance in the diagnostics of first wall contamination for the JET and TFTR tokamaks.

Fig. 1-3. Power from D-T plasma of thermonuclear reaction.



1.4 THE ENERGY REGIONS

Before proceeding to the energy regions of interest for the reactions studied here, a brief description of the Gamow peak is helpful. Consider a thermonuclear reaction of two nuclear species of charge numbers Z_1 and Z_2 and reduced mass μ at a certain temperature T . The reaction rate per pair of reacting nuclei can be expressed [§3.3 and §3.5 in Rol88] as the statistical mean value of σv under the Maxwell-Boltzmann energy distribution

$$\langle \sigma v \rangle = \left(\frac{8}{\pi \mu} \right)^{1/2} \frac{1}{(kT)^{3/2}} \int_0^{\infty} \sigma(E) E e^{-E/kT} dE, \quad (1.3)$$

where E is the CM energy and $\sigma(E)$ the cross section of the reaction. Introducing the astrophysical S-factor $S(E)$ (see §4.2 of Rol88 for derivation in detail), the cross section can be described by

$$\sigma(E) = \frac{S(E)}{E} e^{-\sqrt{E_G/E}}. \quad (1.4)$$

where E_G is the Gamow energy defined as

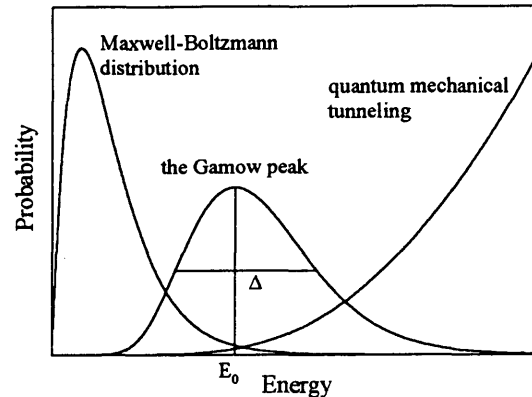
$$E_G = \frac{2\mu\pi^2 e^4 Z_1^2 Z_2^2}{e^4 Z_1^2 Z_2^2} = 0.979 Z_1^2 Z_2^2 \mu \quad (\text{MeV}), \quad (1.5)$$

where, in Eq (1.5), μ is in unit of AMU (atomic mass unit). Then, Eq. (1.3) can be rewritten as

$$\langle \sigma v \rangle = \left(\frac{8}{\pi \mu} \right)^{1/2} \frac{1}{(kT)^{3/2}} \int_0^{\infty} S(E) e^{-(E/kT) - \sqrt{E_G/E}} dE. \quad (1.6)$$

It is obvious from Eq. (1.6) that the reaction rate is governed by two facts: the quantum mechanical tunneling through the Coulomb barrier of the pair of nuclei with the probability proportional to $e^{-\sqrt{E_G/E}}$ and the Maxwell-Boltzmann energy distribution function. The contribution from low energy nuclei to the reaction rate is small because of the tunneling and that from high energy nuclei is also small since very few nuclei are

Fig. 1-4. The Gamow peak. Note that the Gamow peak is approximately symmetrical about the peak energy E_0 . Δ is the width of the Gamow peak. The energy window of a thermonuclear reaction determined by the Gamow peak is from $E_0 - \Delta/2$ to $E_0 + \Delta/2$.



distributed at the high energy region. So the integrand must form a peak, as illustrated by Fig. 1-4. This peak is called the Gamow peak, which can be described by the peak position E_0 and the width Δ :

$$\left. \begin{aligned} E_0 &= 1.22 (Z_1^2 Z_2^2 \mu T_6^2)^{1/3} \quad (\text{keV}) \\ \Delta &= 0.749 (Z_1^2 Z_2^2 \mu T_6^5)^{1/6} \quad (\text{keV}) \end{aligned} \right\} \quad (1.7)$$

Most of the thermonuclear reactions at temperature T will occur in the energy window $(E_0 - \Delta/2, E_0 + \Delta/2)$ defined by the Gamow peak.

Now, with the knowledge of the Gamow peak, it can be said quantitatively that the energy region of interest for a thermonuclear reaction at a temperature T is the energy window given by Eq. (1.7).

As mentioned in Section 1-1, the main objectives of the present study on nuclear reactions are for astrophysical nucleosynthesis, BBN and SP, and for controlled fusion reactions in tokamaks. Now the temperature for each of the three processes, all thermonuclear reactions, can be determined. In BBN, two useful approximate relationships of time-energy [Ree94] and energy-temperature are

$$\left. \begin{aligned} t \text{ (sec.)} &\approx 1/E^2 \text{ (MeV)} \\ E \text{ (MeV)} &\approx T_{10} \end{aligned} \right\}, \quad (1.8)$$

where t is the universe lifetime, E the kinetic energy of the thermal motion of a particle and $T_n = T/10^n \text{K}$. A typical universe lifetime $t = 300 \text{ sec.}$ corresponds to the

temperature $T_9 = 0.6$. In SP, the interior temperature $T_6 = 15$ of the sun, a moderate-sized star, is considered, for the reason that the sun is in the earlier hydrogen burning stage, for which the SP reaction network in Fig. 1-2 is proposed. Another example of temperature is $T_6 = 60$ for hydrogen burning of massive stars [Wea80]. In tokamaks, the temperature of the plasma of the deuterium-tritium fuel is in the order of 10 keV [§1-1 in Wes87], i.e., $T_9 = 0.1$.

The energy regions of Gamow peaks, estimated by Eq. (1-7), of the reactions measured in this thesis are listed in Table 1-1 for the three different processes. Table 1-1 shows that the study of these nuclear reactions at energies from a few 10 keV to ~ 200 keV, the energy region used in the present work, is particularly important.

Table 1-1. The energy windows of the Gamow peaks for the reactions studied in this thesis.

Process	Temperature	Reaction	Energy Window of the Gamow peak (keV)
Big-bang nucleosynthesis	$T_9 = 0.6$ $t = 300$ sec.	${}^7\text{Li}({}^3\text{He}, p_0){}^9\text{Be}(\text{gs})$	210 ~ 530
		${}^7\text{Li}+d$	90 ~ 330
		${}^9\text{Be}+d$	120 ~ 400
		${}^{10}\text{B}+d$ ${}^{11}\text{B}+d$	150 ~ 450
Stellar process	$T_6 = 15$ (sun)	${}^7\text{Li}({}^3\text{He}, p_0){}^9\text{Be}(\text{gs})$	24 ~ 39
	$T_6 = 60$ (massive stars)		56 ~ 102
Tokamak	$T_9 = 0.1$ ($kT = 10$ keV)	${}^9\text{Be}+d$	48 ~ 108
		${}^{10}\text{B}+d$ ${}^{11}\text{B}+d$	59 ~ 124

1.5 AN OVERVIEW OF THE PREVIOUS WORK

Table 1.2 summarizes the previous work on the nuclear reactions that are studied here and in the energy region of the present work. It can be seen clearly that the previous measurements for these low-energy reactions are not complete.

The importance of the reaction ${}^7\text{Li}({}^3\text{He}, p_0){}^9\text{Be}(\text{gs})$ in BBN and SP has been discussed earlier and its energy region of interest in Table 1.1 is from a few 10 keV up to 530 keV. This reaction has been measured by R.N. Boyd and co-workers [Rat90] and Fig. 1.5 shows their measured S-factor $S(E)$. The energy windows of the Gamow peaks for the reaction in Table 1.1 are also shown in Fig. 1.5. It is quite clear that other measurements at the lower energies are important.

Table 1.2. Summary of the previous work on the nuclear reactions studied in this thesis and in the nearby energy regions of the present work.

reaction	energy (keV)	measured	reference
${}^7\text{Li} + d$	175 ~ 300	excitation function at 90°	Man64
${}^9\text{Be} + d$	120, 200	only angular distributions for p_0 , α_0 and α_1	Amb66
	100, 170, 200	only angular distributions for p_0 and t_0	Smi57
${}^{10}\text{B} + d$	140 ~ 280	only for p_0 , p_1 , p_2 and p_3	Har60
	320 ~ 1000	only for p_0 , p_1 , p_2 , α_0 and α_1 no cross sections reported	Lon66
${}^{11}\text{B} + d$	193 ~ 420	only angular distributions for p_0	Bea66
${}^7\text{Li}({}^3\text{He}, p_0){}^9\text{Be}(\text{gs})$	420 ~ 1800	cross section	Rat90

Fig. 1·5. The S-factor measured by Boyd and co-workers [Rat90] and the energy regions of the Gamow peaks.

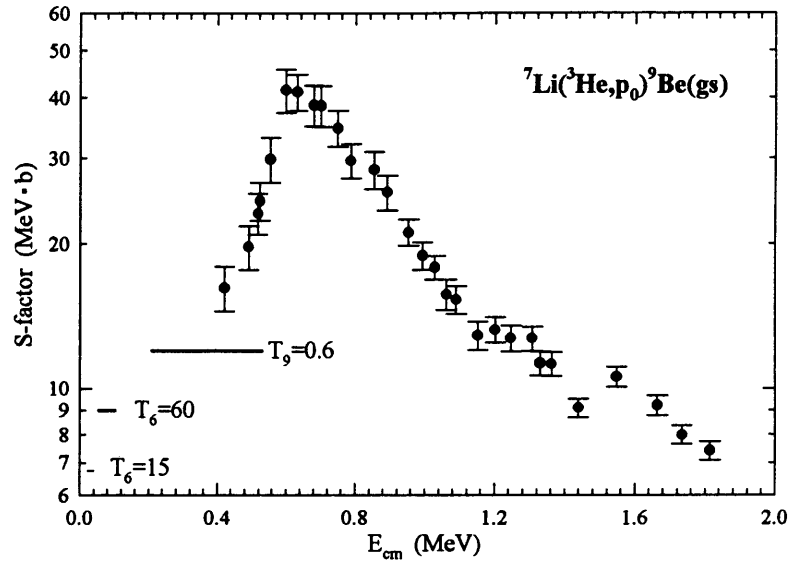


Table 1·3. An overview of the nuclear reactions studied in this thesis with the energy regions.

${}^7\text{Li} + {}^3\text{He} \rightarrow p_0 + {}^9\text{Be}(\text{gs}) ;$	$E_{\text{cm}} = 110 \text{ and } 120 \text{ keV}$
${}^7\text{Li} + d \rightarrow \alpha + {}^5\text{He} ;$	$E_{\text{cm}} = 30 \sim 130 \text{ keV}$
${}^9\text{Be} + d \rightarrow \left\{ \begin{array}{l} p_n + {}^{10}\text{Be}, \quad n = 0, 1 \\ t_0 + {}^8\text{Be} \\ \alpha_n + {}^7\text{Li}, \quad n = 0, 1 \end{array} \right\} ;$	$E_{\text{cm}} = 55 \sim 140 \text{ keV}$
${}^{10}\text{B} + d \rightarrow \left\{ \begin{array}{l} p_n + {}^{11}\text{B}, \quad n = 0, 1, \dots, 5 \\ \alpha_n + {}^{10}\text{Be}, \quad n = 0, 1 \end{array} \right\} ;$	$E_{\text{cm}} = 65 \sim 120 \text{ keV}$
${}^{11}\text{B} + d \rightarrow \left\{ \begin{array}{l} p_0 + {}^{12}\text{B} \\ \alpha_n + {}^9\text{Be}, \quad n = 0, 2 \end{array} \right\} ;$	$E_{\text{cm}} = 80 \sim 145 \text{ keV}$

1-6 SUMMARY AND ORGANIZATION OF THE THESIS

All the nuclear reactions studied in the thesis and the present energy regions are summarized in Table 1-3.

This thesis begins from an introduction in Chapter 1. In Section 1-2, the importance of the studied reactions is discussed from the point of view of astrophysical nucleosynthesis and two networks of reaction pathways are shown which allow ${}^9\text{Be}$, ${}^{10}\text{B}$, ${}^{11}\text{B}$ and, especially, ${}^{12}\text{C}$ to be produced in BBN and in the hydrogen burning stage of the p-p chains of SP, respectively. Section 1-3 sheds light on the significant applicability of the studied deuteron-induced reactions on ${}^9\text{Be}$, ${}^{10}\text{B}$ and ${}^{11}\text{B}$ to the diagnostics of first wall contamination in the JET and TFTR tokamaks. The energy regions of interest are determined in terms of the Gamow peak in Section 1-4, which is followed by a brief overview of the previous work on the reactions and near the energy regions.

Chapter 2 is focused on the experimental details. Section 2-1 describes the accelerator used here, the energy calibration of the accelerated ion beam, the secondary electron suppression in the reaction chamber, the target fabrications, the detection technique and the setups of the electronics. The success of the experimental technique can be found in Section 2-2, where the angular distribution and cross sections measured by other laboratories are reproduced and the data processing techniques are discussed. Section 2-3 presents the experimental details of the ${}^7\text{Li}({}^3\text{He}, p_0){}^9\text{Be}(\text{gs})$ reaction, such as the ${}^3\text{He}^+$ beam contamination and the electronic setups.

In Chapter 3, we present the results of our measurements of the reactions given in Table 1-3 using the techniques described in Chapter 2. Specifically we present total and differential cross sections over the energy regions, again given in Table 1-3. The astrophysical S-factors derived from these measurements are likewise given.

In Chapter 4, we use the S-factors presented in Chapter 3 to generate the reaction rates. These reaction rates are then used to calculate ${}^9\text{Be}$ production rates in primordial and stellar nucleosynthesis and γ -ray count rates in the case of first wall contamination of the fusion plasmas in the JET and TFTR tokamaks. Finally, some results of the single-step DWUCK4 calculations are given in Section 4-3.

The data fitting procedure used in this thesis and the original data of yields measured at different energies for all the studied reactions are given in the appendixes.

Chapter 2

EXPERIMENTAL TECHNIQUE

2·1 APPARATUS

2·1·1 The Accelerator and its Beams

All the experiments were carried out on the low-energy high-current charged-particle accelerator [Cec89] of General Ionex model 1545 in the Nuclear Physics Laboratory at Colorado School of Mines (CSM). Fig. 2·1(a) is a schematic view of the accelerator system. The current measured on target as a function of the programming voltage in the 90°-analyzing magnet power supply during normal hydrogen operation is given in Fig 2·1(b) [Cec89], which shows that the beam species are well separated. The beam is controlled by horizontal and vertical steering magnets and, finally, placed on target after passing through a collimator.

Before all the experiments, the beam energy was calibrated by the known resonance of $^{11}\text{B}(p,\alpha)^8\text{Be}$. The target used in the energy calibration was a thin film of natural boron deposited on a 15 μm Al foil with its thickness being 410 \AA , or, $\Delta = 6.6$ keV at a proton energy of 163 keV, the resonant energy. Because of the finite target thickness, the effective beam energy in target, E_{eff} , has to be considered, which is defined as [§5·5·4 in Rol88]

$$\int_{E_0-\Delta}^{E_0} \frac{1}{E\chi(E)} e^{-\sqrt{E_G/E_{\text{cm}}}} dE = 2 \int_{E_{\text{eff}}}^{E_0} \frac{1}{E\chi(E)} e^{-\sqrt{E_G/E_{\text{cm}}}} dE, \quad (2.1)$$

where E_0 is the beam energy before hitting the target, E_{cm} the CM value of the lab system energy E , and $\chi(E) = dE/dx$ the stopping power of the target material which is known numerically as a function of ion energy E . If we multiply the S-factor to the integrands in

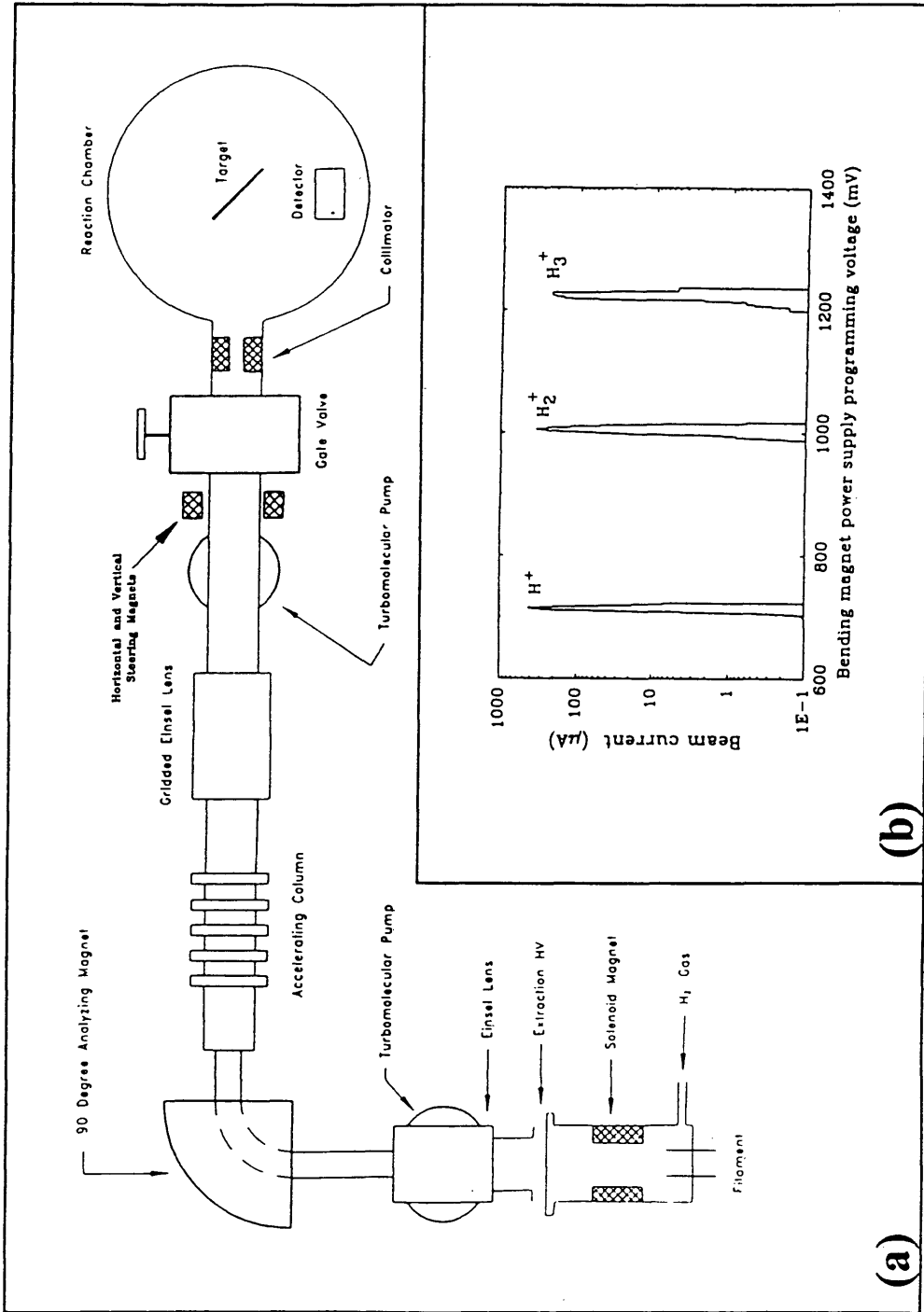


Fig. 2-1. The schematic view of the low-energy charged-particle accelerator in CSM Nuclear Physics lab (a) and current on target during normal hydrogen operation (b). (b) is reproduced from Cec89.

Eq. (2.1), the physical meaning of the effective beam energy in target will become clear: it corresponds to a beam energy in the target at which one half of the total reactions for the full target thickness take place.

The mechanisms of the $^{11}\text{B} + \text{p}$ reaction can be found in Fig. 2.2. The background consists of two continuums of α -particles from direct 3α -breakups and sequential decays via ^8Be . A measured spectrum can be found in Fig. 2.3(a) and Fig. 2.3(b) shows the measured resonance for the $^{11}\text{B}(p, \alpha_1)^8\text{Be}^*(3.04\text{MeV})$ reaction. The values for $E_{\text{eff-lab}}$ are computed from Eq. (2.1) with E_0 being the metered, i.e., uncalibrated, energy of the accelerator system. The solid line in Fig. 2.3(b) represents a fit of the measured data with a Breit-Wigner resonance [§4.3 in Rol88] plus a quadratic background

$$\left. \begin{aligned} f(E) &= \frac{a}{(E-b)^2 + c^2} + d + eE + fE^2 \\ f(E) &= \text{counts per } \mu\text{C}; \quad E = E_{\text{eff-lab}} \text{ in keV} \\ a &= 848; \quad b = 163.3; \quad c = 5.16 \\ d &= 422; \quad e = -5.42; \quad f = 0.017 \end{aligned} \right\} \quad (2.2)$$

Compared with the resonant energy and width (FWHM) in the lab system

$$\left. \begin{aligned} E &= 163.1 \text{ keV [Dav79]}; \quad 161.9 \pm 0.1 \text{ keV [Bec87]} \\ \Gamma &= 5.7 \pm 0.5 \text{ keV [Dav79]}; \quad 5.8 \pm 0.2 \text{ keV [Bec87]} \end{aligned} \right\}, \quad (2.3)$$

the uncalibrated beam energy has a negligible deviation of 0.2 keV.

Our measured width $\Gamma = 10.3$ keV is considerably larger. This difference in width can not be related solely to the energy spread in the beam and can also be attributed to several other facts, such as the $\Delta = 6.6$ keV finitely thick target of which the effect is to lower and broaden the measured resonant peak, the fact that Eq. (2.1) does not consider the change of the resonant S-factor with energy, and so on. Since the quoted stability of the accelerator system is about 100 eV, and since the beam line operating vacuum of a few 10^{-7} torr will cause very little beam energy loss or dispersion, the actual energy spread of the beam is probably much less than 1 keV [Cec89].

Used in the energy calibration was the $^{11}\text{B}(p, \alpha_1)^8\text{Be}^*(3.04\text{MeV})$ reaction, of which the α_1 -peaks in the measured spectra overlap with the two continuums (see Fig.

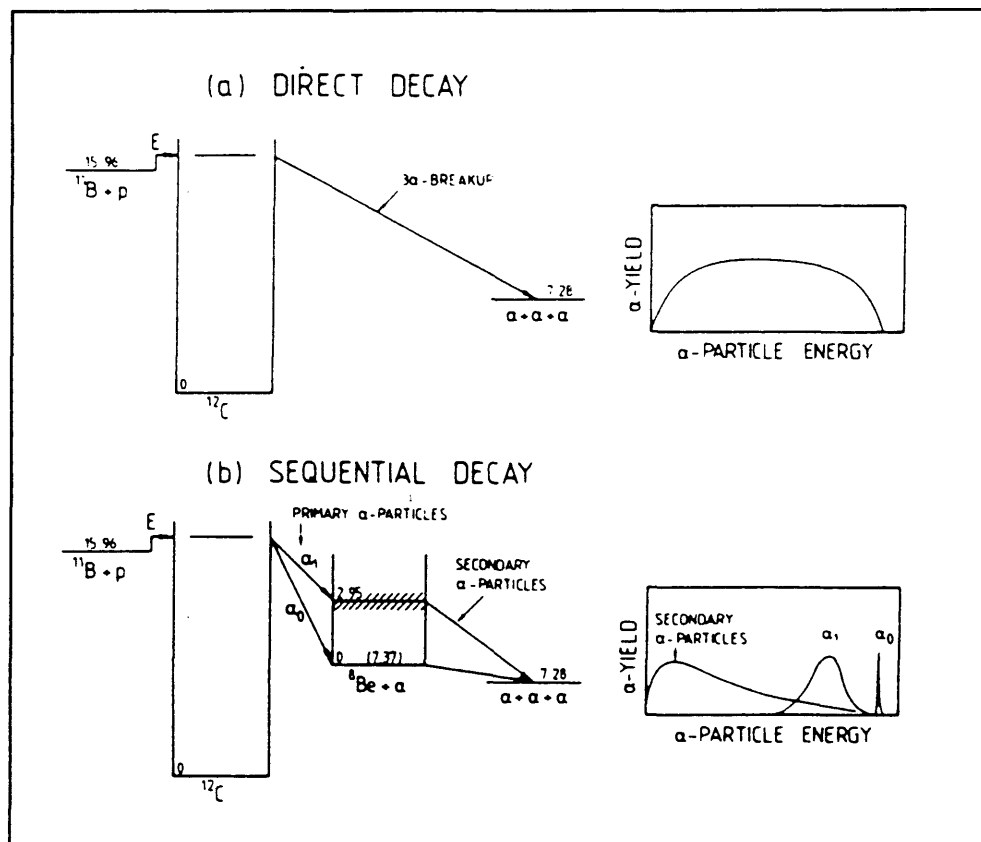


Fig. 2-2. Formation of α -particle spectrum for the $^{11}\text{B} + p$ reaction. (a) is a direct breakup into three α -particles. (b) is a sequential decay via the ground state (FWHM $\Gamma = 6.8$ eV) and the first excited state ($\Gamma = 1.5$ MeV) of ^8Be [Ajz84]. Note that in both cases the spectra comprise a continuum and that the primary α_0 -particle peak is almost uninfluenced by the continuum. The figure is reproduced from Bec87.

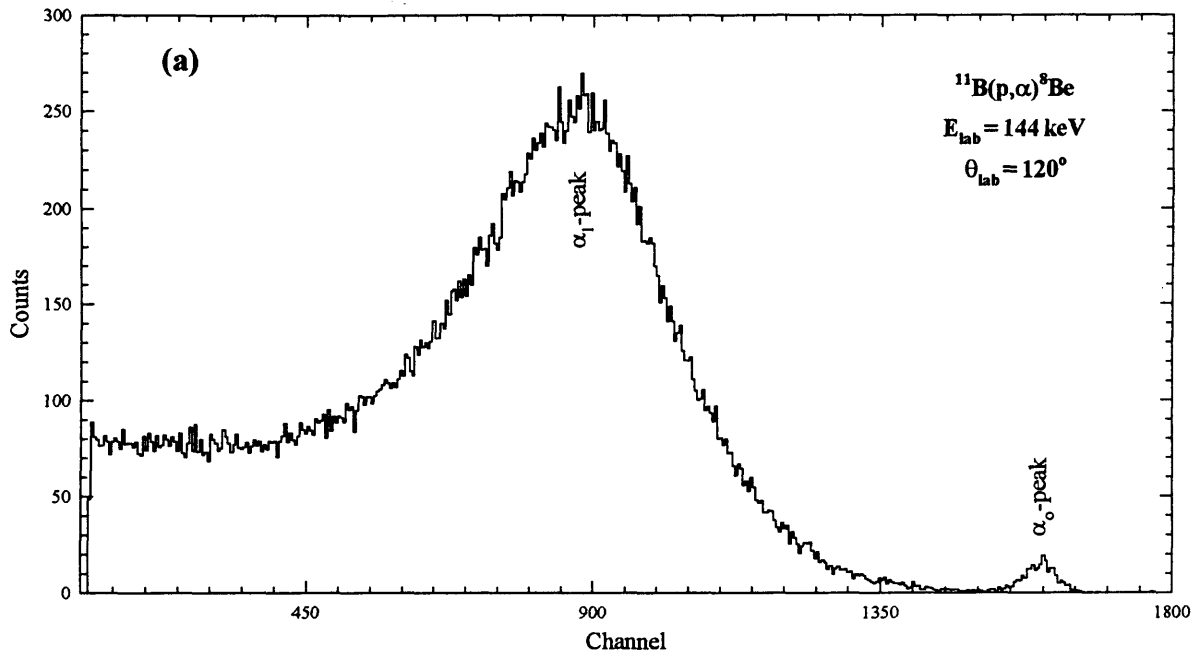
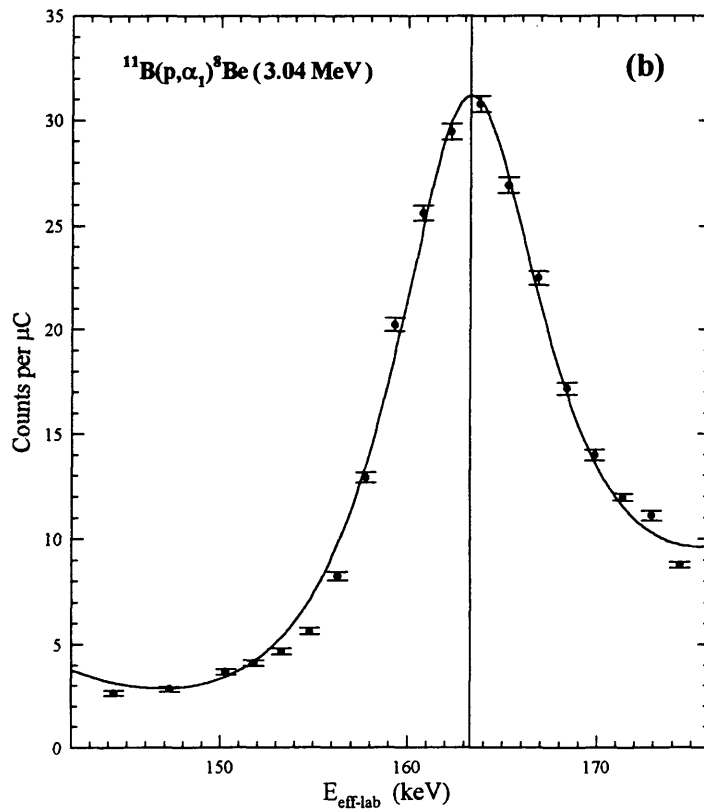


Fig. 2.3. A measured spectrum from $^{11}\text{B}(p,\alpha)^8\text{Be}$ reaction (a) and the energy calibration of the accelerator (b). A thin film target deposited with natural boron was used. The horizontal axis in (b) is the effective beam energy in the target in the lab system resulting directly from the high-voltage reading from the accelerator system. The maximum occurs at 163.3 keV, compared with the true value of 163.1 keV for the resonant energy.



2.2), rendering it difficult and inaccurate to read the counts of the α_1 -particles from the spectra. But this will not create any apparent error in the measured resonant energy since no absolute measurements are needed in an energy calibration.

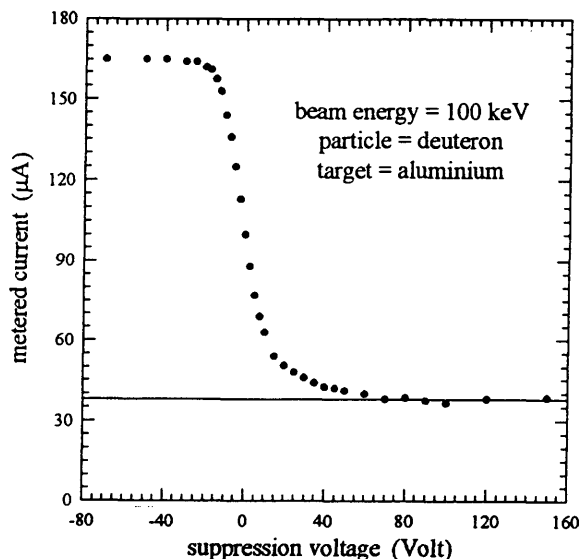
Another important character of the beam is its contamination. The effect of the contamination of the deuteron beams can not be seen on the observed spectra of the deuteron-induced reactions. In the ${}^7\text{Li}({}^3\text{He}, p_0){}^9\text{Be}(\text{gs})$ reaction, the contamination of the ${}^3\text{He}$ beams would cause some problems and will be discussed later on.

2.1.2 Setups in the Reaction Chamber

A reaction chamber of 27 cm diameter was used in all the experiments. The targets were mounted in target holders and were 360°-turnable. The accelerated beams passed through an Al collimator of about 6 mm diameter, were focused into a spot of about the same diameter approximately at the center of targets and, finally, stopped in targets or in the backing materials of thin film targets, which were Al foils of 15 μm , thick enough to stop the beams. The target holders were electrically insulated from the reaction chamber and total charge accumulations were measured from targets.

Accurate measurements of the total charges accumulated in targets by integrating incident beam currents are one of the key factors in obtaining absolute cross sections. A problem associated with these measurements is the production of secondary electrons—when a beam strikes any material, it liberates secondary electrons from the surface of the material, causing an error in the measurement of the beam current. Thus the targets, as beam catchers in our experiments, must have provision for the effective suppression of secondary electrons. We relied on the usual solution to the problem and a positive voltage with respect to our reaction chamber as ground was applied to targets. A measurement of the metered beam current versus the suppression voltage was carried out and yielded Fig. 2.4. When the suppression voltage was greater than 70 V, the minimum effective suppression voltage obtained under the circumstances of our experimental conditions, all secondary electrons were drawn back to the target and, then, only at this stage, did the metered current reflect the real beam current. The value of the minimum effective suppression voltage was found to be roughly independent of the beam

Fig. 2-4. Suppression for the secondary electrons. The minimum effective suppression voltage is about 70V and this value does not change significantly with the beam energy and current.



current and energy. Therefore, for all the experiments on the nuclear reactions studied in the present work, a suppression voltage of 90 V was used.

There are other possible problems which may occur in the experiments, such as carbon buildup on targets and an electron beam accompaniment of the accelerated ion beam. These experimental-condition (or accelerator-condition) dependent problems were demonstrated to be unobservable in our measurements by the successful reproduction of results of ${}^7\text{Li}(p,\alpha){}^4\text{He}$ and ${}^{11}\text{B}(p,\alpha_0){}^8\text{Be}(\text{gs})$ reactions reported in publications (see Section 2-2 for detail).

Silicon surface-barrier detectors, sometimes ΔE -E detector telescopes, were used, which were covered with $1\mu\text{m}$ Ni foils or $6\mu\text{m}$ Al foils to stop the intense flux of elastically scattered particles from targets. The active areas of detectors and detector telescopes were defined by detector apertures that were put on the front of them. For the deuteron-induced reactions, since the distances of about 9 cm from beam spots on targets to detector apertures are relatively large, the solid angles of detectors were determined by these carefully measured distances and by the aperture areas. Sometimes, monitors fixed at 90° at a distance of about 6 cm from targets were used and some of the experimental problems, for example, the evaporation of target materials due to heating by beam bombardments and the error in the integration of beam current to get the total charge,

could be eliminated when using the ratio of counts of the same peak from the detector spectrum to that from the monitor spectrum.

The thin film targets were fabricated by evaporation of natural LiF or natural boron onto 15 μm Al foils. The thicknesses of the thin films were measured by the Alpha-Step Profiler in CSM Department of Physics. Since these thin film targets were used only in the measurements of relative quantities, such as angular distributions and the energy calibration, their thicknesses are not critical in the measurement precision. When thin film targets were used, the beam currents were controlled to be as low as 5 μA , so that the target evaporation was not observed.

The targets for ${}^9\text{Be} + d$ reaction were a plate of pure (purity >99%) beryllium metal with a polished surface. The infinitely thick targets used in studied reactions of ${}^7\text{Li} + d$, ${}^{10}\text{B} + d$ and ${}^{11}\text{B} + d$, and in the test experiments on reactions of ${}^7\text{Li}(p, \alpha){}^4\text{He}$ and ${}^{11}\text{B}(p, \alpha_0){}^8\text{Be}(\text{gs})$, were made by pressing natural LiF powder (purity >99%), 90%-enriched ${}^{10}\text{B}$ powder and natural boron powder (purity >99%) into target holders of 3~4 cm diameters, respectively. For each of the LiF targets, a fine metal mesh electrically connected to the target holder was placed right under the LiF surface.

In measurements of angular distributions, active windows of detectors and detector telescopes were limited by slit apertures, such as $\sim 3.5 \times 14 \text{ mm}^2$. Detectors could be rotated from 0° to 160° and the beam was placed at the rotation axis. The accuracy in angular positions was estimated to be $\pm 2^\circ$.

2-1-3 The Electronics Setups

The electronics used with single-detector measurements and the beam current integration electronics are shown in Fig. 2-5. These setups were used with the experiments on the ${}^2\text{H}(d, p){}^3\text{H}$, ${}^7\text{Li}(p, \alpha){}^4\text{He}$, ${}^{11}\text{B}(p, \alpha_0){}^8\text{Be}(\text{gs})$, ${}^7\text{Li} + d$, ${}^9\text{Be} + d$, ${}^{10}\text{B} + d$ and ${}^{11}\text{B} + d$ reactions. The dead time of the electronics was controlled to be less than about 1% by selecting low beam currents and small detector apertures.

The electronics setups used with ΔE -E detector telescopes are given in Fig. 2-6. These setups were used with the experiments on the ${}^{10}\text{B} + d$ and ${}^7\text{Li}({}^3\text{He}, p_0){}^9\text{Be}(\text{gs})$ reactions.

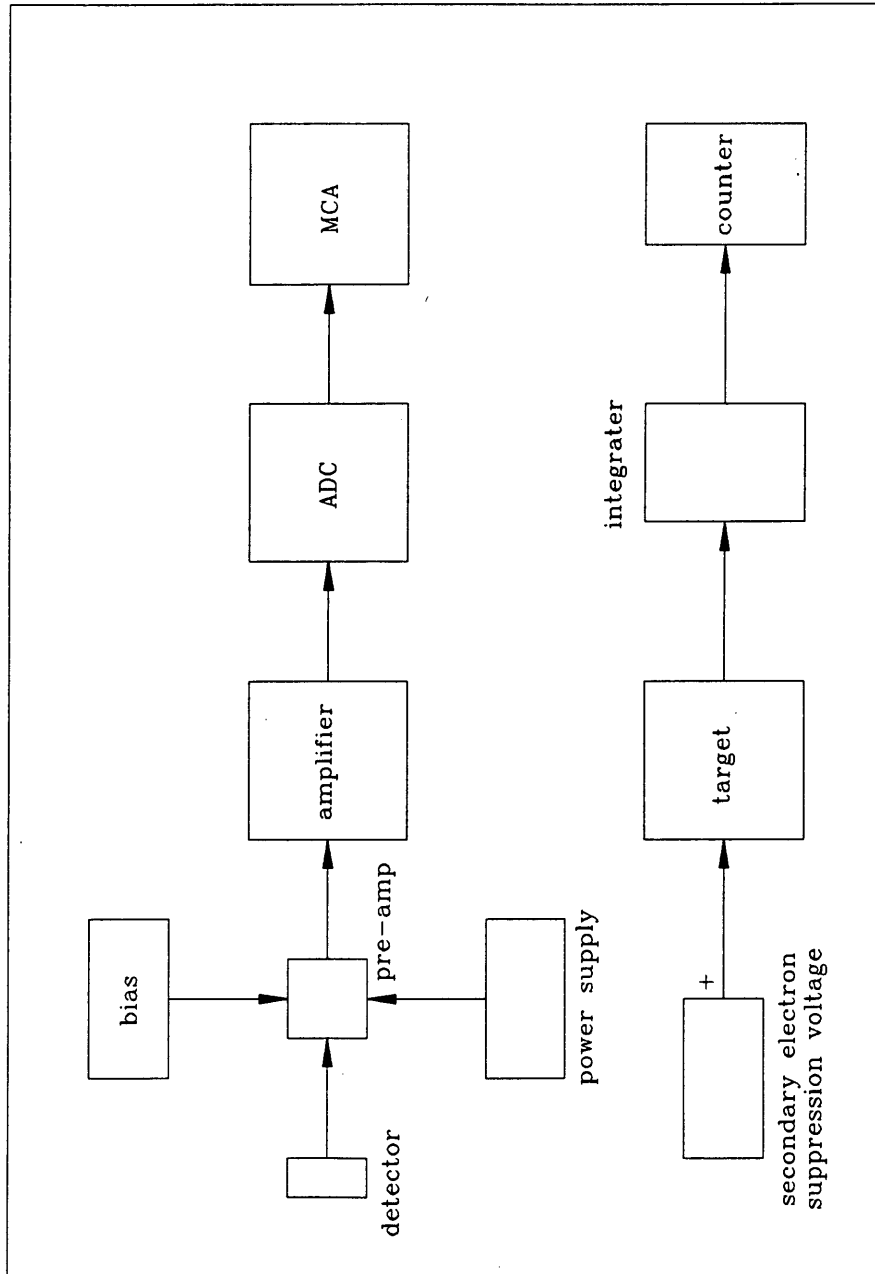


Fig. 2.5. The electronics setups for single-detector measurements.

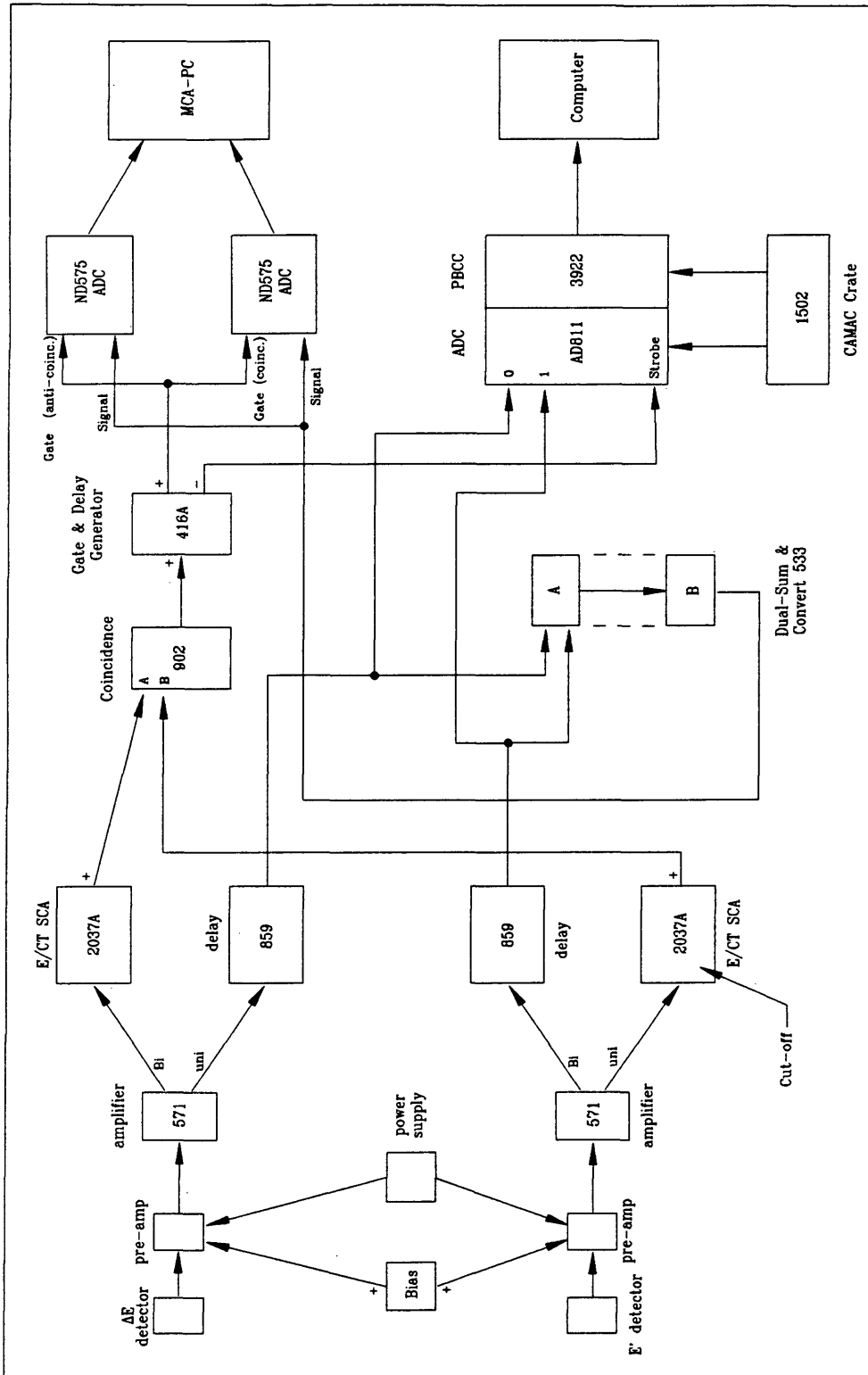


Fig. 2-6. The electronics setups for ΔE -E measurements.

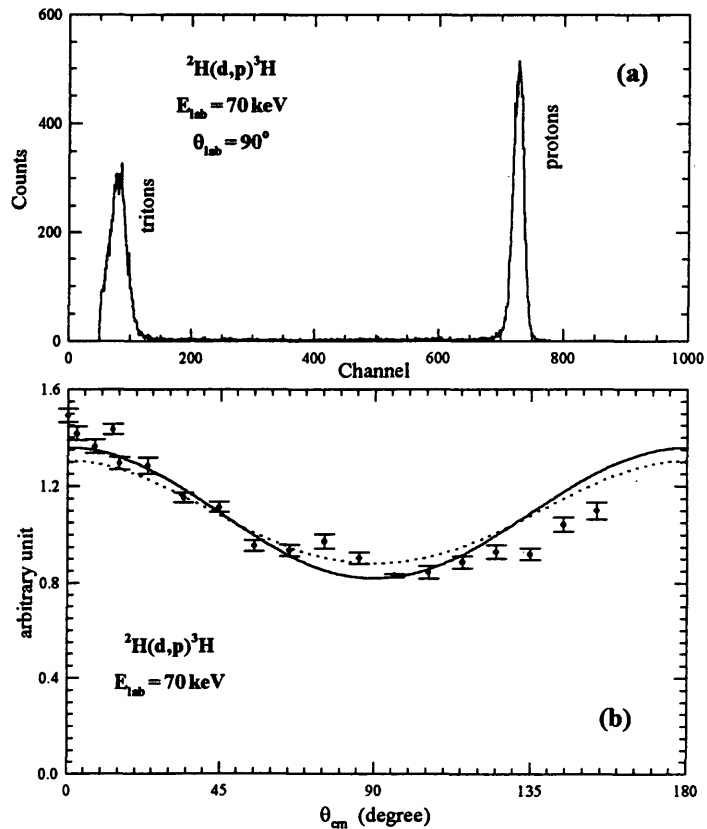
2-2 TEST EXPERIMENTS

In order to check the technique used in the present work, three test experiments were accomplished on the reactions of ${}^2\text{H}(d,p){}^3\text{H}$, ${}^7\text{Li}(p,\alpha){}^4\text{He}$ and ${}^{11}\text{B}(p,\alpha_0){}^8\text{Be}(\text{gs})$, of which each has been measured carefully by several well-known laboratories.

2-2-1 The Angular Distribution of ${}^2\text{H}(d,p){}^3\text{H}$

The used target was a $23\mu\text{m}$ Al foil that was deuterium-saturated prior to the experiment by bombardments with deuteron beams of energy from 10 keV up to 120 keV at 10 keV steps. The angular distribution was measured at a 70 keV deuteron energy. Both a detector and a monitor were used. Fig. 2-7(a) illustrates a measured spectrum of

Fig. 2-7. A measured spectrum (a) and the measured angular distribution (b) for the ${}^2\text{H}(d,p){}^3\text{H}$ reaction. Data were read from the proton peaks of the spectra. The solid line in (b) is the least-squares fit to our measured data while the dotted line reproduces the result from reference [Bro90] for comparison.



charged particles. The 0.8 MeV ^3He particles produced from $^2\text{H}(d,^3\text{He})n$ of 3.27 MeV Q-value were stopped in the $6\mu\text{m}$ Al foils on the front of the detector and monitor, thus can not be seen from the spectrum.

Fig. 2-7(b) is our measured angular distribution at $E_d = 70$ keV. The data point at each angle resulted from the ratio of counts of the proton peak in the detector spectrum to that in the monitor spectrum and this would remove the effect of the accumulation of beam deuterons in the target. The measured data were fitted by least-squares to

$$\left. \begin{aligned} W(\theta_{\text{cm}}) &= 1 + a_2 P_2(\cos\theta_{\text{cm}}) \\ a_2 &= 0.36 \pm 0.02 \end{aligned} \right\}, \quad (2.4)$$

where $P_l(x)$ is a Legendre polynomial. Because of the identical character of the bosons in the entrance channel, $W(\theta_{\text{cm}})$ does not have any odd Legendre polynomial terms and is symmetrical about $\theta_{\text{cm}} = 90^\circ$. The recently published data for the angular distribution at the same bombarding energy are

$$\left. \begin{aligned} W(\theta_{\text{cm}}) &= 1 + a_2 P_2(\cos\theta_{\text{cm}}) + a_4 P_4(\cos\theta_{\text{cm}}) \\ a_2 &= 0.31 \pm 0.02; \quad a_4 = 0.04 \pm 0.03; \quad [\text{Kra87}] \\ a_2 &= 0.313; \quad a_4 = 0.015; \quad [\text{Bro90}] \end{aligned} \right\}. \quad (2.5)$$

The errors in the Bro90's data are not available since, in the paper [Bro90], the angular distribution was reported in the form of $W(\theta_{\text{cm}}) = a + b \cos^2\theta_{\text{cm}} + c \cos^4\theta_{\text{cm}}$ and the error matrix for a, b and c was not given. The dotted line in Fig. 2-7(b) plots the shape of the angular distribution from Bro90.

It is clear in Fig. 2-7(b) and by comparison of Eq. (2-4) with Eq. (2-5) that the angular distributions are consistent with each other. Note that Eq. (2-5) and the dotted line in Fig. 2-7(b) are the thin target results while our angular distribution is measured with a thick target. But, since the contributions to our thick target angular distribution are mainly from the high energy part, the comparison between the present and published data is approximately valid.

2.2.2 Measurements from Infinitely Thick Targets

The commonly used targets include gas targets and thin film targets, but some of the targets used in this thesis were made of bulk materials, with the thicknesses greater than the penetration range of the incident beam particles at the used energy, hence called infinitely thick targets. In addition to the convenience of fabrications, there are other advantages in the use of infinitely thick targets. First, these targets will increase the detector counting rates. This is particularly important for the ${}^7\text{Li}({}^3\text{He}, p_0){}^9\text{Be}(\text{gs})$ reaction where the cross sections at the present energies are as small as 10^{-5} μb . The second advantage is that thin films of some materials tend to be very difficult to handle in experiments or in the film fabrications; one example is related to lithium, an extremely active element that will be oxidized very quickly in the air, and beryllium, a toxic material, is another example.

The disadvantage brought by infinitely thick targets is that each measured spectrum comes from an integration over an energy region from zero to the bombarding energy and the cross section at each energy can not be obtained directly from one measurement in an explicit way. Therefore, techniques for data reduction must be developed to get cross sections.

The first method used in this thesis is to fit the measured yields¹ of an infinitely thick target using an appropriate S-factor. Among the measured N yields, the i^{th} yield Y_i at a bombarding energy E_i and angle θ_i can be formulated by

$$Y_i = \frac{1}{4\pi} \nu n_t \int_0^{E_i} \frac{\sigma(E)}{\chi(E)} \left[\int_{\Omega_d} W_i(\theta, E) d\Omega \right] dE, \quad (i = 1, 2, \dots, N),$$

where Ω_d is the solid angle of the detector², ν the number of detected particles produced from each reaction (e.g., $\nu=2$ for ${}^7\text{Li}(p, \alpha){}^4\text{He}$), n_t the number density of the target

¹ The terminology "yield" used in this thesis implies the ratio of the detected particles to the total charge of the beam integration in the detection, unless otherwise specified.

² For a low bombarding energy, i.e., an energy much smaller than the Q-value, Ω_d is approximately the same in both the lab and CM systems, and is approximately independent of the bombarding energy. In the present work, where bombarding energies are less than 180 keV and the Q-values for the studied reactions are larger than a few MeV, the same value of Ω_d is used regardless of the lab and CM systems and the bombarding energy.

nuclei, E an energy in the lab system and $W_i(\theta, E)$ the CM angular distribution for the measurement of the yield Y_i . The effect of the beam energy spread has been ignored in the above equation. With the average value $\overline{W}_i(E)$ of the angular distribution at θ_i over Ω_d , the above equation can be rewritten as

$$Y_i = \frac{\Omega_d}{4\pi} v n_t \int_0^{E_i} \frac{\sigma(E)}{\chi(E)} \overline{W}_i(E) dE. \quad (2.5a)$$

In this thesis, the angular distributions for the deuteron-induced reactions on ^9Be , ^{10}B and ^{11}B were measured with infinitely thick targets. These infinitely thick target angular distributions, symbolized by $\overline{\overline{W}}_i(E_i)$, have represented the average values over the energy regions from zero to E_i . Hence, we have

$$Y_i = \frac{\Omega_d}{4\pi} v n_t \overline{\overline{W}}_i(E_i) \int_0^{E_i} \frac{\sigma(E)}{\chi(E)} dE. \quad (2.6)$$

Using the S-factor in Eq. (1.4), Eq. (2.6) can be expressed as

$$Y_i = \frac{\Omega_d}{4\pi} v n_t \overline{\overline{W}}_i(E_i) \int_0^{E_i} \frac{S(E_{cm})}{E_{cm} \chi(E)} e^{-\sqrt{E_\alpha/E_{cm}}} dE, \quad (2.7)$$

where E_{cm} in the integrand is the CM energy with respect to E . With the known knowledge of the infinitely thick target angular distribution, after given an appropriate expression of the S-factor, the measured yields $\{Y_i | i = 1, 2, \dots, N\}$ can be fitted numerically and the S-factor as a function of energy can be obtained.

If there is no resonance encountered within the region of the bombarding energies, that is, any energy value within the region does not fall in the limits between $E_R - 2\Gamma$ and $E_R + 2\Gamma$ for any possible resonance of energy E_R and width (FWHM) Γ , the S-factor is a slowly changing function of energy. In the present study, since the region of bombarding energy is relatively narrow, from 30 keV to 180 keV, a quadratic polynomial of energy can be good enough to express the S-factor. If there do exist resonances, like Eq. (2.2), an expression with Breit-Wigner terms plus a nonresonant background must be used.

The other method used here is to take the difference of two successive yields. If the difference between E_i and E_{i-1} is sufficiently small, Eq. (2.6) will lead to

$$\sigma(E_{\text{eff}}) = \frac{4\pi\chi(E_{\text{eff}})}{\Omega_d v n_t W_i(E_{\text{eff}})} \frac{Y_i - Y_{i-1}}{E_i - E_{i-1}}, \quad (2.8)$$

where E_{eff} is the effective energy calculated between E_i and E_{i-1} by Eq. (2.1). The precaution on the method must be given in the following. On the one hand $E_i - E_{i-1}$ must be small enough to have a good approximation by E_{eff} , on the other hand the closer E_i and E_{i-1} will certainly result in a smaller difference between Y_i and Y_{i-1} , from which comes $\sigma(E_{\text{eff}})$, thus a larger error in the cross section will inevitably exist in taking place. Therefore, because of the dilemma, the author prefers the first method, the S-factor fit.

The following two examples show our measurements and data reduction from infinitely thick targets with and without a resonance.

2.2.3 Yield Measurements on ${}^7\text{Li}(p,\alpha){}^4\text{He}$ Reaction: An Example without Resonance

Since the ${}^7\text{Li}(p,\alpha){}^4\text{He}$ reaction ($Q = 17.35$ MeV), as the most important process to destroy the ${}^7\text{Li}$ produced in BBN and SP, is of significant astrophysical interest, it has been re-measured recently by three groups of experimentalists [Rol86; Rai90; and Eng92]. This reaction was selected as one of our test experiments and the measurements of infinitely thick LiF targets were done. Fig. 2.8(a) is an observed spectrum of charged particles. Since the natural targets were used, the proton beams would react with the target ${}^6\text{Li}$ nuclei (abundance = 7.5%), yielding ${}^3\text{He}$ and α -particles of energy 2.3 MeV and 1.7 MeV, respectively, from ${}^6\text{Li}(p,{}^3\text{He}){}^4\text{He}$ reaction ($Q = 4.02$ MeV). The leftover energy of the ${}^3\text{He}$ particles after punching through the $6\mu\text{m}$ Al foil on the front of the detector is 0.7 MeV while the α -particles will stop in the foil. The peak at the left in Fig. 2.8(a) came from the ${}^3\text{He}$ particles.

The angular distributions at different energies have been measured in Rol86 and Rai90, and their results show that the a_2 coefficient in the Legendre polynomial expansion

$W(\theta_{\text{cm}}) = 1 + a_2 P_2(\cos\theta_{\text{cm}})$ is less than 0.05 in the CM energy region from 40 to 120 keV, which is also the energy region used in the test experiment. Therefore, isotropic angular distributions were assumed in the test experiment and all the measurements of yields were carried out at an angle of 90° in the lab system. This would bring in errors less than 2.5%, i.e., $a_2/2$, to the measured yields.

The open circles in Fig. 2-8(b) symbolize the measured yields. Yields calculated from the published data [Rol86; and Eng92] are also plotted in Fig. 2-8(b) by the dotted and dashed lines for comparison. The solid line in this figure is the S-factor fit to our measured yields and the found S-factor is

$$S \text{ (in MeV} \cdot \text{b)} = 0.056 + 0.22E_{\text{cm}} + 0.06E_{\text{cm}}^2, \quad (E_{\text{cm}} \text{ in MeV}). \quad (2-9)$$

This S-factor is shown in Fig. 2-9(a). The second method of reduction for cross section by Eq. (2-8) was used and the obtained cross section is given in Fig. 2-9(b) with the error bars being only from the statistics in counts. Note that a good agreement has been achieved in both S-factor and cross section with the published data.

The data points represented by open circles in Fig. 2-8(a) were measured without use of a beam collimator at the entrance of the reaction chamber. In order to see if a collimator will create some problems, for example, electrons possibly pulled out of the collimator material by the sweeping-over beam that may be drawn to the target by the 90V secondary electron suppression voltage, a collimator was used and the above measurements were briefly repeated. The yields measured with a collimator are plotted by the filled squares in Fig. 2-8(b) and the reduced cross section is given in Fig. 2-9(b). This brief experiment confirms that a collimator will not lead to any observable problems, hence collimators were used later on.

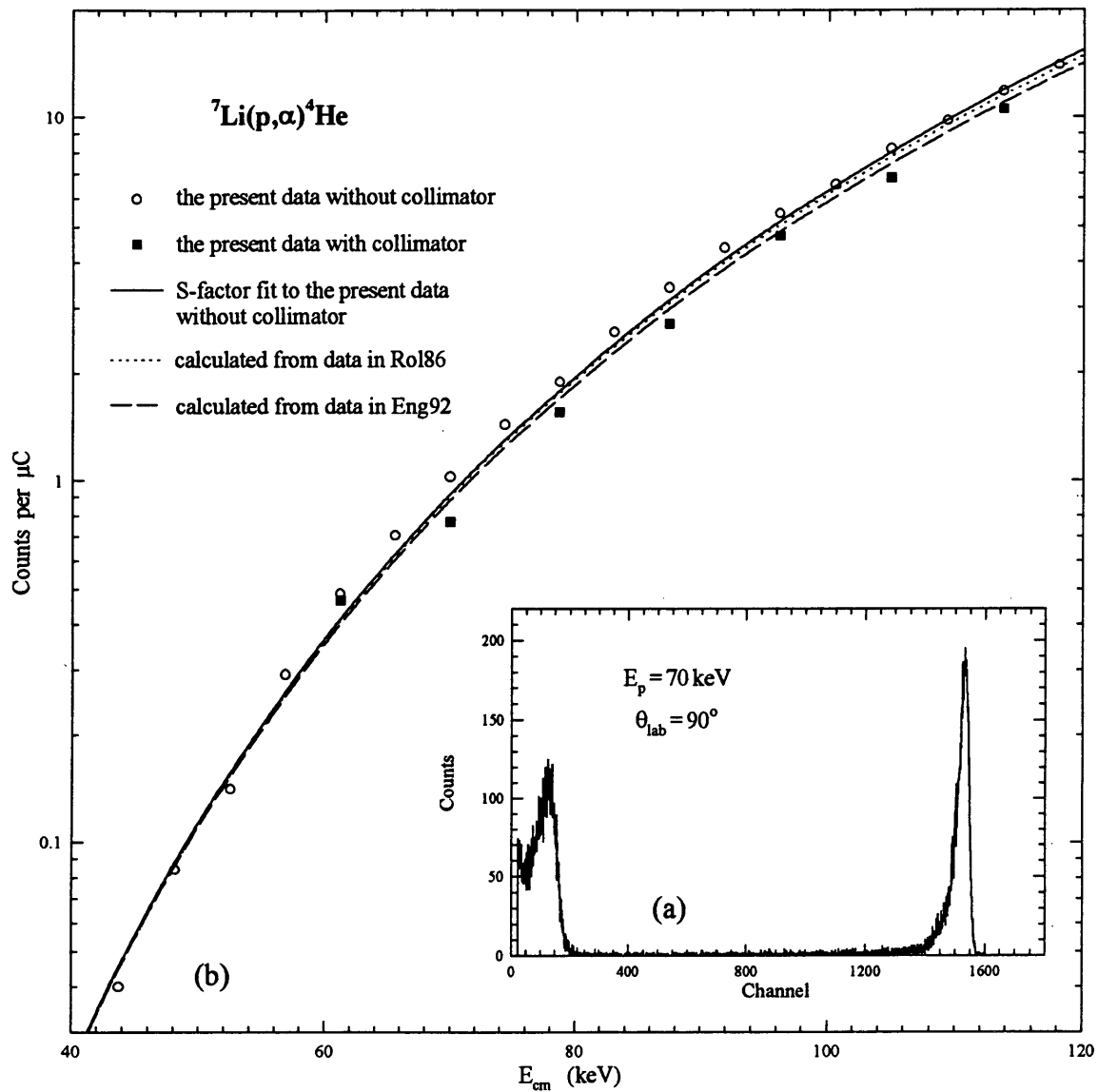


Fig. 2-8. A spectrum (a) and the yields (b) measured for ${}^7\text{Li}(p,\alpha){}^4\text{He}$ reaction. The used targets were made of natural LiF with infinite thicknesses. The peak at lower energy in (a) is from ${}^6\text{Li}(p,{}^3\text{He}){}^4\text{He}$ reaction. The yields were measured with and without a collimator for the incident proton beams. Yields calculated from published data [Rol86; and Eng92] are also plotted as comparison. The solid line is a fit to the present data without collimator using a quadratic S-factor.

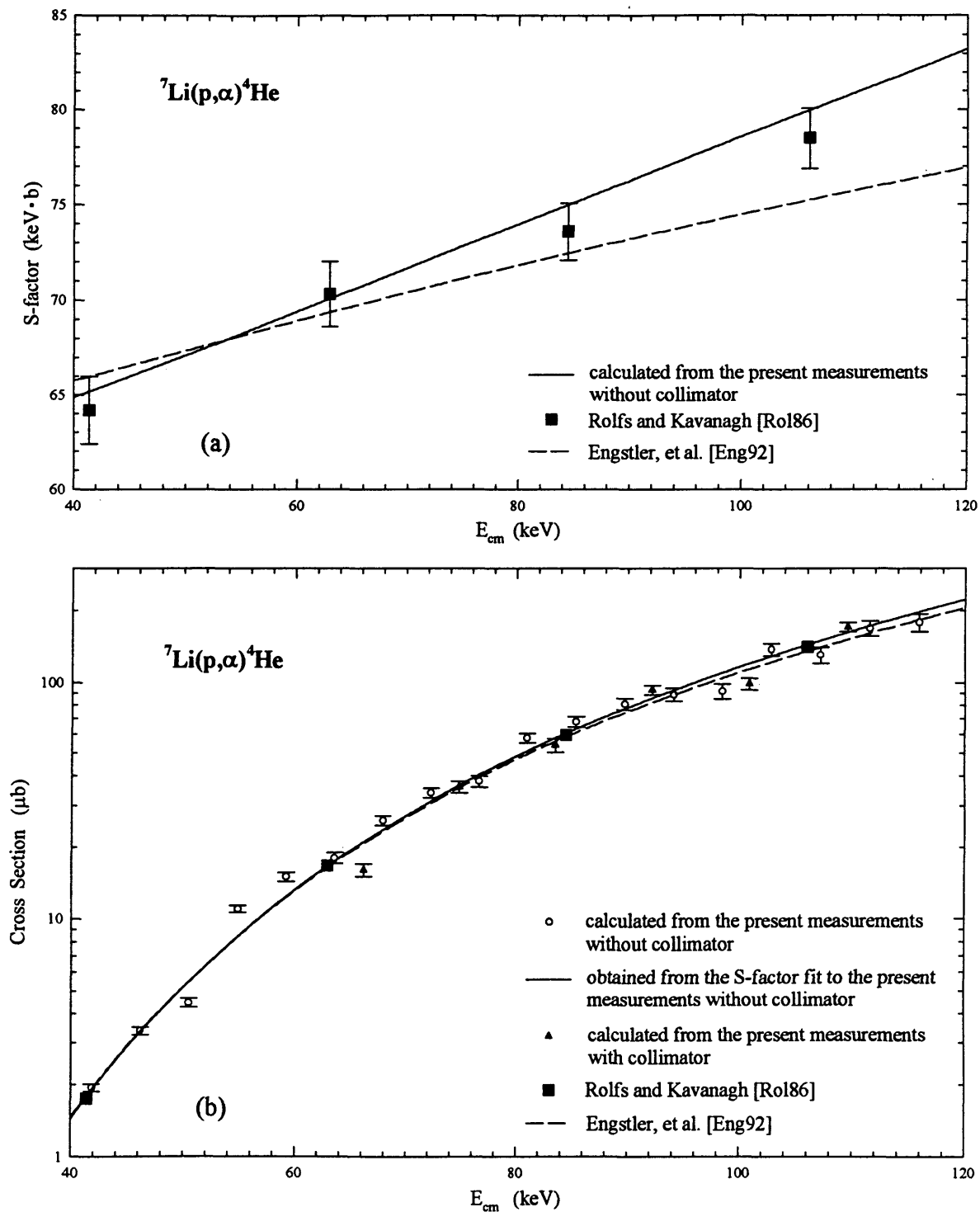


Fig. 2-9. The S-factor (a) and cross section (b) for ${}^7\text{Li}(p,\alpha){}^4\text{He}$.

2·2·4 Yield Measurements on $^{11}\text{B}(p,\alpha_0)^8\text{Be}(\text{gs})$ Reaction: An Example with a Resonance

The mechanisms of the $^{11}\text{B}+p$ reaction were previously given in Fig. 2·2 and a measured spectrum can be found in Fig. 2·3(a). From the energy values in Fig. 2·2, and assuming a low bombarding energy (~ 0.1 MeV), quick estimations in kinetics will lead to the following numbers: The maximum energy of the 3α -breakup spectrum is 4.4 MeV, the maximum energy of the secondary α -particles is 2.6 MeV, and the very sharp α_0 -peak is at 5.8 MeV. Therefore, the α_0 -peak from the $^{11}\text{B}(p,\alpha_0)^8\text{Be}(\text{gs})$ reaction is a "clean" peak without the background from the two continuums. The yields of the α_0 -peak were measured with infinitely thick targets of natural boron at an angle of 91° in the CM system. The data points in Fig. 2·10 plot the measured yields.

The angular distributions for the reaction has been measured in Dav79 and Bec87. Fig.2·11 illustrates the trend in the a_1 and a_2 coefficients of the Legendre polynomial expansion

$$W(\theta_{\text{cm}}) = 1 + a_1 P_1(\cos\theta_{\text{cm}}) + a_2 P_2(\cos\theta_{\text{cm}}). \quad (2·10)$$

In order to compare our measured yields with the published data, the solid line in Fig. 2·10 was calculated with the published differential cross section [Bec87] at $\theta_{\text{cm}} = 91^\circ$. Note that in the region where $a_2=0$, no matter what value a_1 takes, a measurement at $\theta_{\text{cm}} = 90^\circ$ will always yield the average value of angular distribution, hence it is only the nonzero a_2 at an energy between 140 keV and 160 keV that will affect the calculated yield at $\theta_{\text{cm}} = 90^\circ$.

It can be seen from Fig. 2·10 that our measured yields agree with the published data even in the resonant region.

To conclude this Section, an angular distribution for the $^2\text{H}(d,p)^3\text{H}$ reaction and yields from infinitely thick targets on the reactions of $^7\text{Li}(p,\alpha)^4\text{He}$ and $^{11}\text{B}(p,\alpha_0)^8\text{Be}(\text{gs})$ were measured, and two procedures of data processing for the measured yields were summarized. The results of the angular distribution and yields are in excellent agreement with those published, thus demonstrating that the experimental technique and data reduction methods are successful.

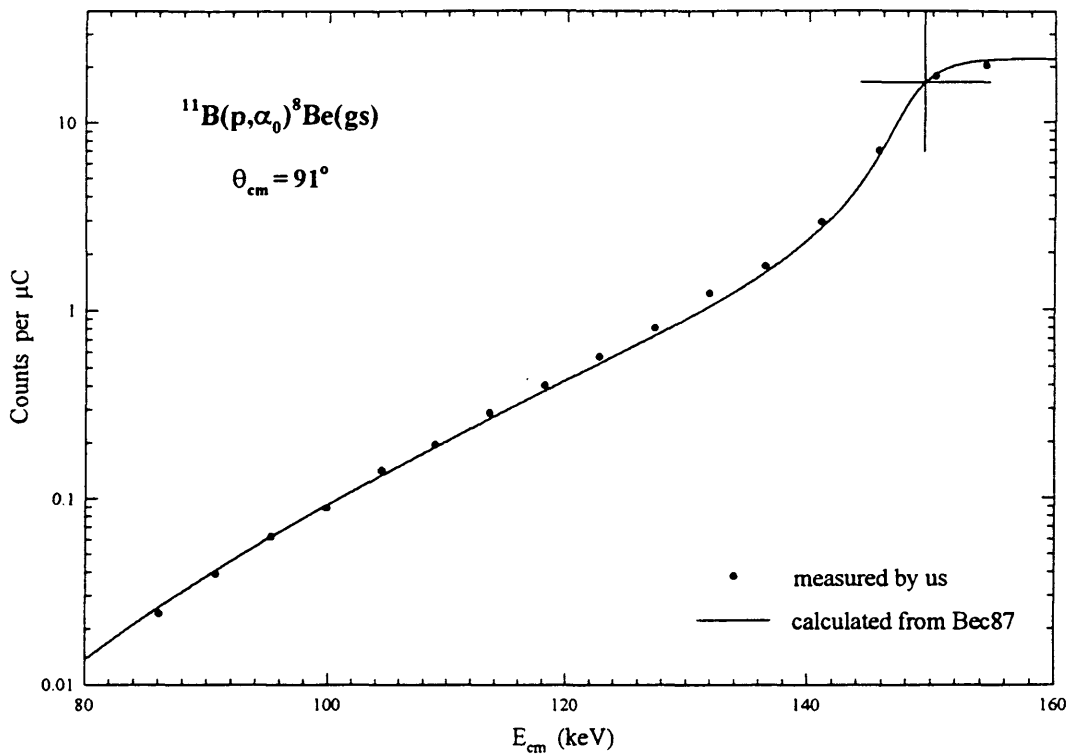
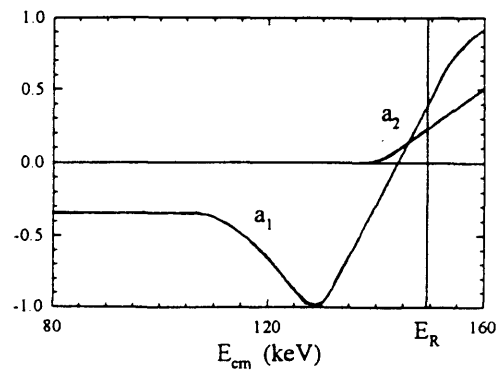


Fig.2-10. The measured yields for the $^{11}\text{B}(p,\alpha_0)^8\text{Be}(\text{gs})$ reaction. The reaction exhibits a resonance of 149.4 keV resonant energy and 5.3 keV width in the CM system [Ajz84], as shown by the cross. Yield (the solid line) is also calculated from the published data [Bec87].

Fig. 2-11. The trend in angular distribution for the $^{11}\text{B}(p,\alpha_0)^8\text{Be}(\text{gs})$ reaction. This figure reproduces the results in Dav79 and Bec87. a_1 and a_2 are the coefficients in $W(\theta_{\text{cm}}) = 1 + a_1P_1(\cos\theta_{\text{cm}}) + a_2P_2(\cos\theta_{\text{cm}})$ and E_R is the resonant energy.



2-3 EXPERIMENTAL DETAILS ON THE ${}^7\text{Li}({}^3\text{He}, p_0){}^9\text{Be}(\text{gs})$ REACTION

2-3-1 The Setups

Since the bombarding energy of the ${}^3\text{He}^+$ particles, around 160keV, was far below the Coulomb barrier for the ${}^7\text{Li}({}^3\text{He}, p_0){}^9\text{Be}(\text{gs})$ reaction, a very small cross section could be expected, making it essential to increase the counting rate of the protons produced from the reaction. Two measures were taken in the experiment, i.e., use of a pure lithium target and close detector geometry.

Targets of pure lithium, instead of any compound of lithium, were used for the sake of maximizing the number density of target nuclei. These targets were made of natural lithium metal (analytically pure), containing 7.5% of ${}^6\text{Li}$ nuclei, with infinite thicknesses in the point of view of the incident ${}^3\text{He}^+$ beams. In order to reduce the oxidation, the targets were operated and polished under Ar gas and, then, kept under vacuum of less than 10^{-6} torr. Glinting surfaces of the targets could be seen before bombardment.

A close geometry in detection was adopted and no aperture was used on the front of the detector telescope. The solid angles of detection were determined by ${}^{10}\text{B}(\text{d}, p){}^{11}\text{B}$ reaction, of which the cross sections and angular distributions had been measured carefully in the present work prior to the ${}^7\text{Li}({}^3\text{He}, p_0){}^9\text{Be}(\text{gs})$ experiment. Two identical target holders, one for ${}^{10}\text{B}(\text{d}, p){}^{11}\text{B}$ reaction and the other for ${}^7\text{Li}({}^3\text{He}, p_0){}^9\text{Be}(\text{gs})$, and two pairs of pins and pin points in the reaction chamber could keep the solid angle unchanged when switching from ${}^{10}\text{B}(\text{d}, p){}^{11}\text{B}$ reaction to ${}^7\text{Li}({}^3\text{He}, p_0){}^9\text{Be}(\text{gs})$.

A detector telescope consisting of a $150\mu\text{m}$ ΔE detector followed by a $500\mu\text{m}$ E' detector and an arrangement of the coincident and anti-coincident electronics were used. Fig. 2-12 gives a principle schematic diagram of the electronics. The energy signals (solid lines) from ΔE and E' detectors were summed up while the gating signals (dashed lines) were analyzed by a coincident electronic unit. One measurement could be recorded in three ways, coincident and anti-coincident spectra and a 2-D plot of ΔE vs. $\Delta E + E'$. The

energy of the particles recorded in the coincident spectrum and 2-D plot, of which both required the simultaneous existence of both energy and gating signals, was the sum of those from ΔE and E' detectors. The detail electronic settings are in Fig. 2-6.

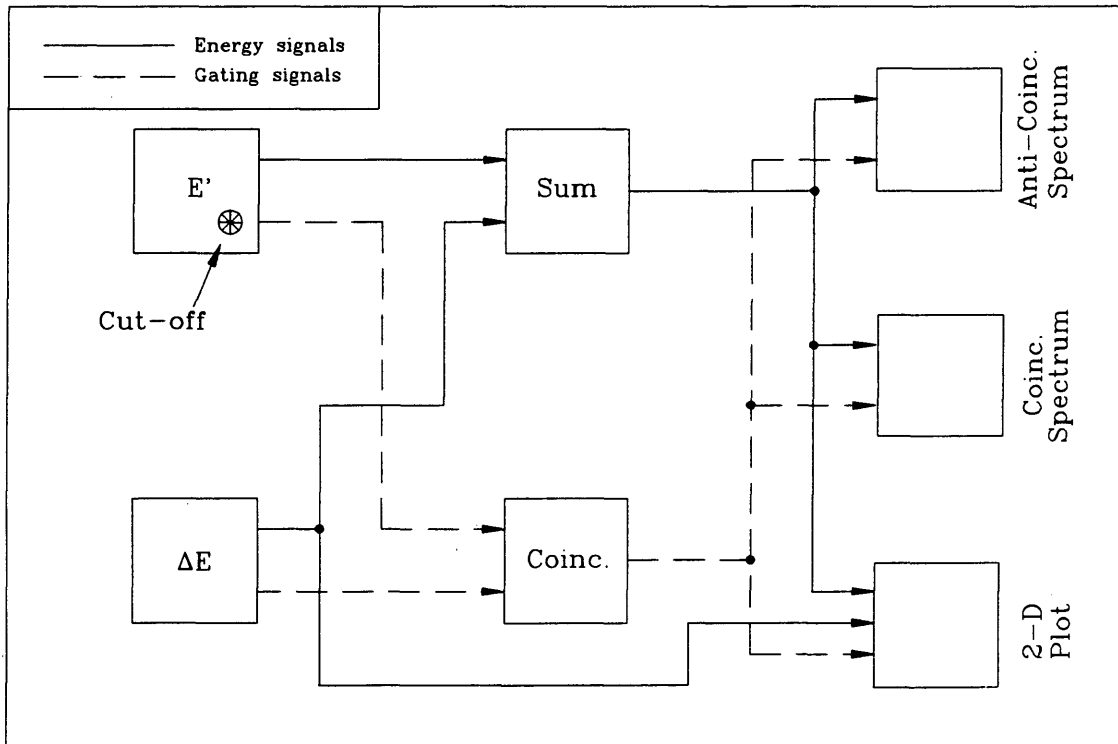


Fig. 2-12. A principle schematic diagram of the used electronics.

2.3.2 The Beam Contamination

Before the ${}^7\text{Li}({}^3\text{He}, p_0){}^9\text{Be}(\text{gs})$ experiment, the accelerator had been used for several months with proton and deuteron particles. We would thus expect significant embedding of hydrogen and deuterium on the inner walls of the accelerator, including the drift tube and the ion source. In the ${}^7\text{Li}({}^3\text{He}, p_0){}^9\text{Be}(\text{gs})$ experiment, they could be kicked out by the accelerated ${}^3\text{He}^+$ particles, then, they would either be ionized, be accelerated and be part of the beam, or drift backward to the ion source, form singly-charged proton-deuterium molecular ions, which have roughly the same mass and charge as ${}^3\text{He}^+$, and become a portion of the beam. Another source of the beam contamination came from the hydrogen and deuterium impurities of the ${}^3\text{He}$ gas going into the ion source.

The proton and deuteron contamination of the beam can be seen from the measured anti-coincident spectrum (Fig. 3-51) through the two α -peaks, each from the ${}^7\text{Li}(p, \alpha){}^4\text{He}$ or ${}^6\text{Li}(d, \alpha){}^4\text{He}$ reaction. The peaks, in turn, provide a way to calculate the amount of protons and deuterons in the beam. With the published data [Rol86; and Eng92] of the cross sections for the two reactions and the assumption of isotropic angular distributions, it is found that the ratios of the number of protons and deuterons in the beam to that of ${}^3\text{He}^+$ ions are

$$\left. \begin{aligned} \frac{N(p)}{N({}^3\text{He})} &= 3.5 \times 10^{-7} \\ \frac{N(d)}{N({}^3\text{He})} &= 5.8 \times 10^{-7} \end{aligned} \right\} \quad (2.11)$$

Since the time the accelerator was run with deuterons is longer than that with protons, the above numbers seem reasonable.

Bombarding the infinitely thick targets of natural lithium of 7.5% ${}^6\text{Li}$ abundance with the proton and deuteron contaminated ${}^3\text{He}^+$ beams would result in contaminant reactions between the species, accompanied with ${}^7\text{Li}({}^3\text{He}, p_0){}^9\text{Be}(\text{gs})$, hence called accidental reactions. Some of the important accidental reactions are listed in Table 2.1.

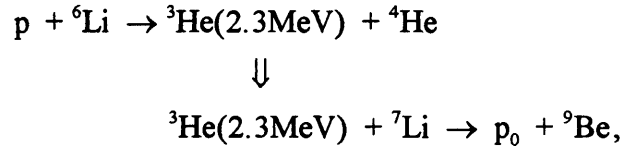
Table 2-1. A list of the important accidental reactions encountered with the ${}^7\text{Li}({}^3\text{He}, p_0){}^9\text{Be}(\text{gs})$ experiment due to the proton- and deuteron-contamination of the beam and the existence of ${}^6\text{Li}$ in the natural Li target.

Reaction	Q (MeV)	Particle	T (MeV)	T' (MeV)
${}^3\text{He} + {}^7\text{Li} \rightarrow p + {}^9\text{Be}$	11.201	p_0	10.0	9.9
		p_1	8.6	8.5
		p_2	7.9	7.8
${}^3\text{He} + {}^7\text{Li} \rightarrow d + {}^8\text{Be}$	11.761	d_0	9.5	9.4
		d_1	6.8	6.6
$d + {}^3\text{He} \rightarrow p + \alpha$	18.353	p	14.96	14.9
		α	3.55	2.2
${}^3\text{He} + {}^3\text{He} \rightarrow p + {}^5\text{Li}$	10.893	p	8.95	8.9
${}^3\text{He} + {}^3\text{He} \rightarrow 2p + \alpha$	12.860	p	10.42*	10.4*
$p + {}^6\text{Li} \rightarrow {}^3\text{He} + {}^4\text{He}$	4.020	${}^3\text{He}$	2.32†	—†
$d + {}^6\text{Li} \rightarrow 2\alpha$	22.373	α	11.19	10.6
$p + {}^7\text{Li} \rightarrow 2\alpha$	17.347	α	8.66	8.0
$d + {}^7\text{Li} \rightarrow \alpha + {}^5\text{He}$	14.255	α	7.89	7.2
$d + {}^7\text{Li} \rightarrow 2\alpha + n$	15.123	α	7.56*	6.8*

- 1) T — energy of the outgoing particles produced at $E_{\text{lab}} = 160\text{keV}$ and measured at $\theta_{\text{lab}} = 105^\circ$.
- 2) T' — energy of the particles after going through a $6\mu\text{m}$ Al foil that was put on front of the detector telescope.
- 3) * — the maximum energy of the particles.
- 4) † — the 2.32MeV ${}^3\text{He}$ particles are of importance only in the consideration of the secondary reactions.

2-3-3 The Sequential Reaction

It is important to notice from Table 2-1 that the 2.3MeV ^3He from the $p+^6\text{Li}$ accidental reaction will react with the ^7Li target nuclei through the following sequential reaction



forming a possible source of experimental error in the expected $^7\text{Li}(^3\text{He}, p_0)^9\text{Be}(\text{gs})$ reaction at our bombarding energies. Such an error can be estimated by using the published value [Eng92] for the S-factor of the $^6\text{Li}(p, ^3\text{He})^4\text{He}$ reaction and assuming a constant S-factor for $^7\text{Li}(^3\text{He}, p_0)^9\text{Be}(\text{gs})$ reaction. By defining the reaction probability of an infinitely thick target yield (dimensionless), $P_A(E_{\text{lab}})$, for reaction A at a bombarding energy E_{lab} , i.e., the probability of a reaction A in an infinitely thick target induced by one incident particle with energy E_{lab} ,

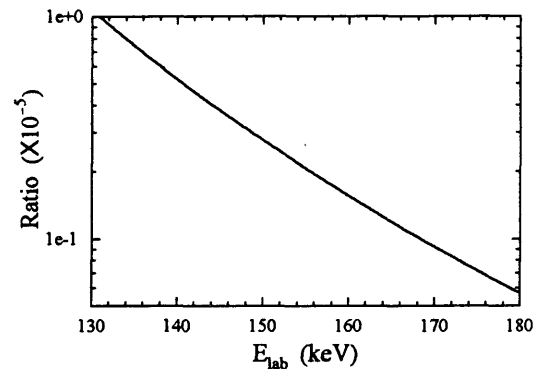
$$P_A(E_{\text{lab}}) = n_t \int_0^{E_{\text{lab}}} \frac{\sigma(E)}{\chi(E)} dE, \quad (2-12)$$

the ratio of the number of the sequential reactions to that of the expected reactions can be found to be

$$\text{the ratio at } E_{\text{lab}} = \frac{N(p)}{N(^3\text{He})} \cdot \frac{P_A(E_{\text{lab}}) \cdot P_B(2.3\text{MeV})}{P_B(E_{\text{lab}})}, \quad (2-13)$$

where A and B indicate $^6\text{Li}(p, ^3\text{He})^4\text{He}$ and $^7\text{Li}(^3\text{He}, p_0)^9\text{Be}(\text{gs})$, respectively. A plot of the ratio vs. E_{lab} is given in Fig. 2-13. Note that Eq. (2-12) and Fig. 2-13 are just ratio of reaction numbers. If the change in the $^7\text{Li}(^3\text{He}, p_0)^9\text{Be}(\text{gs})$ angular distribution is assumed to be within the same order, the ratio of the number of the detected protons from the sequential reaction to that from the $^7\text{Li}(^3\text{He}, p_0)^9\text{Be}(\text{gs})$ reaction will be in the same order as given in Eq. (2-13) and Fig. 2-13.

Fig. 2-13. The calculated ratio of the number of the sequential reactions, ${}^6\text{Li}(p, {}^3\text{He}){}^4\text{He}$ plus ${}^7\text{Li}({}^3\text{He}, p_0){}^9\text{Be}(\text{gs})$, to that of the expected reactions, ${}^7\text{Li}({}^3\text{He}, p_0){}^9\text{Be}(\text{gs})$, vs. bombarding energy.



2-3-4 The ${}^3\text{He}(\text{d}, \text{p}){}^4\text{He}$ Accidental Reaction

As shown in Table 2-1, the $\text{d} + {}^3\text{He} \rightarrow \text{p} + {}^4\text{He}$ accidental reaction would take place in the experiment. With a large S-factor [Kra87] and a much lower Coulomb barrier, this reaction has a very large cross section compared with the expected ${}^7\text{Li}({}^3\text{He}, p_0){}^9\text{Be}(\text{gs})$ reaction, leading to a large number of the 14.9 MeV protons produced from it. In our experiment, bombarding energy being $E_{\text{lab}} = 160$ keV and beam current $I \sim 40$ μA , the counting rate of the 14.9 MeV protons was ~ 100 per second, while that of the protons from the ${}^7\text{Li}({}^3\text{He}, p_0){}^9\text{Be}(\text{gs})$ reaction was $\sim 2 \times 10^{-3}$. These 14.9 MeV protons would go through the ΔE detector and be recorded by the PC computer in the 2-D plot. The computer worked in such a way that after each a certain number of events, say, 10 events, it would store the 2-D plot data to the hard disk, a rather slow action, much slower than the rate of the incoming 14.9 MeV protons. This would cause an unacceptably large dead time.

This problem can be solved by kicking the 14.9 MeV protons out of the 2-D plot. A comparison of the following energy losses E' in the 500 μm -thick E' detector,

$$E' = 3.5 \text{ MeV for the 14.9 MeV protons from } {}^3\text{He}(\text{d}, \text{p}){}^4\text{He},$$

$$E' = 8.4 \text{ MeV for the 9.9 MeV protons from } {}^7\text{Li}({}^3\text{He}, p_0){}^9\text{Be}(\text{gs}),$$

enables us to know that, if a window is opened to the gating signals (see Fig. 2-12) and the lower limit of the window is set to be 4.2 MeV, the 14.9 MeV protons will not create any

gating signal and, then, will not be recorded in both the coincident spectrum and 2-D plot. This, called "cut-off electronic settings" in the present summary, has been done by setting the Lower Level to be 2.80 in the Edge/Crossover Timing Single Channel Analyzer (see Fig. 2-6). Note that the 14.9MeV protons will disappear only from the coincident spectrum and 2-D plot (see Section 3-3-3 for further discussions).

2-3-5 A Test Experiment

A successful test experiment was run with the protons from the $^{10}\text{B}(d,p)^{11}\text{B}$ reaction before the $^7\text{Li}(^3\text{He},p_0)^9\text{Be}(\text{gs})$ measurements, which ensured that all the electronic system worked properly. The cut-off electronic settings were not used in the test experiment. The 2-D plot of the protons obtained from the test experiment is shown in Fig. 2-14. The three proton groups, p_0 , p_1 and p_2 , are quite clear and the counts in each group are equal to those in the corresponding peak in the coincident spectrum.

The shape of each proton group in Fig. 2-14 is determined by the fact that we used a close detector geometry and no aperture on the front of the detector telescope. When a produced proton is detected with a large angle θ , see Particle E in Fig. 2-15, it will lose more energy in the ΔE detector while the total energy $\Delta E + E'$ keeps the same since the proton can not penetrate the E' detector. This will make the proton group form an upward band in the 2-D plot, with the upper end of the band corresponding to the protons of largest angle θ . The length of the band in the unit of energy is

$$\delta E = \int_d^{d/\cos\theta_{\max}} \chi(E) dx, \quad (2-14)$$

where x is the distance the proton travels in the ΔE detector of thickness d . In Fig. 2-14, the p_2 group has the lowest energy, so, the largest stopping power, hence the largest length δE .

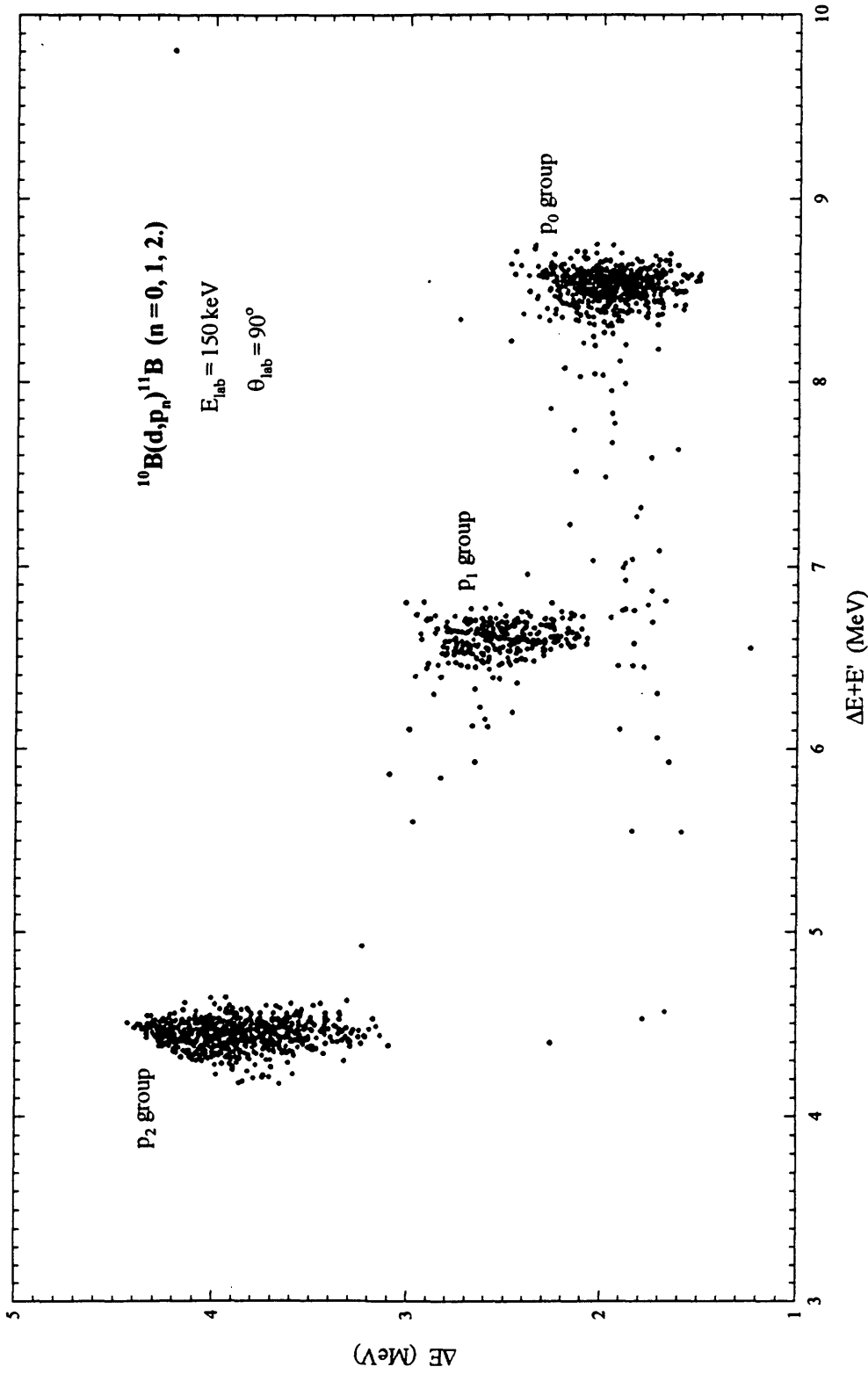


Fig. 2-14. A 2-D plot of protons produced by deuteron bombardment of a thick target of 90% enriched ^{10}B and measured by a detector telescope consisting of a $150\mu\text{m}$ ΔE detector and a $500\mu\text{m}$ E' detector. A close detector geometry was used and a $6\mu\text{m}$ Al foil was put on the front of the detector telescope.

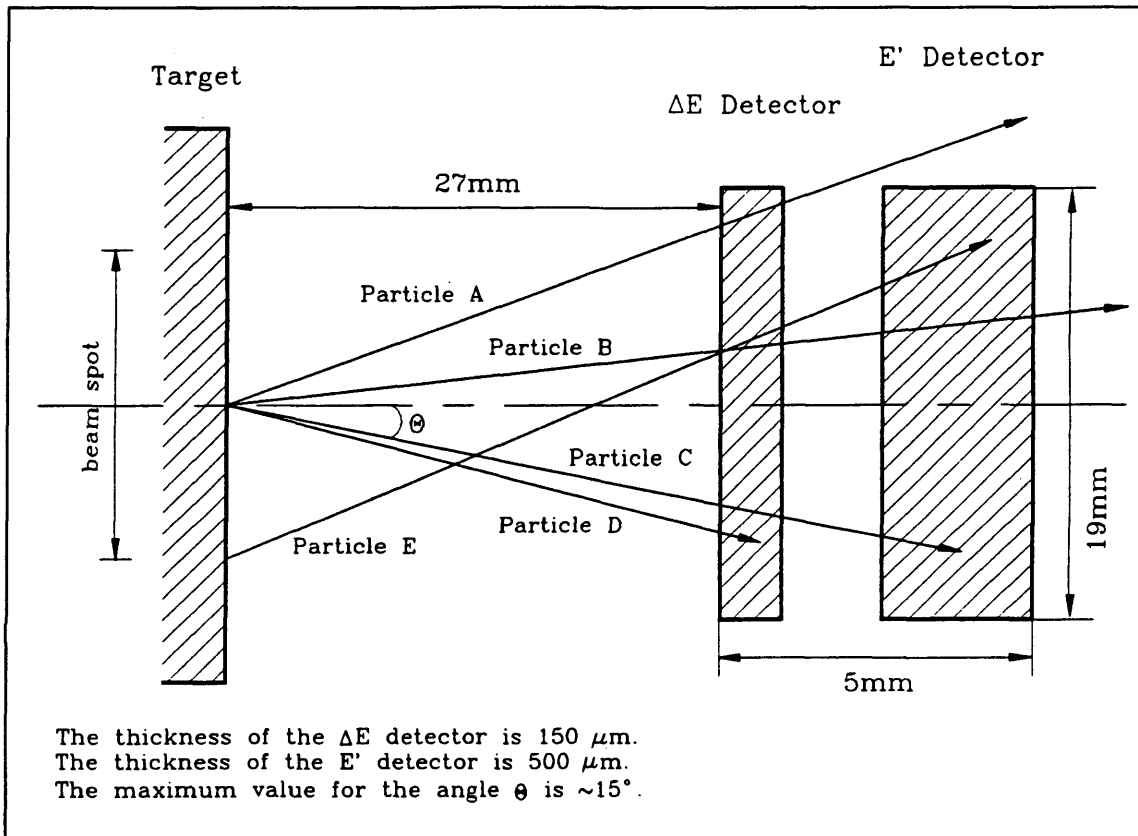


Fig. 2-15. The detected particles.

Chapter 3

RESULTS

3-1 THE ${}^7\text{Li}(d,\alpha){}^5\text{He}$ REACTION

The ${}^7\text{Li}(d,\alpha){}^5\text{He}$ reaction continues to prove most interesting by virtue of the multifragment nature of α -particle producing reactions which compete with the direct two-body reaction. As shown in Fig. 3-1, which gives the schematic diagram of the formation of the α -particle spectrum for the reaction, the α -particle spectrum is made up by competition of a direct breakup and a sequential decay. The direct breakup proceeds in a single step into two α -particles and one neutron while the sequential decay mainly via the ${}^5\text{He}$ ground state of 1.36 MeV [Bal91] width (FWHM) is characterized by the primary α -particles resulting in a peak of width according to that of the ${}^5\text{He}$ ground state and by the subsequent breakup of the ${}^5\text{He}$ recoil nuclei into α -particles and neutrons resulting in a continuous energy distribution of the secondary α -particles. A brief estimation indicates that the energy region of the α -particles from direct decay is between 0 and 7.6 MeV, that from the ${}^5\text{He}$ subsequent breakup between 3.4 MeV and 7.2 MeV, and that the primary α -particles will peak at 8.0 MeV. Note that the peak has an intrinsic width, i.e., a width without experimental broadening, of 1.36 MeV and will overlap seriously with the continuums, especially with that from the direct breakup. Therefore, the counts of the primary α -particles can not be read directly from the peak.

A measured spectrum of charged particles during deuteron bombardment of an infinitely thick target is given in Fig. 3-2, in which three peaks are produced by the deuteron-induced reactions on ${}^6\text{Li}$ nuclei of the natural LiF target and a proton peak comes from the ${}^2\text{H}(d,p){}^3\text{H}$ reaction due to the deuteron accumulation in the target. The energy value in the measured spectrum comes from a careful energy calibration, in which

the effect of the 6 μm Al foil on the front of the detector on the α -particle energy has also been eliminated. But since only the α -particle stopping power has been considered in this elimination, the three proton peaks are indicated at incorrect energies.

In order to better understand the complexity of the formation of the α -particle spectrum and separate the primary α -particle peak from the continuums, a collaboration was established with Dr. G.M. Hale at Los Alamos National Laboratory, and co-workers, who have developed a light-ion multichannel reaction code "SPECT" that is based on the R-matrix theory (see, for example, Lan66, Hal87 and Koe88) and is essentially parameter free. The dotted line is a spectrum calculated by his computer program "SPECT". The measured and calculated spectra agree basically with each other in both shape and position.

One thing that can be noticed is that the measured peak of the primary α -particles is broader than the calculated. This can be attributed to some factors of experimental broadening, such as the straggling of the α -particles in the 6 μm Al foil on the front of the detector, the finite width $\Delta\theta$ in the detector angle θ , and so on. The effect of experimental broadening can be seen clearly from the measured ${}^6\text{Li}(d,\alpha){}^4\text{He}$ peak in Fig. 3-2. This problem in width discrepancy can be solved by smearing the calculated spectrum with the experimental line shape of which the information can be obtained from the measured ${}^6\text{Li}(d,\alpha){}^4\text{He}$ peak. It is expected that the measured and calculated spectra will be in rough agreement after the smearing. Then, a fit of the calculated spectrum with the measured will give the counts of the primary α -particles, which will lead to the angular distributions and cross sections of both the direct decay ${}^7\text{Li}(d,2\alpha)n$ and the sequential decay ${}^7\text{Li}(d,\alpha){}^5\text{He}$. Though, for the time being, all the work, i.e., smearing and fitting, remains to be done in the future, we have made substantial progress and are approaching closure on the reaction.

The angular distributions were measured at two deuteron bombarding energies of 100 keV and 150 keV. The target used in the angular distribution measurements was a thin film of natural LiF with its thickness being 320 \AA , or, 4.1 keV at a deuteron energy of 150 keV. A vertical slit detector aperture of 3.2 mm \times 13.5 mm was put on the front of the detector. A monitor fixed at 90 $^\circ$ was used and the ratios of counts from the detector

spectra to those from the monitor spectra were considered. Fig. 3-3 plots the measured angular distributions for the direct and sequential decays at the two energies.

The yields at different bombarding energies between 40 keV and 160 keV were measured with infinitely thick targets of natural LiF at an angle of 90° in the lab system. With an assumption of isotropic angular distributions, the cross section values can be calculated from the measured yields by Eq. (2-8). Fig. 3-4(a) shows the cross sections for both the decay processes. The S-factors, given in Fig. 3-4(b), are then calculated from the cross sections. The S-factors for the both processes exhibit obvious dropping tendencies from low energy to $E_{cm} \approx 100$ keV. This fact is due to a resonance, the so-called subthreshold resonance [§4-5 in Rol88], in the ${}^7\text{Li} + d$ reaction to the 17.67 MeV ${}^9\text{Be}$ energy level of 41 keV width (FWHM), about 20 keV lower than the reaction threshold of ${}^7\text{Li} + d$ in ${}^9\text{Be}$ [Ajz84].

Note that all the results including the angular distributions, cross sections and S-factors are obtained from rough reading of the measured spectra.

In order to determine the errors in the reported cross sections, three factors can be noticed. The first factor is the assumption of isotropic angular distributions. It can be known from Fig. 3-3 that the measured angular distributions for the sequential decay are nearly isotropic. For the direct decay, the measured angular distributions in Fig. 3-3 can roughly be described by $(a + b \cos\theta)$, hence, the yield measurements at 90° will produce the average values of the angular distributions. Therefore, this assumption will not have a significant contribution to the errors in the cross sections. The second is the use of Eq. (2-8). This equation is derived from Eq. (2-6), which requires that the angular distribution remains the same shape in the energy region from zero to the highest bombarding energy (see Eq. (2-5a)). Since Fig. 3-3 indicates that the shapes of the angular distributions for each of the two decays do not change considerably at the two energies, Eq. (2-8) is approximately valid for the ${}^7\text{Li} + d$ reaction. The last factor regarding the errors in the cross sections is the rough reading of the measured spectra and is the main source of the errors. The error bars in Fig. 3-4(a) are the estimated errors only from the rough reading.

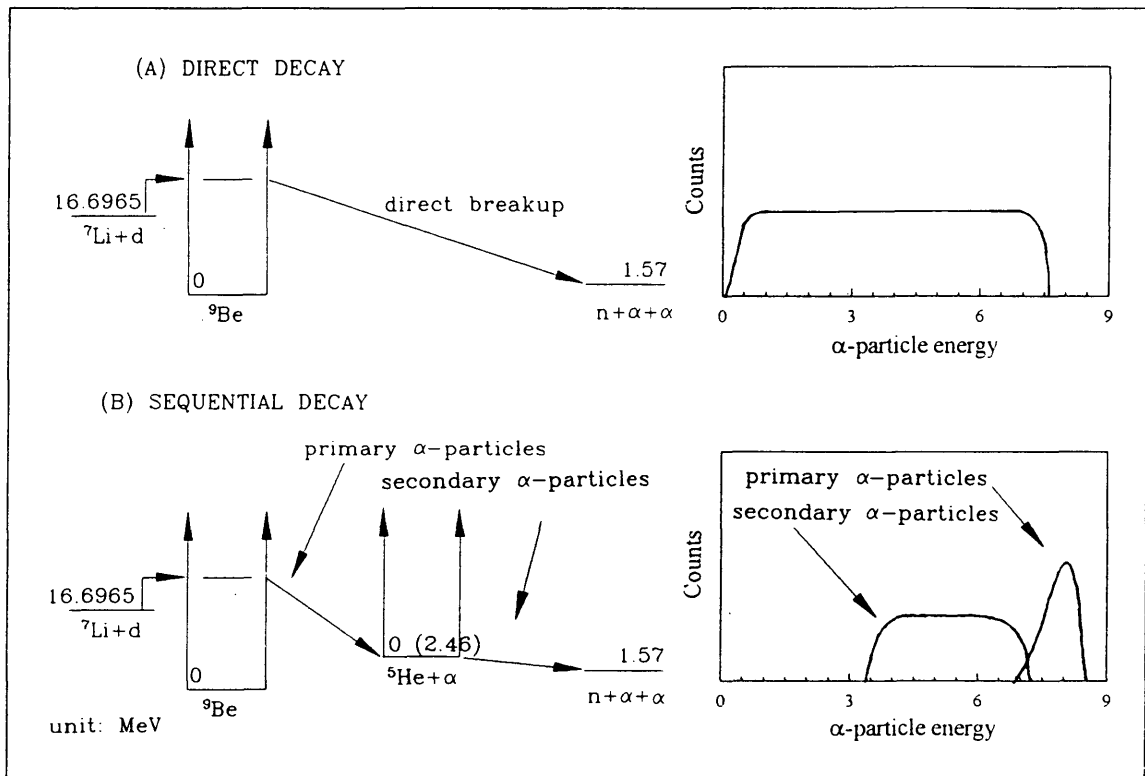


Fig. 3-1. Formation of the α -particle spectrum for the ${}^7\text{Li} + d$ reaction.

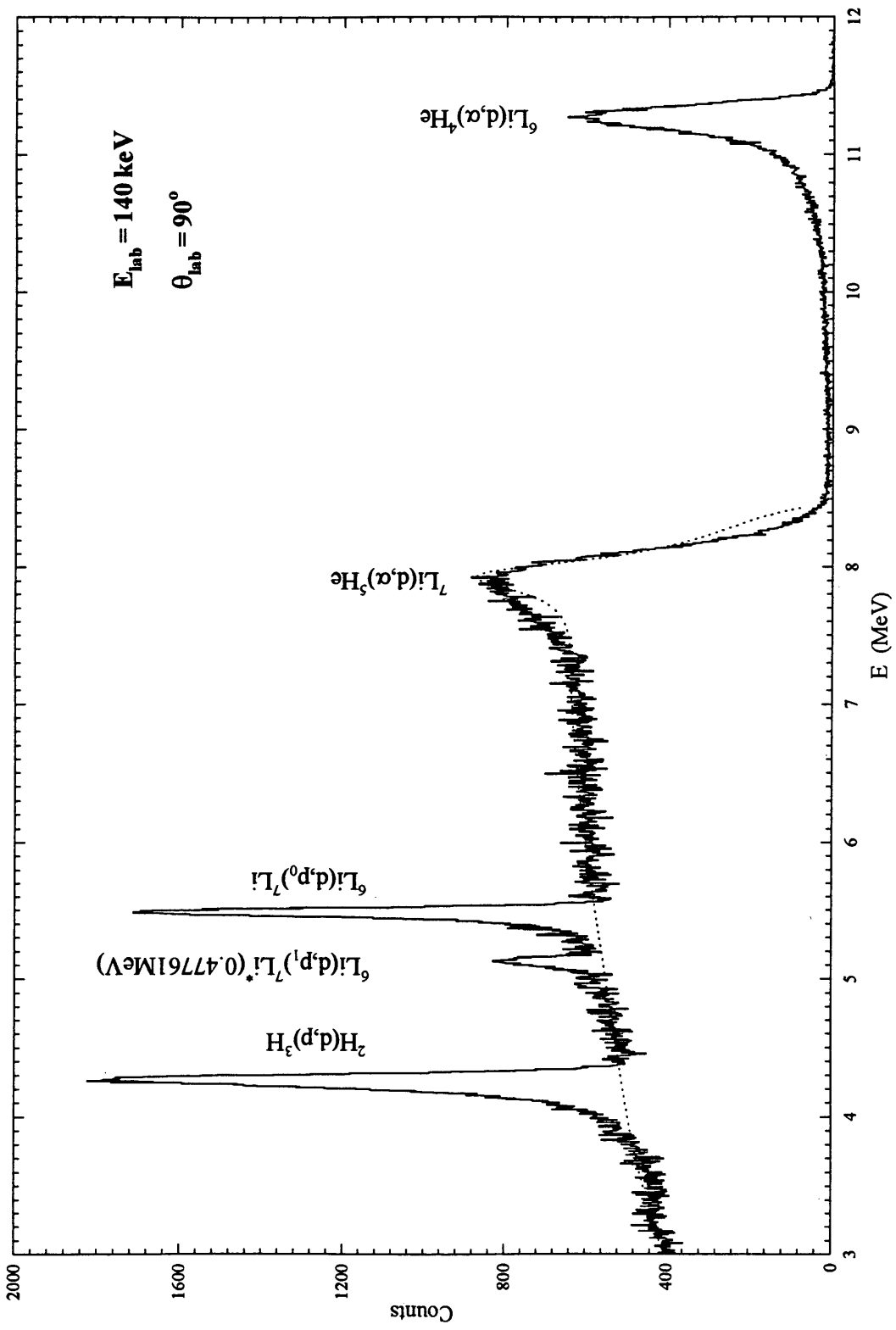


Fig. 3 - 2. Measured (solid line) and calculated (dotted line) spectra for ${}^7\text{Li}+d$ reaction.

Fig. 3-3. Measured angular distributions for ${}^7\text{Li}(d,2\alpha)n$, resulting from rough reading of the spectra.

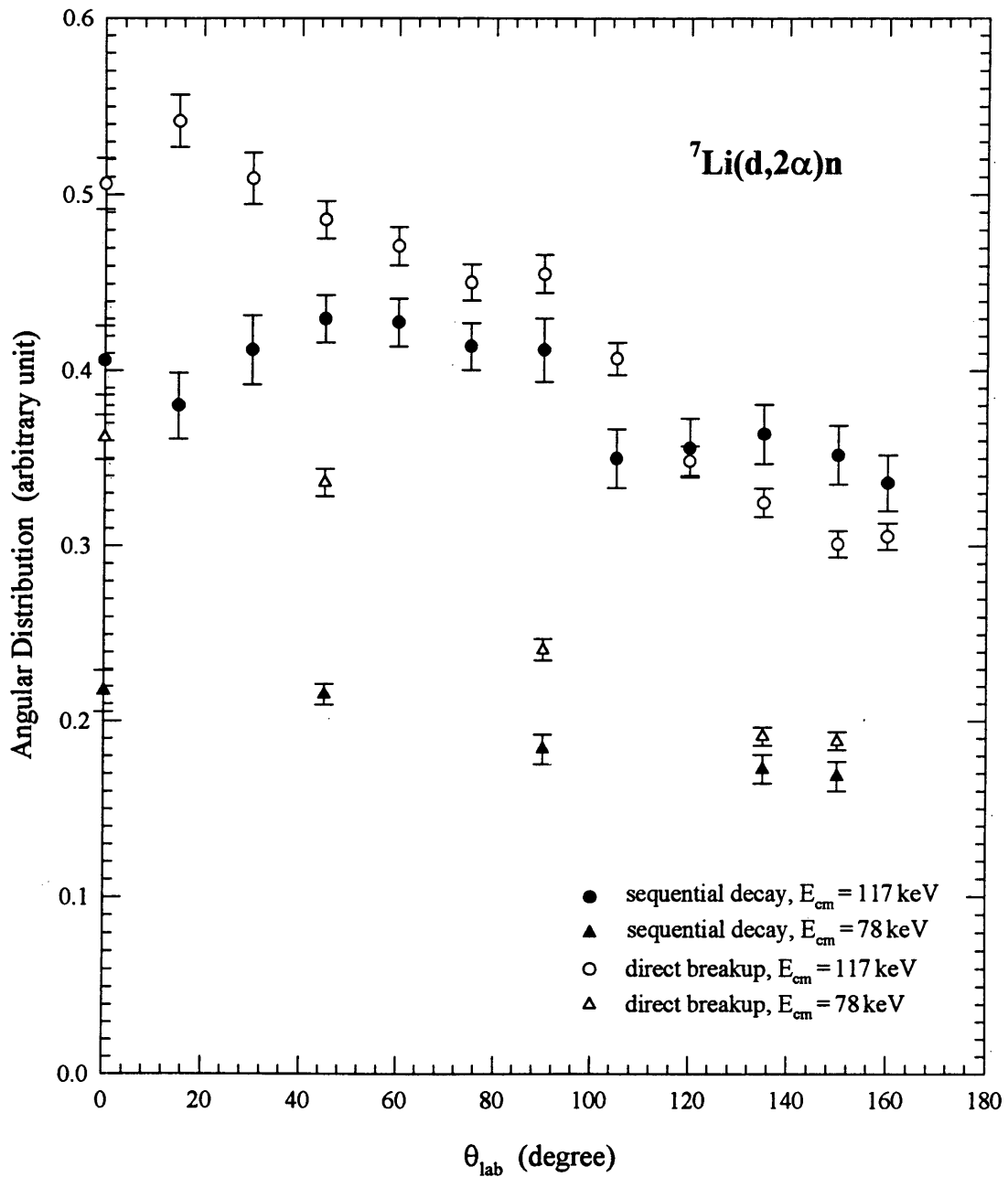


Fig. 3-4(a). Measured cross sections for ${}^7\text{Li}+d$ reaction, resulting from rough reading of the spectra.

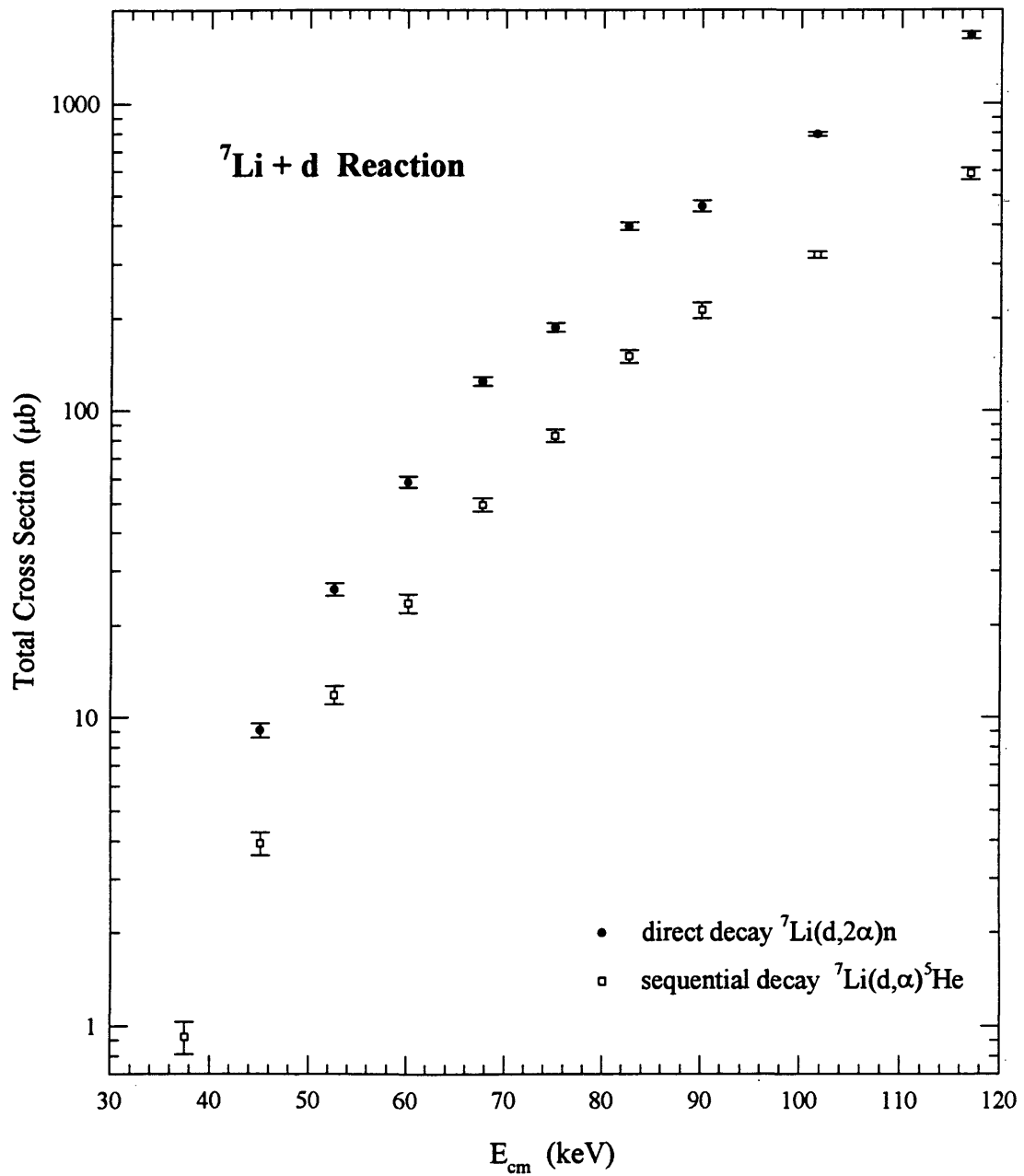
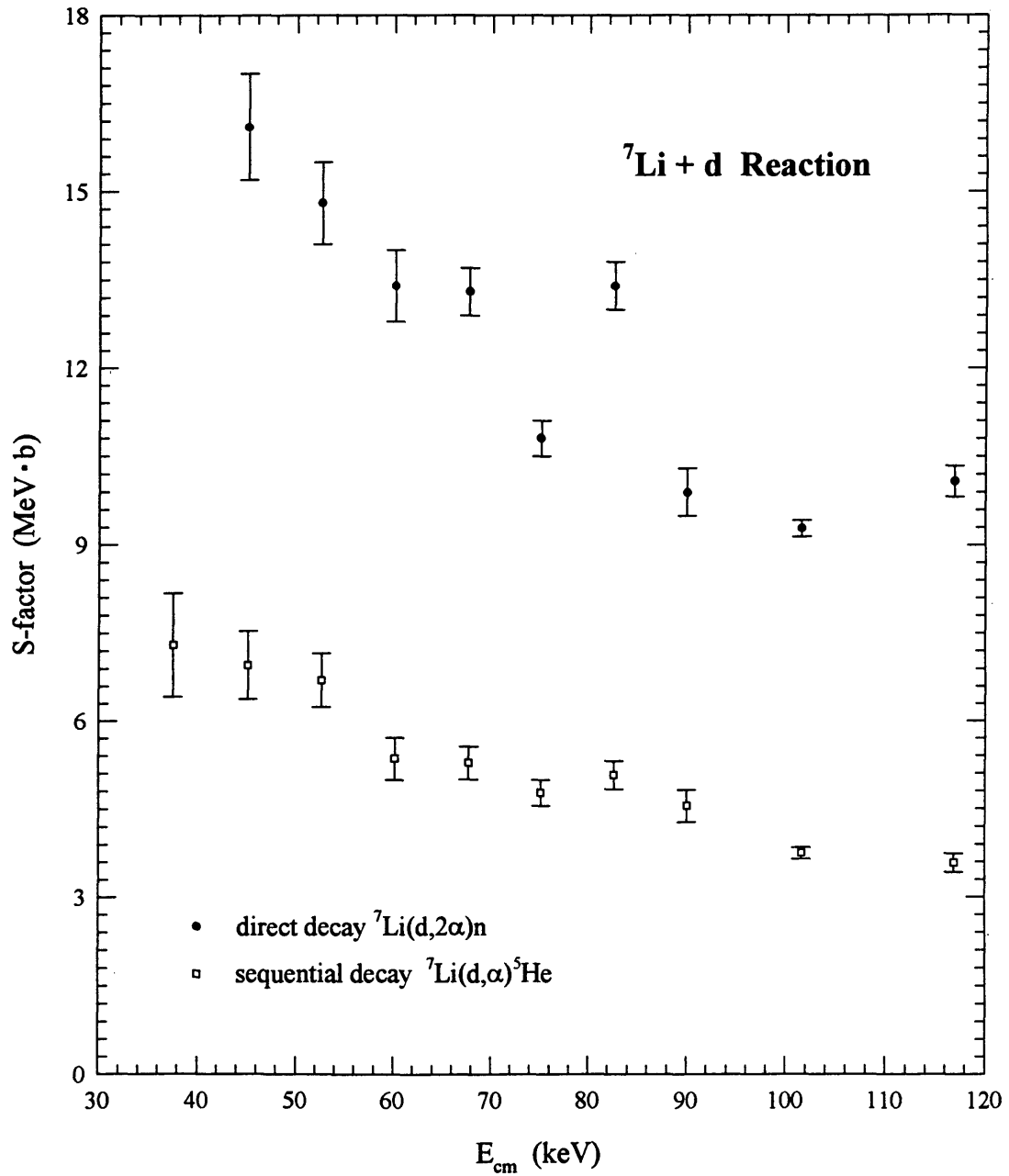


Fig. 3-4(b). Measured S-factors for ${}^7\text{Li}+d$ reaction, resulting from rough reading of the spectra.



3-2 The DEUTERON-INDUCED REACTIONS ON ^9Be , ^{10}B AND ^{11}B

In the center-of-mass system, the differential cross section of a reaction as a function of energy E_{cm} and angle θ_{cm} can be formulated as

$$\left(\frac{d\sigma}{d\Omega}\right)_{\text{cm}} = \frac{1}{4\pi} W_{\text{cm}}(\theta_{\text{cm}}, E_{\text{cm}}) \sigma(E_{\text{cm}}), \quad (3-1)$$

where $W_{\text{cm}}(\theta_{\text{cm}}, E_{\text{cm}})$ is the normalized angular distribution and $\sigma(E_{\text{cm}})$ the cross section of the reaction that can be expressed by the S-factor. We can write the normalized angular distribution in terms of Legendre polynomials

$$W_{\text{cm}}(\theta_{\text{cm}}, E_{\text{cm}}) = 1 + \sum_{\ell=1}^{\infty} A_{\ell}(E_{\text{cm}}) P_{\ell}(\cos\theta_{\text{cm}}). \quad (3-2)$$

The coefficient of the expansion, $A_{\ell}(E_{\text{cm}})$, is a function of E_{cm} and can be expanded in a power series of E_{cm}

$$A_{\ell}(E_{\text{cm}}) = \sum_{k=0}^{\infty} a_{\ell}^{(k)} E_{\text{cm}}^k \quad (3-3)$$

Inserting Eq. (3-3) into Eq. (3-2), we can get

$$W_{\text{cm}}(\theta_{\text{cm}}, E_{\text{cm}}) = 1 + \sum_{\ell=1}^{\infty} \sum_{k=0}^{\infty} a_{\ell}^{(k)} E_{\text{cm}}^k P_{\ell}(\cos\theta_{\text{cm}}). \quad (3-4)$$

In this Section, the measured results of the deuteron-induced reactions on ^9Be , ^{10}B and ^{11}B are reported in terms of the normalized angular distributions and cross sections.

3-2-1 The $^9\text{Be} + d$ Reaction

The angular distributions were measured at two deuteron bombarding energies of 110 keV and 150 keV and the yields were measured at an angle of 140° in the lab system with deuteron beam energies between 70 keV and 170 keV. All these measurements were carried out with infinitely thick targets of beryllium metal with polished surfaces.

Fig. 3-5 illustrates a measured energy spectrum of charged particles with its energy calibration which was made with the energy values of the particles after punching through the 1 μ m Ni foil on the front of the detector. Again the deuteron accumulation in the target will produce the proton and triton peaks from the ${}^2\text{H}(d, p){}^3\text{H}$ reaction.

The angular distributions at the two energies are fitted to $1 + w_1 P_1(\cos\theta_{\text{cm}}) + w_2 P_2(\cos\theta_{\text{cm}})$ and the coefficients, w_1 and w_2 , are given in Table 3-1. Figs. 3-6 through 3-15 show these measured angular distributions (in fact, the differential cross sections $(d\sigma/d\Omega)_{\text{cm}}$ given by Eq. (3-1) are plotted in these figures), with the error bars being statistical only. Also plotted in Figs. 3-11, 3-13 through 3-15 are the results of angular distributions for ${}^9\text{Be}(d, p_0){}^{10}\text{Be}(\text{gs})$ [Smi57; and Amb66], ${}^9\text{Be}(d, t_0){}^8\text{Be}(\text{gs})$ [Smi57], ${}^9\text{Be}(d, \alpha_0){}^7\text{Li}(\text{gs})$ [Amb66], and ${}^9\text{Be}(d, \alpha_1){}^7\text{Li}^*(0.47761 \text{ MeV})$ [Amb66] from other authors. It is quite clear that our measurements are consistent with the references.

In examining if there are resonances encountered, the diagram [Ajz85] of energy levels of ${}^{11}\text{B}$, the compound nucleus for the ${}^9\text{Be} + d$ reaction, shows no significant (sharp) resonance in or near the present energy region, i.e., the ${}^{11}\text{B}$ excitation energy of 15.86 ~ 15.97 MeV. Hence $W_{\text{cm}}(\theta_{\text{cm}}, E_{\text{cm}})$ will change slowly with both θ_{cm} and E_{cm} and will exhibit an isotropic distribution at $E_{\text{cm}} = 0$. Therefore, Eq. (3-4) can be simplified as

$$W_{\text{cm}}(\theta_{\text{cm}}, E_{\text{cm}}) = 1 + a_1^{(1)} E_{\text{cm}} P_1(\cos\theta_{\text{cm}}) + a_2^{(1)} E_{\text{cm}} P_2(\cos\theta_{\text{cm}}). \quad (3-5)$$

The values of $a_1^{(1)}$ and $a_2^{(1)}$ are listed in Table 3-1(a).

But some people have pointed out that at energies far below the Coulomb barrier anisotropic angular distributions still need to be considered (see §5-5-5 in Rol88). This implies that Eq. (3-5) may not be valid. Then, another assumption can be made that the angular distributions will remain the same shapes for the entire energy region, i.e.,

$$W_{\text{cm}}(\theta_{\text{cm}}, E_{\text{cm}}) = 1 + b_1 P_1(\cos\theta_{\text{cm}}) + b_2 P_2(\cos\theta_{\text{cm}}), \quad (3-5a)$$

where b_1 and b_2 are constants.

Since there is no significant resonance encountered, as mentioned above, the S-factors for all the measured particle species can be described as

$$S(E_{\text{cm}}) = s_0 + s_1 E_{\text{cm}} + s_2 E_{\text{cm}}^2. \quad (3-6)$$

The coefficients, s_0 , s_1 and s_2 , can be obtained by fitting the measured yields with Eq. (2-7). Now, the different angular distribution equations, Eqs. (3-5) and (3-5a), the obtained S-factors will be different. Fig. 3-15(a) shows the S-factors resulting from the two equations. It is important to notice that, in the narrow energy region, the S-factors are insensitive to these angular distribution assumptions, i.e., Eqs. (3-5) and (3-5a), and the relative deviations for most cases are within 10%.

The experimental values of s_0 , s_1 and s_2 obtained with the use of Eq. (3-5) are given in Table 3-2. Figs. 3-16 through 3-20 are the cross sections (the solid lines) resulting from the S-factors with these values for s_0 , s_1 and s_2 . The data points in Figs. 3-16 through 3-20 are calculated by Eq. (2-8), again, with the use of Eq. (3-5). Note that the solid lines in Figs. 3-16 through 3-20 are not the curves fitting the data points.

The values for s_0 , s_1 and s_2 obtained with the use of Eq. (3-5a) are given in Table 3-2(a).

Table 3-1. Summary of the angular distributions measured at the two energies for the ${}^9\text{Be} + d$ reaction.

Reaction	$E_{\text{cm}} = 90\text{keV}$	$E_{\text{cm}} = 90\text{keV}$	$E_{\text{cm}} = 123\text{keV}$	$E_{\text{cm}} = 123\text{keV}$
	w_1	w_2	w_1	w_2
${}^9\text{Be}(d, p_0){}^{10}\text{Be}(\text{gs})$	-0.97 ± 0.11	None	-0.788 ± 0.037	None
${}^9\text{Be}(d, p_1){}^{10}\text{Be}^*(3.3680 \text{ MeV})$	-0.34 ± 0.10	None	-0.272 ± 0.044	None
${}^9\text{Be}(d, t_0){}^8\text{Be}(\text{gs})$	-0.34 ± 0.14	-0.39 ± 0.21	-0.617 ± 0.090	-0.349 ± 0.093
${}^9\text{Be}(d, \alpha_0){}^7\text{Li}(\text{gs})$	-0.374 ± 0.070	None	-0.175 ± 0.027	None
${}^9\text{Be}(d, \alpha_1){}^7\text{Li}^*(0.47761 \text{ MeV})$	$+0.472 \pm 0.039$	None	$+0.268 \pm 0.032$	None

Table 3-1(a). Summary of the angular distributions for the ${}^9\text{Be} + d$ reaction. Eq. (3-5) is used.

Reaction	$a_1^{(1)} (\text{MeV})^{-1}$	$a_2^{(1)} (\text{MeV})^{-1}$
${}^9\text{Be}(d, p_0){}^{10}\text{Be}(\text{gs})$	-6.67 ± 0.29	None
${}^9\text{Be}(d, p_1){}^{10}\text{Be}^*(3.3680 \text{ MeV})$	-2.37 ± 0.34	None
${}^9\text{Be}(d, t_0){}^8\text{Be}(\text{gs})$	-4.79 ± 0.66	-2.98 ± 0.72
${}^9\text{Be}(d, \alpha_0){}^7\text{Li}(\text{gs})$	-1.62 ± 0.21	None
${}^9\text{Be}(d, \alpha_1){}^7\text{Li}^*(0.47761 \text{ MeV})$	$+3.00 \pm 0.23$	None

Table 3-2. Summary of the S-factors obtained with Eq. (3-5) for the ${}^9\text{Be} + d$ reaction.

Reaction	s_0 (b·MeV)	s_1 (b)	s_2 (b·(MeV) ⁻¹)	Graph
${}^9\text{Be}(d, p_0){}^{10}\text{Be}(\text{gs})$	9.59 ± 0.38	-25.2 ± 3.4	155 ± 27	Fig. 3-16
${}^9\text{Be}(d, p_1){}^{10}\text{Be}^*(3.3680 \text{ MeV})$	11.3 ± 0.45	6.5 ± 3.7	None	Fig. 3-17
${}^9\text{Be}(d, t_0){}^8\text{Be}(\text{gs})$	7.08 ± 0.28	None	None	Fig. 3-18
${}^9\text{Be}(d, \alpha_0){}^7\text{Li}(\text{gs})$	7.62 ± 0.31	37.0 ± 3.5	39 ± 13	Fig. 3-19
${}^9\text{Be}(d, \alpha_1){}^7\text{Li}^*(0.47761 \text{ MeV})$	10.26 ± 0.41	64.4 ± 3.5	189 ± 14	Fig. 3-20

Table 3-2(a). Summary of the S-factors obtained with Eq. (3-5a) for the ${}^9\text{Be} + d$ reaction.

Reaction	s_0 (b·MeV)	s_1 (b)	s_2 (b·(MeV) ⁻¹)
${}^9\text{Be}(d, p_0){}^{10}\text{Be}(\text{gs})$	5.90 ± 0.36	15.0 ± 1.5	15.4 ± 2.3
${}^9\text{Be}(d, p_1){}^{10}\text{Be}^*(3.3680 \text{ MeV})$	9.28 ± 0.59	22.5 ± 2.3	None
${}^9\text{Be}(d, t_0){}^8\text{Be}(\text{gs})$	5.58 ± 0.41	16.1 ± 1.7	18.2 ± 2.8
${}^9\text{Be}(d, \alpha_0){}^7\text{Li}(\text{gs})$	6.59 ± 0.41	40.4 ± 4.1	75 ± 11
${}^9\text{Be}(d, \alpha_1){}^7\text{Li}^*(0.47761 \text{ MeV})$	14.2 ± 1.0	55.6 ± 5.9	51.9 ± 8.0

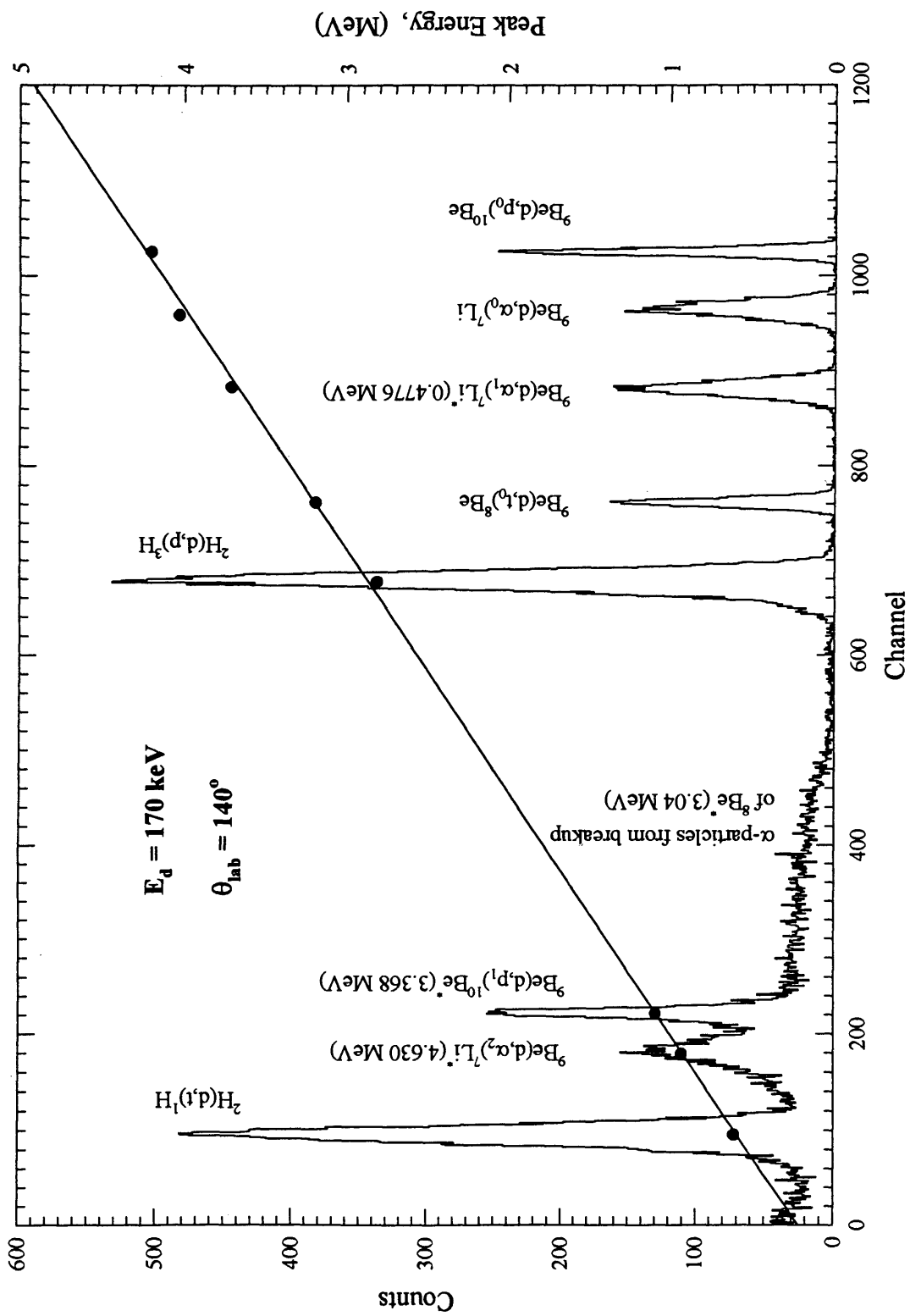


Fig. 3 • 5. A measured spectrum for ${}^9\text{Be}+d$ reaction with energy calibration.

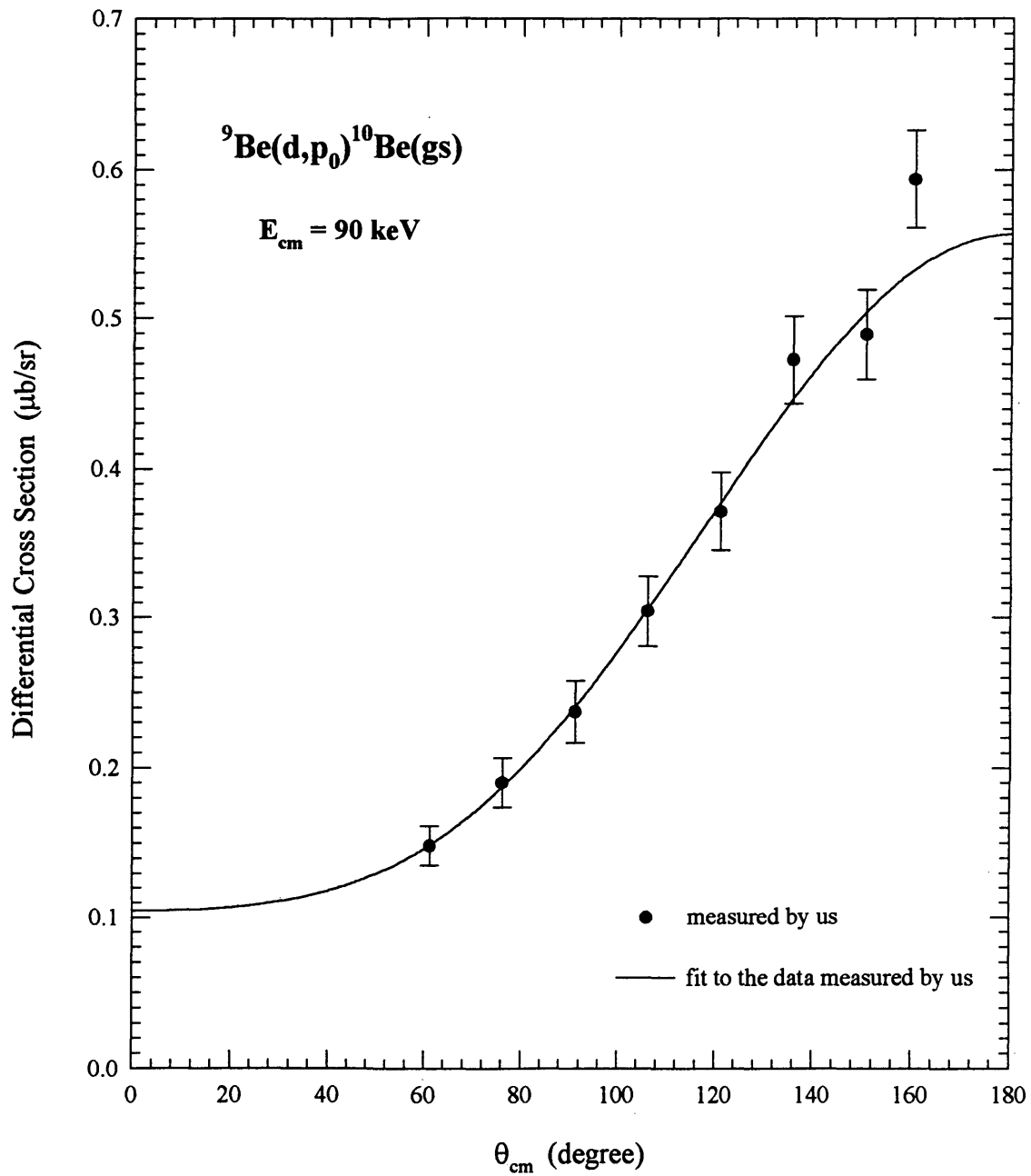
Fig. 3-6. Measured angular distribution for ${}^9\text{Be}(d,p_0){}^{10}\text{Be}(\text{gs})$ at $E_{\text{cm}} = 90 \text{ keV}$.

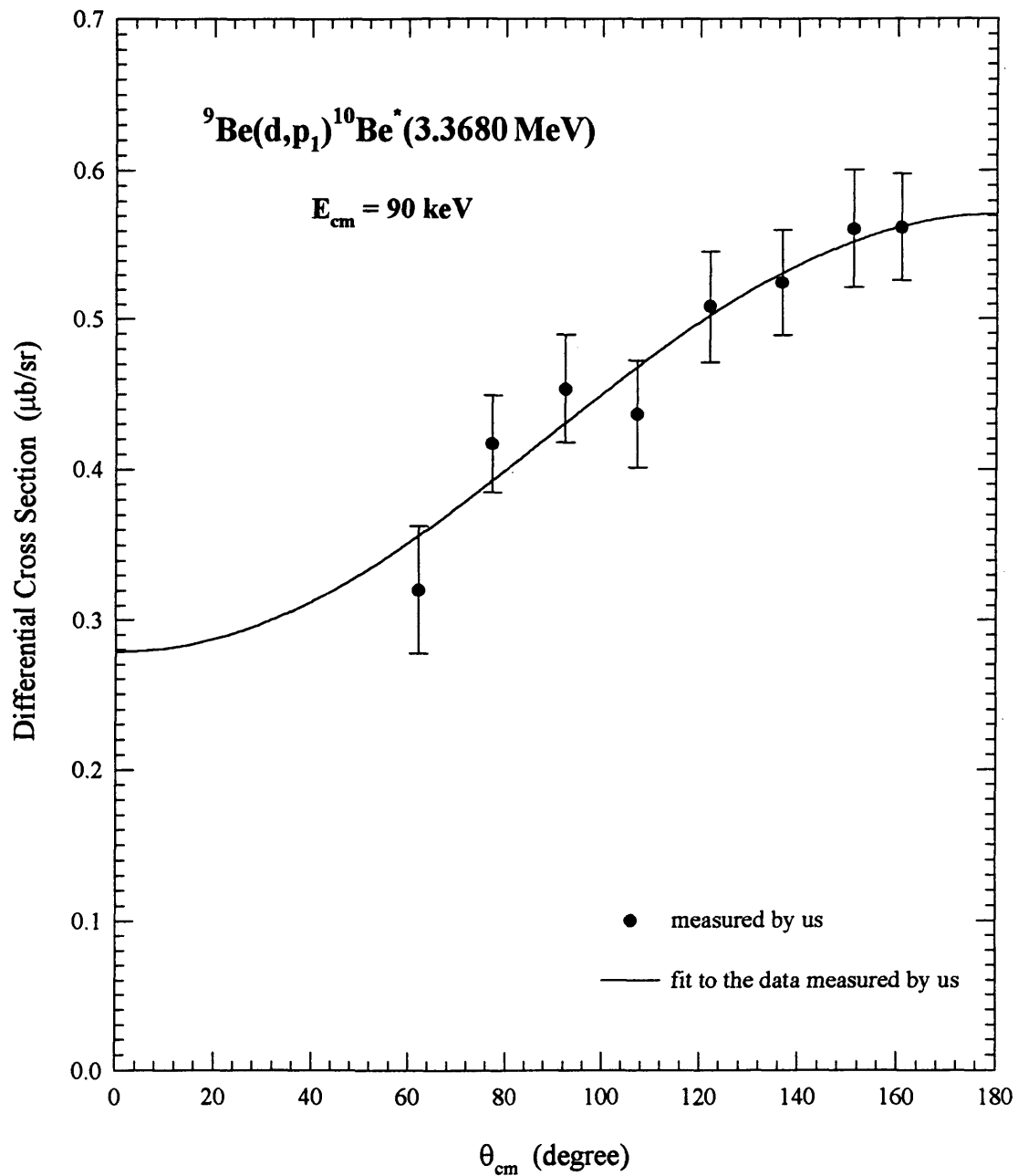
Fig. 3-7. Measured angular distribution for ${}^9\text{Be}(d,p_1){}^{10}\text{Be}^*(3.3680\text{ MeV})$ at $E_{\text{cm}} = 90\text{ keV}$.

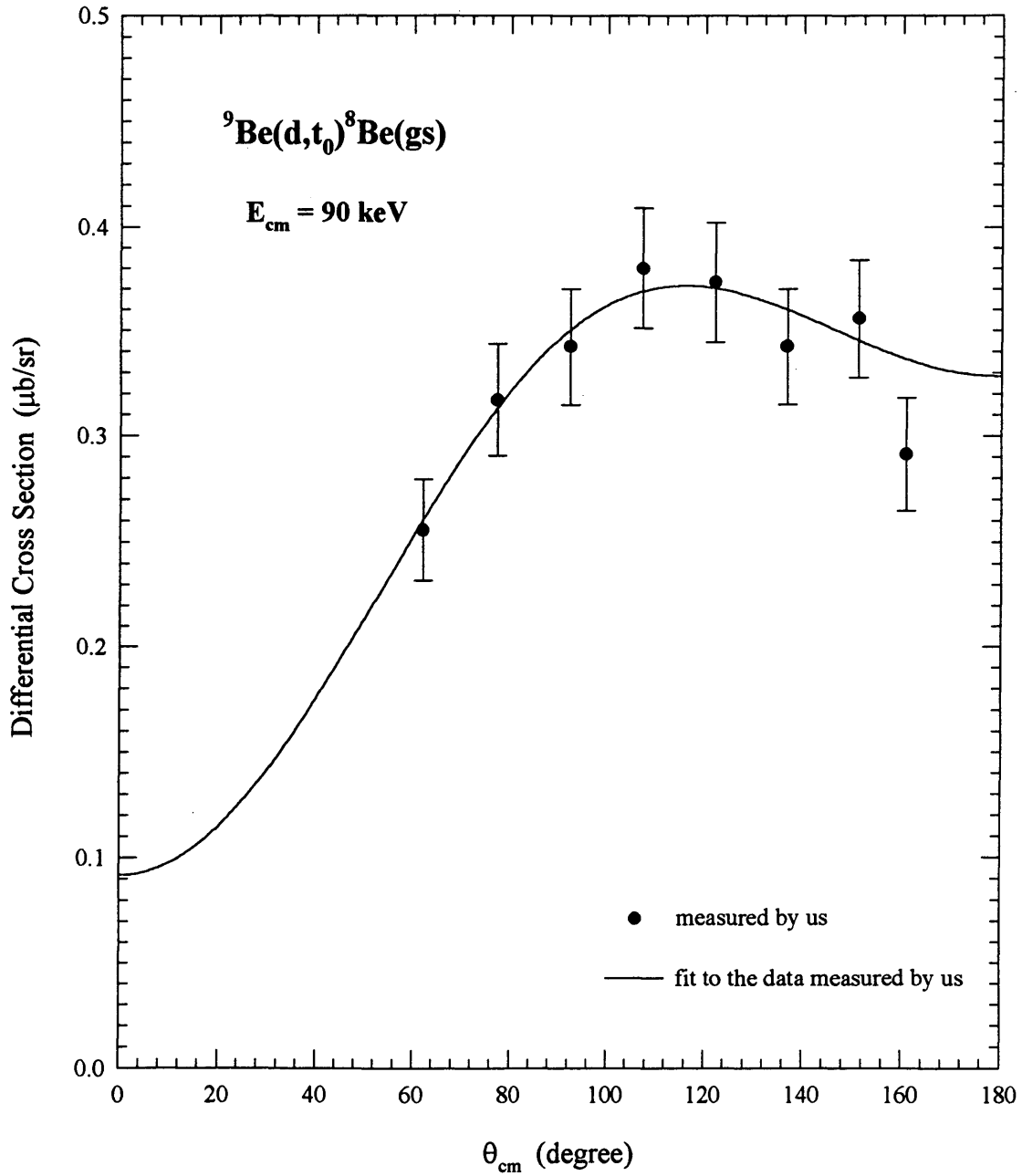
Fig. 3·8. Measured angular distribution for ${}^9\text{Be}(d,t_0){}^{10}\text{Be}(\text{gs})$ at $E_{\text{cm}} = 90$ keV.Fig. 3·8. Measured angular distribution for ${}^9\text{Be}(d,t_0){}^{10}\text{Be}(\text{gs})$ at $E_{\text{cm}} = 90$ keV.

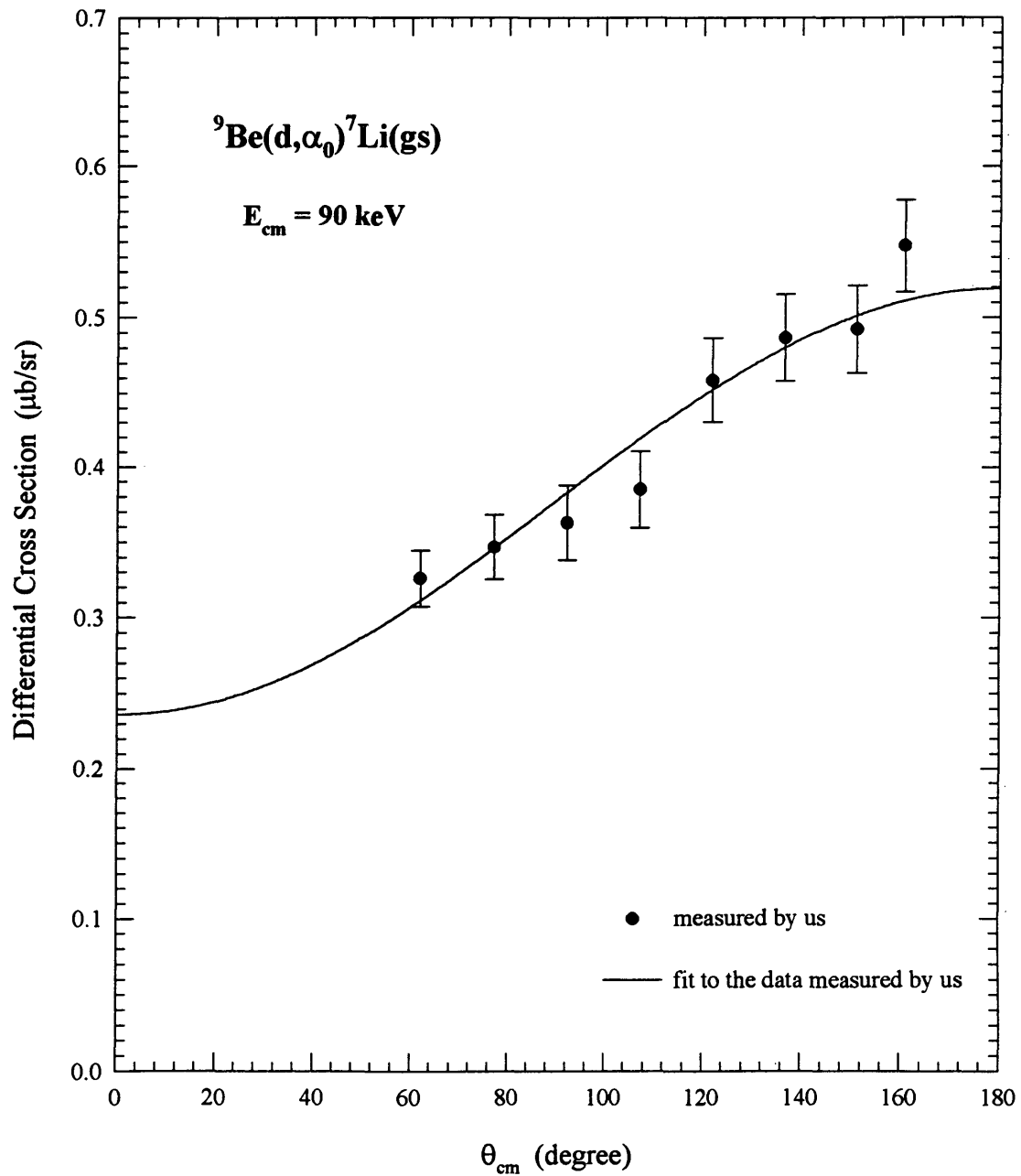
Fig. 3-9. Measured angular distribution for ${}^9\text{Be}(d,\alpha_0){}^7\text{Li}(\text{gs})$ at $E_{\text{cm}} = 90 \text{ keV}$.

Fig. 3-10. Measured angular distribution for ${}^9\text{Be}(d,\alpha_1){}^7\text{Li}^*(0.47761\text{ MeV})$ at $E_{\text{cm}} = 90\text{ keV}$.

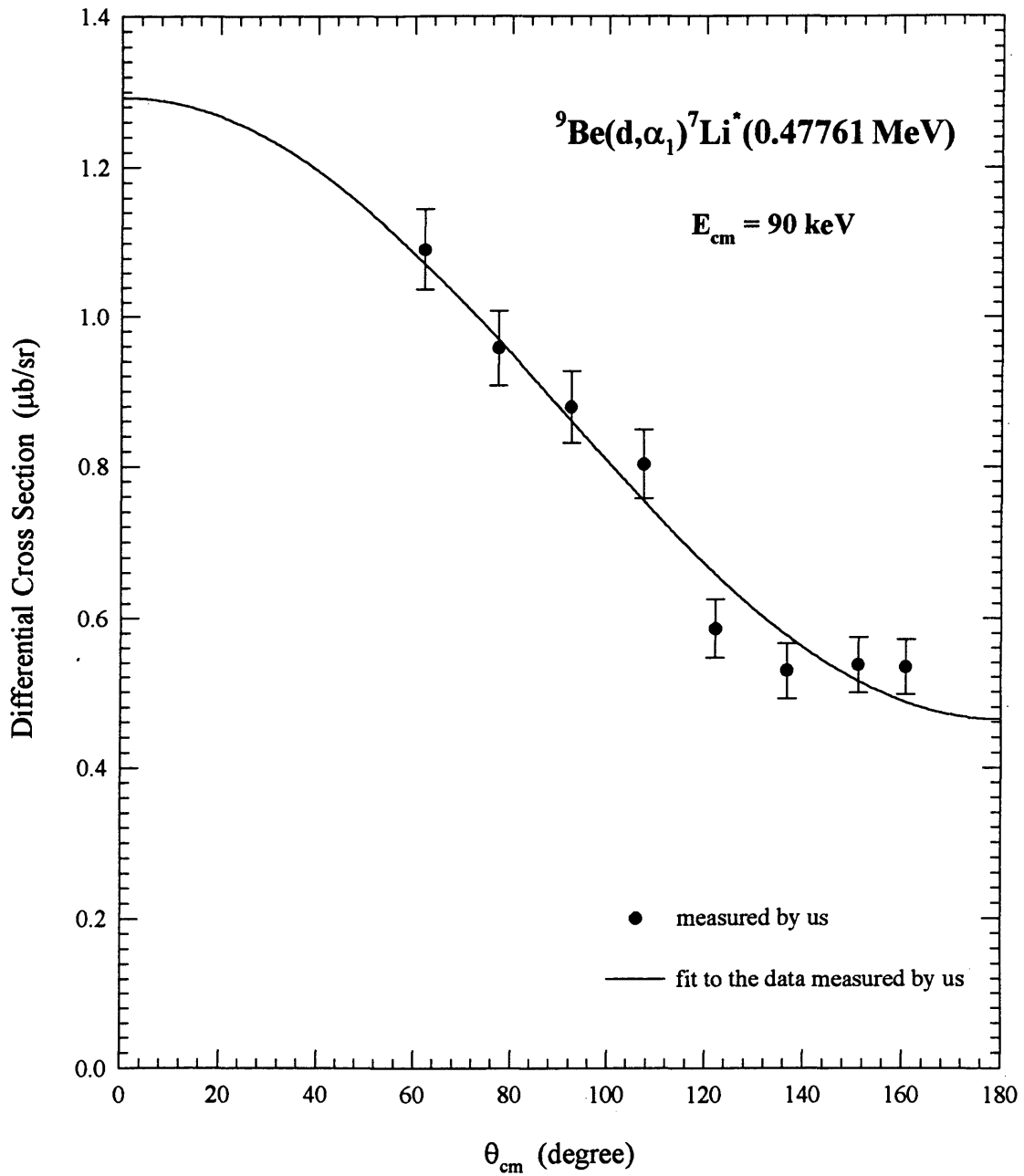


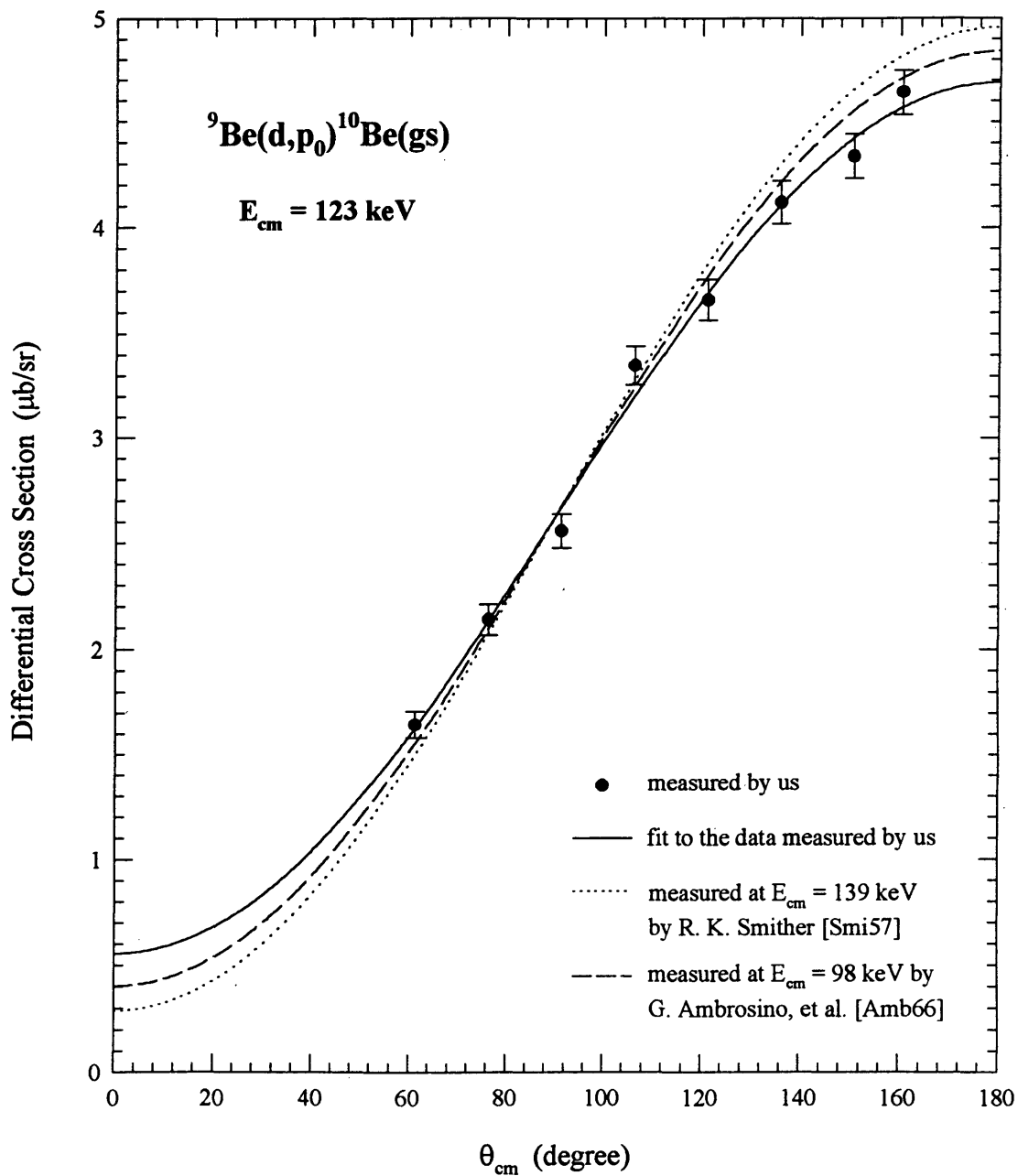
Fig. 3-11. Measured angular distribution for ${}^9\text{Be}(d,p_0){}^{10}\text{Be}(\text{gs})$ at $E_{\text{cm}} = 123 \text{ keV}$.

Fig. 3 · 12. Measured angular distribution for ${}^9\text{Be}(d,p_1){}^{10}\text{Be}^*$ (3.3680 MeV) at $E_{\text{cm}} = 123$ keV.

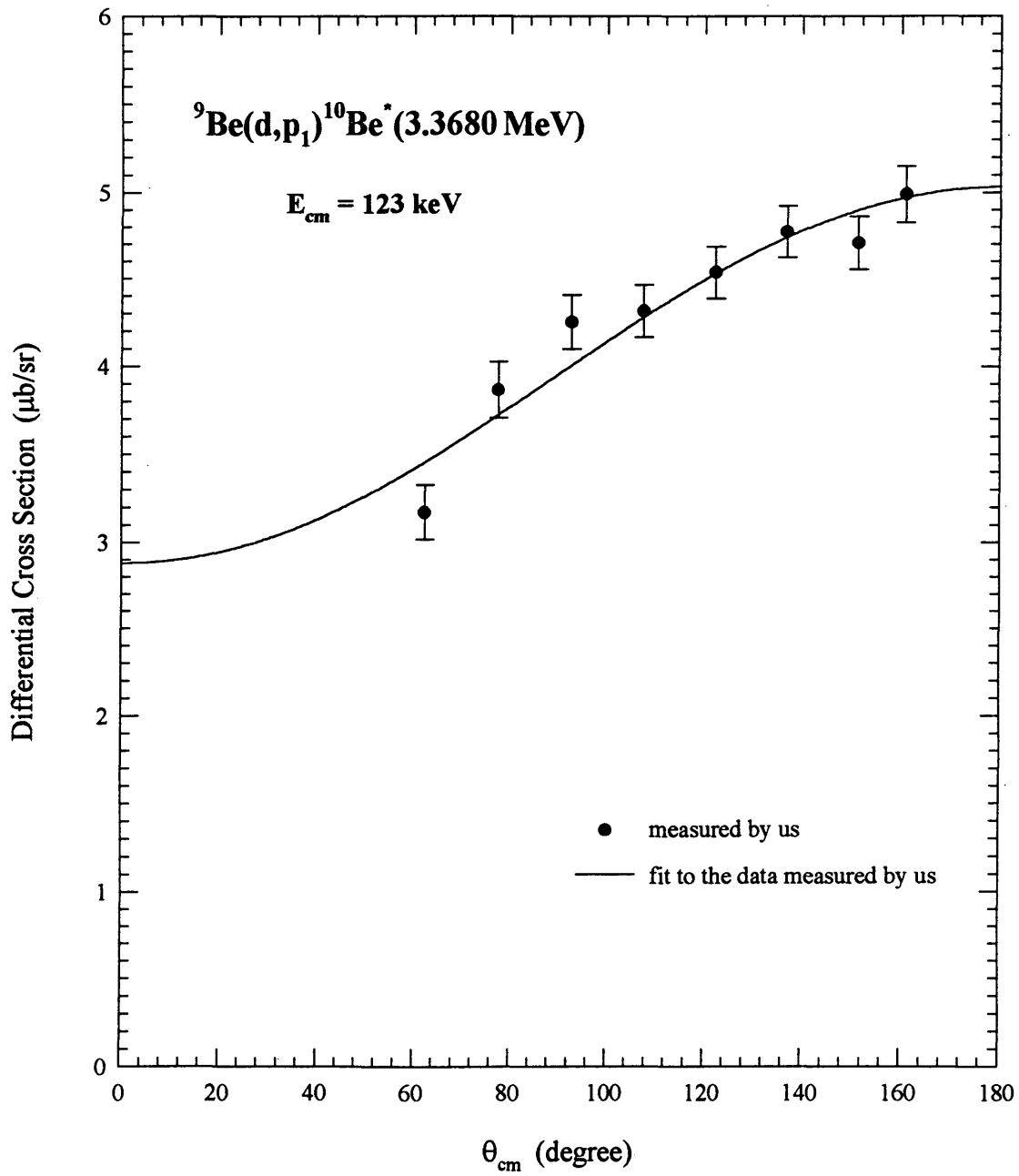


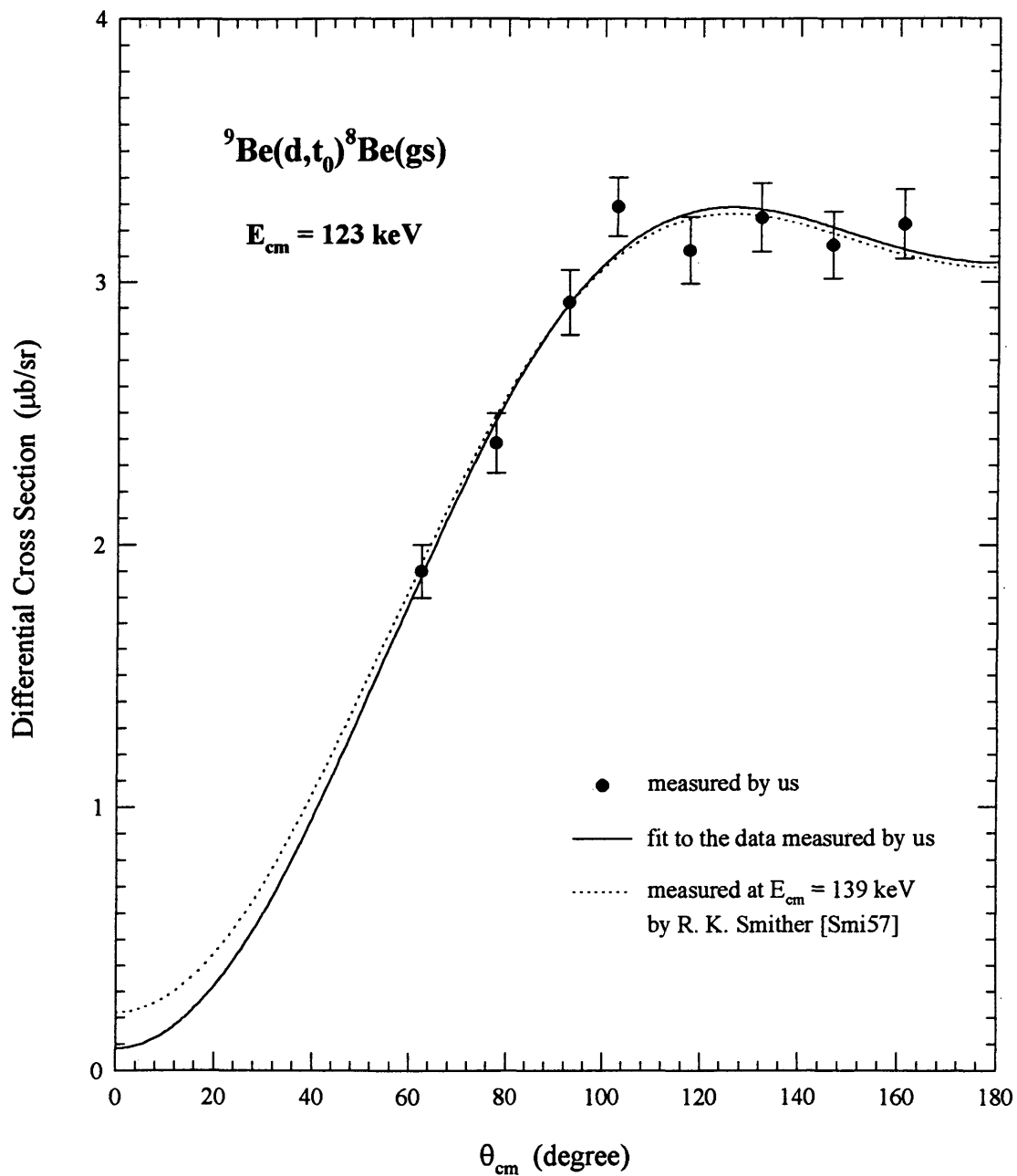
Fig. 3-13. Measured angular distribution for ${}^9\text{Be}(d,t_0){}^8\text{Be}(\text{gs})$ at $E_{\text{cm}} = 123 \text{ keV}$.

Fig. 3·14. Measured angular distribution for ${}^9\text{Be}(d,\alpha_0){}^7\text{Li}(\text{gs})$ at $E_{\text{cm}} = 123 \text{ keV}$.

Fig. 3-15. Measured angular distribution for ${}^9\text{Be}(d,\alpha_1){}^7\text{Li}^*(0.47761\text{ MeV})$ at $E_{\text{cm}} = 123\text{ keV}$.

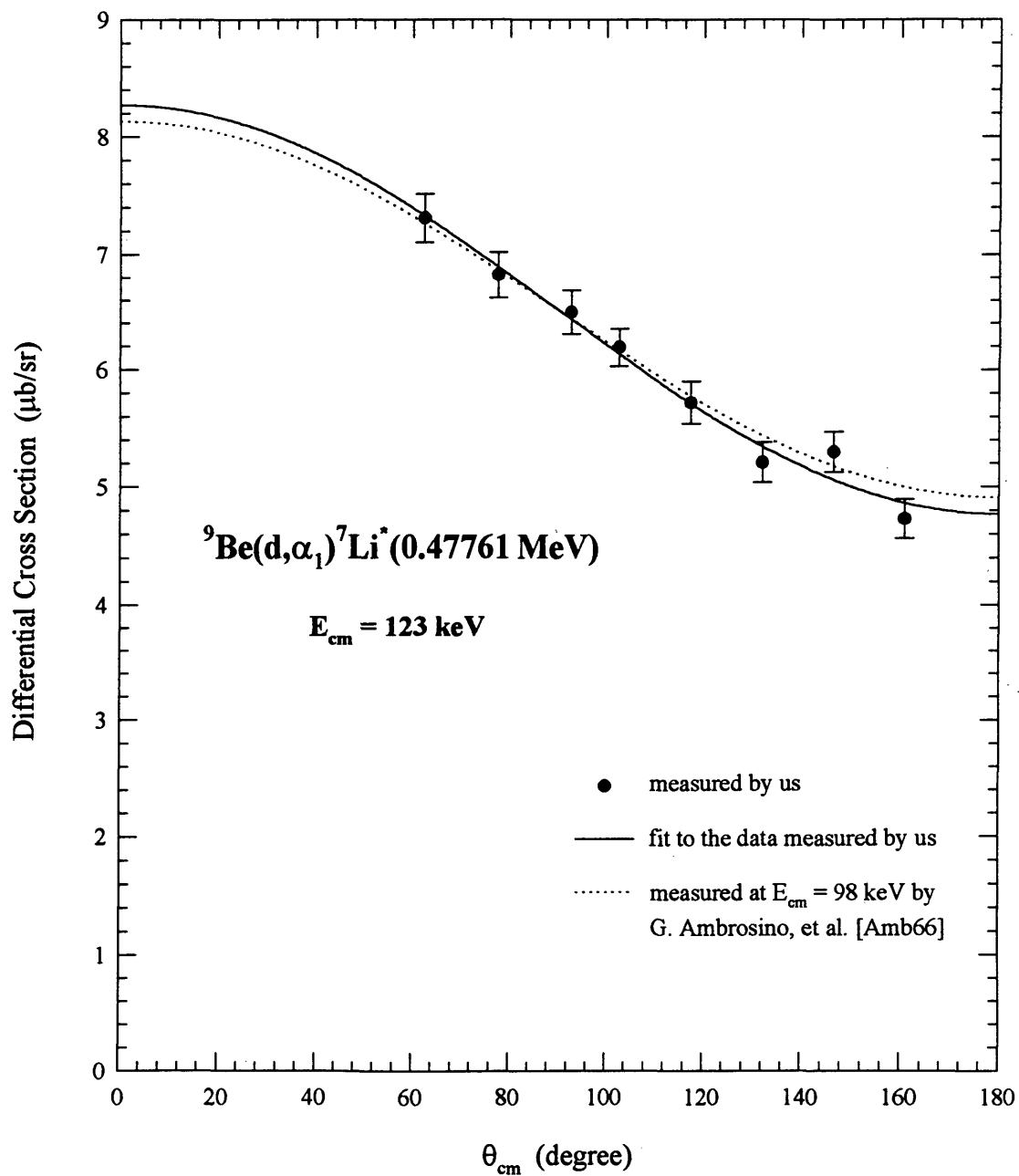


Fig. 3-15(a). The S-factors (the solid lines and the dotted lines) obtained from different fitting equations (Eq. (3-5) and Eq. (3-5a), respectively) of angular distributions.

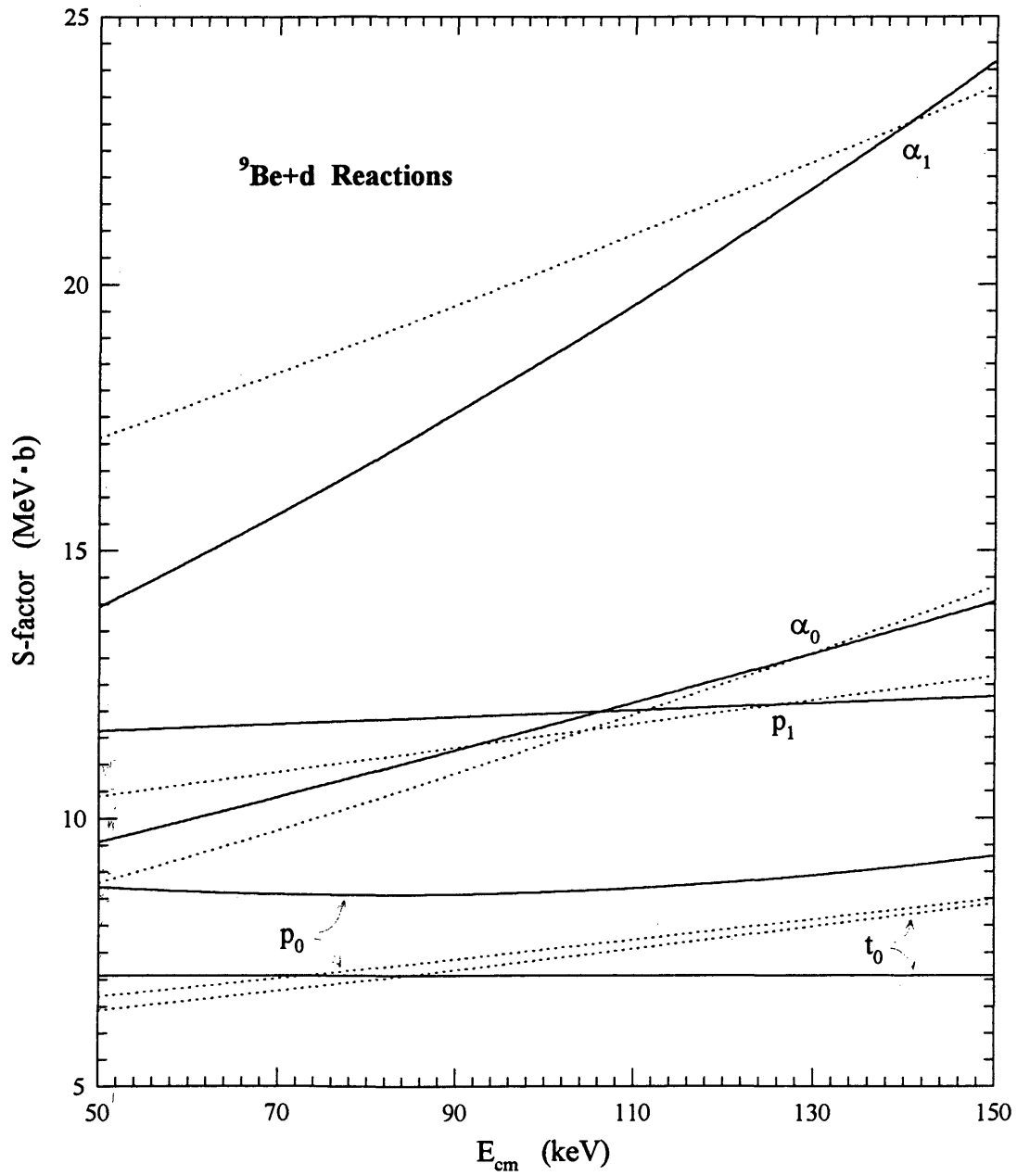


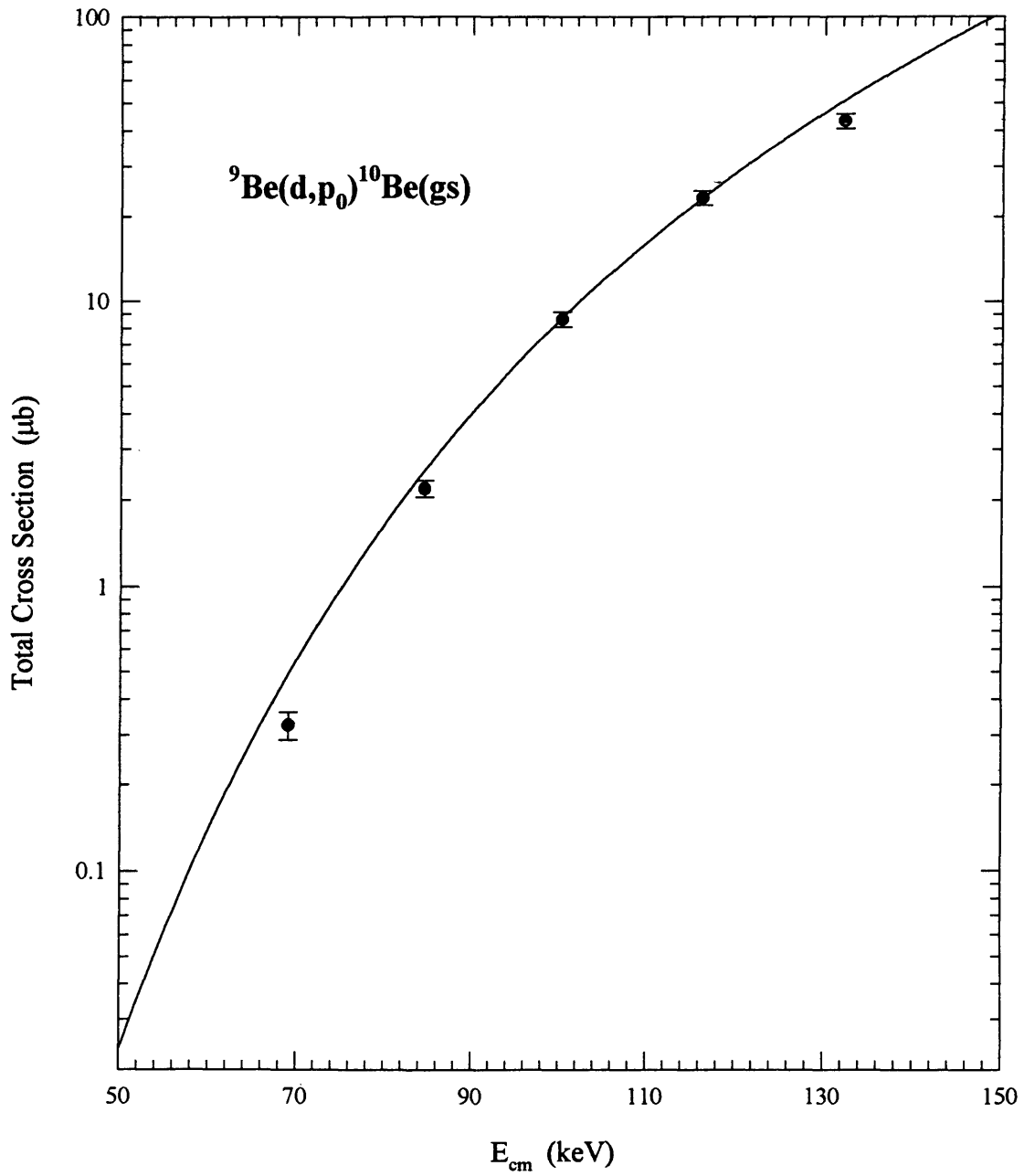
Fig. 3-16. Measured cross section for ${}^9\text{Be}(d,p_0){}^{10}\text{Be}(\text{gs})$.

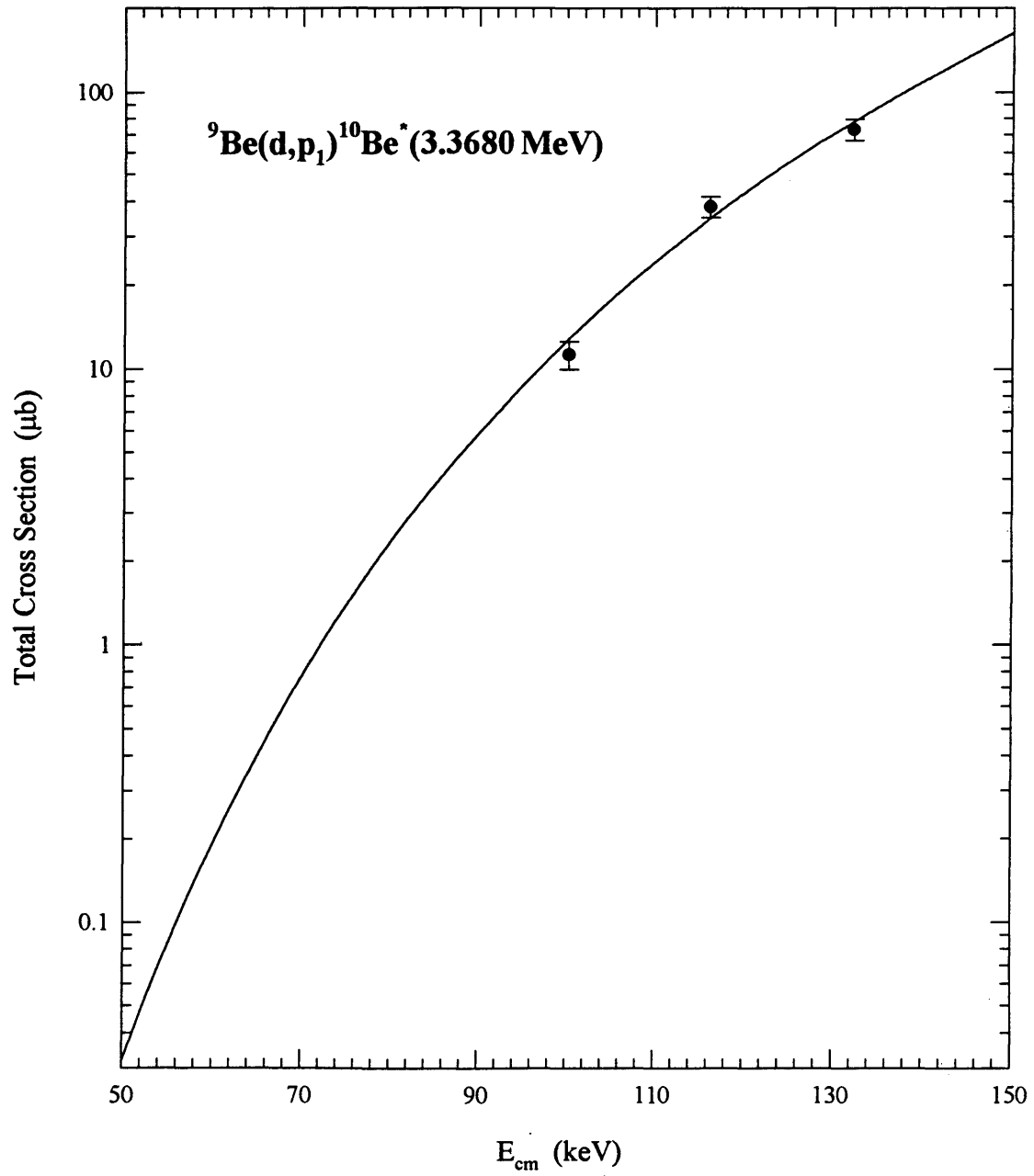
Fig. 3-17. Measured cross section for ${}^9\text{Be}(d,p_1){}^{10}\text{Be}^*$ (3.3680 MeV).

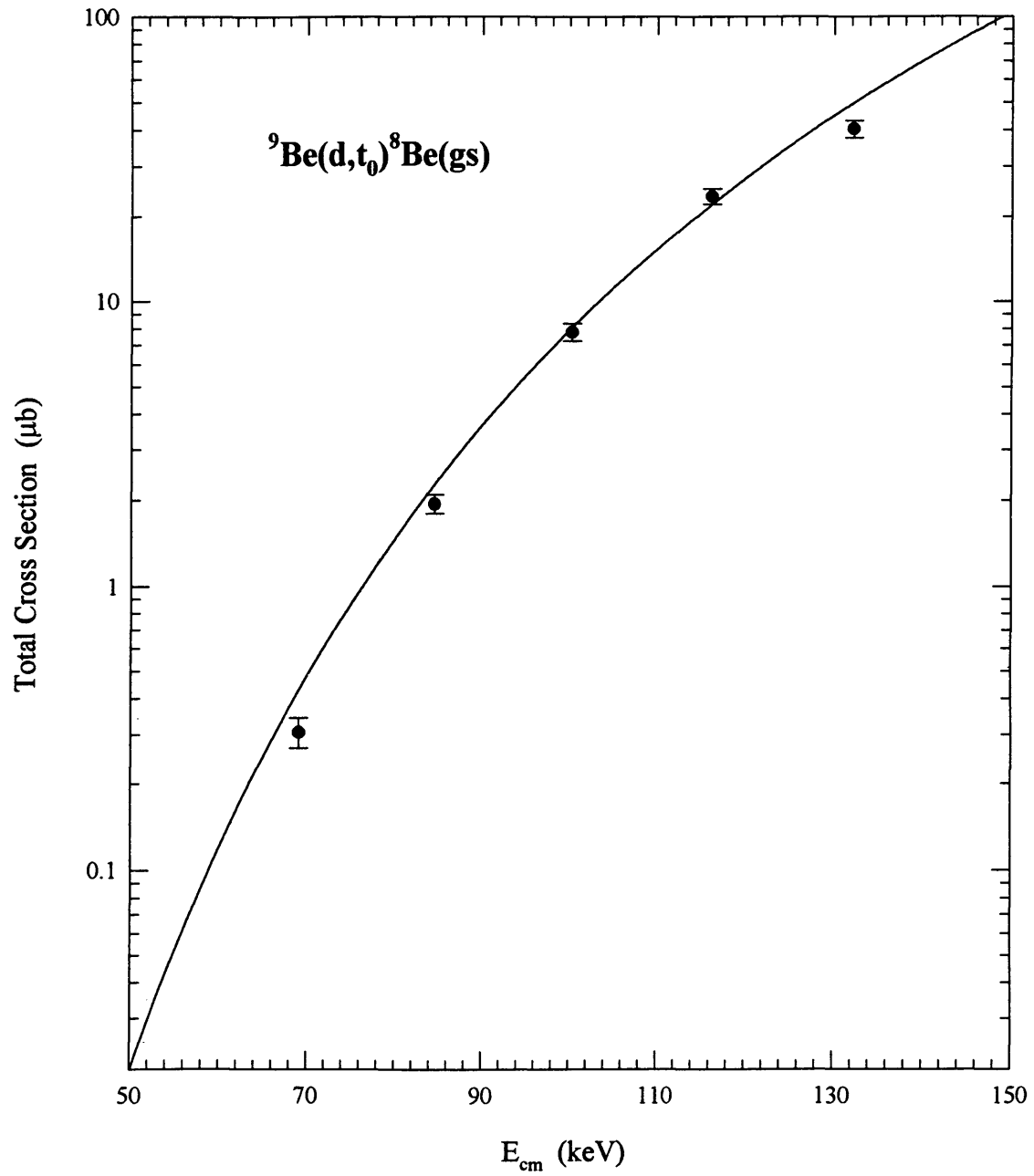
Fig. 3-18. Measured cross section for ${}^9\text{Be}(d,t_0){}^8\text{Be}(\text{gs})$.

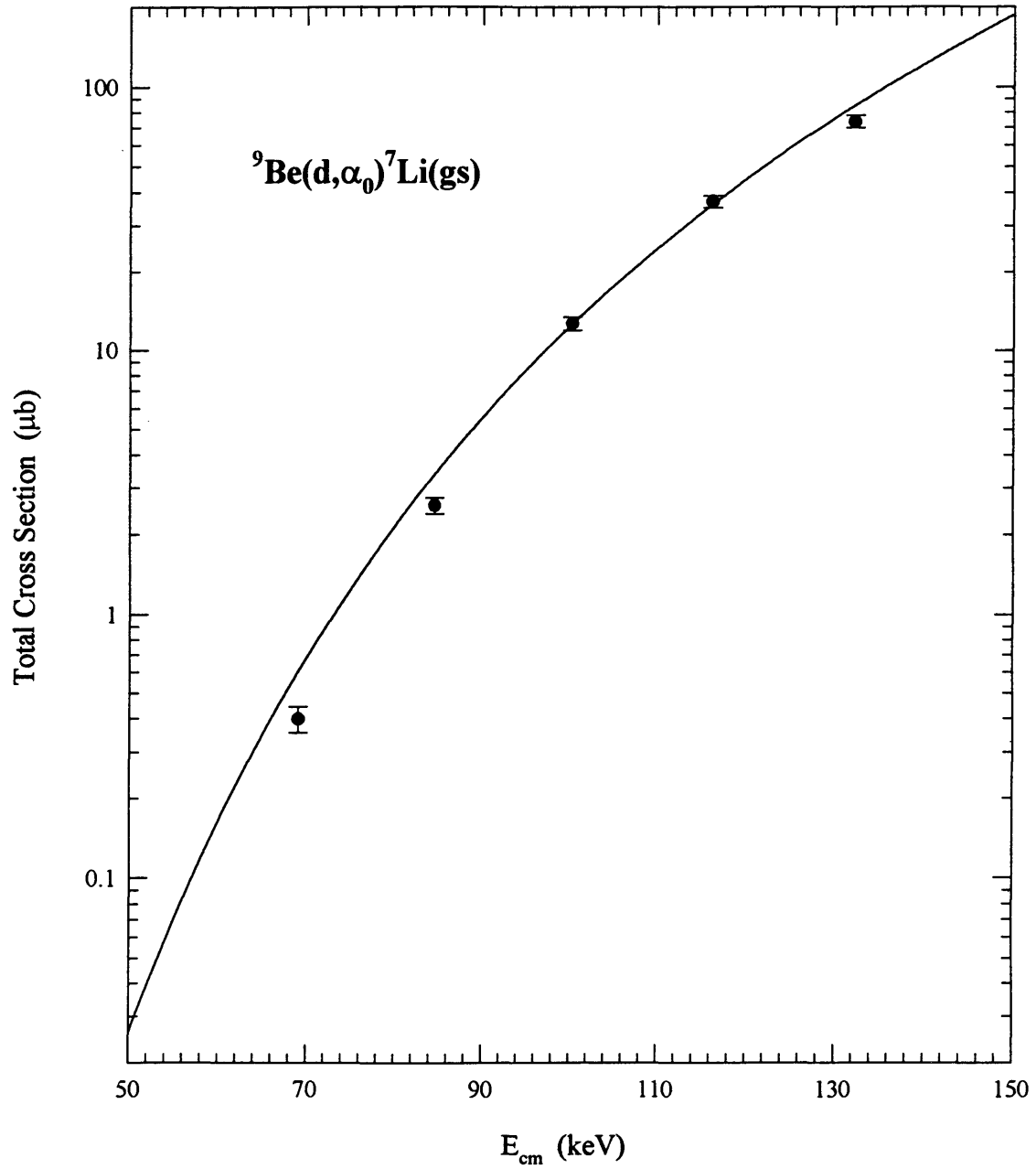
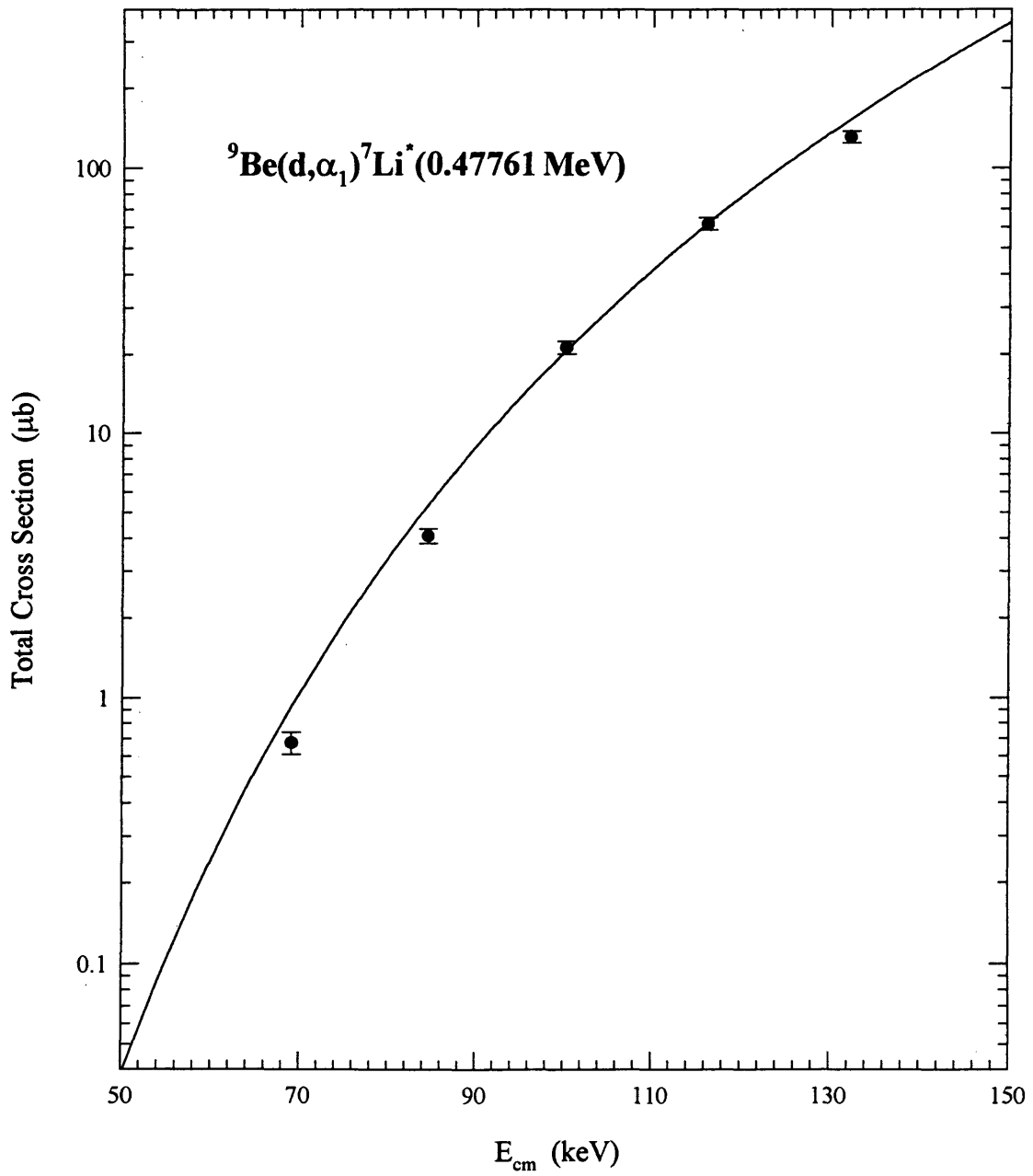
Fig. 3-19. Measured cross section for ${}^9\text{Be}(d,\alpha_0){}^7\text{Li}(\text{gs})$.

Fig. 3-20. Measured cross section for ${}^9\text{Be}(d,\alpha_1){}^7\text{Li}^*(0.47761\text{ MeV})$.

3.2.2 The $^{10}\text{B} + \text{d}$ Reaction

The angular distributions were measured at a deuteron bombarding energy of 160 keV and the yields were measured at an angle of 90° in the lab system with deuteron beam energies between 80 keV and 170 keV. All these measurements were carried out with infinitely thick targets of 90% enriched ^{10}B . Fig. 3-21 illustrates a measured energy spectrum of charged particles with its energy calibration which was made with the energy values of the particles after punching through the $1\mu\text{m}$ Ni foil on the front of the detector. Again the deuteron accumulation in the target will produce the proton and triton peaks from the $^2\text{H}(\text{d},\text{p})^3\text{H}$ reaction.

From the energy levels [Ajz85] of ^{12}C , the compound nucleus for the $^{10}\text{B} + \text{d}$ reaction, it can be known that all the resonances which the $^{10}\text{B} + \text{d}$ reaction encounters in the energy region of the present work are very broad, with the widths (FWHM) being 2000, 510 and 920 keV, compared with the CM energy region $60 \sim 150$ keV within which our results are reported. Therefore, it is reasonable to assume that the angular distributions measured at $E_{\text{cm}} = 133$ keV will remain the same shapes for the entire energy region and that the S-factor will not change significantly. These considerations will simplify Eq. (3.4) to

$$W_{\text{cm}}(\theta_{\text{cm}}, E_{\text{cm}}) = 1 + w_1 P_1(\cos\theta_{\text{cm}}) + w_2 P_2(\cos\theta_{\text{cm}}), \quad (3.7)$$

where w_1 and w_2 are constants, and will make Eq. (3.6), i.e.,

$$S(E_{\text{cm}}) = s_0 + s_1 E_{\text{cm}} + s_2 E_{\text{cm}}^2,$$

remain valid.

The values of w_1 and w_2 resulting from fitting our measured angular distributions to Eq. (3.7) are listed in Table 3-3. Figs. 3-22 through 3-29 are our measured angular distributions (in fact, the differential cross sections $(d\sigma/d\Omega)_{\text{cm}}$ given by Eq. (3.1) are plotted in these figures), with the error bars being statistical only.

The values of s_0 , s_1 and s_2 for the $^{10}\text{B} + \text{d}$ reaction obtained by the S-factor fit using Eq. (3.6) are given in Table 3-4. Figs. 3-30 through 3-37 are the cross sections (the solid lines) calculated from these experimental values of s_0 , s_1 and s_2 . The data points in Figs. 3-30 through 3-32, 3-36 and 3-37 are obtained by Eq. (2.8). Note that the solid lines

in these figures are not the curves fitting the data points. The measured cross sections from a reference [Har60] are also plotted in Figs. 3-30 through 3-33 by the open squares and are in agreement with the present results. Each of Figs. 3-33 through 3-35 is obtained from a yield measurement at a single energy with the assumption of a constant S-factor, hence, no data point can be obtained by Eq. (2-8).

Table 3-3. Summary of the angular distributions for the $^{10}\text{B} + \text{d}$ reaction. Eq. (3-7) is used.

Reaction	w_1	w_2	Graph
$^{10}\text{B}(\text{d}, \text{p}_0)^{11}\text{B}(\text{gs})$	-0.45 ± 0.14	-0.22 ± 0.14	Fig. 3-22
$^{10}\text{B}(\text{d}, \text{p}_1)^{11}\text{B}^*(2.1247 \text{ MeV})$	None	-0.223 ± 0.080	Fig. 3-23
$^{10}\text{B}(\text{d}, \text{p}_2)^{11}\text{B}^*(4.4451 \text{ MeV})$	$+0.808 \pm 0.035$	$+0.250 \pm 0.034$	Fig. 3-24
$^{10}\text{B}(\text{d}, \text{p}_3)^{11}\text{B}^*(5.021 \text{ MeV})$	None	$+0.51 \pm 0.14$	Fig. 3-25
$^{10}\text{B}(\text{d}, \text{p}_4)^{11}\text{B}^*(6.743 \text{ MeV})$	None	None	Fig. 3-26
$^{10}\text{B}(\text{d}, \text{p}_5)^{11}\text{B}^*(7.286 \text{ MeV})$	None	None	Fig. 3-27
$^{10}\text{B}(\text{d}, \alpha_0)^8\text{Be}(\text{gs})$	-0.572 ± 0.059	-0.390 ± 0.067	Fig. 3-28
$^{10}\text{B}(\text{d}, \alpha_1)^8\text{Be}^*(3.04 \text{ MeV})$	-0.580 ± 0.043	-0.184 ± 0.046	Fig. 3-29

Table 3-4. Summary of the S-factors for the $^{10}\text{B} + \text{d}$ reaction. Eq. (3-6) is used.

Reaction	s_0 (b·MeV)	s_1 (b)	s_2 (b·(MeV) ⁻¹)	Graph
$^{10}\text{B}(\text{d}, \text{p}_0)^{11}\text{B}(\text{gs})$	29.0 ± 2.1	-16.4 ± 1.5	-27.9 ± 3.5	Fig. 3-30
$^{10}\text{B}(\text{d}, \text{p}_1)^{11}\text{B}^*(2.1247 \text{ MeV})$	11.52 ± 0.62	-6.38 ± 0.50	2.96 ± 0.34	Fig. 3-31
$^{10}\text{B}(\text{d}, \text{p}_2)^{11}\text{B}^*(4.4451 \text{ MeV})$	42.6 ± 1.9	34.2 ± 2.5	38.2 ± 4.3	Fig. 3-32
$^{10}\text{B}(\text{d}, \text{p}_3)^{11}\text{B}^*(5.021 \text{ MeV})$	6.0 ± 1.2	None	None	Fig. 3-33
$^{10}\text{B}(\text{d}, \text{p}_4)^{11}\text{B}^*(6.743 \text{ MeV})$	49.3 ± 4.2	None	None	Fig. 3-34
$^{10}\text{B}(\text{d}, \text{p}_5)^{11}\text{B}^*(7.286 \text{ MeV})$	17.7 ± 2.3	None	None	Fig. 3-35
$^{10}\text{B}(\text{d}, \alpha_0)^8\text{Be}(\text{gs})$	7.09 ± 0.35	-3.27 ± 0.25	-4.92 ± 0.56	Fig. 3-36
$^{10}\text{B}(\text{d}, \alpha_1)^8\text{Be}^*(3.04 \text{ MeV})$	95.7 ± 4.3	-24.1 ± 1.8	-40.9 ± 4.6	Fig. 3-37

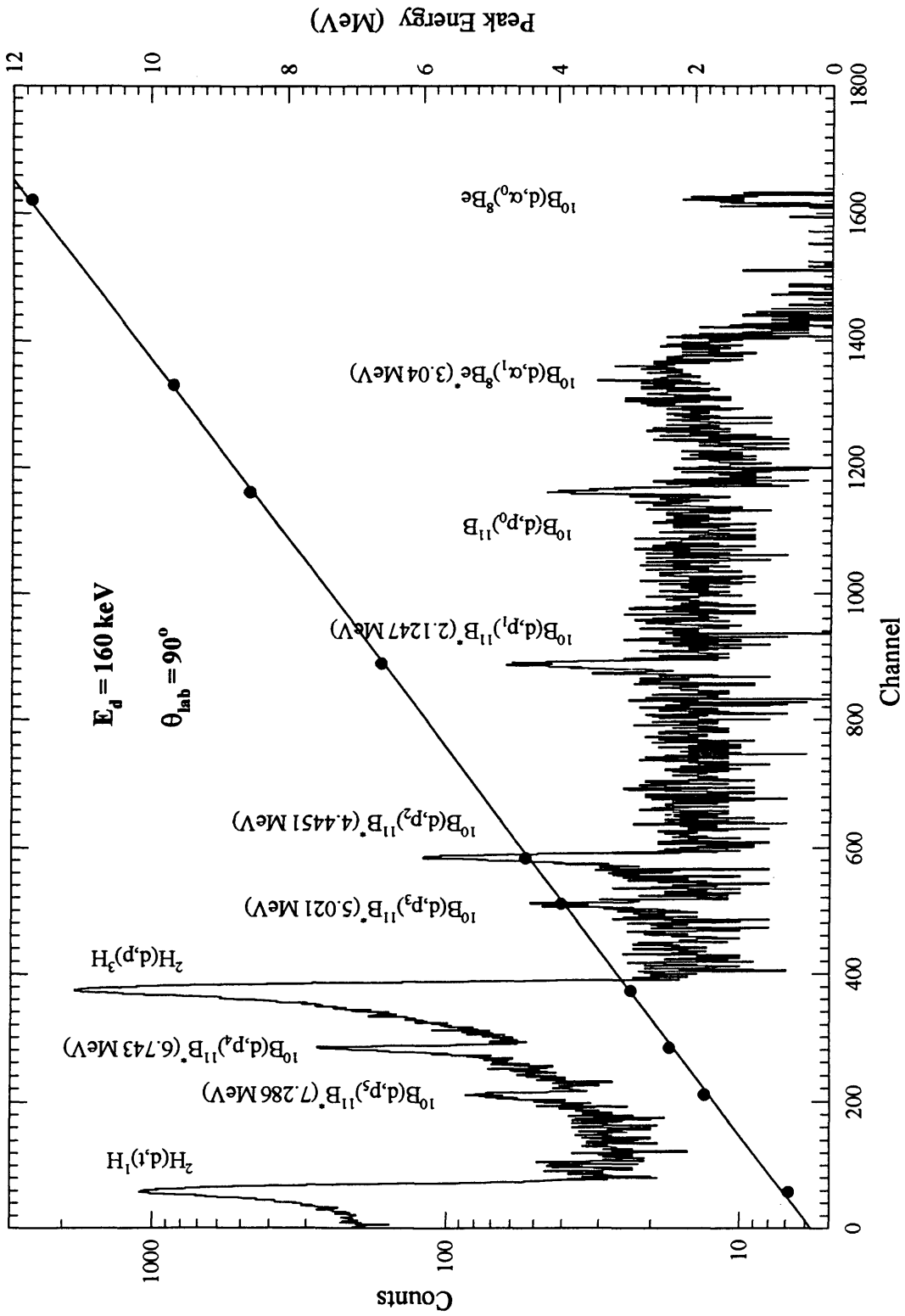


Fig. 3-21. A measured spectrum for $^{10}\text{B} + \text{d}$ reaction with energy calibration.

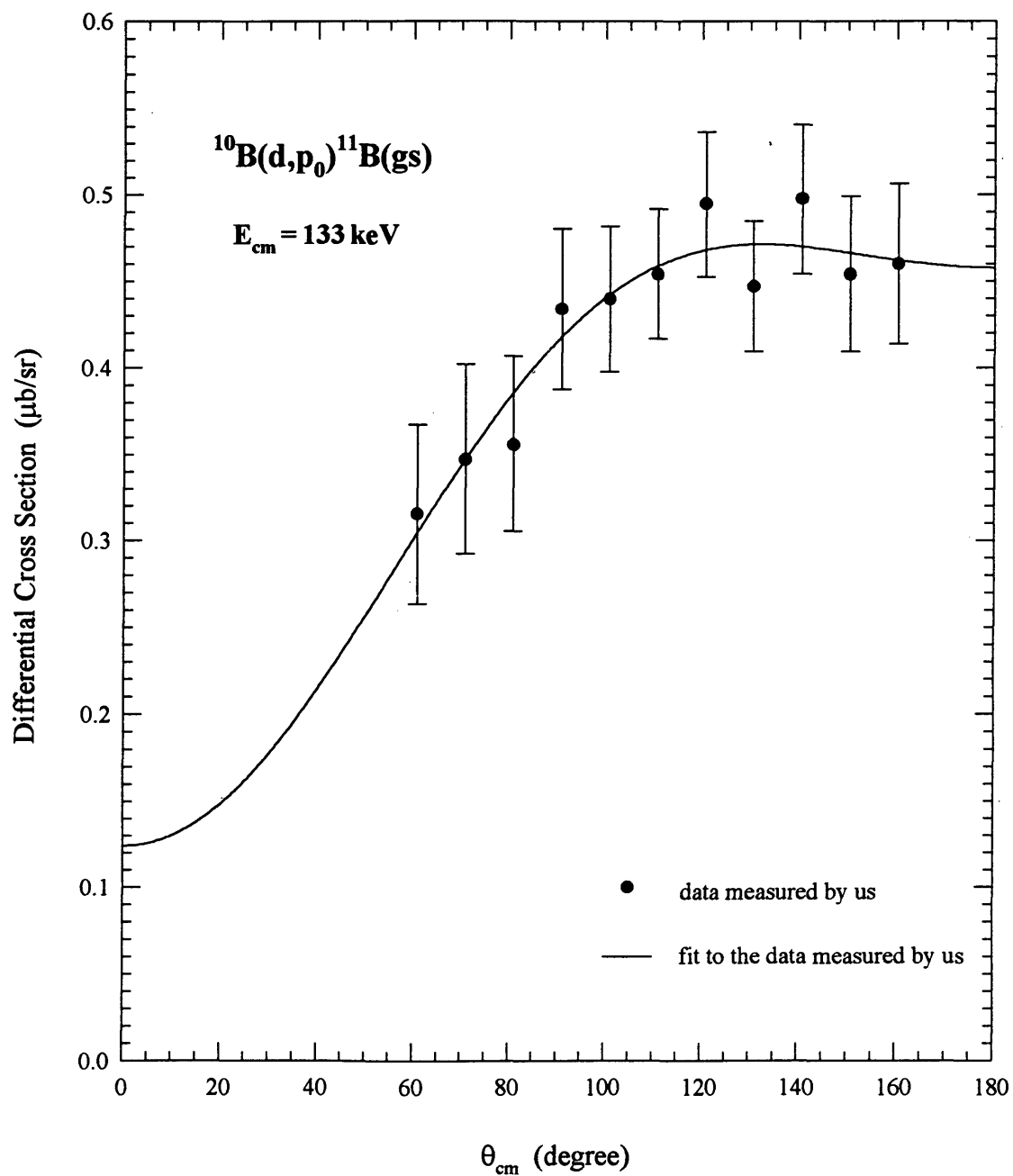
Fig. 3-22. A measured angular distribution for $^{10}\text{B}(d,p_0)^{11}\text{B}(\text{gs})$.

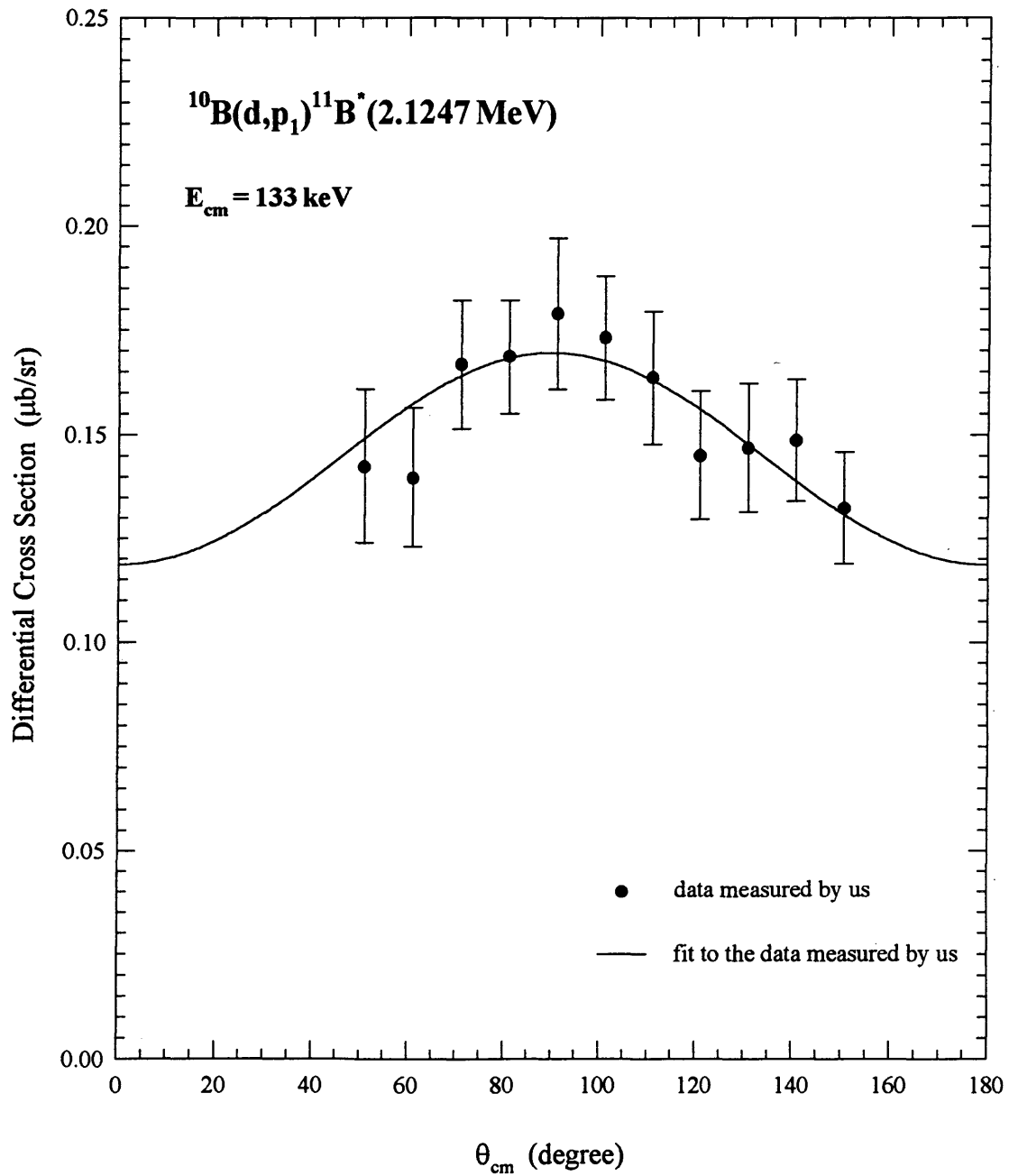
Fig. 3-23. A measured angular distribution for $^{10}\text{B}(d,p_1)^{11}\text{B}^*$ (2.1247 MeV).

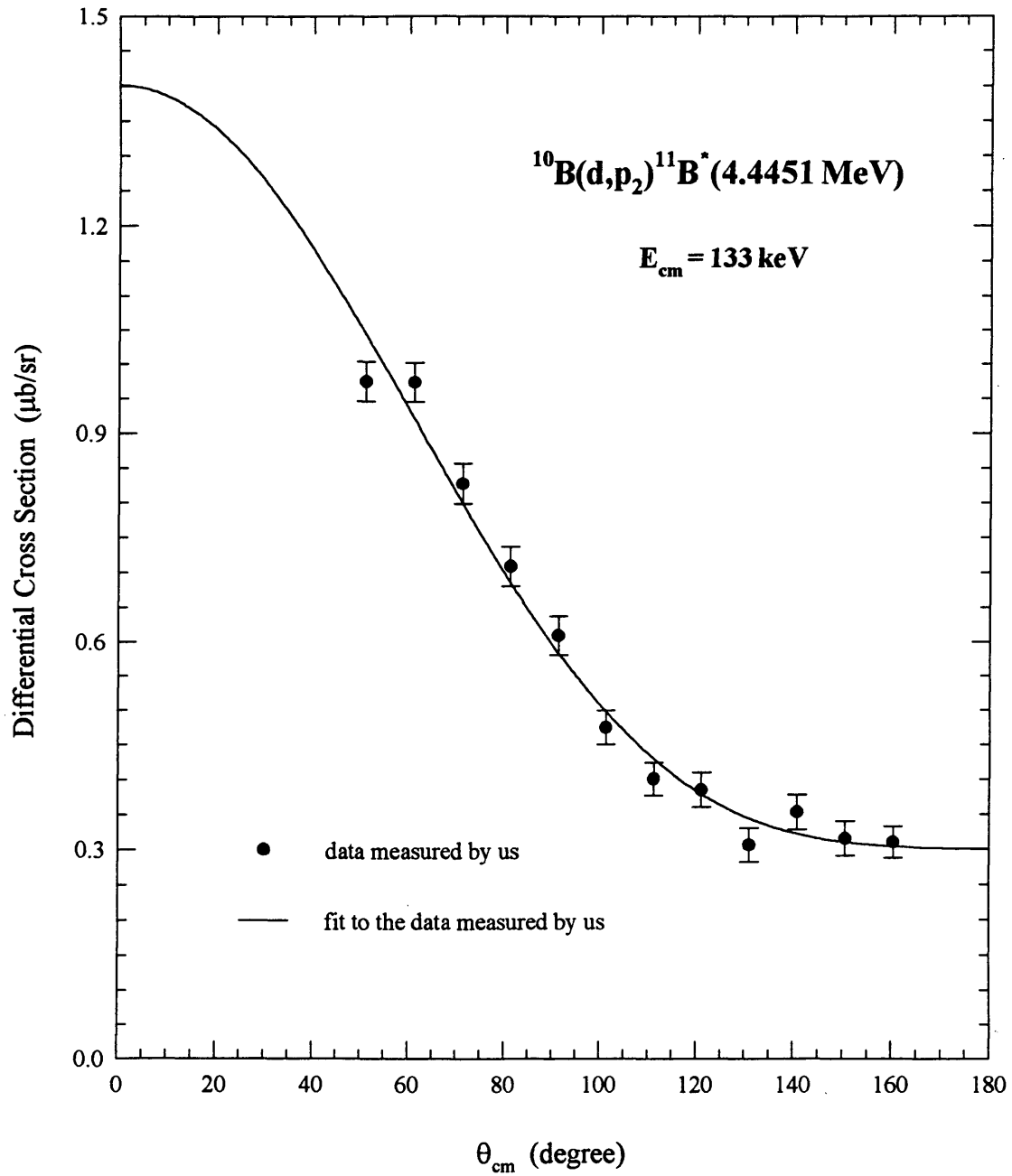
Fig. 3·24. A measured angular distribution for $^{10}\text{B}(d,p_2)^{11}\text{B}^*(4.4451\text{ MeV})$.

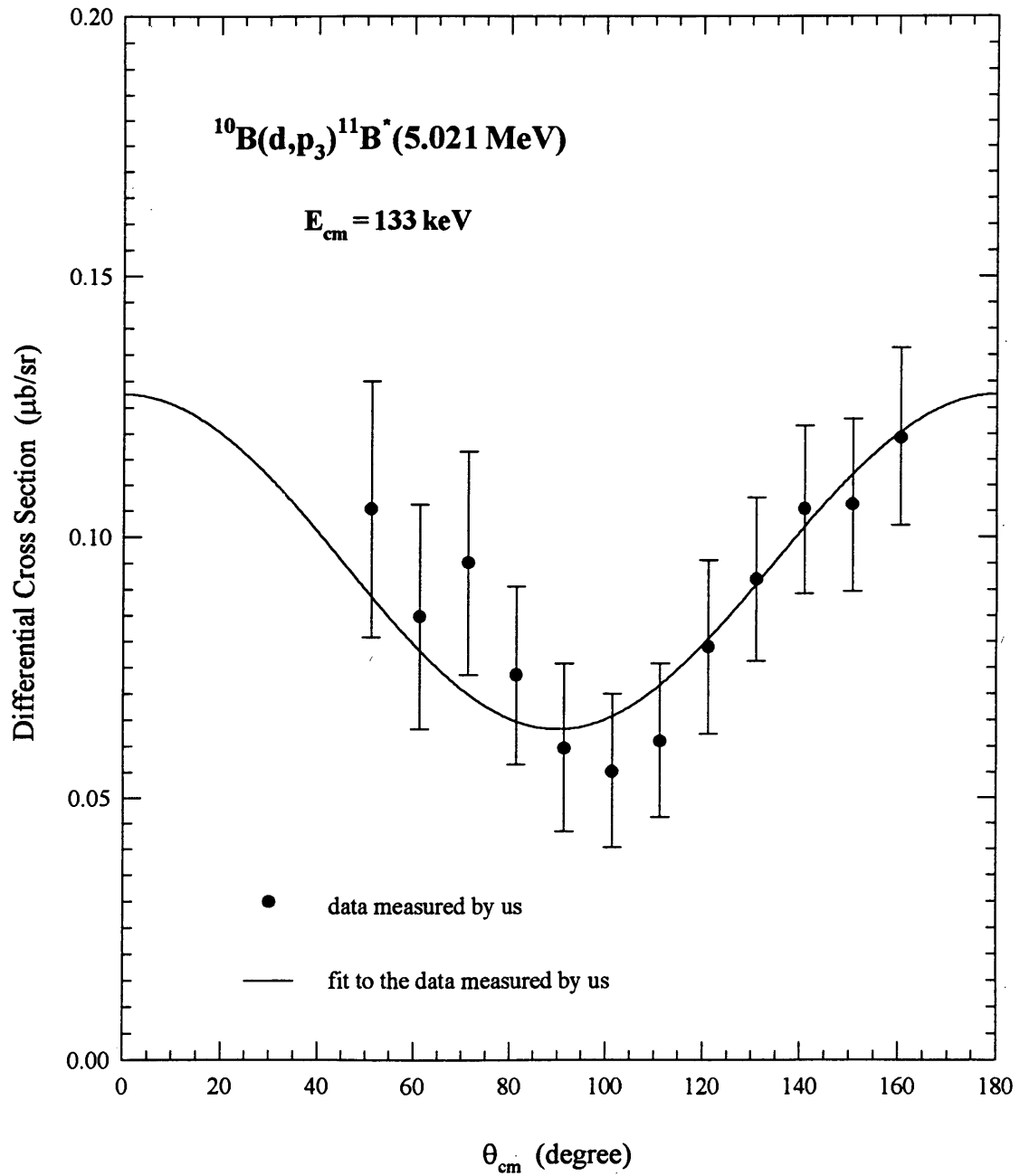
Fig. 3-25. A measured angular distribution for $^{10}\text{B}(d,p_3)^{11}\text{B}^*$ (5.021 MeV).

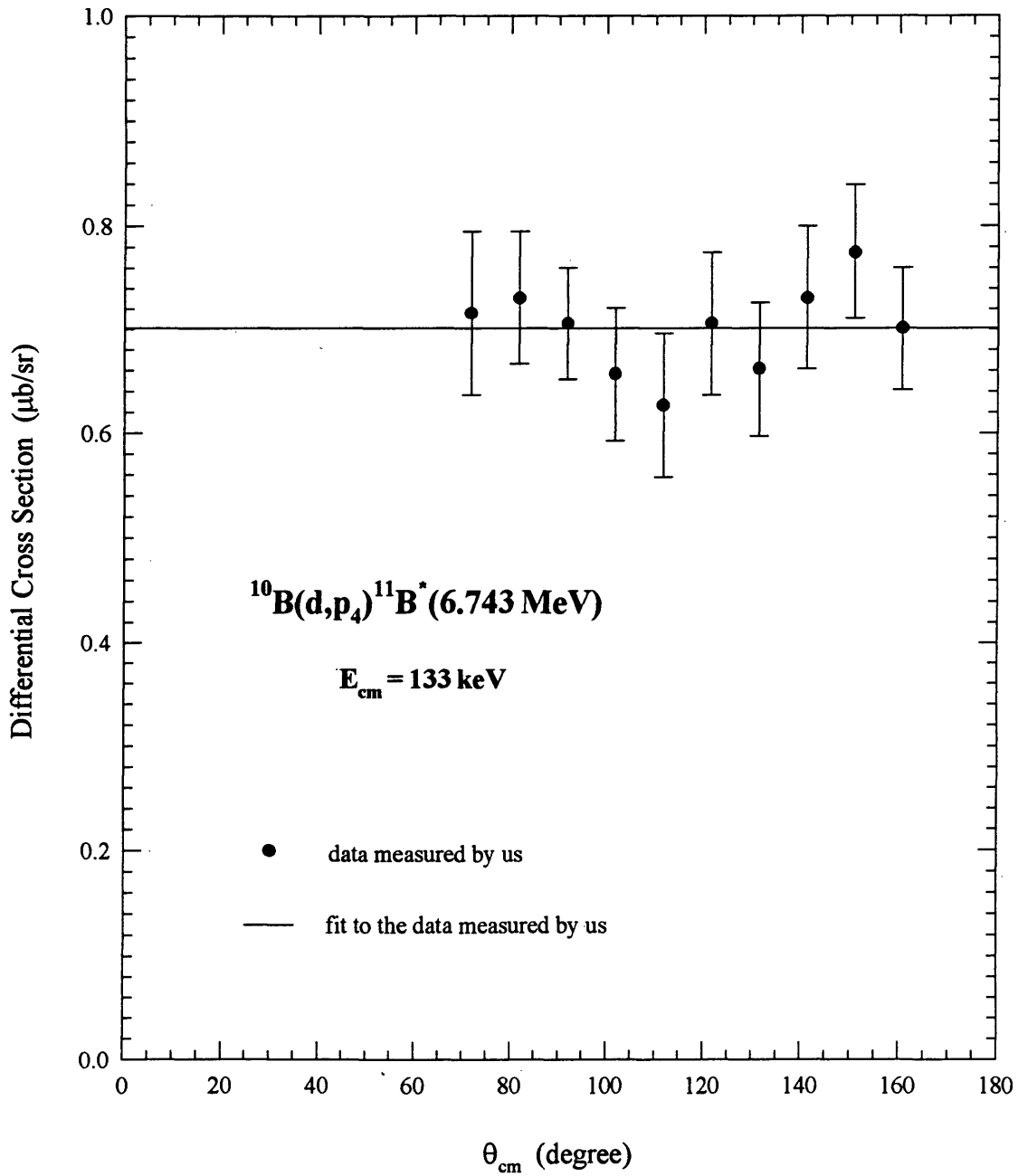
Fig. 3-26. A measured angular distribution for $^{10}\text{B}(d,p_4)^{11}\text{B}^*$ (6.743 MeV).

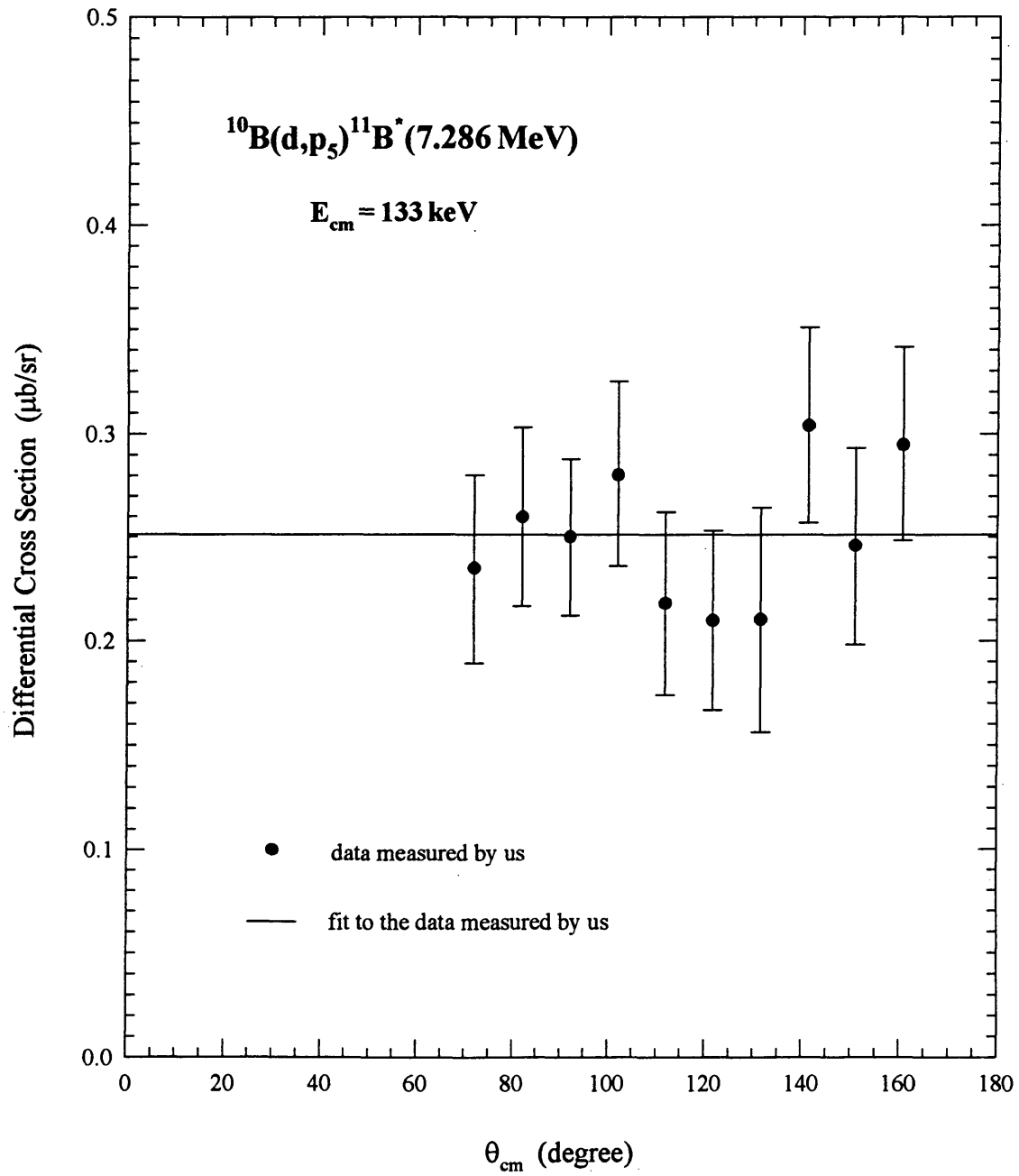
Fig. 3-27. A measured angular distribution for $^{10}\text{B}(d,p_5)^{11}\text{B}^*(7.286\text{ MeV})$.

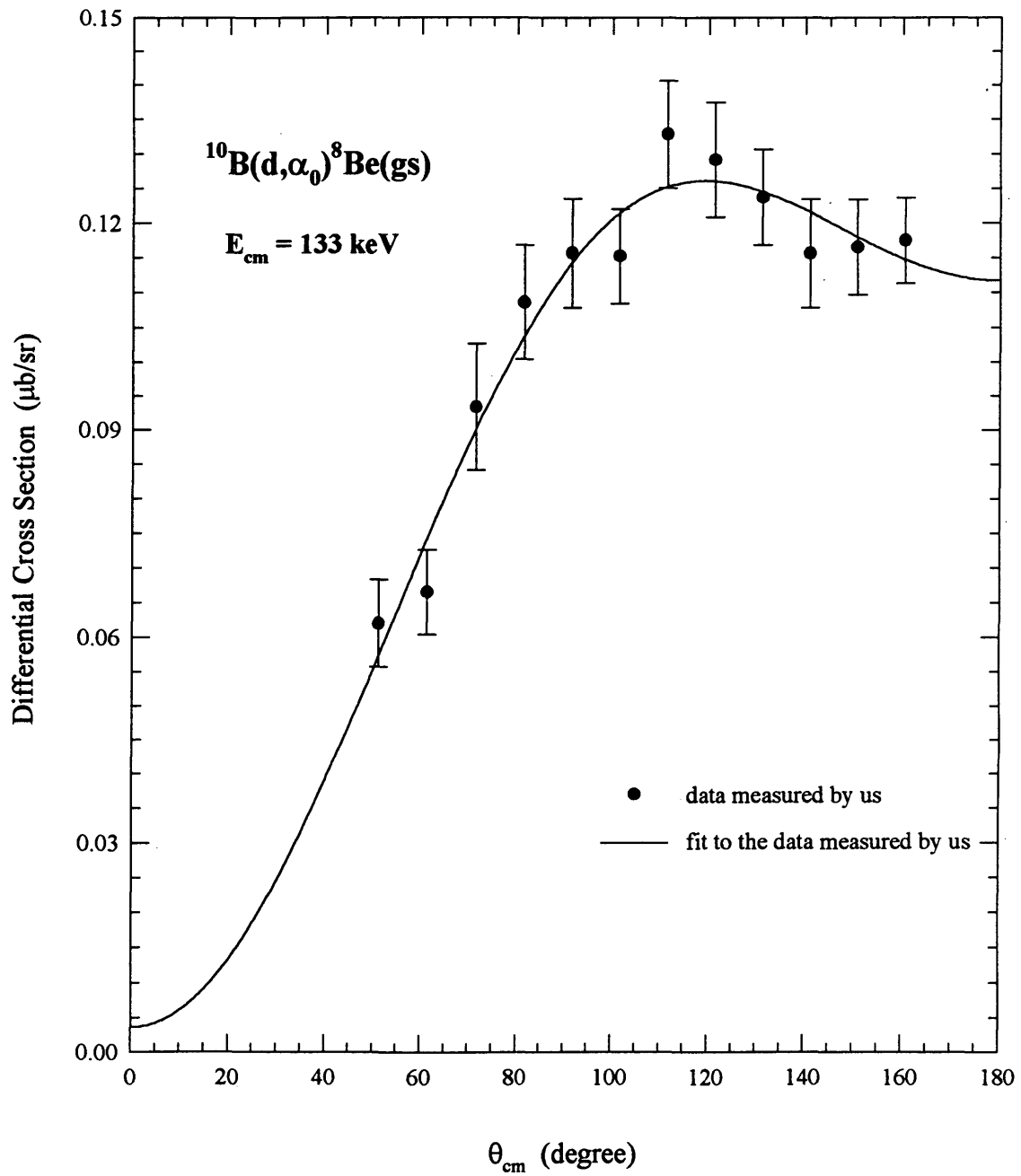
Fig. 3-28. A measured angular distribution for $^{10}\text{B}(d,\alpha_0)^8\text{Be}(\text{gs})$.

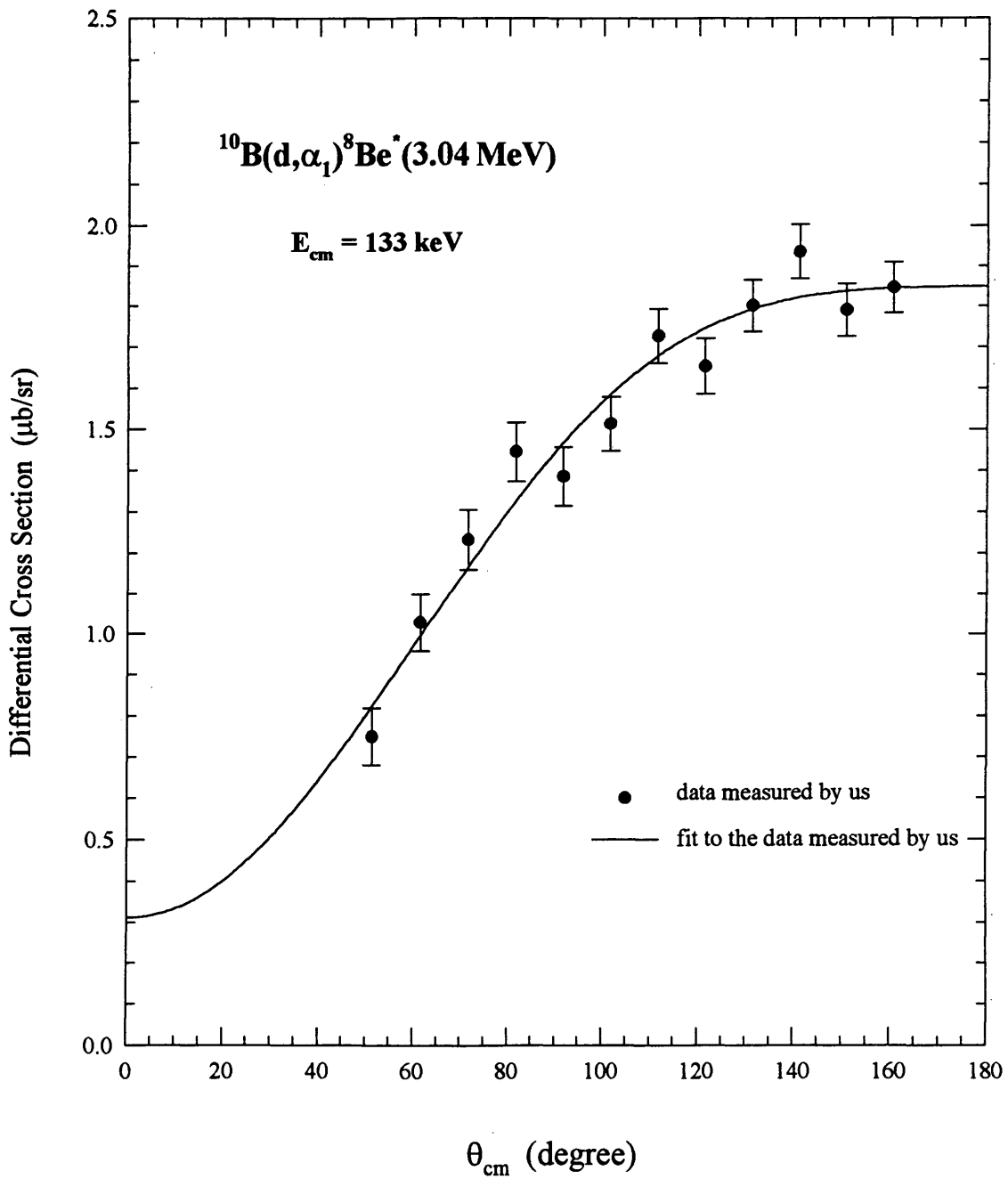
Fig. 3-29. A measured angular distribution for $^{10}\text{B}(d,\alpha_1)^8\text{Be}^*$ (3.04 MeV).

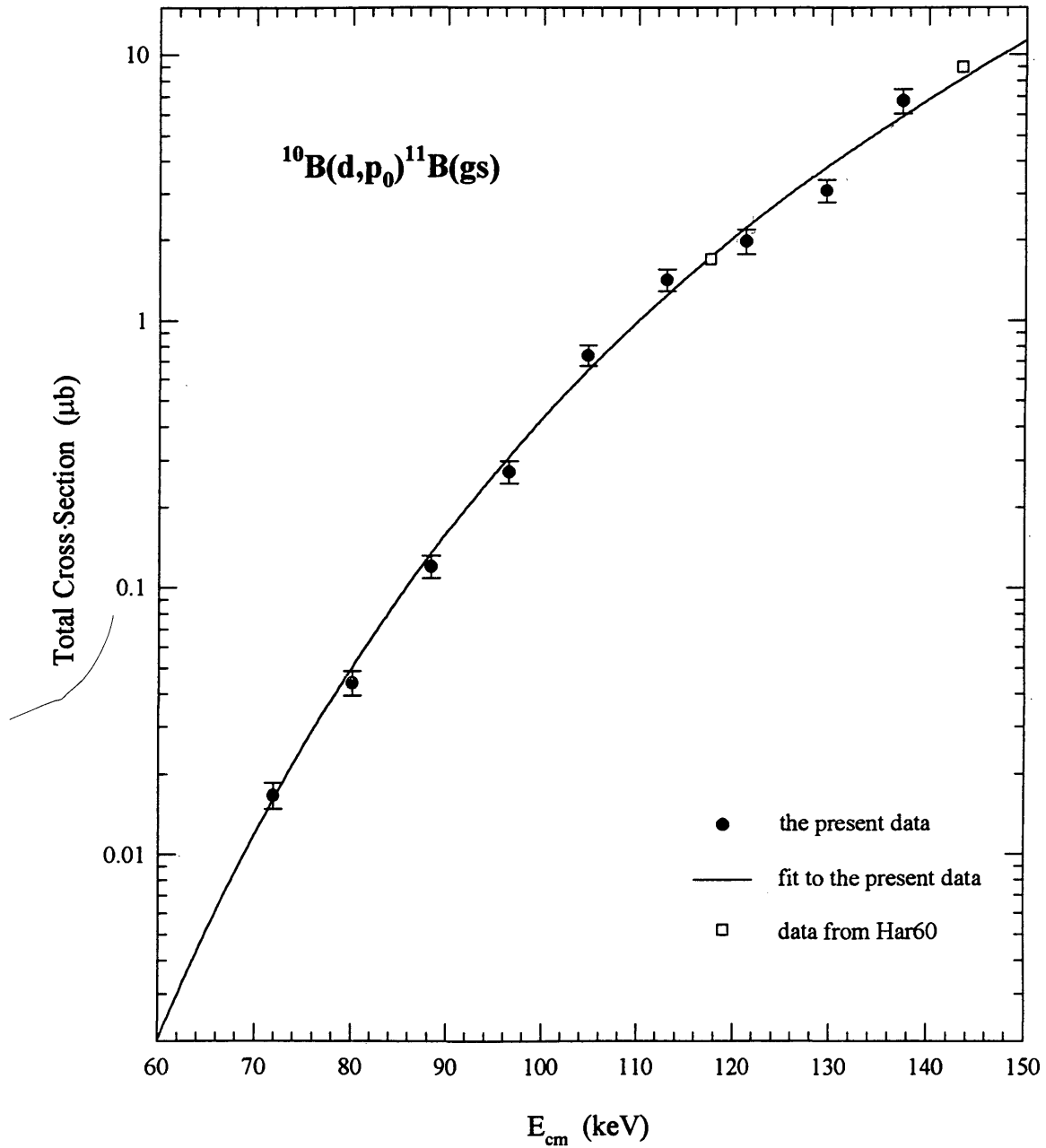
Fig. 3-30. Measured cross section for $^{10}\text{B}(d,p_0)^{11}\text{B}(\text{gs})$ reaction.

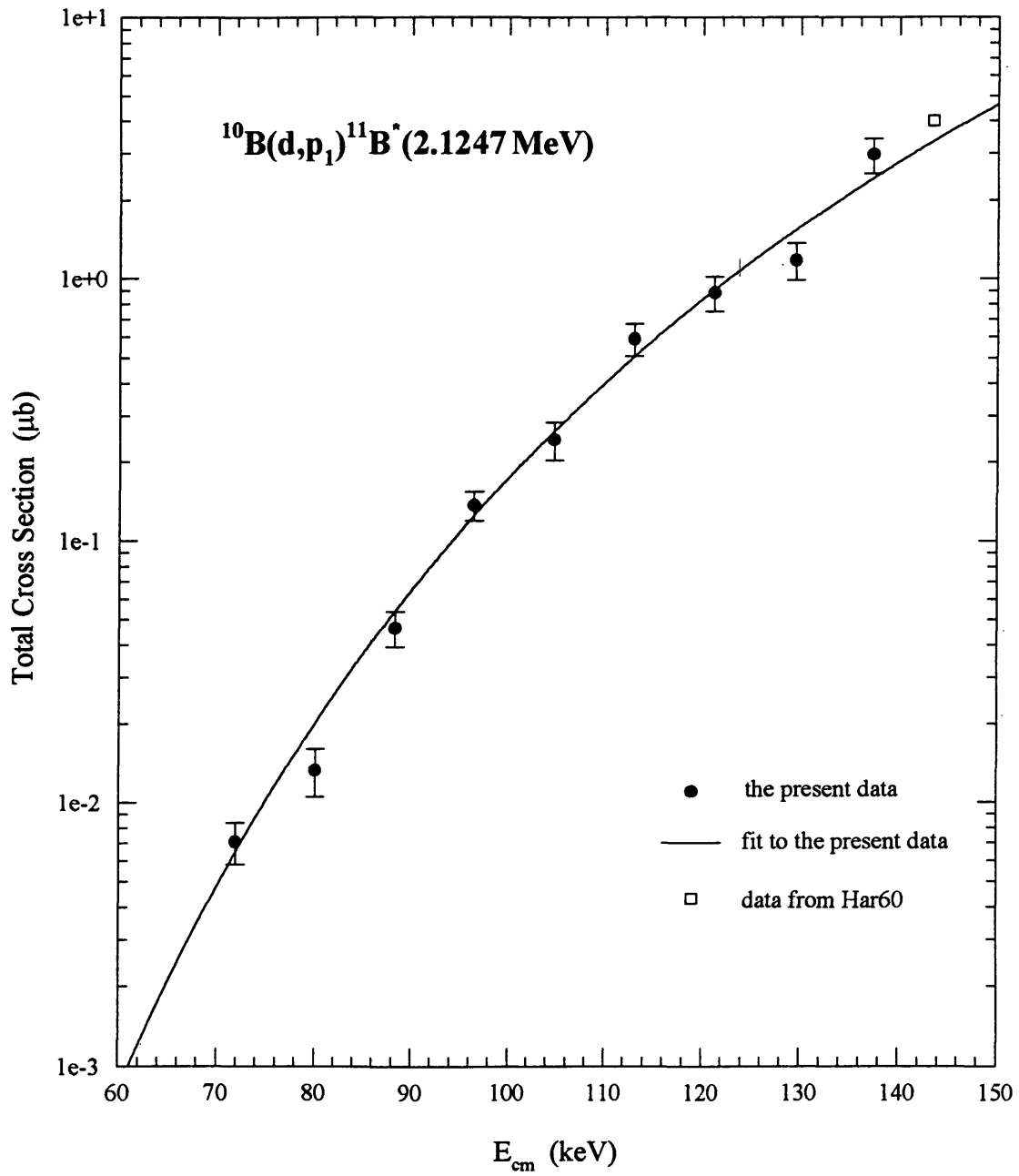
Fig. 3-31. Measured cross section for $^{10}\text{B}(d,p_1)^{11}\text{B}^*(2.1247\text{ MeV})$ reaction.

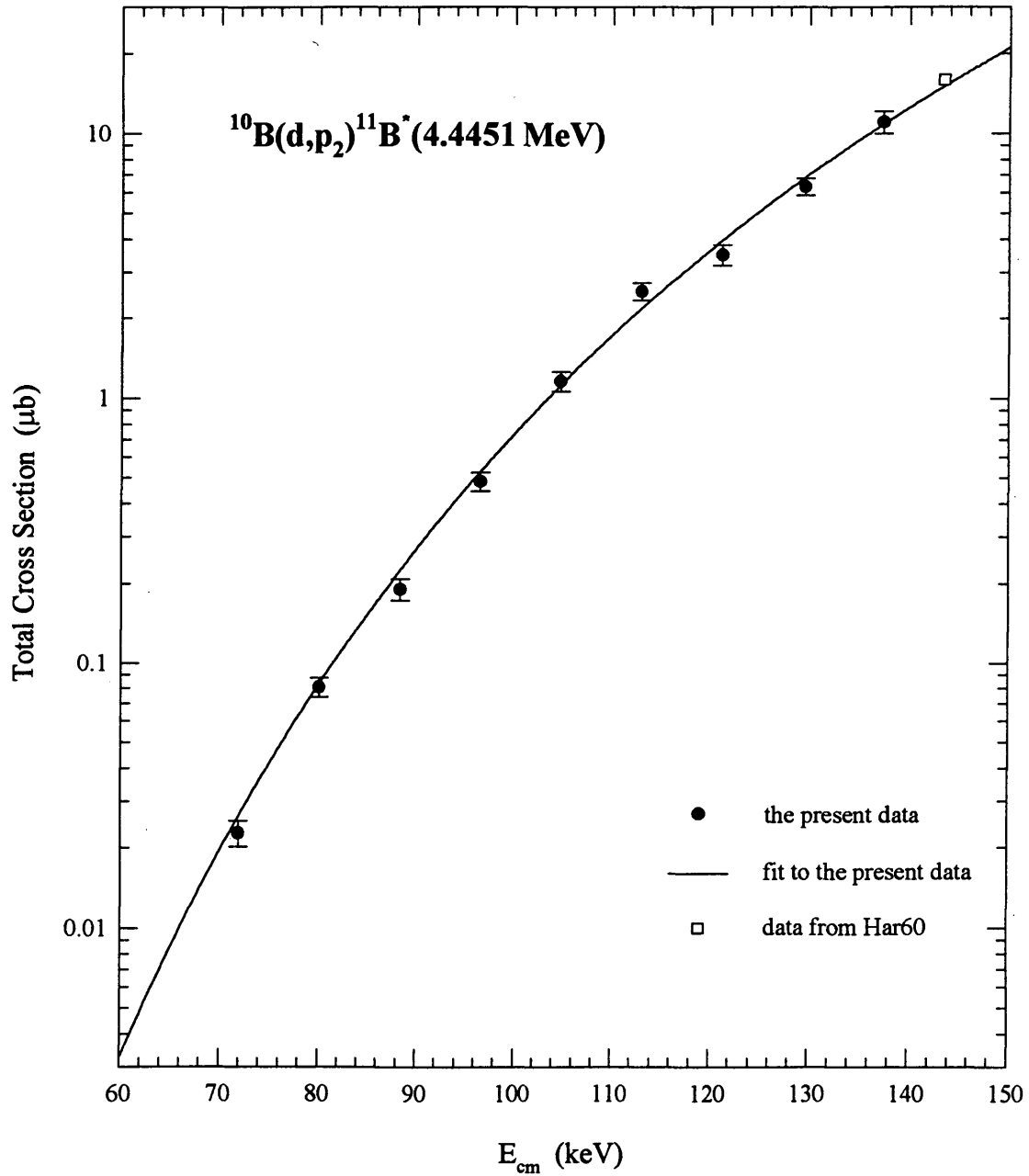
Fig. 3-32. Measured cross section for $^{10}\text{B}(d,p_2)^{11}\text{B}^*(4.4451\text{ MeV})$ reaction.

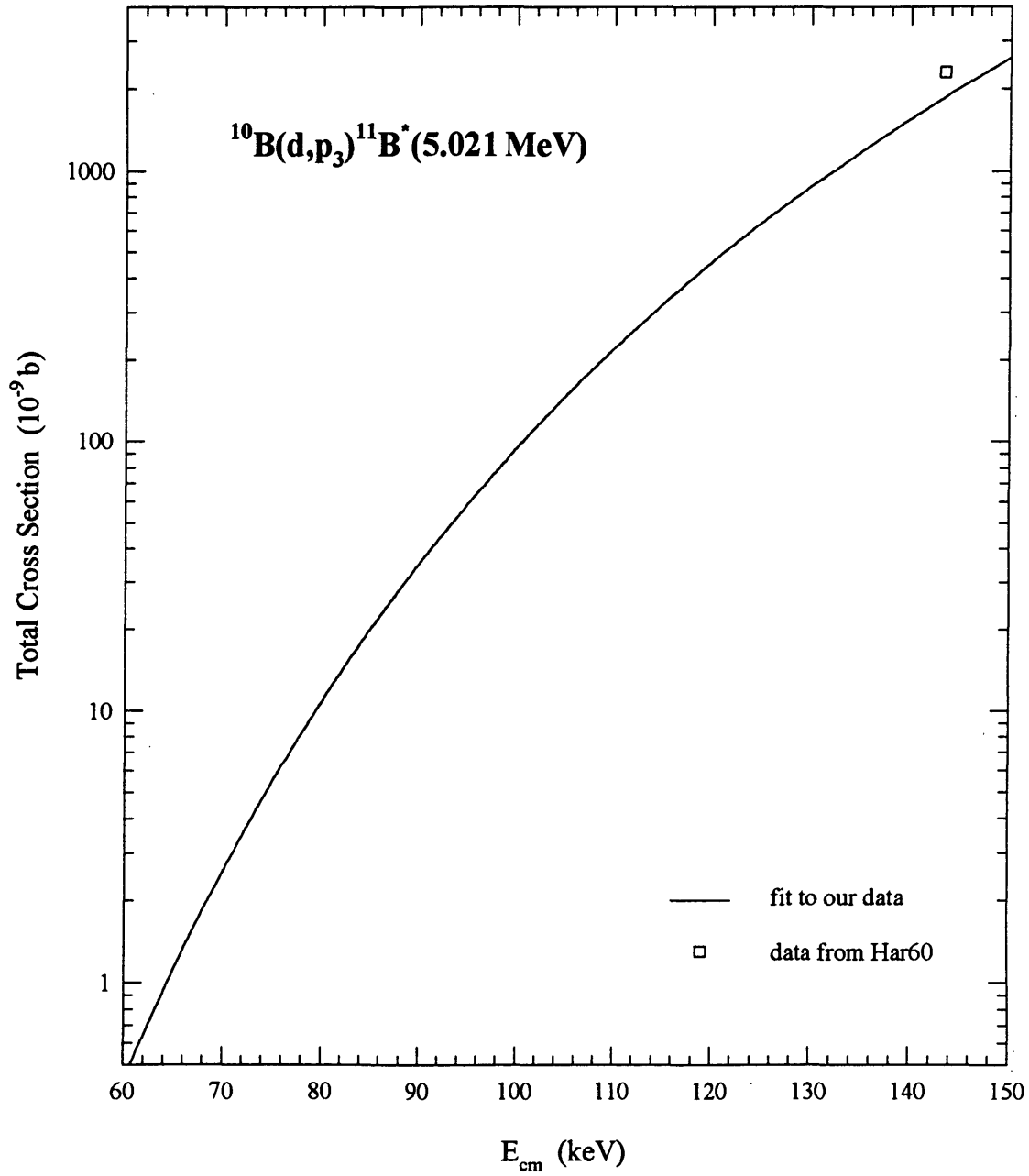
Fig. 3-33. Measured cross section for $^{10}\text{B}(d,p_3)^{11}\text{B}^*(5.021\text{ MeV})$ reaction.

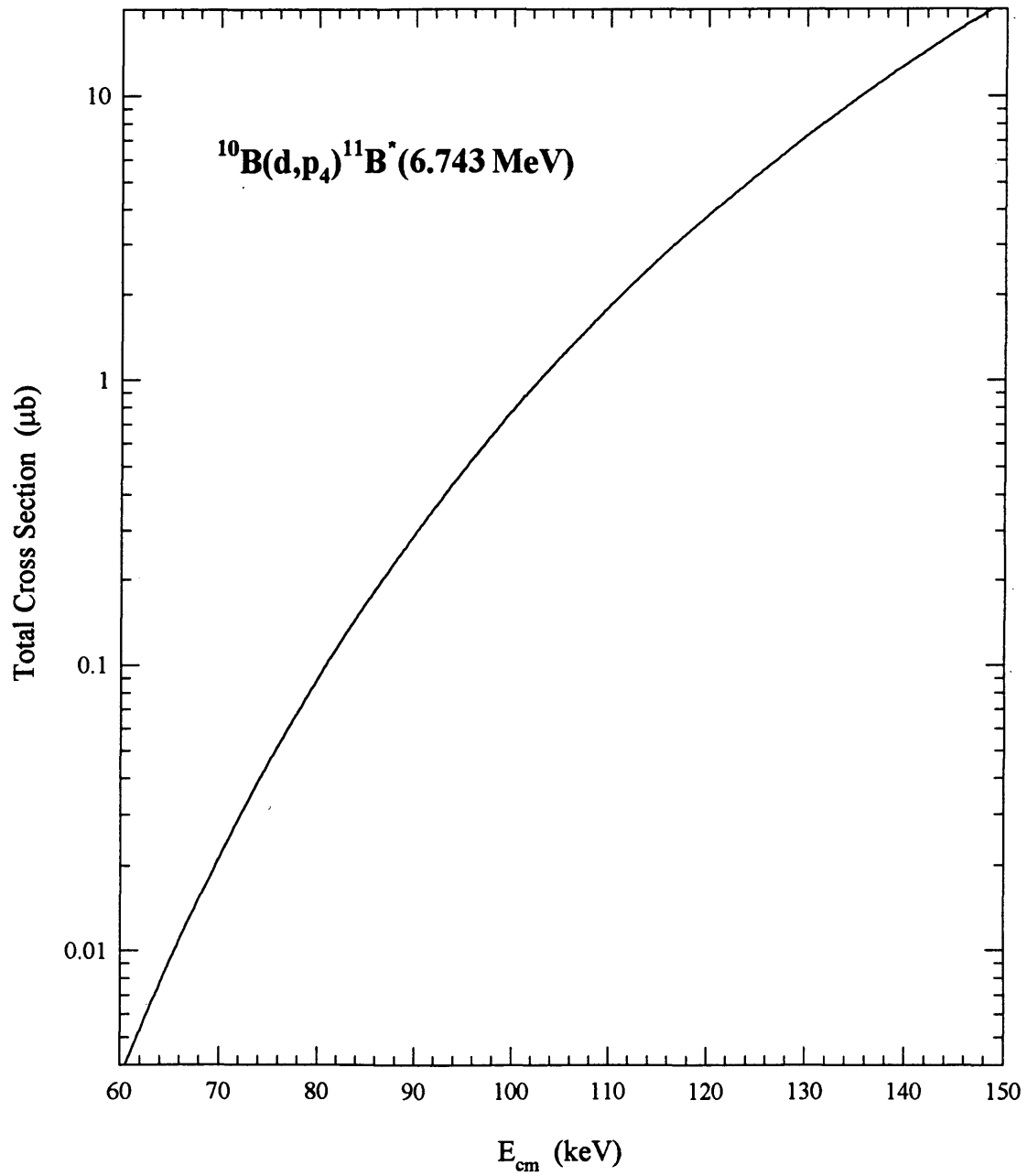
Fig. 3-34. Measured cross section for $^{10}\text{B}(d,p_4)^{11}\text{B}^*(6.743\text{ MeV})$ reaction.

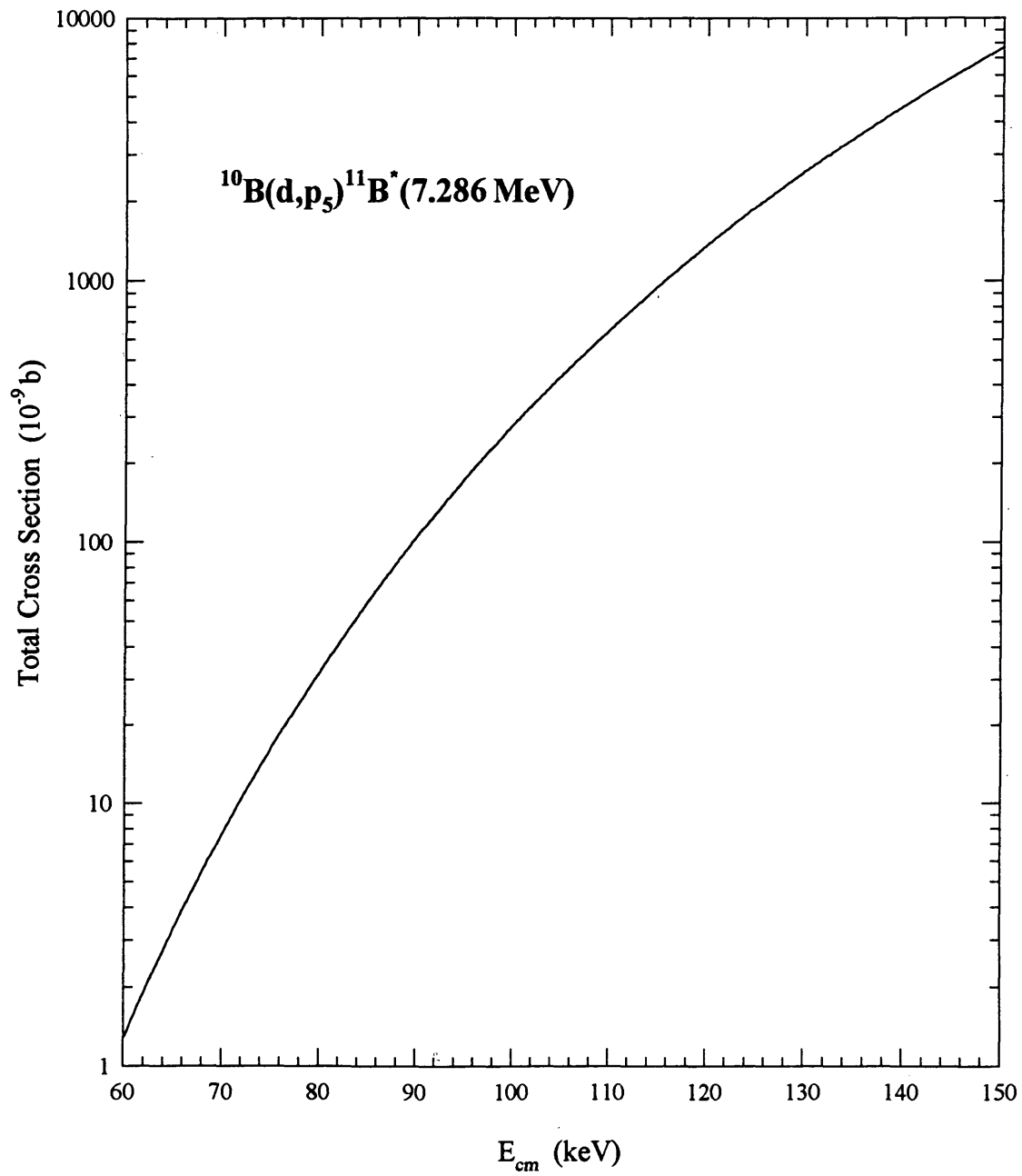
Fig. 3-35. Measured cross section for $^{10}\text{B}(d,p_5)^{11}\text{B}^*(7.286\text{ MeV})$ reaction.

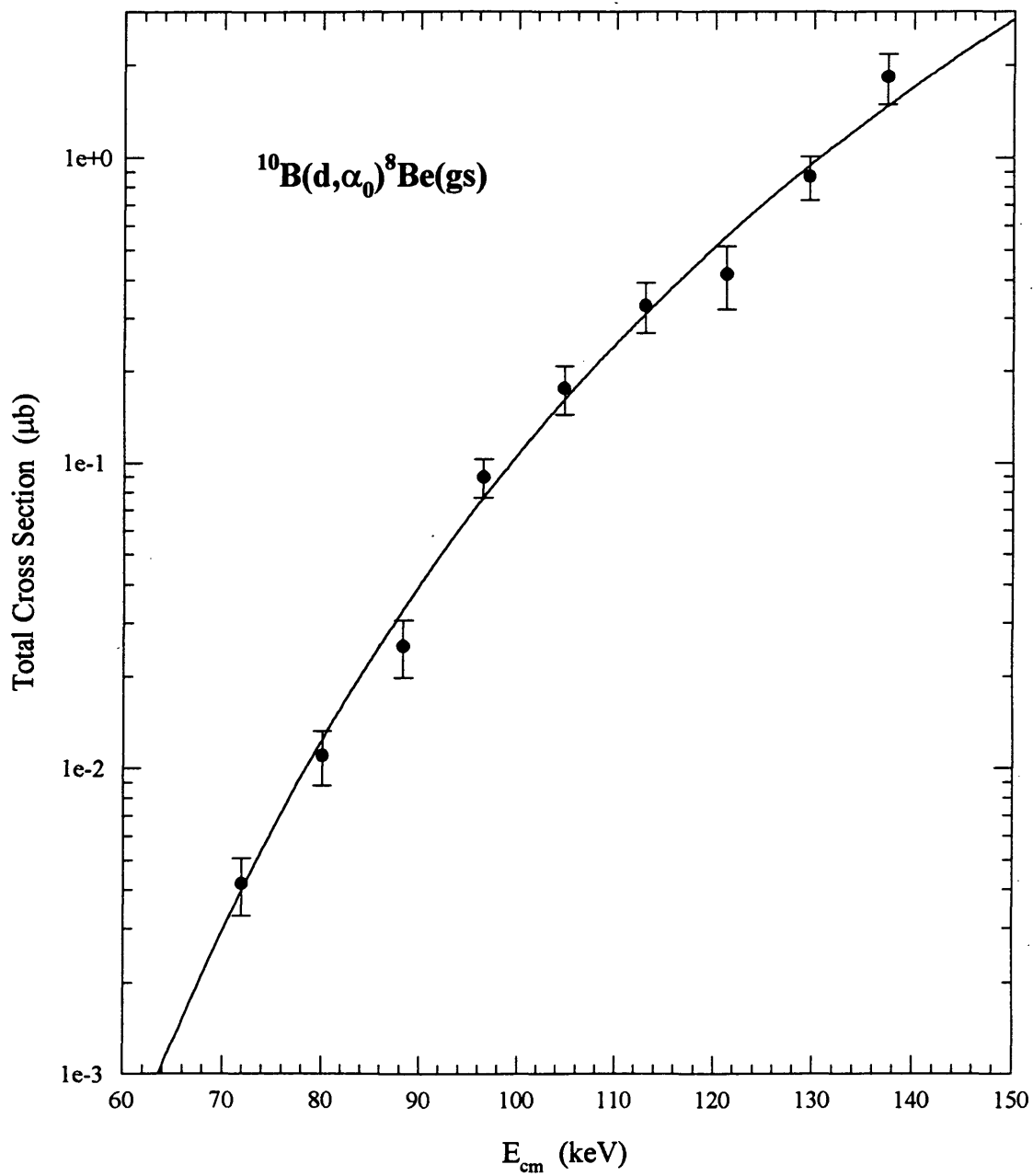
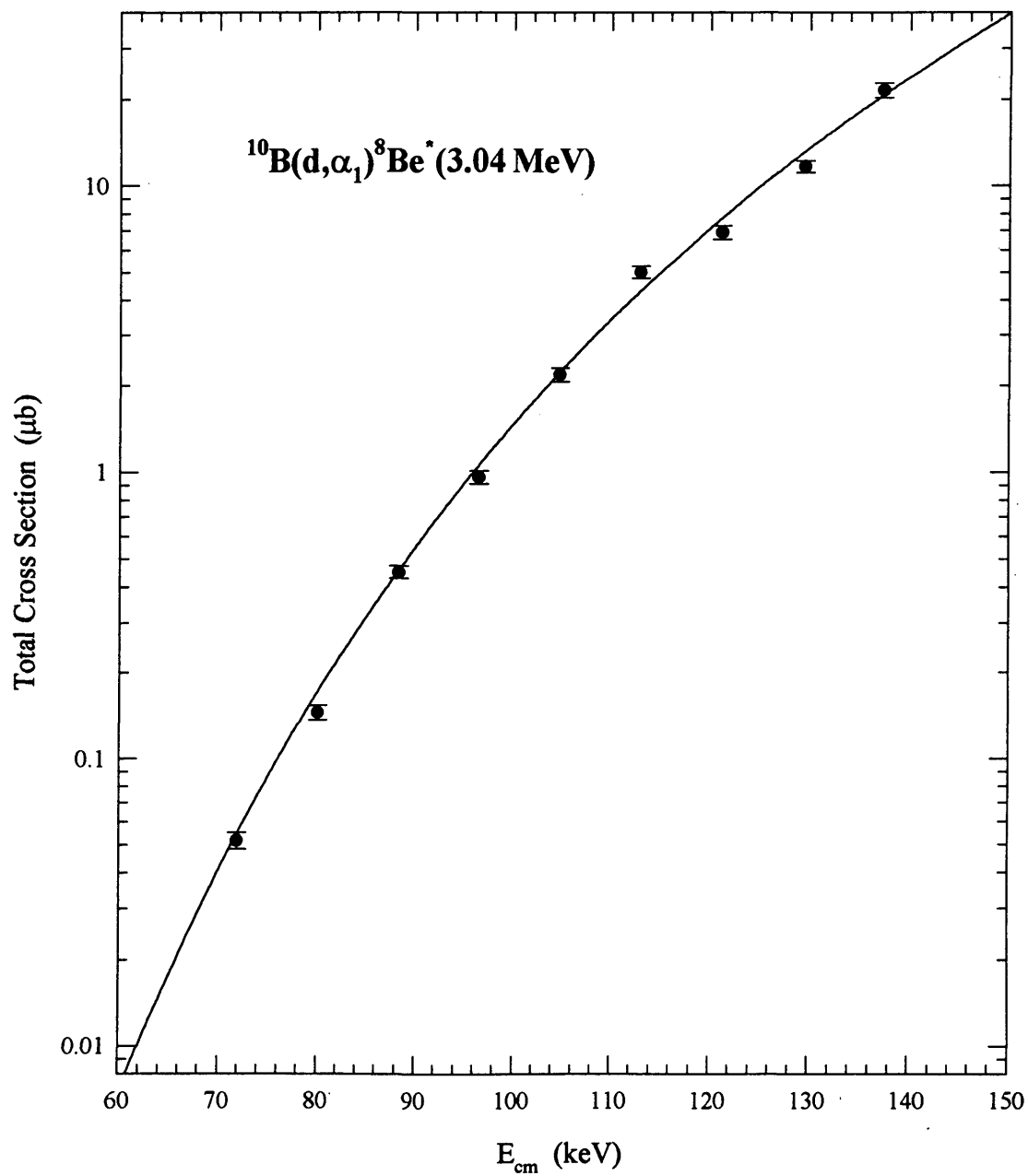
Fig. 3-36. Measured cross section for $^{10}\text{B}(d,\alpha_0)^8\text{Be}^*(\text{gs})$ reaction.

Fig. 3-37. Measured cross section for $^{10}\text{B}(d,\alpha_1)^8\text{Be}^*(3.04\text{ MeV})$ reaction.

3·2·3 The $^{11}\text{B} + \text{d}$ Reaction

The angular distributions were measured at two deuteron bombarding energies of 120 keV and 168 keV and the yields were measured at an angle of 130° in the lab system with deuteron beam energies between 100 keV and 170 keV. All these measurements were carried out with infinitely thick targets of natural boron. Fig. 3·38 illustrates a measured energy spectrum of charged particles with its energy calibration which was made with the energy values of the particles after punching through the $1\mu\text{m}$ Ni foil on the front of the detector. Again, the deuteron accumulation in the target will produce the proton and triton peaks from the $^2\text{H}(\text{d},\text{p})^3\text{H}$ reaction and the existence of ^{10}B in the target will result in the deuteron-induced reactions on ^{10}B .

The angular distributions at the two energies are fitted to $1 + w_1 P_1(\cos\theta_{\text{cm}}) + w_2 P_2(\cos\theta_{\text{cm}})$ and the coefficients, w_1 and w_2 , are given in Table 3·5. Figs. 3·39 through 3·44 are these measured angular distributions (in fact, the differential cross sections $(d\sigma/d\Omega)_{\text{cm}}$ given by Eq. (3·1) are plotted in these figures), with the error bars being statistical only.

This case of the $^{11}\text{B} + \text{d}$ reaction is similar with that of $^9\text{Be} + \text{d}$ by inspecting the energy levels [Ajz86] of ^{13}C . Hence, Eqs. (3·5) and (3·5a), i.e.,

$$W_{\text{cm}}(\theta_{\text{cm}}, E_{\text{cm}}) = 1 + a_1^{(1)} E_{\text{cm}} P_1(\cos\theta_{\text{cm}}) + a_2^{(1)} E_{\text{cm}} P_2(\cos\theta_{\text{cm}})$$

and

$$W_{\text{cm}}(\theta_{\text{cm}}, E_{\text{cm}}) = 1 + b_1 P_1(\cos\theta_{\text{cm}}) + b_2 P_2(\cos\theta_{\text{cm}}),$$

respectively, can be used to examine the S-factor dependence on the angular distributions. With the expression given in Eq. (3·6), i.e.,

$$S(E_{\text{cm}}) = s_0 + s_1 E_{\text{cm}} + s_2 E_{\text{cm}}^2. \quad (3·6)$$

the S-factors resulting from the use of Eqs. (3·5) and (3·5a) are shown in Fig. 3·44(a). Again, it can be noticed that the S-factors are insensitive to these angular distribution assumptions. Fig. 3·44(a) does not give the S-factors for the $^{11}\text{B}(\text{d}, \alpha_2)^9\text{Be}^*(2.429 \text{ MeV})$ reaction since its angular distributions are measured to be constants at the two energies, as

shown in Table (3-5), and its S-factors will not change with these angular distribution assumptions.

The values of $a_1^{(1)}$ and $a_2^{(1)}$ in Eq. (3-5) are listed in Table 3-5(b).

The experimental values of s_0 , s_1 and s_2 for the $^{11}\text{B} + \text{d}$ reaction obtained with the use of Eq. (3-5) are given in Table 3-6. Figs. 3-45 through 3-47 are the cross sections (the solid lines) calculated from these values of s_0 , s_1 and s_2 . The data points in these figures are obtained by Eq. (2-8). Note that the solid lines in Figs. 3-45 through 3-47 are not the curves fitting the data points.

The values for s_0 , s_1 and s_2 obtained with the use of Eq. (3-5a) are given in Table 3-6(a).

Table 3-5. Summary of the angular distributions measured at the two energies for the ${}^9\text{Be} + \text{d}$ reaction.

Reaction	$E_{\text{cm}} = 101\text{keV}$	$E_{\text{cm}} = 101\text{keV}$	$E_{\text{cm}} = 142\text{keV}$	$E_{\text{cm}} = 142\text{keV}$
	w_1	w_2	w_1	w_2
${}^{11}\text{B}(\text{d}, \text{p}_0){}^{12}\text{B}(\text{gs})$	-0.82 ± 0.17	None	-0.737 ± 0.039	None
${}^{11}\text{B}(\text{d}, \alpha_0){}^9\text{Be}(\text{gs})$	None	-0.241 ± 0.089	None	-0.460 ± 0.027
${}^{11}\text{B}(\text{d}, \alpha_2){}^9\text{Be}^*(2.429 \text{ MeV})$	None	None	None	None

Table 3-5(a). Summary of the angular distributions for the ${}^{11}\text{B} + \text{d}$ reaction. Eq. (3-5) is used.

Reaction	$a_1^{(1)} (\text{MeV})^{-1}$	$a_2^{(1)} (\text{MeV})^{-1}$
${}^{11}\text{B}(\text{d}, \text{p}_0){}^{12}\text{B}(\text{gs})$	-5.26 ± 0.27	None
${}^{11}\text{B}(\text{d}, \alpha_0){}^9\text{Be}(\text{gs})$	None	-3.20 ± 0.19
${}^{11}\text{B}(\text{d}, \alpha_2){}^9\text{Be}^*(2.429 \text{ MeV})$	None	None

Table 3-6. Summary of the S-factors obtained with Eq. (3-5) for the $^{11}\text{B} + \text{d}$ reaction.

Reaction	s_0 (b·MeV)	s_1 (b)	s_2 (b·(MeV) ⁻¹)	Graph
$^{11}\text{B}(\text{d}, \text{p}_0)^{12}\text{B}(\text{gs})$	158.1 ± 6.3	-853 ± 42	$(1.96 \pm 0.28)\text{E}+3$	Fig. 3-45
$^{11}\text{B}(\text{d}, \alpha_0)^9\text{Be}(\text{gs})$	39.9 ± 1.6	-27.1 ± 3.6	-433 ± 46	Fig. 3-46
$^{11}\text{B}(\text{d}, \alpha_2)^9\text{Be}^*(2.429 \text{ MeV})$	50.3 ± 2.0	-69.7 ± 4.9	-524 ± 58	Fig. 3-47

Table 3-6(a). Summary of the S-factors obtained with Eq. (3-5a) for the $^{11}\text{B} + \text{d}$ reaction.

Reaction	s_0 (b·MeV)	s_1 (b)	s_2 (b·(MeV) ⁻¹)
$^{11}\text{B}(\text{d}, \text{p}_0)^{12}\text{B}(\text{gs})$	105.9 ± 6.5	-200 ± 20	$(-6.9 \pm 1.0)\text{E}+2$
$^{11}\text{B}(\text{d}, \alpha_0)^9\text{Be}(\text{gs})$	42.9 ± 2.6	-51.0 ± 5.1	-451 ± 68
$^{11}\text{B}(\text{d}, \alpha_2)^9\text{Be}^*(2.429 \text{ MeV})$	50.3 ± 2.0	-69.7 ± 4.9	-524 ± 58

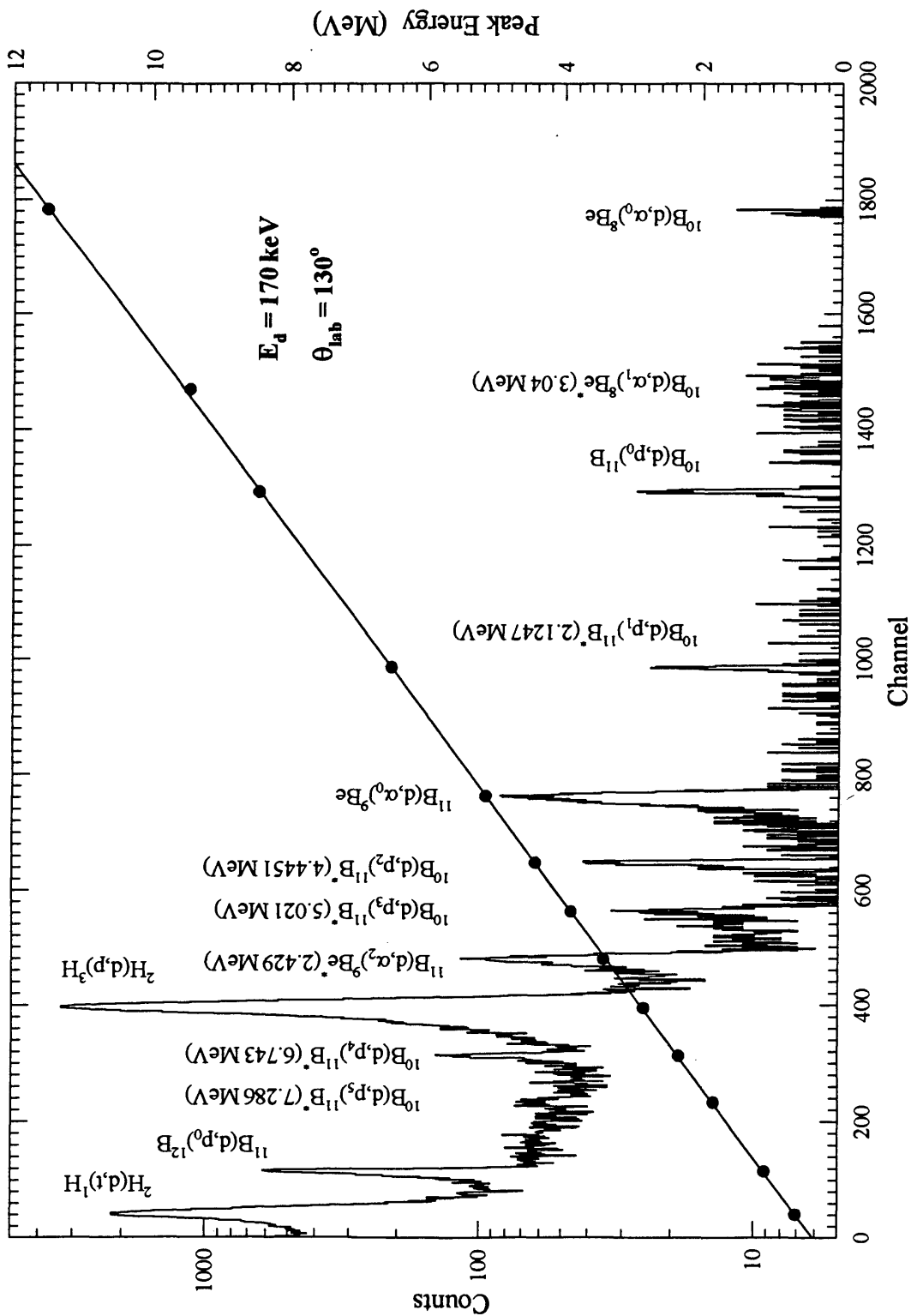


Fig. 3 - 38. A measured spectrum for $^{11}\text{B}+d$ reaction with energy calibration

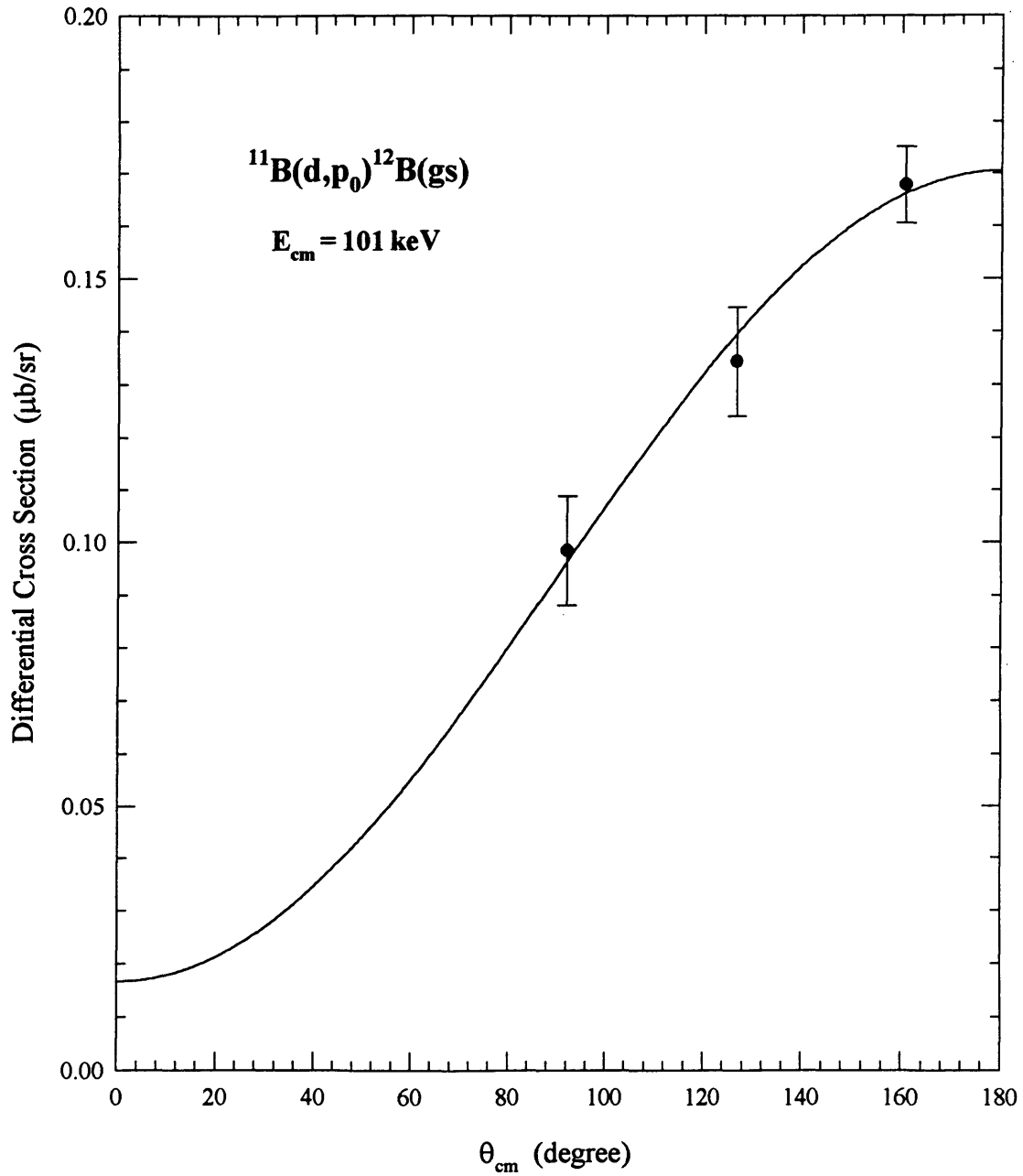
Fig. 3-39. Measured angular distribution for $^{11}\text{B}(d,p_0)^{12}\text{B}(\text{gs})$ at $E_{\text{cm}} = 101 \text{ keV}$.

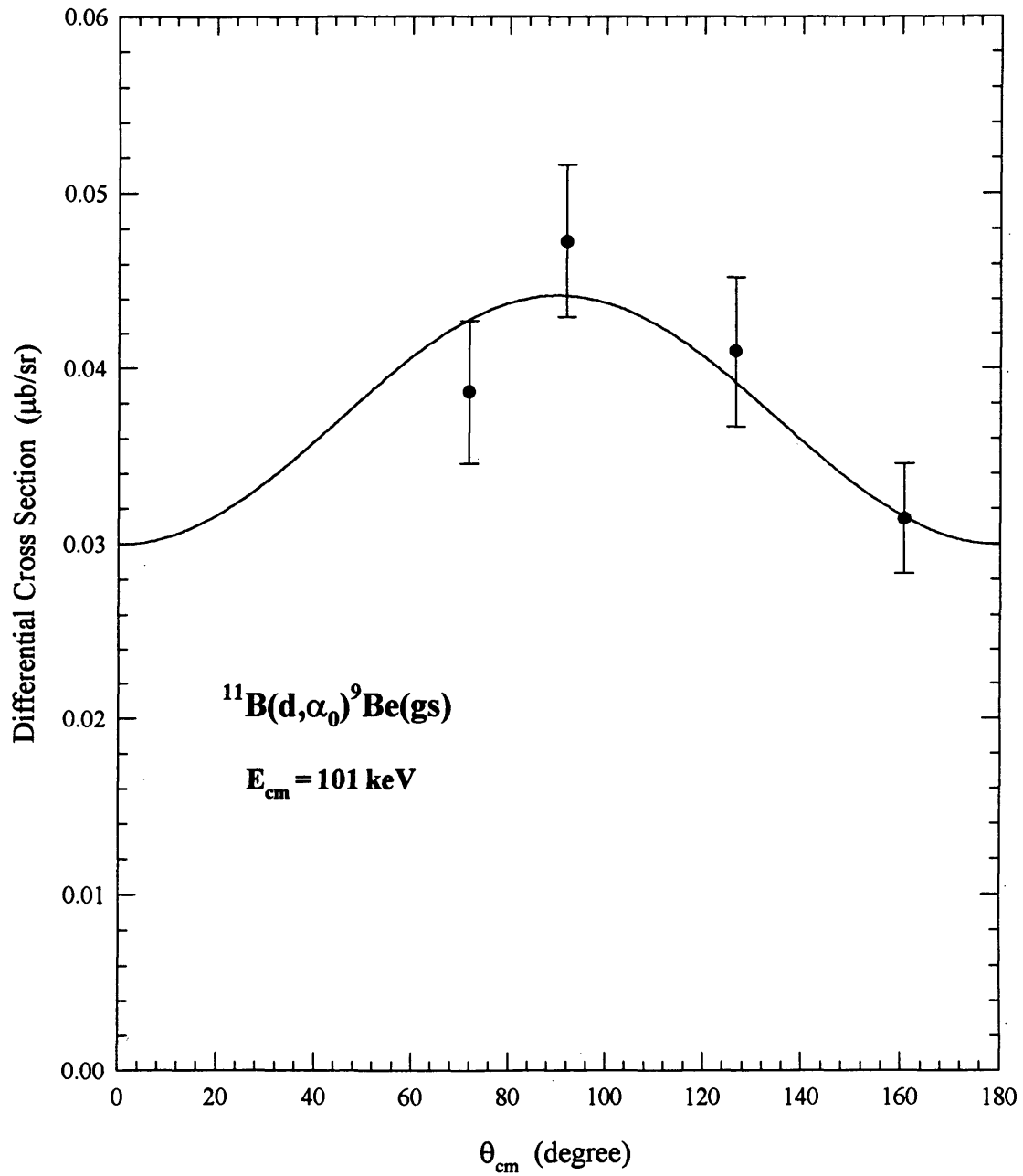
Fig. 3-40. Measured angular distribution for $^{11}\text{B}(d,\alpha_0)^9\text{Be}(\text{gs})$ at $E_{\text{cm}} = 101$ keV.

Fig. 3-41. Measured angular distribution for $^{11}\text{B}(d,\alpha_2)^9\text{Be}^*(2.429\text{ MeV})$ at $E_{\text{cm}} = 101\text{ keV}$.

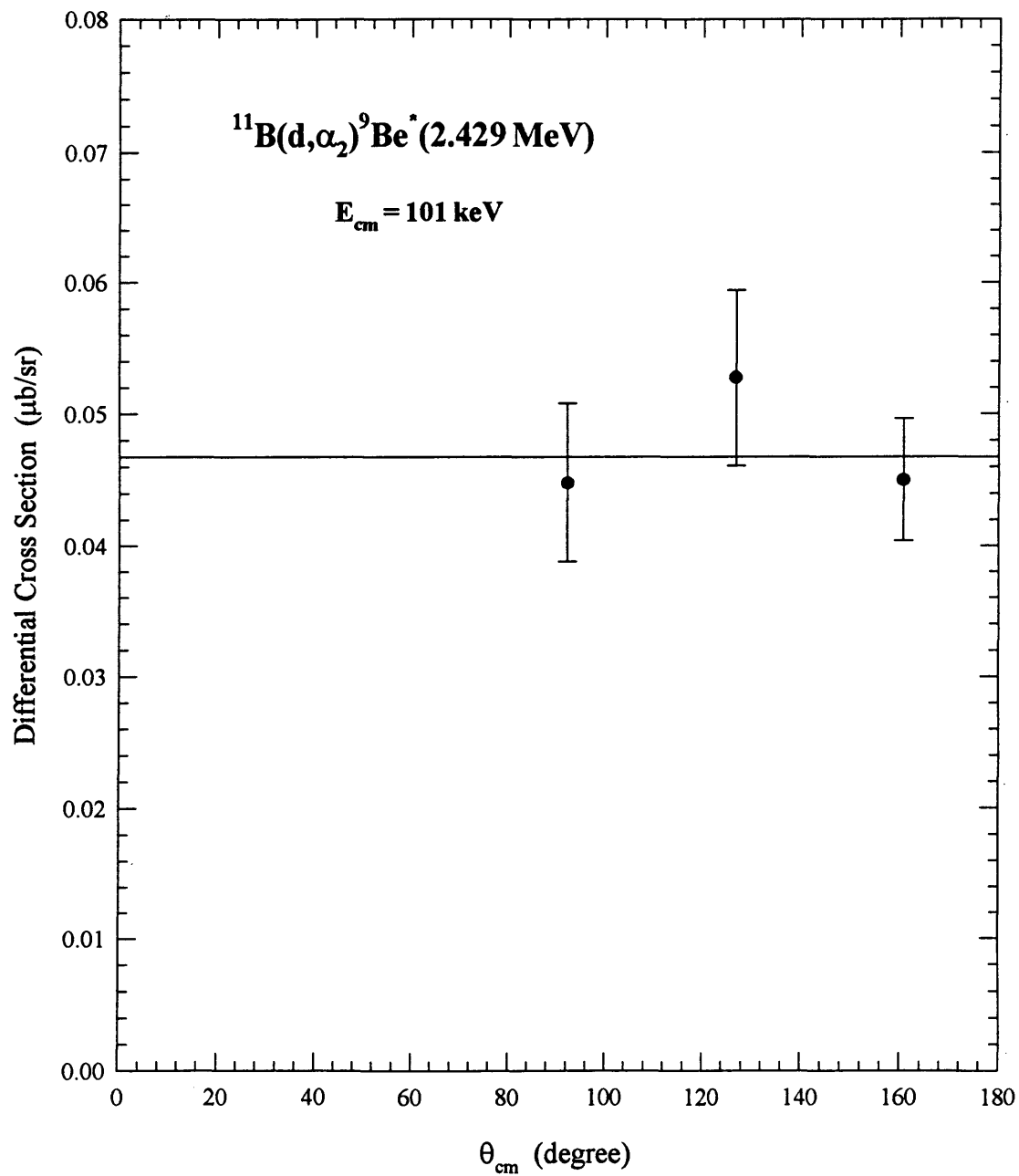


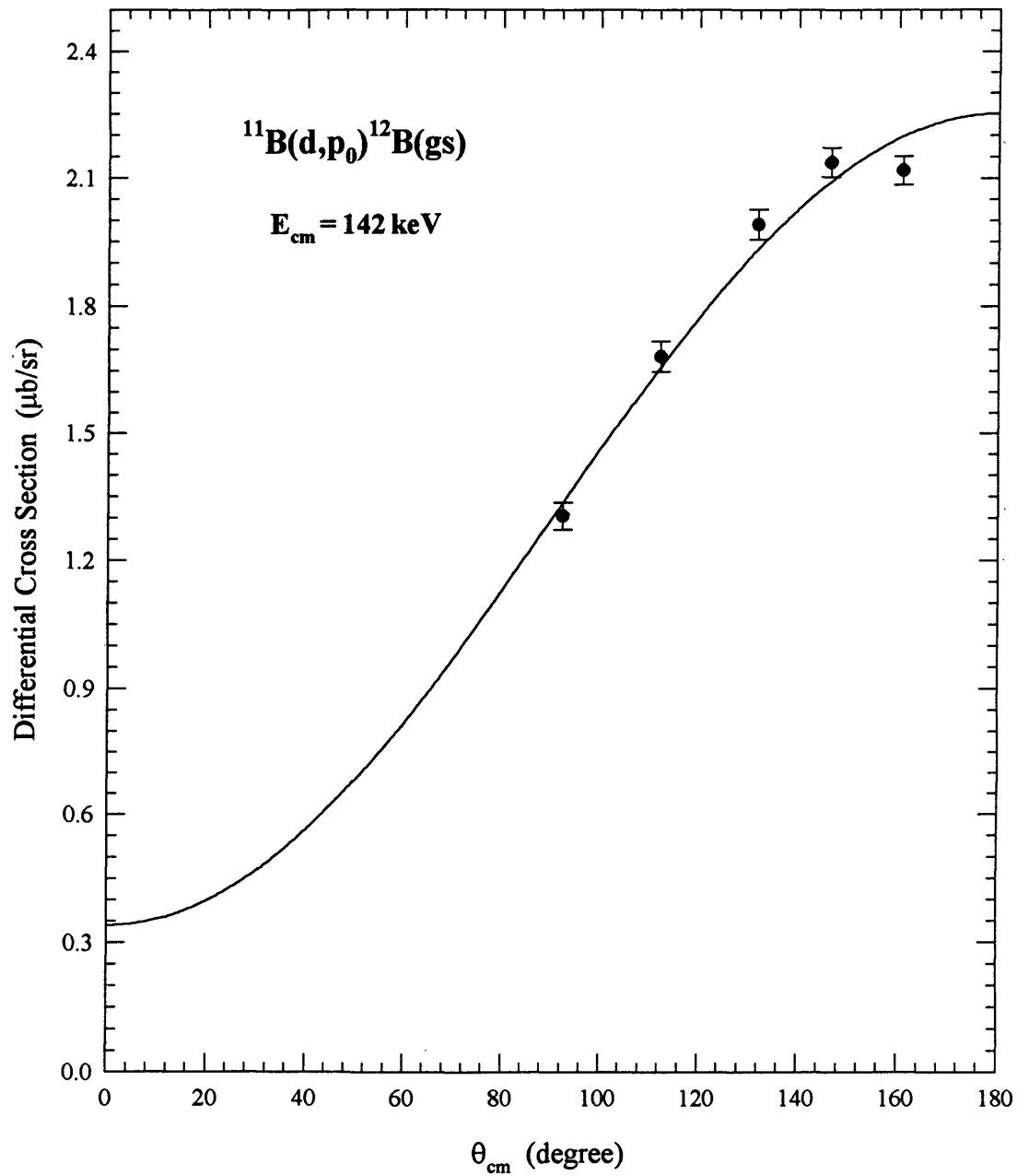
Fig. 3-42. Measured angular distribution for $^{11}\text{B}(d,p_0)^{12}\text{B}(\text{gs})$ at $E_{\text{cm}} = 142 \text{ keV}$.

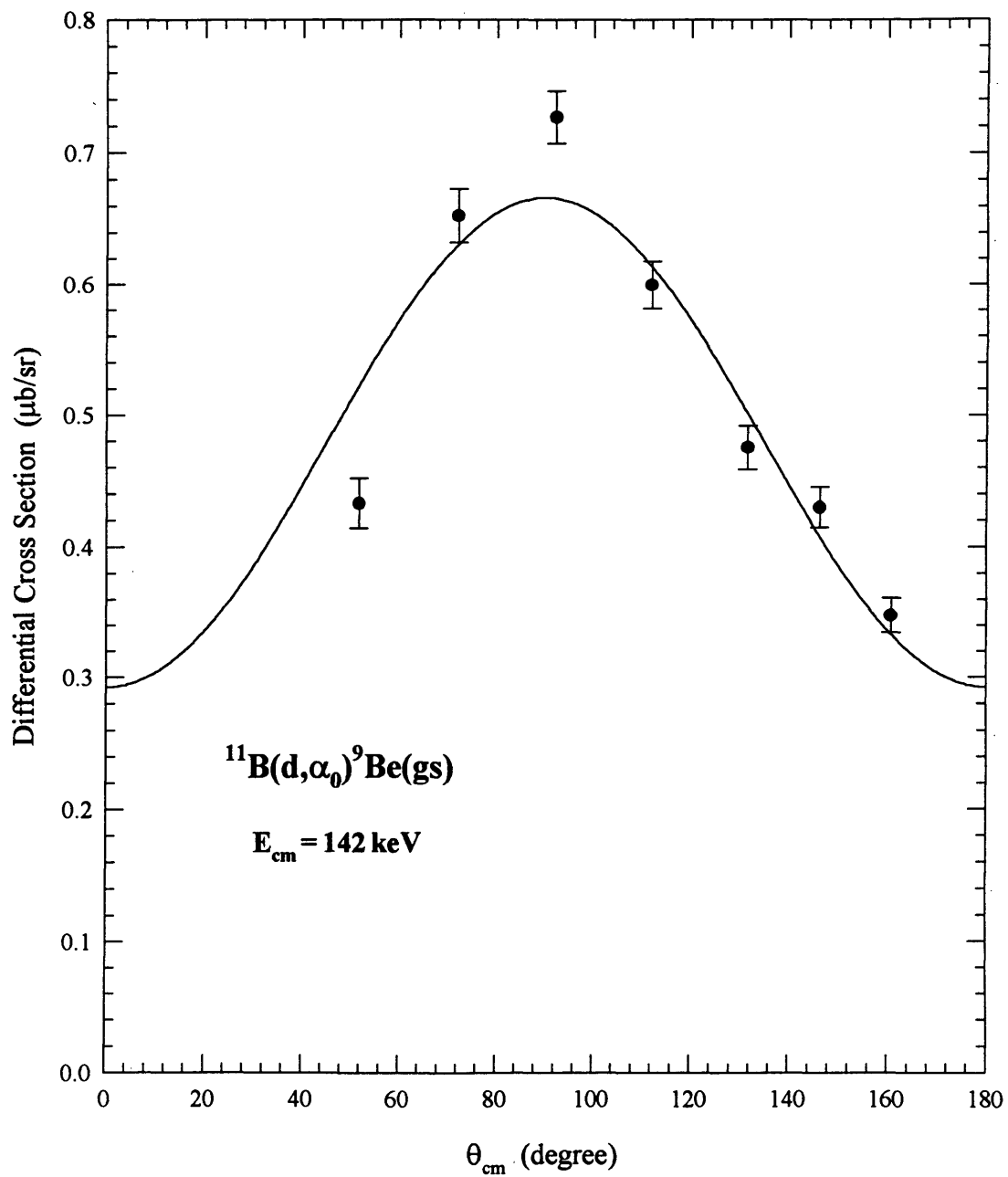
Fig. 3-43. Measured angular distribution for $^{11}\text{B}(d,\alpha_0)^9\text{Be}(\text{gs})$ at $E_{\text{cm}} = 142$ keV.

Fig. 3-44. Measured angular distribution for $^{11}\text{B}(d,\alpha_2)^9\text{Be}(2.429\text{ MeV})$ at $E_{\text{cm}} = 142\text{ keV}$.

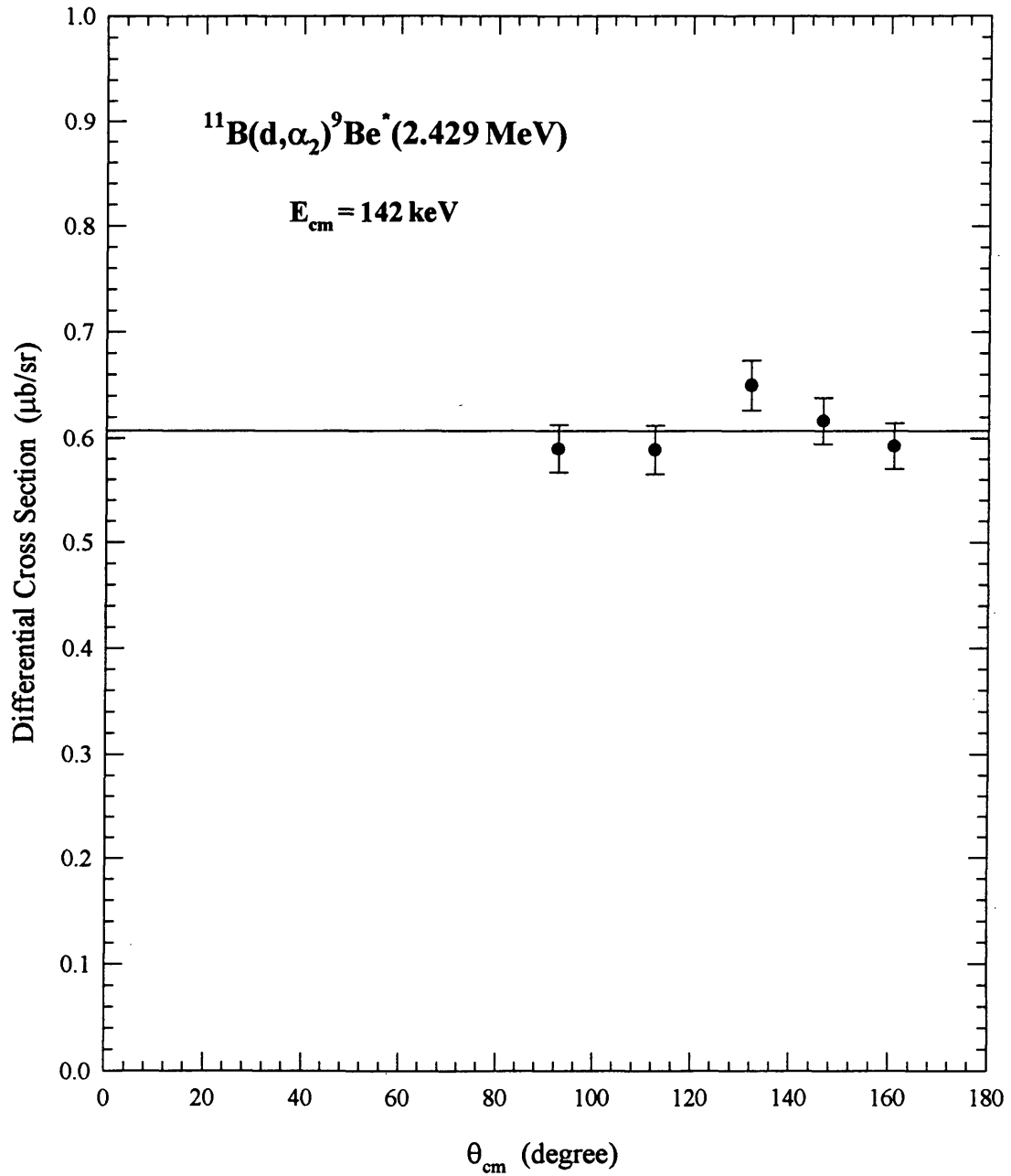


Fig. 3·44(a). The S-factors (the solid lines and the dotted lines) obtained from different fitting equations (Eq. (3·5) and Eq. (3·5a), respectively) of angular distributions.

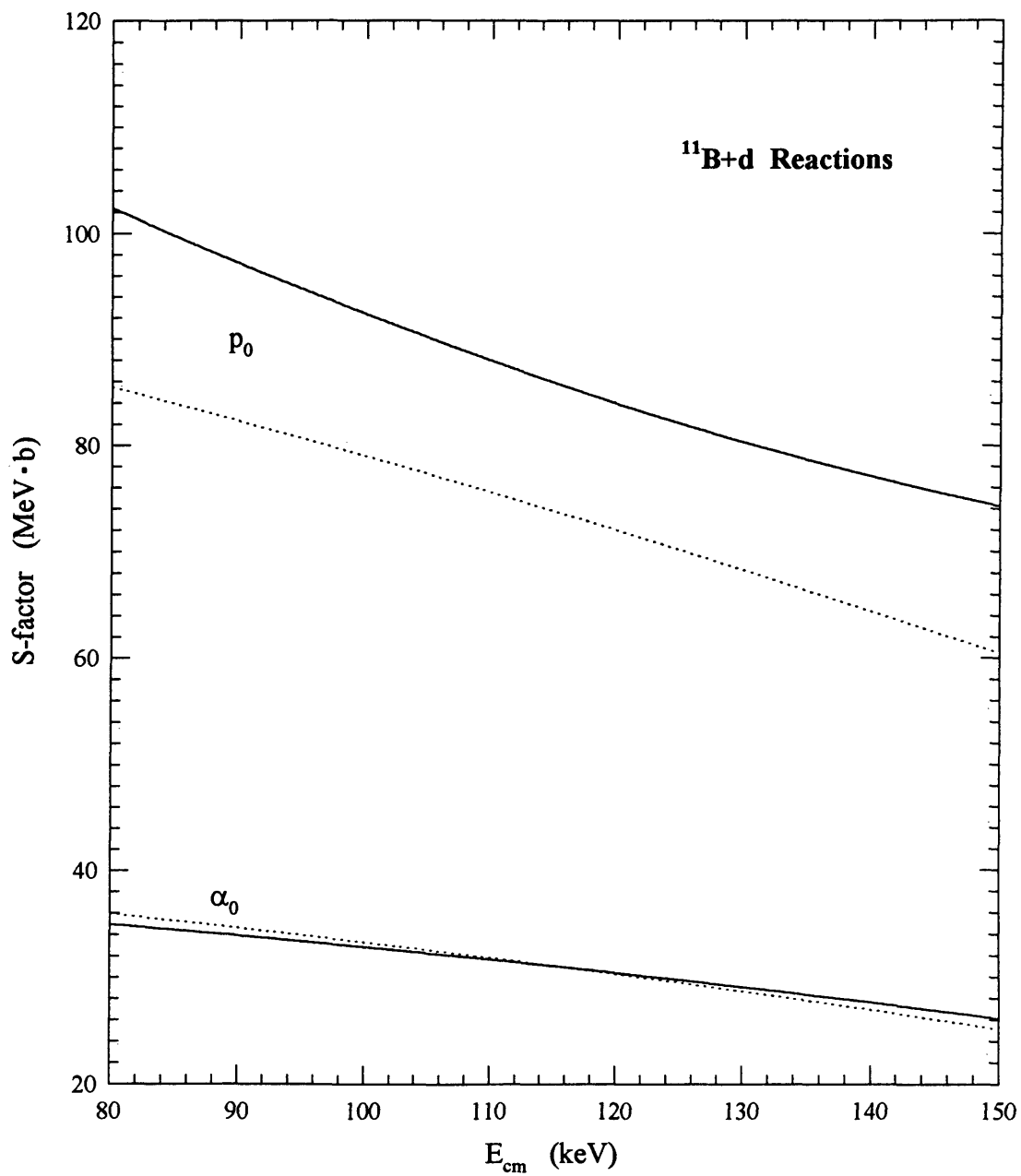


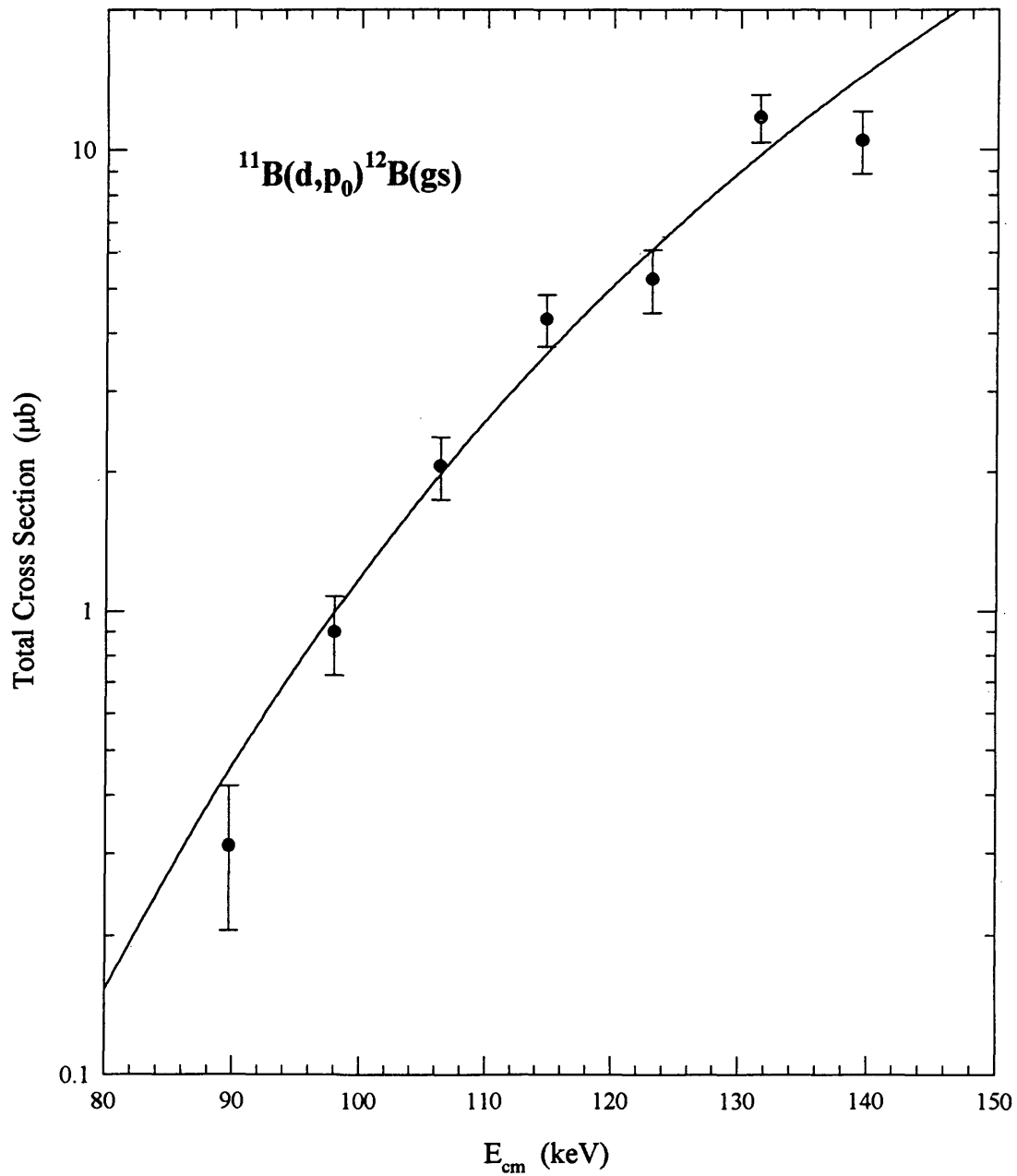
Fig. 3-45. Measured cross section for $^{11}\text{B}(d,p_0)^{12}\text{B}(\text{gs})$ reaction.

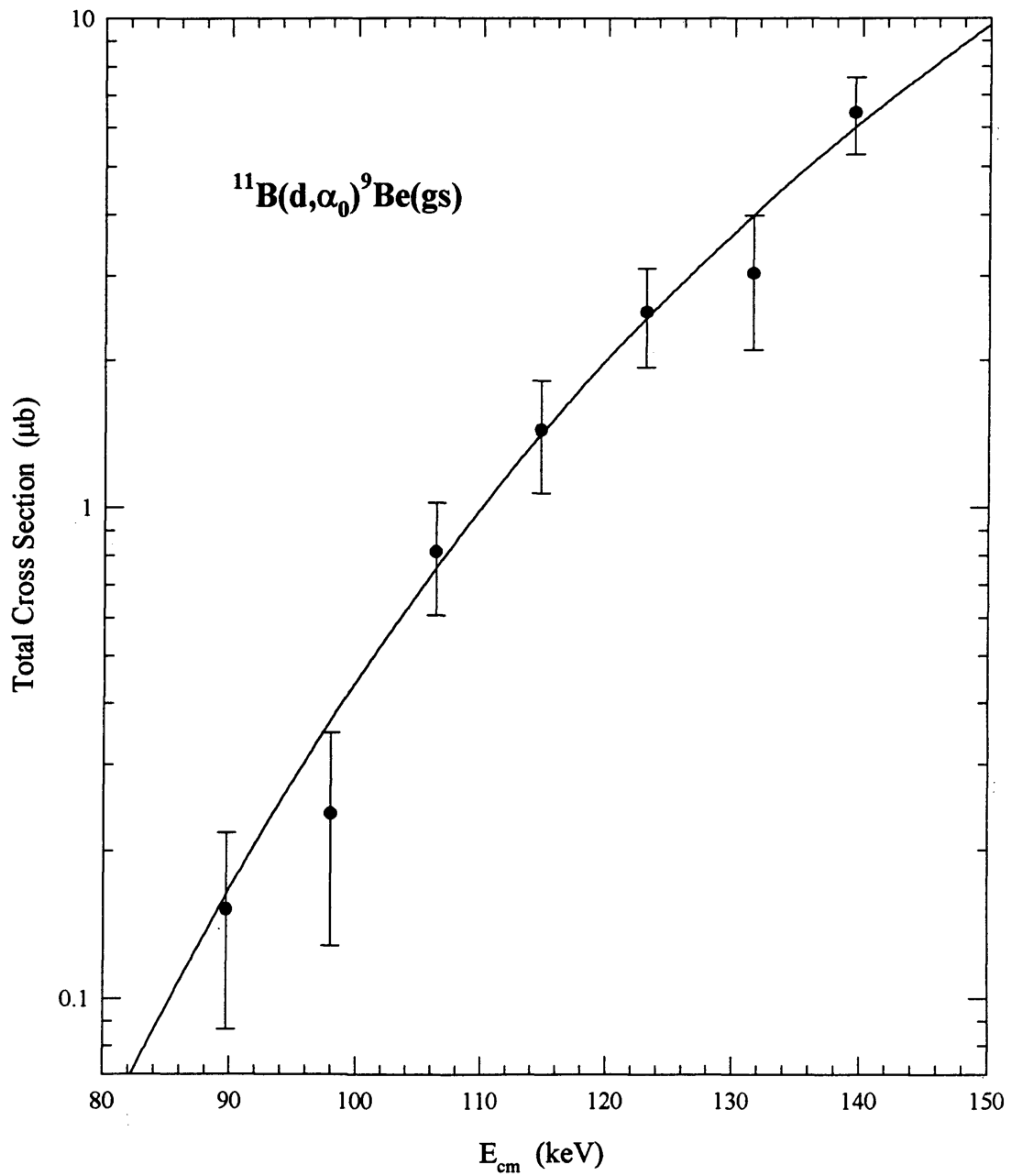
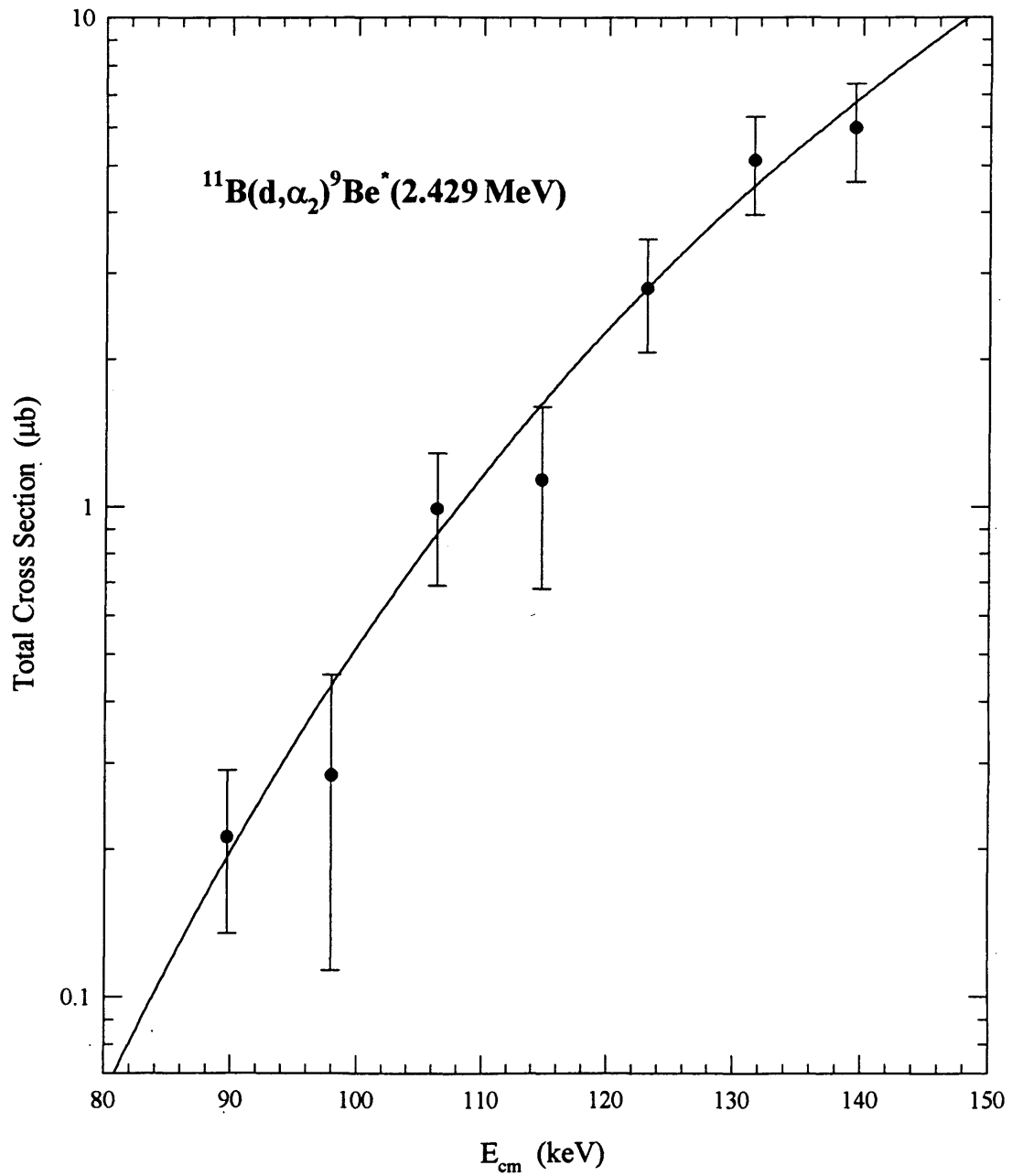
Fig. 3-46. Measured cross section for $^{11}\text{B}(d,\alpha_0)^9\text{Be}(\text{gs})$ reaction.

Fig. 3-47. Measured cross section for $^{11}\text{B}(d,\alpha_2)^9\text{Be}^*(2.429\text{ MeV})$ reaction.

3-3 THE ${}^7\text{Li}({}^3\text{He}, p_0){}^9\text{Be}(\text{gs})$ REACTION

3-3-1 A Simulated 2-D Plot

To understand the measured 2-D plot thoroughly, a computer-simulated one is generated and given in Fig. 3-48. In the simulation, the thicknesses of the ΔE and E' detectors are 150 μm and 500 μm , respectively, the maximum value of the angle θ (see Fig. 2-15) is 15° and the cut-off energy value of the cut-off electronic settings is 4.2 MeV—all are the actual values in the measurements.

Protons with lower energy that can not go through the ΔE detector (see Particle D in Fig. 2-15) will fall as a single point in the straight line to the left of Point A in the proton trace line in Fig. 3-48. Moderate energy protons that stop in the E' detector (see Particle C in Fig. 2-15) will lie between the Points A and C along the line. Protons of higher energy (> 9.8 MeV) will punch through both detectors (see Particle B in Fig. 2-15), lose less energies in both detectors as the proton energy goes even higher and construct the trace line from Point C through E.

Points B and D in Fig. 3-48 represent the effect of the cut-off electronic settings on the proton 2-d plot. All the protons with $E' < 4.2\text{MeV}$, including the 14.9MeV proton group from ${}^3\text{He}(\text{d}, p){}^4\text{He}$ reaction, will not appear on any measured 2-D plot, but we have included them in Fig. 3-48.

We have pointed out in Section 2-3-5 that, since the incident angle θ of protons onto the detectors (see Fig. 2-15) can be relatively large, each group of protons which stop in E' detector will construct a vertical band, as shown by groups ${}^7\text{Li}({}^3\text{He}, p_1){}^9\text{Be}^*(1.69\text{MeV})$ and ${}^7\text{Li}({}^3\text{He}, p_2){}^9\text{Be}^*(2.429\text{MeV})$ in Fig. 3-48. The shape of the ${}^7\text{Li}({}^3\text{He}, p_0){}^9\text{Be}(\text{gs})$ group is determined by the fact that the protons with small angle θ will penetrate the E' detector while those with large θ will stop in it. The 14.9 MeV protons from ${}^3\text{He}(\text{d}, p){}^4\text{He}$ reaction will punch through both detectors, lose more energy in both detectors as angle θ gets larger and form the band shown in Fig. 3-48. Note that the right end of the band corresponds to the largest θ .

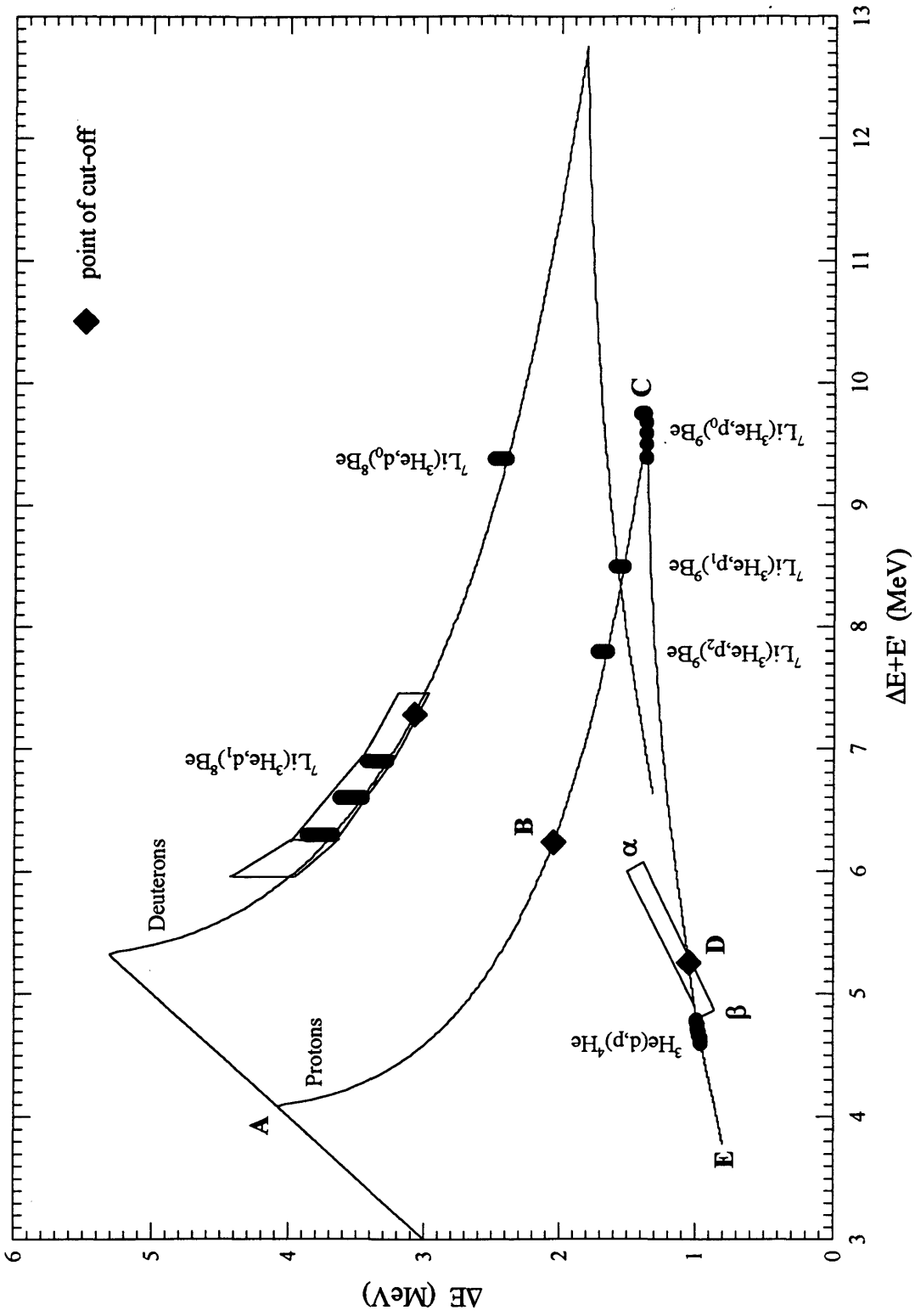


Fig. 3 • 48. A simulated 2-D plot.

If the energy of a particle group has a certain width, for example, the width (FWHM) of the deuterons from ${}^7\text{Li}({}^3\text{He}, d){}^8\text{Be}^*(3.04\text{MeV})$ is ~ 1.5 MeV [Ajz84], at each value of energy within the width the particles will make a vertical band in the 2-d plot due to the effect of θ and the collection of the bands at different energies will form an area, as shown in Fig. 3-48, with the bottom ($\theta = 0^\circ$) of the area lying in the line.

3-3-2 A Measured 2-D Plot and Coincident Spectrum

A measured 2-D plot is given in Fig. 3-49 and is in good agreement with the simulated one, Fig. 3-48. In the measured 2-D plot, Group A is a part of the deuteron group from the ${}^7\text{Li}({}^3\text{He}, d){}^8\text{Be}^*(3.04\text{MeV})$ reaction while the other part of the group can not be seen due to the cut-off electronic settings (see Table 2-1 for the energies of the particle groups). The ${}^7\text{Li}({}^3\text{He}, d_0){}^8\text{Be}(\text{gs})$ group does not appear, since it has a relatively small cross section [Rat90]. Group B represents the expected ${}^7\text{Li}({}^3\text{He}, p_0){}^9\text{Be}(\text{gs})$ reaction. The protons from the ${}^7\text{Li}({}^3\text{He}, p_1){}^9\text{Be}^*(1.69\text{MeV})$ reaction are in Group C. The protons from Group D through E come mainly from the ${}^7\text{Li}({}^3\text{He}, p_n){}^9\text{Be}$ ($n \geq 2$) reactions [Rat90].

Group F in Fig. 3-49 seems somewhat strange because it lies between points B and D of Fig. 3-48, i.e., it is not positioned in the proton trace line. This problem can be solved by a further analysis. Let us consider an area in the lower energy tail of the proton peak from ${}^3\text{He}(d, p){}^4\text{He}$ (peak energy 14.9 MeV), e.g., an area of the peak tail around 14 MeV. Since the peak is very big, the area will have a lot of counts. The position of the protons of the area in the 2-D plot will be to the right of the center position of the ${}^3\text{He}(d, p){}^4\text{He}$ group. If the effect of θ is taken into account, or, furthermore, consider the case illustrated by Particle E in Fig. 2-15, protons from the area will build a band as shown by the " α - β " band in Fig. 3-48. Note that the " α " end of the band corresponds to the largest θ and will not be placed in the trace line. The cut-off electronic settings will chop most of the band, only a part of it near " α " will be left in the measured 2-D plot. This part is Group F in Fig. 3-49 (see below for further discussion).

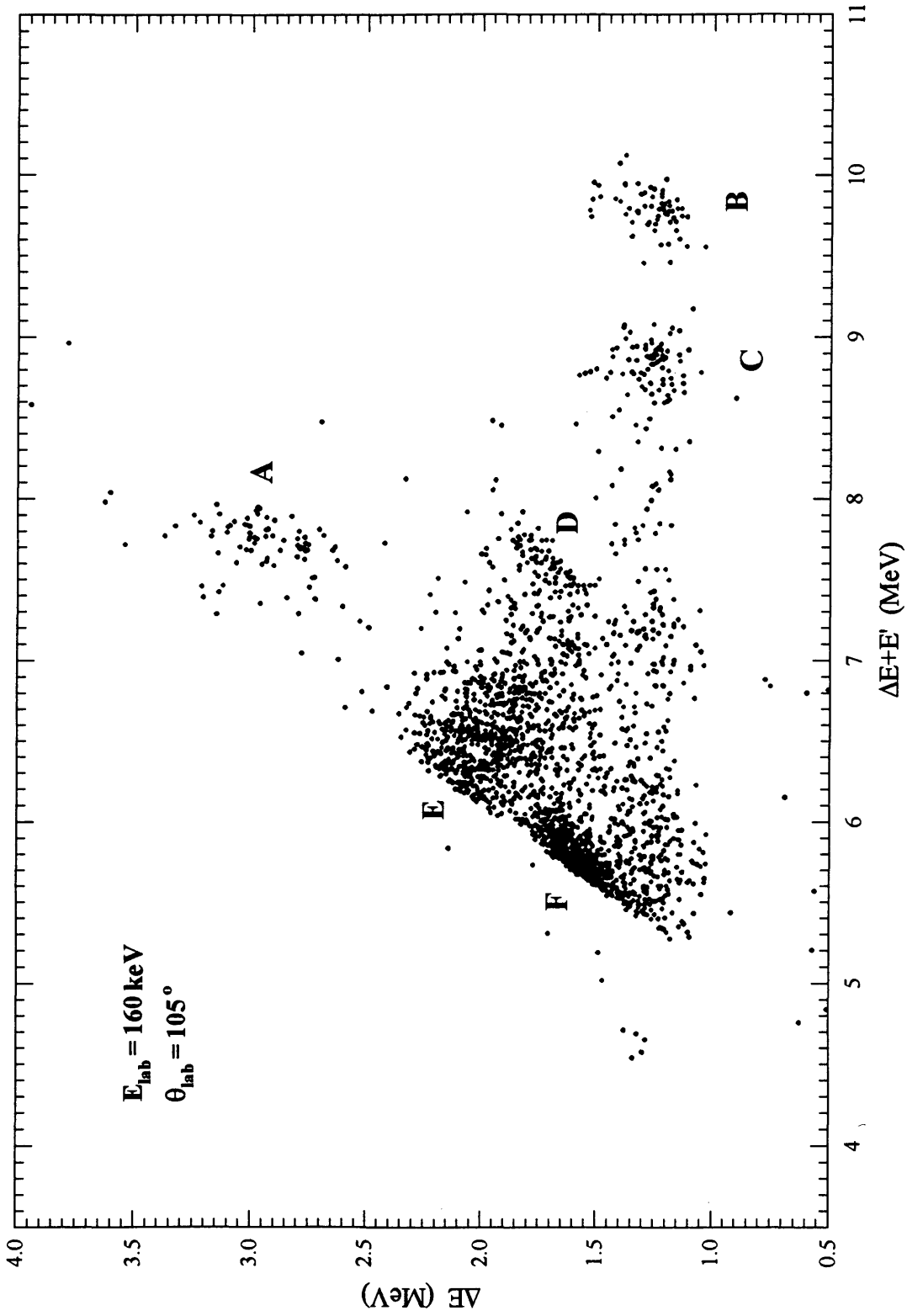


Fig. 3-49. A measured 2-D plot for ${}^7\text{Li}({}^3\text{He}, p){}^9\text{Be}(\text{gs})$ reaction.

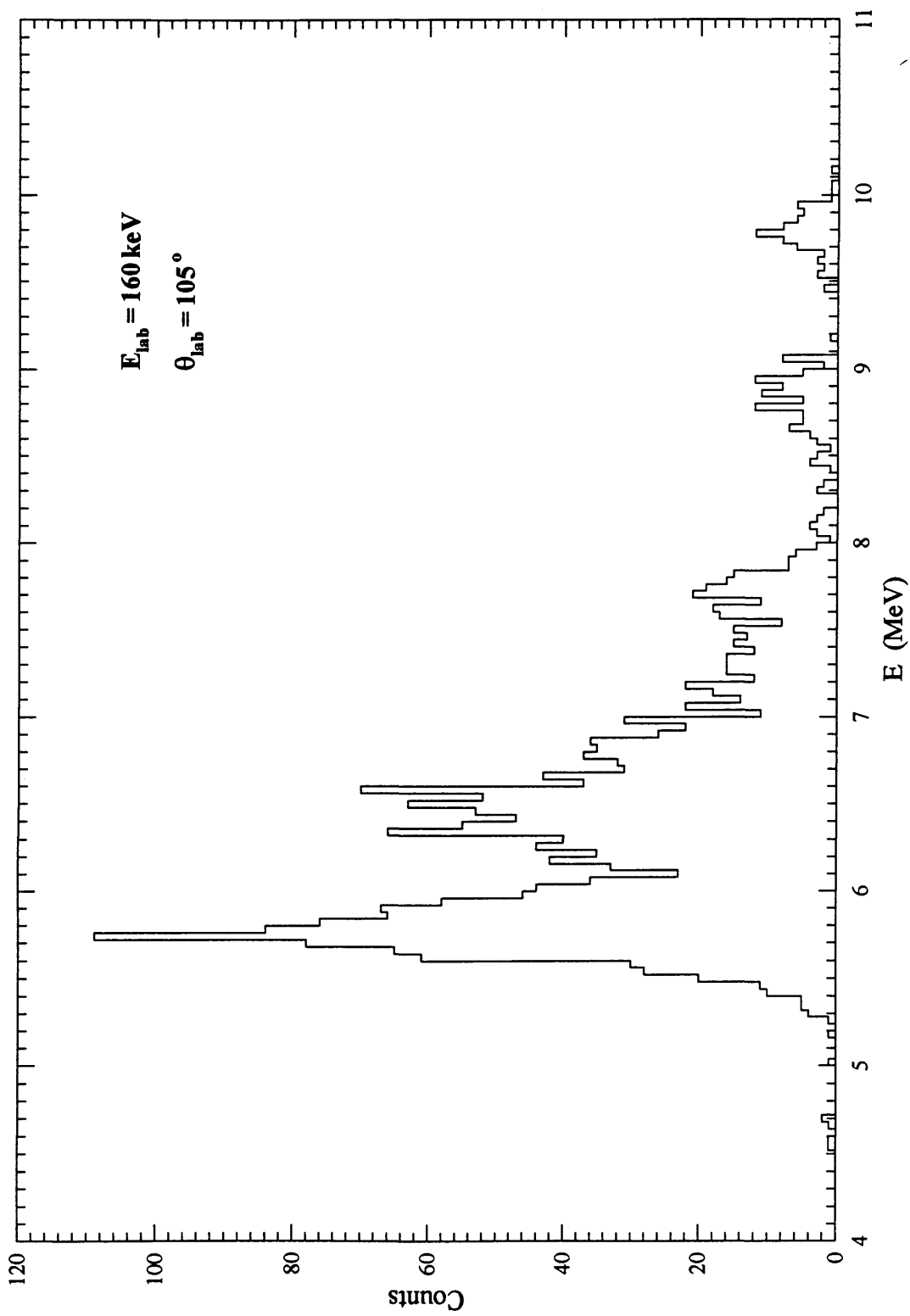


Fig. 3 - 50. A measured coincident spectrum for ${}^7\text{Li}({}^3\text{He}, p_0){}^9\text{Be}(\text{gs})$ reaction.

A measured coincident spectrum is given in Fig. 3-50. The peak at 9.8 MeV comes from the expected ${}^7\text{Li}({}^3\text{He}, p_0){}^9\text{Be}(\text{gs})$ protons, i.e., Group B in Fig. 3-49. The counts in the peak are the same as those in Group B.

Now, as listed in Table 2-1, the maximum energy of the protons from the three-body direct breakup of the ${}^3\text{He}+{}^3\text{He}$ reaction into two protons and an α -particle is 10.4 MeV. If these protons did appear in our experiment, they will be mixed up with the expected proton group of ${}^7\text{Li}({}^3\text{He}, p_0){}^9\text{Be}(\text{gs})$. This ${}^3\text{He}+{}^3\text{He}$ reaction has been carefully measured [Dwa71; and Kra87a] and it can be concluded [Kra87a] that the three-body direct breakup is dominant at low energy, $E_{\text{cm}} < 1$ MeV, and the low energy spectrum of the protons is a flat continuum over the energy region from 0 up to 10.4 MeV. From our measured 2-D plots and coincident spectra, Fig. 3-49 and Fig. 3-50, any continuous background can not be found in this energy region, hence comes the assertion that the ${}^3\text{He}+{}^3\text{He}$ reaction was not seen in our experiment.

3-3-3 A Measured Anti-Coincident Spectrum

A measured anti-coincident spectrum is shown in Fig. 3-51 with energy calibration, in which the energies of the particles after going through the $6\mu\text{m}$ Al foil on the front of the detector telescope are plotted. The background from Channel 0 up to 1000 comprise the α -particles from ${}^7\text{Li}(d, 2\alpha)n$ and from the breakup of ${}^5\text{He}$ nuclei of ${}^7\text{Li}(d, \alpha){}^5\text{He}$ (see Fig. 3-1 for details).

Peak B in Fig. 3-51 results from the 14.9 MeV protons of the ${}^3\text{He}(d, p){}^4\text{He}$ reaction which have penetrated the ΔE detector but missed the E' detector, as shown by Particle A in Fig. 2-15. It can be known from Fig. 3-48 that the 14.9 MeV protons will lose 0.9 MeV energy in the ΔE detector (the dot under Peak B in Fig. 3-51 represents the 0.9 MeV peak energy), when they incident perpendicularly. The measured energy of Peak B is higher than 0.9 MeV, since the protons come to the detector telescope with an angle larger than 15° . This consideration can be proven experimentally. With an 80 keV ${}^3\text{He}^+$ beam bombarding a deuterium-enriched CD_2 (polyethylene) thick target while other detection arrangements remained the same as used for the ${}^7\text{Li}({}^3\text{He}, p_0){}^9\text{Be}(\text{gs})$ experiment, two test measurements were accomplished, one with a small aperture and the other

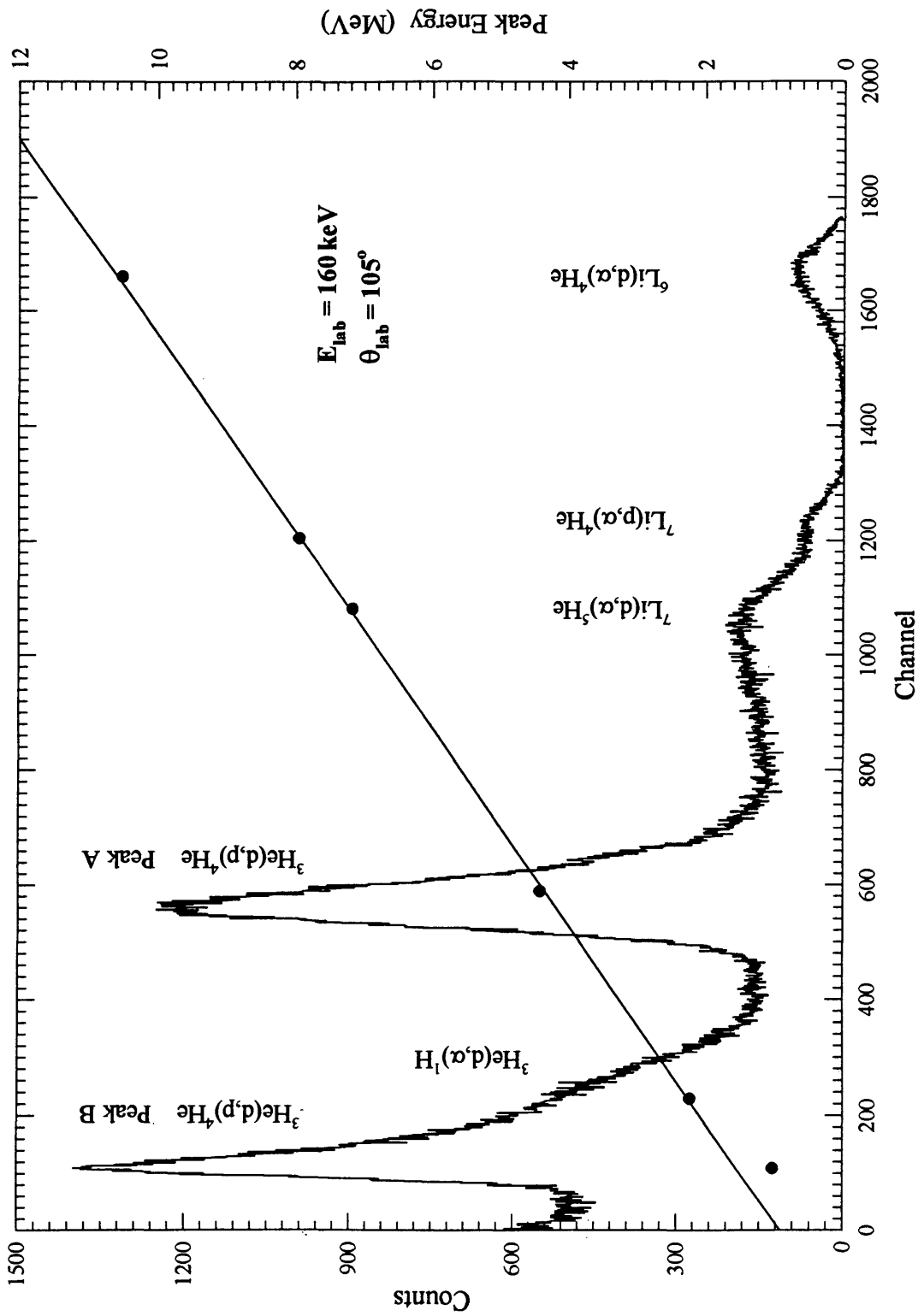
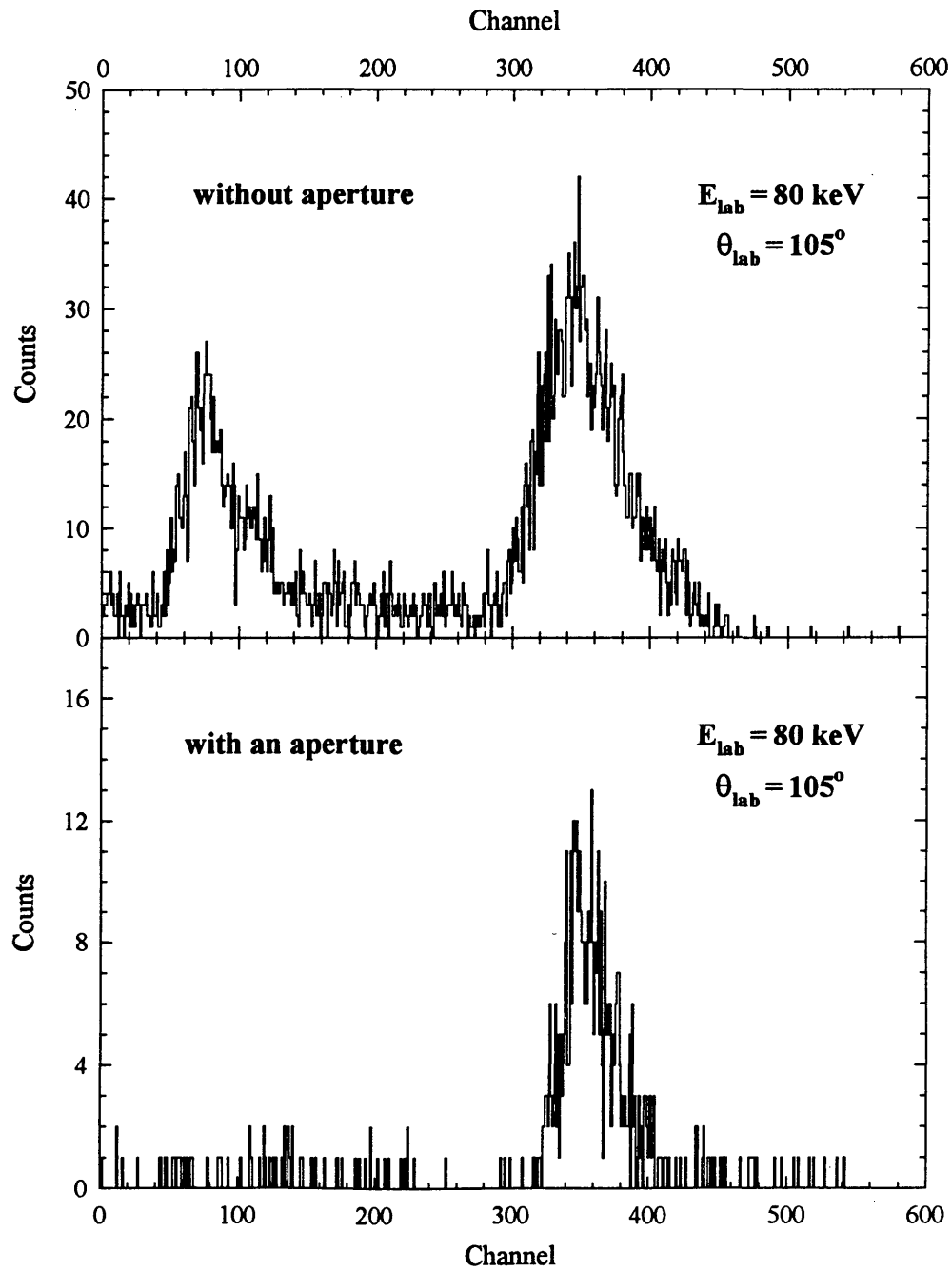


Fig. 3 - 51. A measured anti-coincident spectrum for ${}^7\text{Li}({}^3\text{He}, p_0){}^9\text{Be}(\text{gs})$ reaction.

without. The anti-coincident spectra from the test measurements are shown in Fig. 3-52. It is very obvious from this figure that the aperture has blocked the detector telescope from the protons of large angle θ , showing that the analysis on the origin of Peak B in Fig. 3-51 is correct.

Peak A in Fig. 3-51 comes from the 14.9 MeV protons of ${}^3\text{He}(d,p){}^4\text{He}$ which have punched through both detectors. The peak is located at 4.4 MeV, which is known from Fig. 3-48 to be the total loss of energy $\Delta E + E'$ of the protons in the two detectors. The appearance of the peak in the anti-coincident spectrum, instead of the coincident spectrum and 2-D plot, is attributed to the influence of the cut-off electronic settings. From Fig. 3-48, it can be known that the protons will lose 3.6 MeV in the E' detector, less than the cut-off value 4.2 MeV. Therefore, the protons will not create any gating signals (see Fig. 2-12) and will be recorded only in the anti-coincident spectrum. As mentioned previously in Section 2-3-4, the somewhat unusual non-occurrence of the protons in the coincident spectrum and 2-D plot is just what we want in order to solve the problem of a too-high counting rate of the protons. To prove the above analysis, a test experiment was run and a deuterium-enriched CD_2 thick target was bombarded by 80 keV ${}^3\text{He}^+$ beam. Two measurements, with and without the cut-off electronic settings, were recorded and the results are plotted in Fig. 3-52, from which it has been made clear that the protons act in an ordinary way, i.e., being detected by both detectors and recorded in the coincident spectrum and 2-D plot, when the cut-off electronic settings are not used while the protons appear in the anti-coincident spectrum when cut-off is in use.

We have pointed out in Section 3-3-2 that Group F in the measured 2-D plot (Fig. 3-49) is the protons from the tail at the lower energy side of the big 14.9 MeV peak of ${}^3\text{He}(d,p){}^4\text{He}$. This has been demonstrated by Fig. 3-53. Comparing the two coincident spectra in Fig. 3-53, it can be found that the very bottom and right part of the foothill of the peak has survived from the cut-off electronic settings (i.e., $E' > 4.2\text{MeV}$) and made the group in the "2D plot with cut-off" of Fig. 3-53. It has to be emphasized that, since the 14.9 MeV protons have penetrated both detectors, the peak is "leftside-right", that is, the right side of the peak in the "coincident spectrum without cut-off" of Fig. 3-53 represents the lower energy side of the peak. This can be seen from Fig. 3-48 by the fact that the line is drawn from Point D to E when proton energy goes higher. Therefore

Fig. 3-52. Anti-coincident spectra for ${}^3\text{He}(d,p){}^4\text{He}$ reaction.

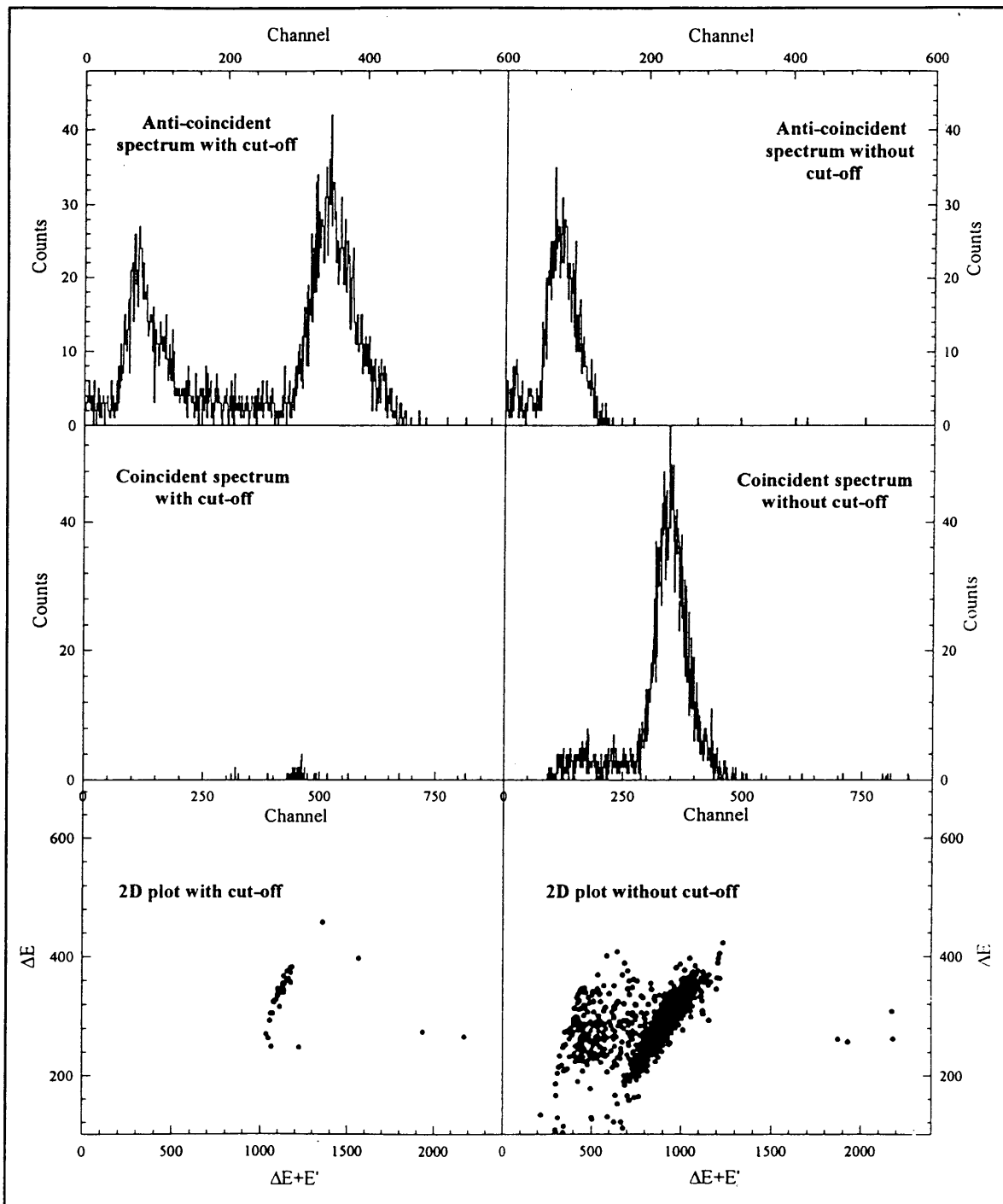


Fig. 3-53. Spectra and 2-D plots for ${}^3\text{He}(d,p){}^4\text{He}$. ($E_{\text{lab}} = 80 \text{ keV}$ and $\theta_{\text{lab}} = 105^\circ$)

comes the conclusion that the group in the "2D plot with cut-off" of Fig. 3-53, as well as Group F in Fig. 3-49, originates from the protons in the lowest energy foothill of the ${}^3\text{He}(d, p){}^4\text{He}$ peak.

3-3-4 The Results

Our measured data of the ${}^7\text{Li}({}^3\text{He}, p_0){}^9\text{Be}(\text{gs})$ experiment can be summarized in the following.

E_{lab} (keV)	charge (C)	counts	Ω_d	S (MeV·b)
160	1.285	64	0.467 ± 0.019	6.0 ± 0.8
170	0.5785	51	0.349 ± 0.019	6.5 ± 1.0

The counts were read from the ${}^7\text{Li}({}^3\text{He}, p_0){}^9\text{Be}(\text{gs})$ groups of the 2-D plots. The values for the detector solid angle, Ω_d , were determined by measurements of the ${}^{10}\text{B}(d, p_n){}^{11}\text{B}$ ($n=0,1$) reactions. All the measurements were made at a detector angle of 105° with respect to the beam direction. With an assumption of isotropic angular distributions at such low energies, each value for the S-factor was obtained by fitting the corresponding measured yield, i.e., counts per unit charge, with a constant S-factor, using Eq. (2-5).

This reaction has been investigated at CM energies between 420 keV and 1750 keV by Boyd's group at Ohio State University and their measured S-factor has been published in Rat90. The data points in Fig. 3-54 show our values of the S-factor, together with those in Rat90. A fit of the S-factor can be made with all the values from the present work and Rat90 and the result can be formulated by

$$\left. \begin{aligned}
 S(E_{\text{cm}}) &= \frac{c_1}{(E_1 - E_{\text{cm}})^2 + (\Gamma_1/2)^2} + \frac{c_2}{(E_2 - E_{\text{cm}})^2 + (\Gamma_2/2)^2} + c_3 + c_4 E_{\text{cm}} \\
 c_1 &= 0.764 \text{ (MeV)}^3 \text{ b}; & E_1 &= 0.665 \text{ MeV}; \\
 \Gamma_1 &= 0.302 \text{ MeV}; & c_2 &= 1.063 \text{ (MeV)}^3 \text{ b}; \\
 E_2 &= 0.978 \text{ MeV}; & \Gamma_2 &= 0.716 \text{ MeV}; \\
 c_3 &= 2.72 \text{ MeV} \cdot \text{b}; & c_4 &= 1.91 \text{ b}.
 \end{aligned} \right\}, \quad (3-8)$$

where the two broad resonances correspond to the ${}^{10}\text{B}$ energy levels of 18.43 MeV and 18.8 MeV [Ajz84]. The solid line in Fig. 3-54 represents this fit.

Fig. 3-55 illustrates the measured cross section, where our data points symbolize those calculated from the above listed S-factor values. Note that our cross section is as small as $3 \times 10^{-4} \mu\text{b}$.

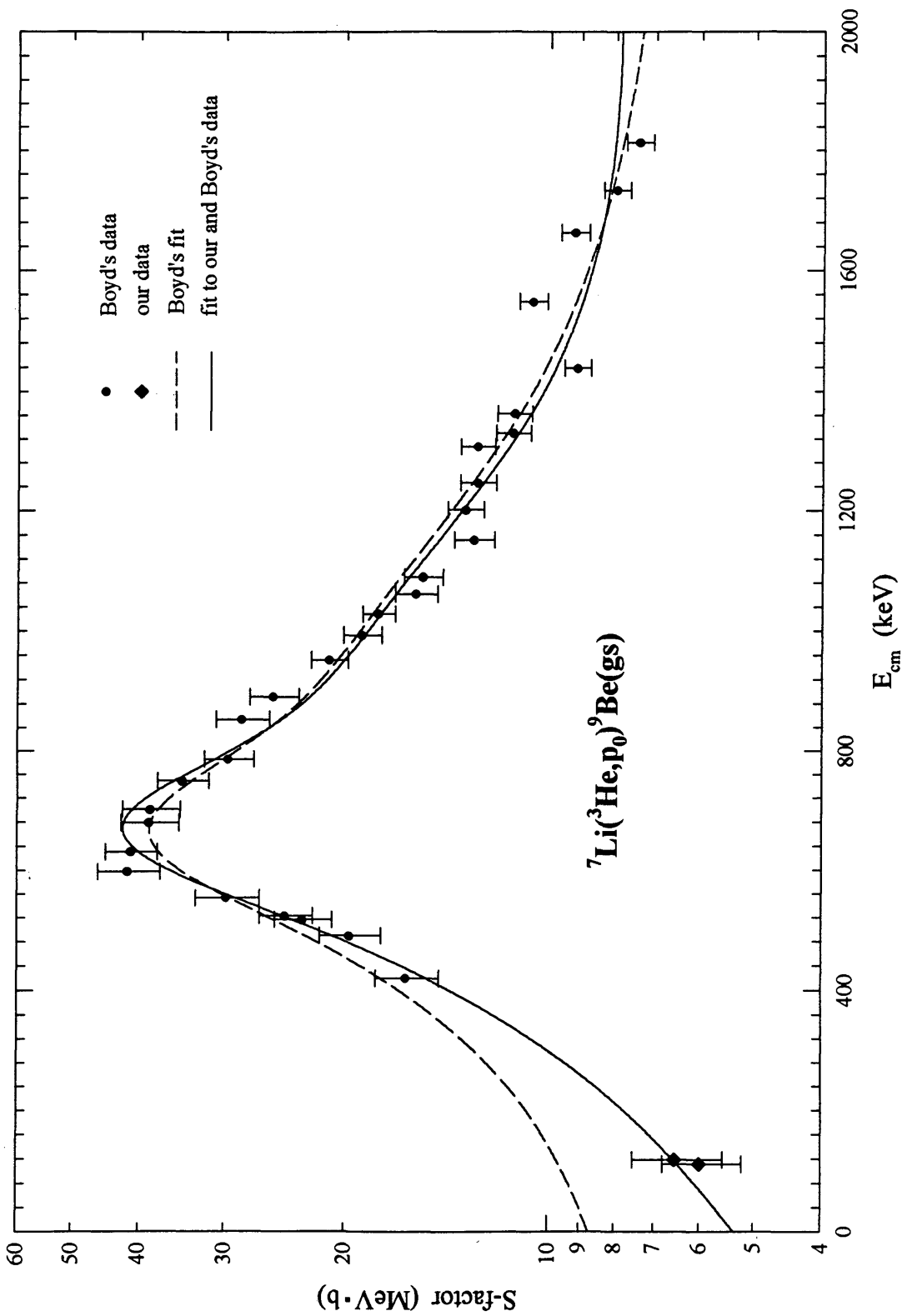


Fig. 3-54. The S-factor for the ${}^7\text{Li}({}^3\text{He}, p_0){}^9\text{Be}(\text{gs})$ reaction.

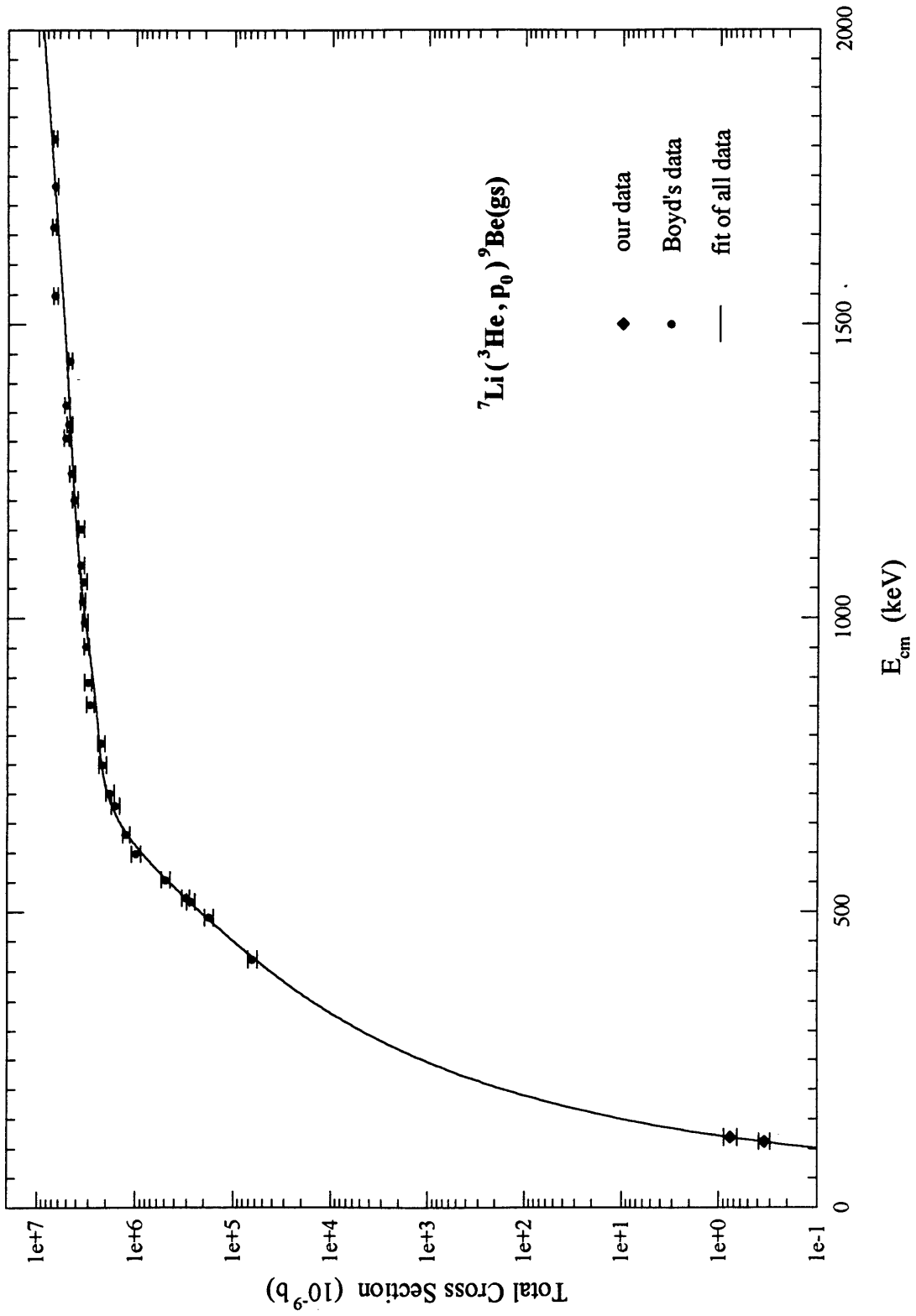


Fig. 3 · 55. The cross section for the ${}^7\text{Li}({}^3\text{He}, p_0){}^9\text{Be}(\text{gs})$ reaction.

Chapter 4

DISCUSSIONS AND CONCLUSIONS

As having pointed out in Chapter 1, the nuclear reactions investigated in this thesis can be used in astrophysical nucleosynthesis and in the diagnostics of first wall contamination of fusion plasmas in the JET and TFTR tokamaks. Now, with the present data reported in Chapter 3, these applications are possible. In this chapter, several examples in these two areas of application will be calculated in order to demonstrate the applicability of our measured data.

At first, it may be helpful to have a brief description about the reaction rate since it is involved in these applications. In a thermonuclear reaction $A(x,y)B$, the reaction rate per particle pair of A and x has been given in Eq. (1.6). Hence the $A(x,y)B$ reaction rate per unit volume, in other words, the production rate of B per unit volume is

$$R(B) = n(A) n(x) \langle \sigma v \rangle, \quad (4.1)$$

where $n(A)$ and $n(x)$ are the number density of A and x, respectively.

4.1 APPLICATIONS IN ASTROPHYSICAL NUCLEOSYNTHESIS

4.1.1 ${}^9\text{Be}$ Production by ${}^7\text{Li}({}^3\text{He}, p_0){}^9\text{Be}(\text{gs})$ in BBN

In Chapter 1, the significance of the ${}^9\text{Be}$ production by the ${}^7\text{Li}({}^3\text{He}, p_0){}^9\text{Be}(\text{gs})$ reaction in primordial nucleosynthesis has been discussed in two aspects of serving as a

possible test for SM and NDM and being the start point of the alternative reaction network in Fig. 1-2(a). Now, the relative abundance of ${}^9\text{Be}$ nuclei synthesized in BBN with respect to that of ${}^1\text{H}$ can be estimated.

As a rough estimate, the relative abundance can be found by using Eq. (4-1) to be

$$\frac{n({}^9\text{Be})}{n({}^1\text{H})} = \frac{n({}^7\text{Li})}{n({}^1\text{H})} \frac{n({}^3\text{He})}{n({}^1\text{H})} \frac{N_A \langle \sigma v \rangle}{N_A} \Delta t n({}^1\text{H}), \quad (4.2)$$

where N_A is the Avogadro's number and Δt the time duration of the primordial nucleosynthesis. Some typical values for the parameters in Eq. (4-2) can be found in Sch77 to be

$$\frac{n({}^7\text{Li})}{n({}^1\text{H})} = 10^{-10}; \quad \frac{n({}^3\text{He})}{n({}^1\text{H})} = 10^{-5}; \quad \Delta t = 10^3; \quad n({}^1\text{H}) = 10^{21} \text{ cm}^{-3}. \quad (4.3)$$

With the S-factor given in Eq.(3-8), Fig. 4-1 plots the calculated reaction rate $N_A \langle \sigma v \rangle$ of the ${}^7\text{Li}({}^3\text{He}, p_0){}^9\text{Be}(\text{gs})$ reaction as a function of temperature. Substituting the reaction rate value at $T_9 = 0.6$ from Fig. 4-1, the relative abundance of ${}^9\text{Be}$ to that of ${}^1\text{H}$ in BBN can be calculated to be

$$\frac{n({}^9\text{Be})}{n({}^1\text{H})} = 3 \times 10^{-13}, \quad (4.4)$$

compared with the published value of $\sim 10^{-16}$ [Kaj90] (see also Boy89 and Yam93 for details).

It has to be emphasized herein that $n({}^1\text{H})$, $n({}^3\text{He})$ and $n({}^7\text{Li})$ are functions of time and the calculated $N_A \langle \sigma v \rangle$ is also a function of time since the universe temperature is related to time through Eq. (1-8), hence, an accurate calculation of the relative abundance must be carried out by integration over the nucleosynthesis time. On the other hand, the destruction of the produced ${}^9\text{Be}$ nuclei by nuclear reactions such as the proton- and deuteron-induced reactions has not been considered in the above calculation, therefore, a complete calculation must include all the possible reactions, that is to say, use a complete reaction network. Thus the disagreement between the present and published relative abundance is due to the above two factors.

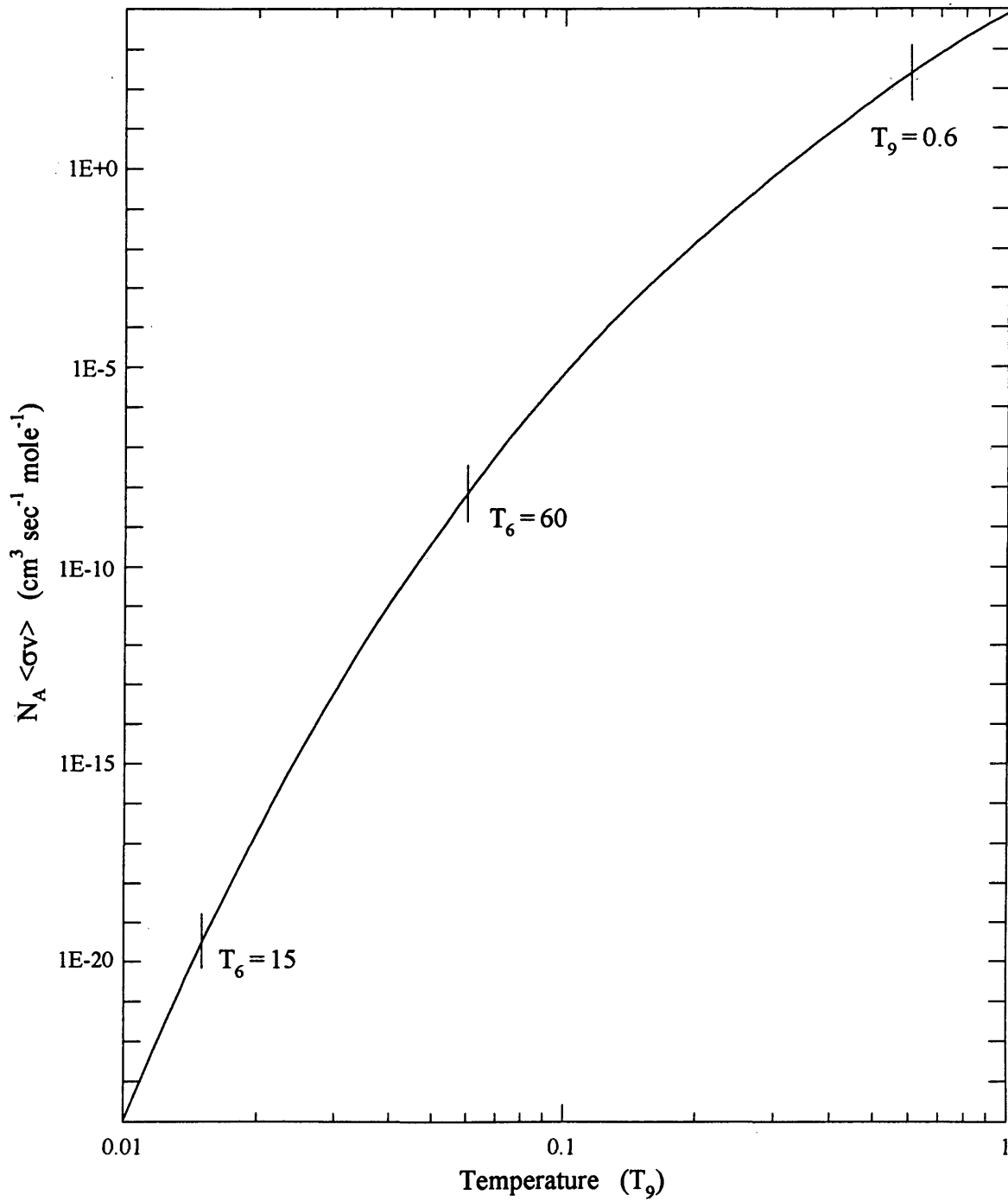


Fig. 4-1. ${}^7\text{Li}({}^3\text{He}, p_0){}^9\text{Be}(\text{gs})$ reaction rate. The three marks show the typical temperatures of BBN and SP processes as listed in Table 1-1.

4-1-2 ^{12}C Production in the Sun

In the stellar nucleosynthesis, as shown by the reaction network in Fig. 1-2(b), where the reactions will take place in the p-p chain burning, ^9Be is a kind of raw material in the production of ^{12}C through this reaction network, which will later serve as a catalyst for the CNO cycles. The question raised in Section 1-2-2 is in what amount the ^{12}C nuclei can be synthesized with this reaction network.

An example for SP is the sun, with the interior temperature $T_6 = 15$, the mass density of the solar interior medium $\rho \approx 10^2 \text{ g cm}^{-3}$, the radius of $7 \times 10^{10} \text{ cm}$ and the age $\Delta t = 3 \times 10^{16}$ seconds. Then the interior number density of ^1H is $n(^1\text{H}) \approx \rho/m_p \approx 6 \times 10^{25} \text{ cm}^{-3}$, where m_p is the proton mass. The relative abundance of ^3He to ^1H is given [Fig. 6-6 in Rol88] to be in the order of 10^{-5} at $T_6 = 15$.

Now, consider the number density of ^7Li in the interior of the sun. ^7Li is produced only in the p-p chain II, of which the branching ratio is 14% [Fig. 6-13 in Rol88] under the conditions of the sun, i.e., 14 ^7Li nuclei can be produced in the sun out of 100 p-p reactions, while the produced ^7Li is destroyed mainly by the $^7\text{Li}(p,\alpha)^4\text{He}$ reaction. Hence, the reaction rate equation can be derived from Eq. (4-1) to be

$$\frac{d n(^7\text{Li})}{dt} = \frac{0.14}{2} \langle \sigma v \rangle_{11} [n(^1\text{H})]^2 - n(^1\text{H}) n(^7\text{Li}) \langle \sigma v \rangle_{17}, \quad (4-5)$$

where $\langle \sigma v \rangle_{11}$ and $\langle \sigma v \rangle_{17}$ are the reaction rate for the p+p and $^7\text{Li}(p,\alpha)^4\text{He}$ reactions, respectively, and the factor of 2 comes from the fact that each p+p reaction will expend two protons. At equilibrium, then,

$$n(^7\text{Li}) = \frac{0.14}{2} \frac{\langle \sigma v \rangle_{11}}{\langle \sigma v \rangle_{17}} n(^1\text{H}). \quad (4-6)$$

With the published values of the S-factors for the two reactions [Table 5-1 in Cla83; Rol86; and Eng92], $\langle \sigma v \rangle_{11}$ and $\langle \sigma v \rangle_{17}$ can be calculated numerically by Eq. (1-6) to be $1.7 \times 10^{-43} \text{ cm}^3 \text{ sec}^{-1}$ and $2 \times 10^{-29} \text{ cm}^3 \text{ sec}^{-1}$ at $T_6 = 15$, respectively. Hence follows

$$n(^7\text{Li}) = 4 \times 10^{10} \text{ cm}^{-3}. \quad (4.7)$$

Then, using the above values, the total number of ^9Be nuclei that have ever been produced through the $^7\text{Li}(^3\text{He}, p_0)^9\text{Be}(\text{gs})$ reaction since the birth of the sun can be estimated and is found to be

$$N(^9\text{Be}) = n(^3\text{He}) n(^7\text{Li}) \langle \sigma v \rangle_{37} V \Delta t = 1 \times 10^{36}, \quad (4.8)$$

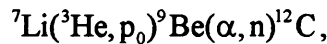
where $\langle \sigma v \rangle_{37}$ is the reaction rate for the $^7\text{Li}(^3\text{He}, p_0)^9\text{Be}(\text{gs})$ reaction, for which a value of $3 \times 10^{-44} \text{ cm}^3 \text{ sec}^{-1}$ at $T_6 = 15$ can be obtained from the present result in Fig. 4.1, V is the volume of the solar interior medium and can be thought to be in the order of 10^{32} cm^3 .

Finally, the production of ^{12}C from the above estimated ^9Be through the reaction network of Fig. 2.1(b) can be expressed by the three branching ratios, $R_b(^9\text{Be})$, $R_b(^{10}\text{B})$ and $R_b(^{11}\text{B})$, of ^9Be , ^{10}B and ^{11}B between the (p, γ) and (p, α) reactions, of which the published values are 1.5×10^{-4} [Cec92], 3×10^{-5} [Pet75] and 1×10^{-5} [Cec92], respectively, and is found to be

$$N(^{12}\text{C}) = N(^9\text{Be}) R_b(^9\text{Be}) R_b(^{10}\text{B}) R_b(^{11}\text{B}) = 1 \times 10^{23}. \quad (4.9)$$

In other words, the total amount of ^{12}C produced in the sun by the reaction network is less than one gram. This is a vanishingly small number compared with the mass of the sun.

The author wants to emphasize that, from Fig. 4.1, the $^7\text{Li}(^3\text{He}, p_0)^9\text{Be}(\text{gs})$ reaction rate for a massive star with a temperature of $T_6 = 60$ is higher than that for the sun by a factor of about 3×10^{11} . On the other hand, the above calculation is based on the reaction network in Fig. 1.2(b), in which the three branching ratios in Eq. (4.9) with the product being 4.5×10^{-14} are inevitable. If the following reaction pathway is considered,



the three branching ratios will not be encountered. Note that the $^9\text{Be}(\alpha, n)^{12}\text{C}$ reaction has a large S-factor, $10^4 \sim 10^5 \text{ MeV}\cdot\text{b}$ in the energy region between 80 keV and 130 keV [Wre94], i.e., the Gamow energy window at $T_6 = 60$. Therefore, it can be expected that a considerable amount of ^{12}C will be produced in a massive star through the above reaction pathway.

4-1-3 ${}^7\text{Li}$ Destruction by ${}^7\text{Li}(d,2\alpha)n$ in BBN

Fig. 1-2(a) shows that the ${}^7\text{Li}(d,2\alpha)n$ reaction provides a reaction pathway of ${}^7\text{Li}$ destruction, which will be particularly important for the low-density neutron-rich region in NDM since deuterium is relatively abundant in this region.

Our measured S-factors, Fig. 3-4(b), for both direct breakup and sequential decay of the reaction can be summed up and formulated by

$$S \approx 30 - 160 E, \quad \text{for } 0.03 \text{ MeV} \leq E \leq 0.13 \text{ MeV}, \quad (4-10)$$

where S is in units of $\text{MeV}\cdot\text{b}$ and E in MeV . With Eq. (1-6), the ${}^7\text{Li}(d,2\alpha)n$ reaction rate, i.e., the destruction rate of ${}^7\text{Li}$ by the (d,α) reaction is calculated and illustrated in Fig. 4-2 by the dashed line. Note that, since the energy region determined by the Gamow peak will exceed that of Eq. (4-10) at a temperature approaching to $T_9 = 1$, the present reaction rate is valid for $T_9 < 1$.

A recent publication [Boy93] has reexamined the ${}^7\text{Li}$ destruction by the (d,p) and (d,n) reactions. The dotted line in Fig. 4-2 plots the reaction rate due to the two reactions using the equations given in Boy93. It can be noticed that the ${}^7\text{Li}$ destruction rate by the present (d,α) reaction is larger than that by both of the (d,p) and (d,n) reactions at $T_9 < 0.4$. The solid line in Fig. 4-2 is the reaction rate of all the three reactions.

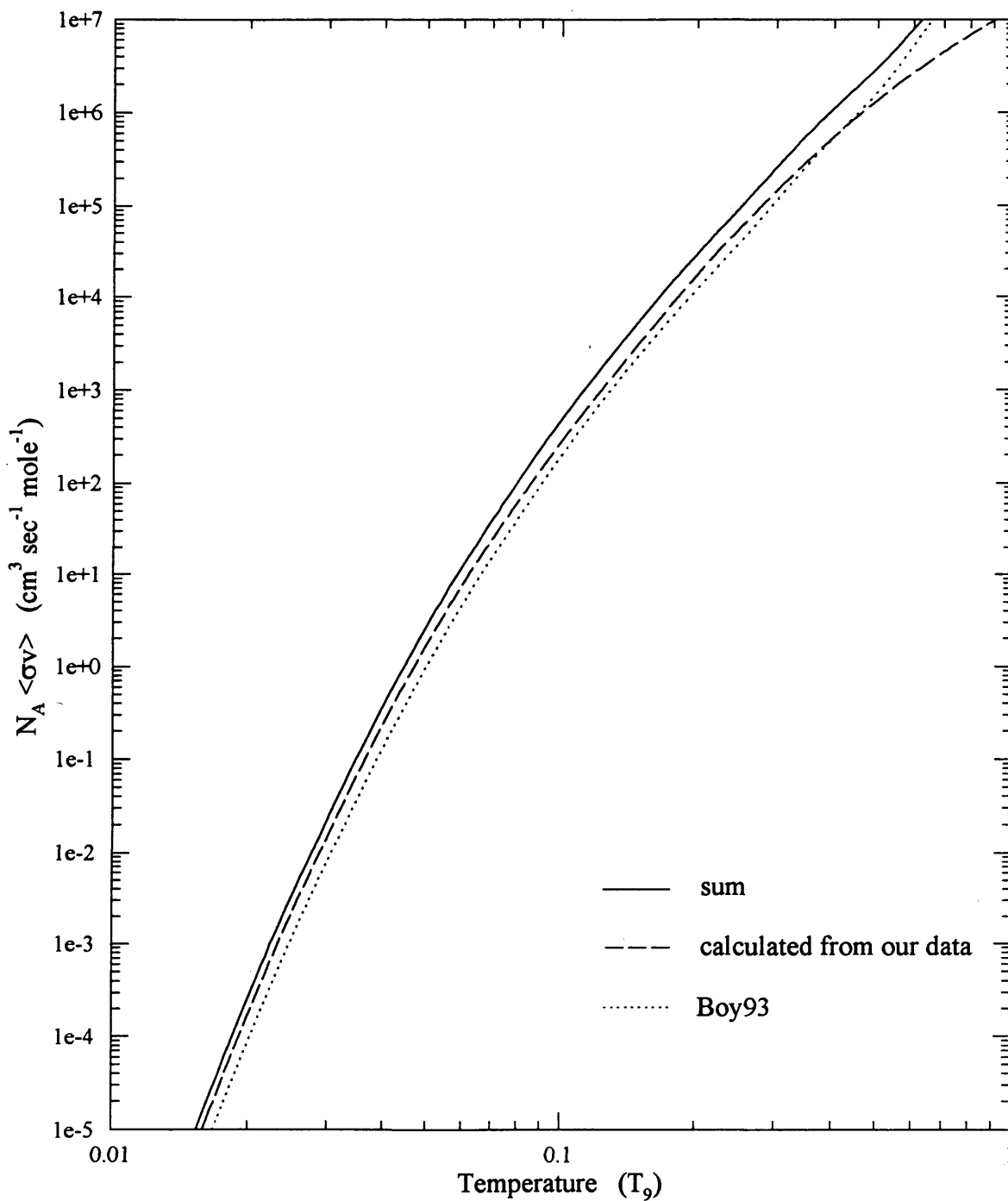


Fig. 4-2. Reaction rate for destruction of ${}^7\text{Li}$ by deuterium. The dashed line is calculated for (d, α) destruction from our data while the dotted line [Boy93] is for (d, p) and (d, n) . The solid line is the sum.

4.2 APPLICATIONS IN TOKAMAKS

The fusion plasma contamination from the first wall may cause some problems in tokamaks, as discussed in Section 1.3. Plasma diagnostics by measurement of the γ -ray radiation from the contaminant has been proposed [Cec84; Med92; and Cec94]. Now, with the present data, this measurement can be simulated.

Consider the JET tokamak, of which the contaminant from the first wall is beryllium. The ${}^9\text{Be}(d, p_1){}^{10}\text{Be}^*(3.368 \text{ MeV})$ reaction rate from the contaminant ${}^9\text{Be}$ nuclei, i.e., the rate of the 3.3 MeV γ -ray radiation from the contaminated fusion plasma per unit volume can be calculated from the S-factor listed in Table 3-2. The measured count rate of the γ -ray is

$$\text{count rate} = n(d) n({}^9\text{Be}) \langle \sigma v \rangle V \varepsilon , \quad (4.11)$$

where V is the plasma volume and ε the absolute γ -ray detection efficiency, i.e., the ratio of γ -rays emitted to that detected. With the typical values of $n(d) = 5 \times 10^{19} \text{ m}^{-3}$, $V = 10 \text{ m}^3$ and $\varepsilon = 4.4 \times 10^{-10}$ [Cec94] and assuming a fraction of 10% of contaminant nuclei to the total plasma ions, i.e., $n({}^9\text{Be}) = 5 \times 10^{18} \text{ m}^{-3}$, the count rate is calculated as a function of plasma temperature and shown in Fig. 4-3 by the solid line. Alternatively, with the measured γ -ray count rate at a plasma temperature, the contaminant percentage can be found using Fig. 4-3.

The dotted line in Fig. 4-3 is the γ -ray count rate calculated for the TFTR tokamak, where $\varepsilon = 8.6 \times 10^{-9}$ [Med92] for the 4.4 MeV γ -ray from the radiation decay of ${}^{10}\text{B}(d, p_2){}^{11}\text{B}^*(4.445 \text{ MeV})$, the ${}^{10}\text{B}$ abundance of 19.9% has been considered and values for other parameters are the same as used for the JET tokamak.

Alternatively, if we assume a non-Maxwellian distribution in which the deuteron energy distribution is concentrated at the energy of the injected neutral beams, E_{beam} , then the γ -ray production rate per unit volume will be, for the TFTR tokamak,

$$R(\gamma) = n({}^{10}\text{B}) n(d) \sigma(E_{\text{beam}}) v , \quad (4.12)$$

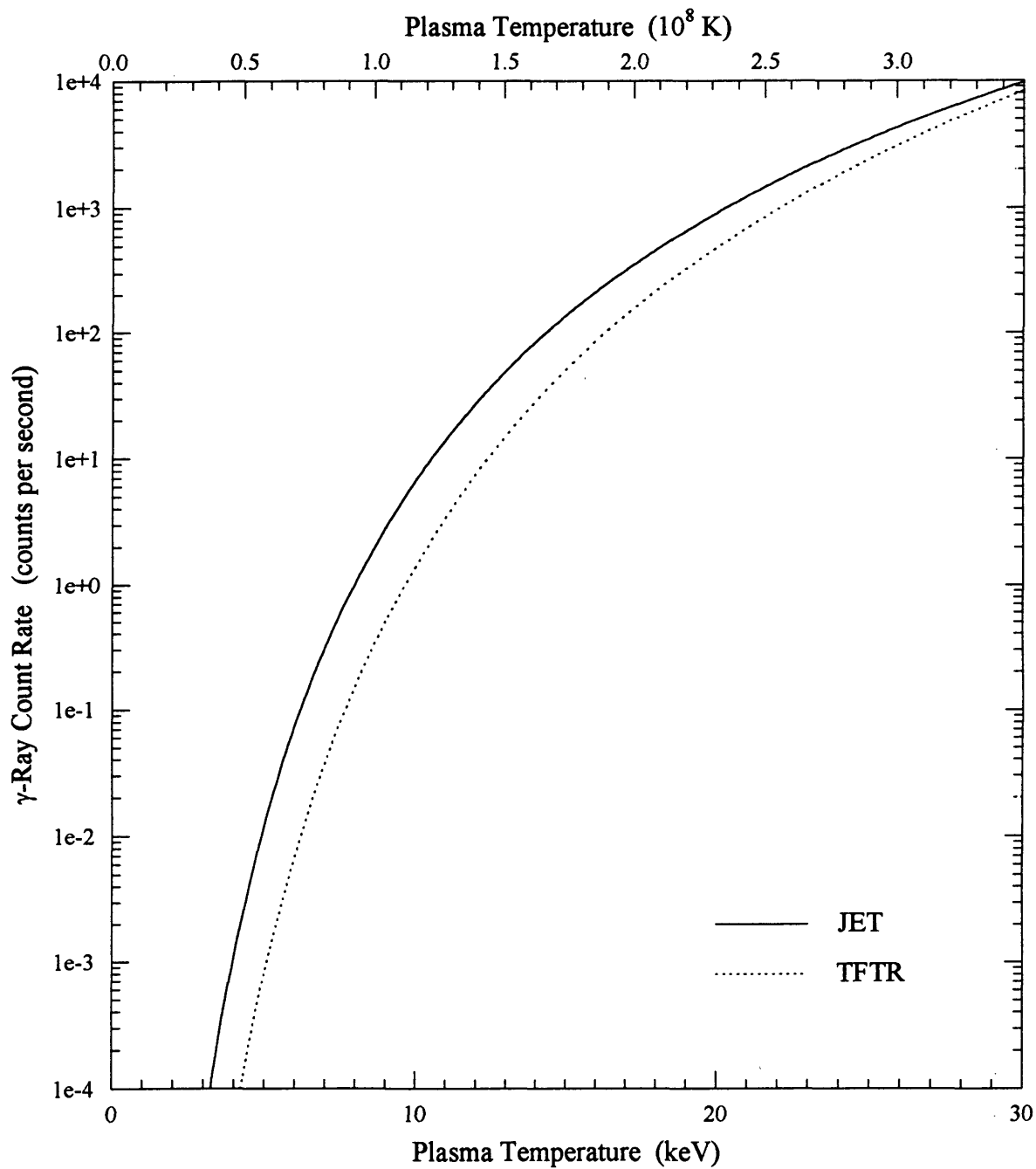
where v is the relative velocity of the injected deuterium to the boron contaminant which can be treated to be at rest. A typical set of parameters of the tokamak might be

$$E_{\text{beam}} = 100 \text{ keV}; \quad I_{\text{beam}} = 50 \text{ Amp}; \quad \Delta t = 1 \text{ sec.} \quad (4.13)$$

Hence an energetic deuteron population of about $3 \times 10^{19} \text{ m}^{-3}$ is introduced with a velocity of $3 \times 10^6 \text{ m/s}$. Again, assuming a 10% boron contamination, of which 19.9% is ^{10}B , the expected count rate from the γ -ray detection of the above efficiency [Med92] can be calculated from the measured cross section of $^{10}\text{B}(d, p_2)^{11}\text{B}^*(4.445\text{MeV})$, Fig. 3-32, and is plotted in Fig. 4-4 by the dotted line. At $E_{\text{beam}} = 100 \text{ keV}$, the count rate found in Fig. 4-4 is about 100 per second.

The solid line in Fig. 4-4 is for the JET tokamak with parameters in Eq. (4.13). A count rate of about 300 per second can be found at $E_{\text{beam}} = 100 \text{ keV}$.

Fig. 4-3. The calculated count rates of γ -ray detection for plasma diagnostics of JET and TFTR tokamaks.



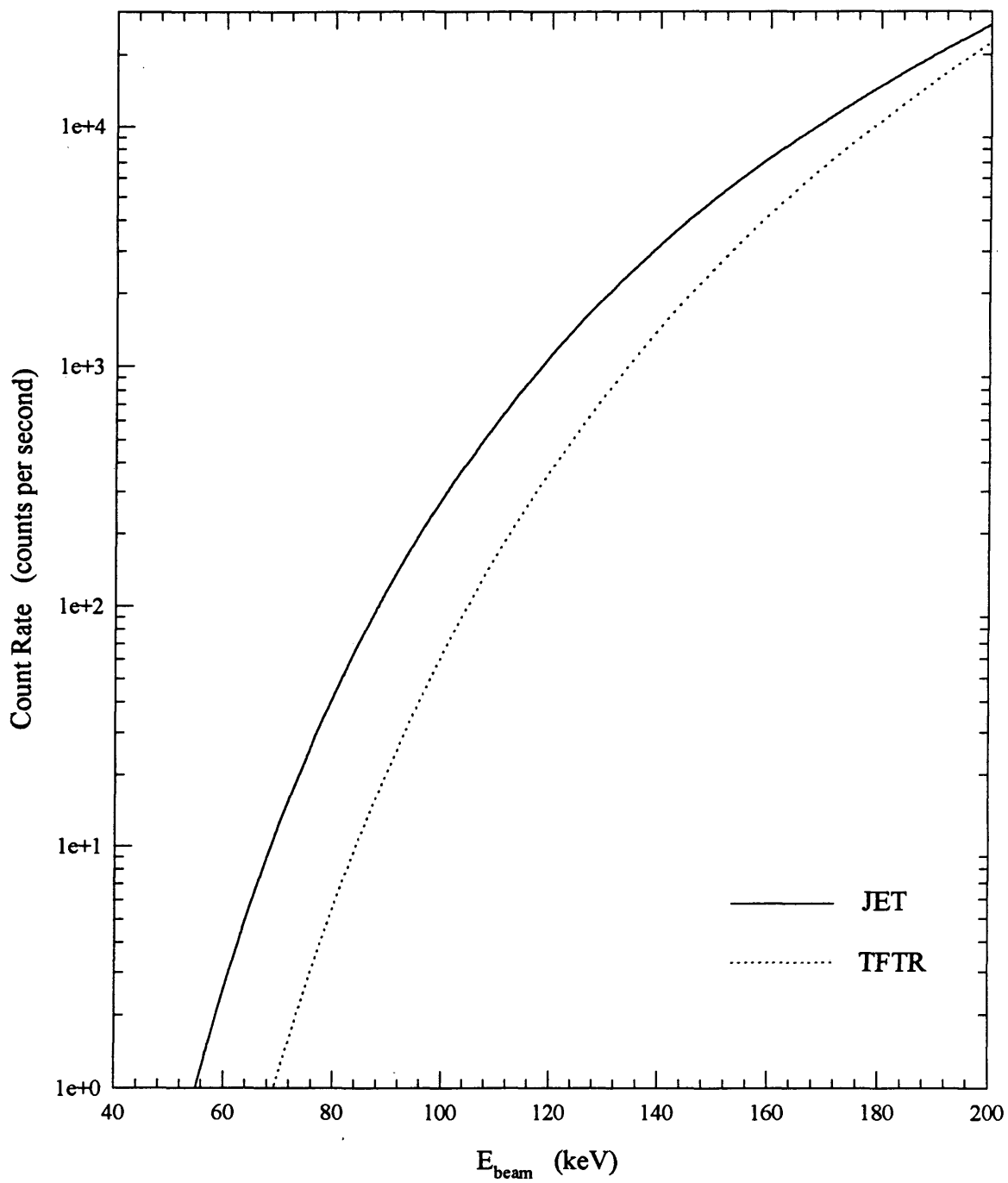


Fig. 4-4. The calculated count rates of γ -ray detection for the injection of neutral beams.

4.3 THE SINGLE-STEP DWUCK4 CALCULATIONS

Another important aspect of this thesis is to study the nuclear reactions theoretically and to compare the calculated results with the measured ones. Some of the single-step DWUCK4 calculations based upon theory of the distorted wave Born approximation [Kun93] have been made for the ${}^9\text{Be}(d,p_0){}^{10}\text{Be}(\text{gs})$, ${}^9\text{Be}(d,t_0){}^8\text{Be}(\text{gs})$, ${}^{11}\text{B}(d,p_0){}^{12}\text{B}(\text{gs})$ and ${}^{10}\text{B}(d,p_0){}^{11}\text{B}(\text{gs})$ reactions, for the reason that, unlike other reactions studied here, the angular momentum of the produced nucleus can easily be coupled by single-particle transfer, for example, for ${}^9\text{Be}(d,p_0){}^{10}\text{Be}(\text{gs})$, by putting a neutron at the $1P_{3/2}$ state of ${}^9\text{Be}(\text{gs})$ in Fig. 4-5, the ground state of ${}^{10}\text{Be}$ will be constructed.

Table 4-1 summarizes some important parameters used in the single-step DWUCK4 calculations. A standard input file for DWUCK4 is given in Table 4-2. A Woods-Saxon potential with proton spin-orbit interaction has been chosen and the differential cross sections of the reactions as a function of θ_{cm} at certain energies have been calculated.

Figs. 4-6 through 4-9 are the calculated differential cross sections of the reactions, together with our measured results as comparison. Also given in Figs. 4-6 through 4-9 are some experimental results from other authors of references [Smi57; and Amb66], showing that our measurements agree with those of the references while the single-step DWUCK4 calculations lead to the results greatly different from the measurements.

The inconsistency between the single-step DWUCK4 calculations and measurements implies that multichannel DWUCK4 calculations may be necessary for the reactions. These multichannel DWUCK4 calculations have been scheduled to be accomplished in the future.

Fig. 4-5. Formation of the ¹⁰Be ground state by single-particle transfer to the ⁹Be ground state.

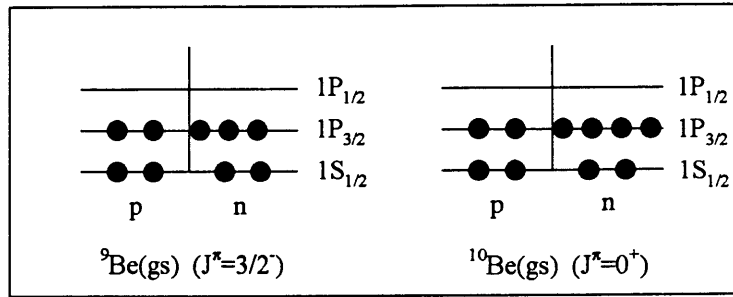


Table 4-1. Summary of the input values of the parameters used in DWUCK4 calculations.

parameter	description	⁹ Be(d, p ₀)	⁹ Be(d, t ₀)	¹⁰ B(d, p ₀)	¹¹ B(d, p ₀)
LTR(I)	the angular transfer for the Ith form factor	1	1	1	1
2·FS	twice the spin transfer of the form factor	1	1	1	1
JTR(I)	twice the total angular momentum transfer for the Ith radial form factor	3	3	3	1

Table 4-2. A standard input file for DWUCK4 calculations.

1002000000000000								
+37	+0.0	+5.0						
+5	+1	+1	+3					
+0.1	+0.0	+12.0						
+0.15	+2.0	+1.0	+9.0	+4.0	+1.4	+0.0	+0.0	+2.0
+1.0	-48.0	+1.112	+0.875	+0.0	+0.0	+1.562	+0.477	
-2.0	+0.0	+1.112	+0.875	+0.0	+25.0	+1.562	+0.477	
+4.588	+1.0	+1.0	+10.0	+4.0	+1.4	+0.0	+0.0	+1.0
+1.0	-48.0	+1.18	+0.7	+0.0	+0.0	+1.18	+0.7	
-2.0	+0.0	+1.18	+0.7	+0.0	+19.8	+1.252	+0.75	
-6.812	+1.0	+0.0	+9.0	+4.0	+1.4	+0.0	+0.0	+1.0
-1.0	-1.0	+1.18	+0.7	+25				
+0.0	+1.0	+3.0	+1.0	+58	+0.0			

Fig. 4-6. An angular distribution calculated by DWUCK4, compared with the measured results from the present work, Smi57 and Amb66.

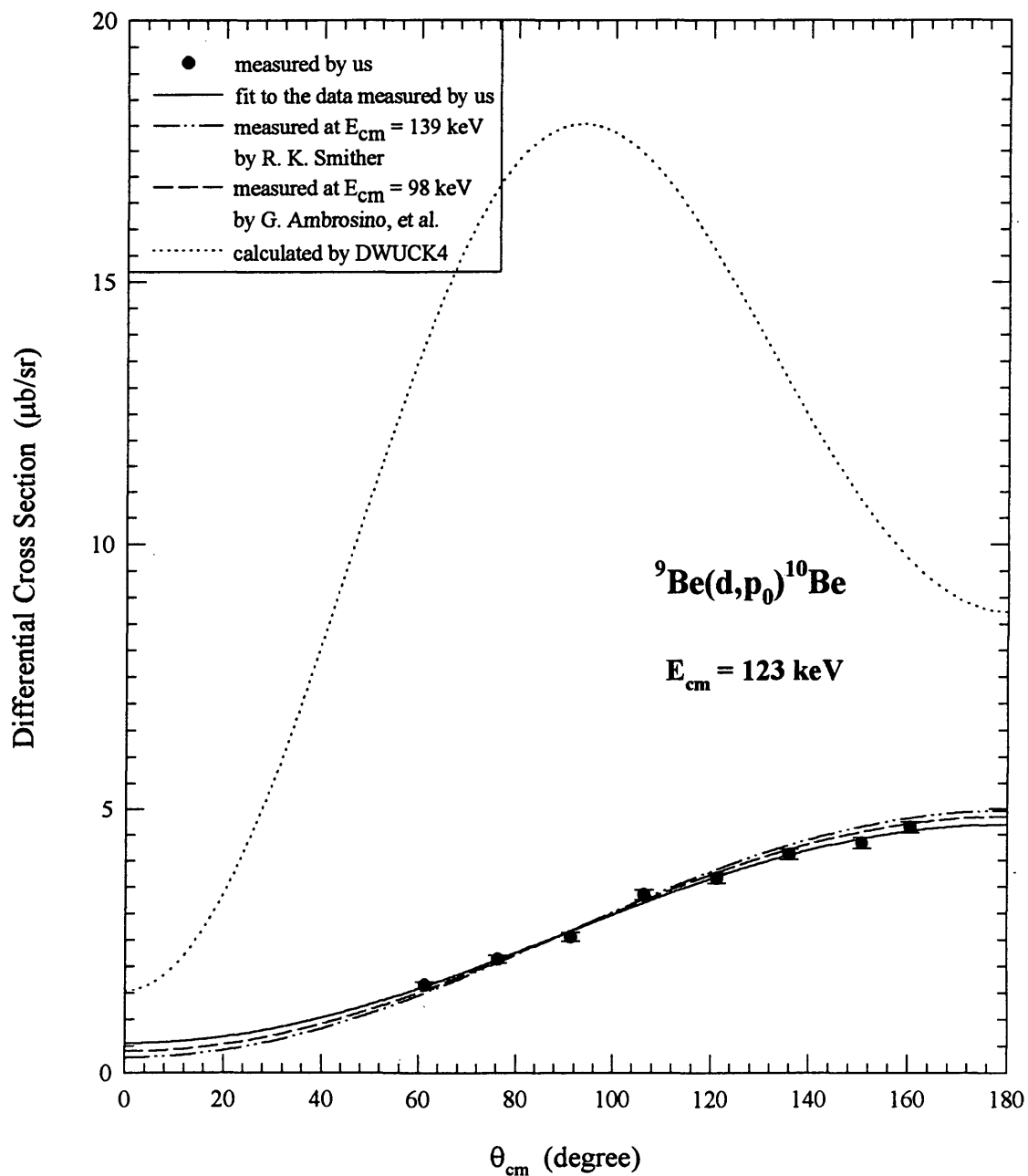


Fig. 4-7. An angular distribution calculated by DWUCK4, compared with the measured results from the present work and Smi57. Note that the plotted curve of DWUCK4 is the real DWUCK4 output multiplied by 0.1.

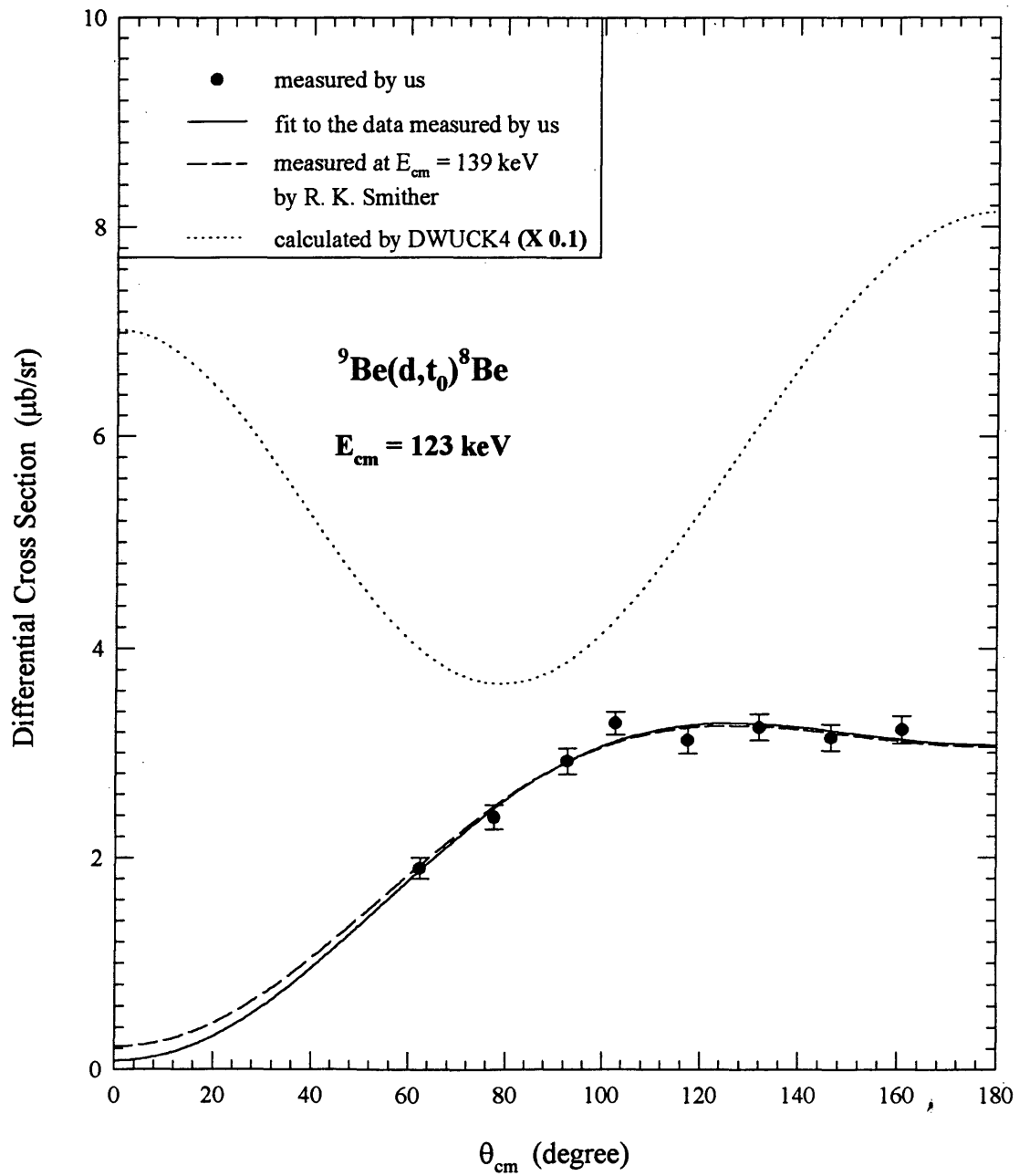


Fig. 4-8. An angular distribution calculated by DWUCK4, compared with our measured result.

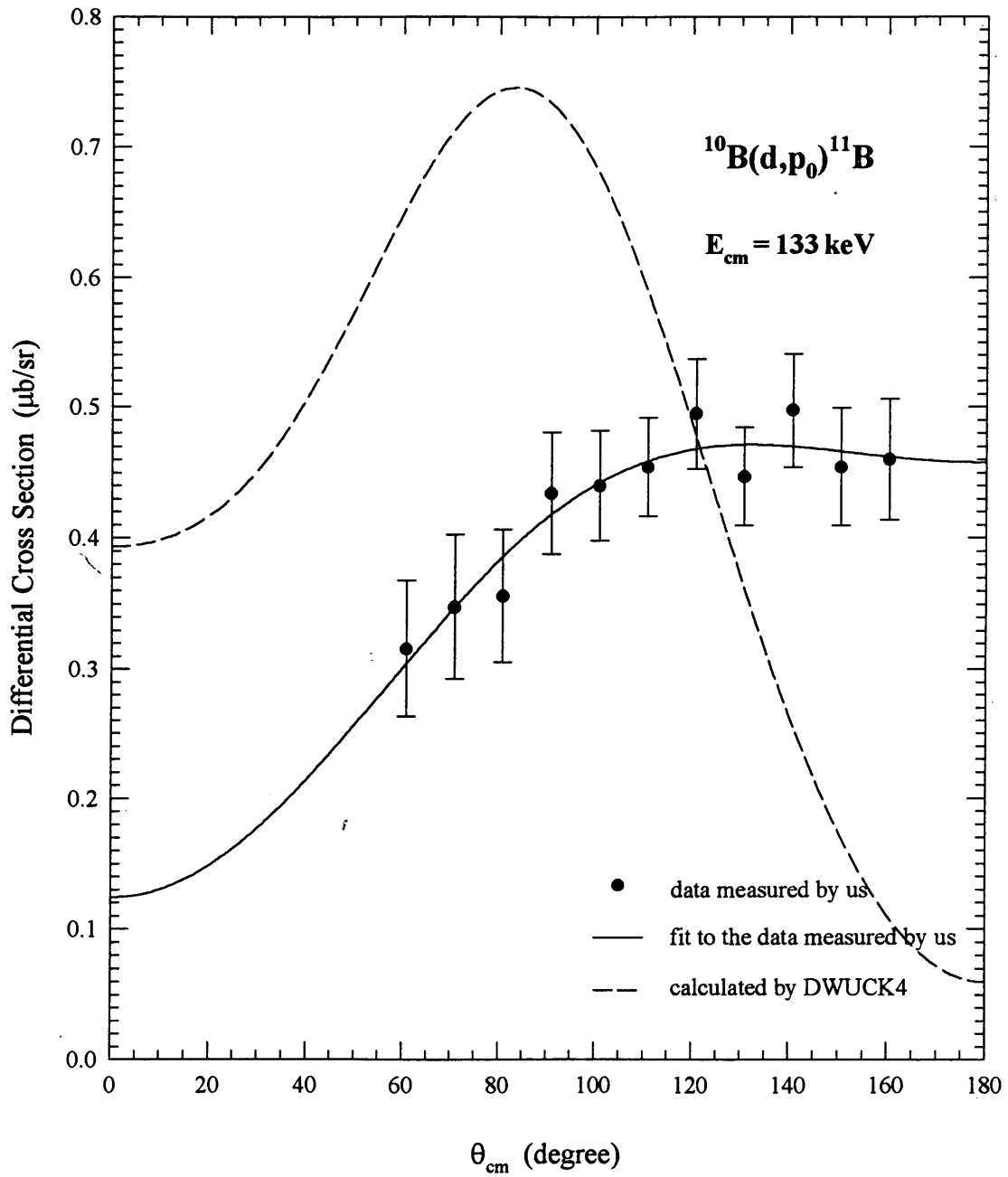
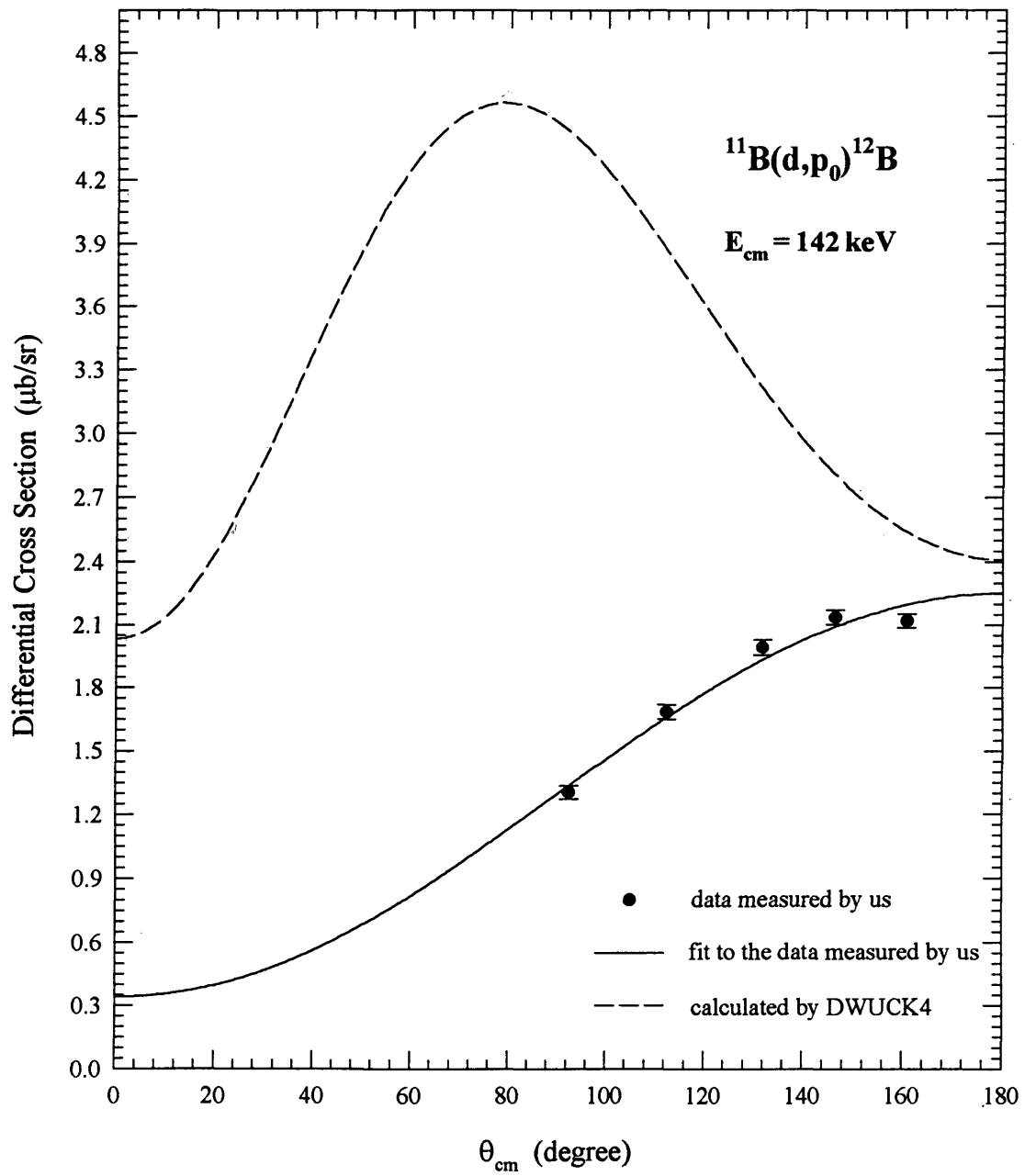


Fig. 4-9. An angular distribution calculated by DWUCK4, compared with our measured result.



REFERENCES CITED

- Ajz84 Ajzenberg-Selove, F., *Nucl. Phys.* A413 (1984) 1.
Ajz85 Ajzenberg-Selove, F., *Nucl. Phys.* A433 (1985) 1.
Ajz86 Ajzenberg-Selove, F., *Nucl. Phys.* A449 (1986) 1.
Alc87 Alcock, C., Fuller, G.M., and Mathews, G.J., *Astrophys. J.* 320 (1987) 439.
Amb66 Ambrosino, G., Crettez, J.P., Lachkar, J., and Perchereau, J., *J. Phys. (Paris) Colloq* 1 (1966) 62.
Bal91 Balbes, M.J., Feldman, G., Kramer, L.H., Weller, H.R., and Tilley, D.R., *Phys. Rev.* C43 (1991) 343.
Bar91 Barhoumi, S, et al., *Nucl. Phys.* A535 (1991) 107.
Bea66 Beaumevieuille, H., Longequeue, N., Longequeue, J.P., and van Sen, N., *J. Phys. (Paris) Colloq.* 1 (1966) 150.
Bec87 Becker, H.W., Rolfs, C., and Trautvetter, H.P., *Z. Phys. A—Atomic Nuclei* 327 (1987) 341.
Boy89 Boyd, R.N., and Kojino, T., *Astrophys. J.* 336 (1989) L55.
Boy93 Boyd, R.N., Mitchell, C.A., and Meyer, B.S., *Phys. Rev.* C47 (1993) 2369.
Bro90 Brown, R.E., and Jarmie, N., *Phys. Rev.* C41 (1990) 1391.
Bru91 Brune, C.R., Kavanagh, R.W., Kellogg, S.E., and Wang, T.R., *Phys. Rev.* C43 (1991) 875
Cec84 Cecil, F.E., and Newman, D.E., *Nucl. Instrum. and Methods* 221 (1984) 441.
Cec89 Cecil, F.E., Ferg, D., King, R., Kriss, B., Liu, H., and Scorby, J., *Nucl. Instr. Meth. Phys. Res.* B40/41 (1989) 934.
Cec92 Cecil, F.E., et al., *Nucl. Phys.* A539 (1992) 75.
Cec94 Cecil, F.E., Belle, P. van, Jarvis, O.N., and Sadler, G.J., *JET Joint Undertaking Technical Report JET-IR(94)04*, November 1994.
Cla83 Clayton, D.D., *Principles of Stellar Evolution and Nucleosynthesis* (Chicago: The University of Chicago Press, 1983).
Coo57 Cook, C.W., Fowler, W.A., Lauritsen, C.C., and Lauritsen, T., *Phys. Rev.* 107 (1957) 508.

- Dav79 Davidson, J.M., et al., *Nucl. Phys.* A315 (1979) 253.
- Dwa71 Dwarakanath, M.R., and Winkler, H., *Phys. Rev.* C4 (1971) 1532.
- Eng92 Engstler, S., et al., *Phys. Lett.* B 279 (1992) 20.
- Ful88 Fuller, G.M., Mathews, G.J., and Alcock, C.R., *Phys. Rev.* D37 (1988) 1380.
- Hag77 Hagler, M.O., and Kristiansen, M., *An Introduction to Controlled Thermonuclear Fusion* (Lexington: D.C. Heath and Company, 1977).
- Hal87 Hale, G.M., Brown, R.E., and Jarmie, N., *Phys. Rev. Lett.* 59 (1987) 763.
- Har60 Harrison, G.R., Schmidt, G.D., and Curtis, C.D., *Phys. Rev.* 117 (1960) 532.
- Hoy53 Hoyle, F., Dunbar, D.N.F., Wenzel, W.A., and Whaling, W., *Phys. Rev.* 92 (1953) 1095.
- Kaj90 Kajino, T., and Boyd, R.N., *Astrophys. J.* 359 (1990) 267.
- Koe88 Koehler, P.E., et al., *Phys. Rev.* C37 (1988) 917.
- Kra87 Krauss, A., Becker, H.W., Trautvetter, H.P., Rolfs, C., and Brand, K., *Nucl. Phys.* A465 (1987) 150.
- Kra87a Krauss, A., Becker, H.W., Trautvetter, H.P., and Rolfs, C., *Nucl. Phys.* A467 (1987) 273.
- Lan66 Lane, A.M., and Robson, D., *Phys. Rev.* 151 (1966) 774.
- Lon66 Longequeue, N., Cavaignac, M.M.J.F., Ligeon, E., and Longequeue, J.P., *J. Phys. (Paris)* 27 (1966) 649.
- Mal88 Malaney, R.A., and Fowler, W.A., *Astrophys. J.* 333 (1988) 14.
- Man64 Manalis, M., and Henkel, J.E., *Phys. Rev.* 136 (1964) B1741.
- Med92 Medley, S.S., Roquemore, A.L., and Cecil, F.E., *Rev. Sci. Instrum.* 63 (1992) 4857.
- Möl77 Möller, W., Hufschmidt, M., and Kamke, D., *Nucl. Instr. and Meth.* 140 (1977) 157.
- Öpi51 Öpik, E.J., *Proc. Roy. Irish Acad.* A54 (1951) 49.
- Pet75 Peterson, R.J., Zaidins, C.S., Fritts, M.J., Roughton, N.A., and Hansen, C.J., *Ann. Nucl. Energy* 2 (1975) 503.
- Rai90 Raimann, G., et al., *Phys. Lett.* B 249 (1990) 191.
- Rat90 Rath, D.P., Boyd, R.N., Hausman, H.J., Islam, M.S., and Kolnicki, G.W., *Nucl. Phys.* A515 (1990) 338.
- Ree94 Reeves, H., *Rev. Mod. Phys.* 66 (1994) 193.

- Rol86 Rolfs, C, and Kavanagh, R.W., *Nucl. Phys.* A455 (1986) 179.
- Rol88 Rolfs, C.E., and Rodney, W.S., *Cauldrons in the Cosmos* (Chicago: The University of Chicago Press, 1988).
- Sal52 Salpeter, E.E., *Phys. Rev.* 88 (1952) 547, and *Astrophys. J.* 115 (1952) 326.
- Sal53 Salpeter, E.E., *Ann. Rev. Nucl. Sci.* 2 (1953) 41.
- Sal57 Salpeter, E.E., *Phys. Rev.* 107 (1957) 516.
- Sch77 Schramm, D.N., and Wagoner, R.V., *Ann. Rev. Nucl. Part. Sci.* 27 (1977) 37.
- Smi57 Smither, R.K., *Phys. Rev.* 107 (1957) 196.
- Sta84 Stacey, Jr., W.M., *Fusion* (New York: John Wiley & Sons, 1984).
- Wag67 Wagoner, R.V., Fowler, W.A., and Hoyle, F., *Astrophys. J.* 148 (1967) 3.
- Wea80 Weaver, T.A., Wilson, J.R., and Bowers, R.L., *Energy and Technology Review*, Lawrence Livermore Laboratory (February, 1980).
- Wes87 Wesson, J., *Tokamaks* (Oxford: Clarendon Press, 1987).
- Wit84 Witten, E., *Phys. Rev.* D30 (1984) 272.
- Wre94 Wrean, P.R., Brune, C.R., and Kavanagh, R.W., *Phys. Rev.* C49 (1994) 1205.
- Yam93 Yamamoto, Y., Kajino, T., and Kubo, K.-I., *Phys. Rev.* C47 (1993) 846.

APPENDIXES

A.1 THE FITTING PROCEDURE

In this thesis, the measured data are fitted by the weighted least squares method. In principle, for a set of measured data points $\{x_k; y_k \pm \Delta y_k\}$ ($k = 1, 2, \dots, N$), after determining the fitting equation $y = y(x)$ which includes the n fitting constants a_i ($i = 0, 1, \dots, n-1$), this method is to choose these a_i so that the weighted deviation

$$V_y = \frac{1}{N-n} \sum_{k=1}^N \frac{1}{(\Delta y_k)^2} [y(x_k) - y_k]^2, \quad (\text{A-1})$$

is minimized. The errors in x_k , i.e., the errors in bombarding energies E_k or in detector angles θ_k , are not considered in fitting.

In the angular distribution data processing, the measured data are fitted to

$$y(\theta) = \sum_{i=0}^{n-1} a_i \cos^i \theta, \quad (\text{A-2})$$

where θ is in the CM system. The criteria for choosing n are: 1) $n \leq 2$, i.e., no more than three fitting constants are used; 2) $n \leq N - 2$, where N is the number of the data points ($n = N - 1$ only in Fig. 3.39); 3) if, after adding an a_i ($i = 1, 2$) to the fitting, the weighted deviation in Eq. (A.1) will not be improved obviously, say, by 10%, then this a_i will not be considered in the fitting.

In processing the data of yields measured at different energies, a quadratic expansion of the S-factor is considered in most cases and the fitting constants, i.e., the expansion coefficients s_i ($i = 0, 1, 2$), have to be numerically calculated with Eq. (2.7). The errors in the fitting constants can be estimated in such a way that, when scanning these s_i in their neighborhoods $s_i \pm \Delta s_i$, most of the measured yields ($\sim 70\%$) will be swept over.

A-2 THE ORIGINAL DATA

The original data obtained when measuring the yields at different energies are given in the following four tables, which list the energies, charges (in μC) and counts.

Table A-1. The original data for the ${}^7\text{Li} + d$ reaction.

Elab (keV)	Q (μC)	#SD	#DB
40	96410	126	----
50	95025	993	2213
60	50008	2392	5491
70	30011	4691	10478
80	20008	7314	17433
90	20029	15898	39049
100	20012	29928	70691
110	8681	23845	59383
120	5081	22823	54008
140	11429	110448	267887
160	1069	20226	52883

Original data for d+7Li reaction 05/10/93 Monday
file-name=(D+7Li-3):\EF\data.txt

Q = Total charge in micro-Coulomb
#SD = measured reaction number for sequential decay
i.e., number of 5He-particles
#DB = measured reaction number for direct breakup
i.e., number of those alpha-particles divided by 2
spectra measured at 90-degree lab angle
target = natural LiF (>99%), infinitely thick
detector solid angle = 0.03806

Note: these data are from ROUGH reading of the spectra.

Table A-2. The original data for the $^9\text{Be} + d$ reaction.

Elab(keV)	Q(uC)	p0	p1	dpl	a0	a1	t0
170	726	2415	2937	79	2790	2959	1835
150	1227	1712	2001	67	1905	2059	1357
130	2399	1023	1008	50	1077	1230	762
110	8282	756	655	50	693	809	571
90	17223	200	---	--	199	257	161
70	57851	28	---	--	33	39	17

Original data for d+9Be reaction
Yield measurements 07/21/93 Wednesday
file-name = (D+9Be-3):\D-9Be-T\data-2.txt

spectra measured at 140-degree lab angle
target = infinitely thick beryllium, polished surface, analytical pure
detector solid angle = 0.02809

Table A.3. The original data for the $^{10}\text{B} + \text{d}$ reaction.

Ecm(kev)	Q(uC)	p0	p1	p2	a0	a1
141	5411	1122	468	1511	316	3765
133	20212	2238	896	3193	606	7905
125	24273	1616	670	2155	402	5486
117	30633	1168	460	1536	308	3910
108	49693	873	326	1091	243	2764
100	125844	857	382	1131	266	3022
92	232795	650	241	814	158	2310
83	523141	524	181	682	141	1687
75	1026565	340	148	363	90	1062
67	1024362	71	35	82	17	239

Original data for d+10B reaction
yield measurement 05/21/93 Friday
file-name = (D+10B-1):\d-10b-t\data-3.txt

spectra measured at 90-degree lab angle
target = 90%-enriched 10B, infinitely thick
detector solid angle = 0.03669
detector telescope used

The results for p3, p4 and p5 are from the angular distribution measurements.

Table A-4. The original data for the $^{11}\text{B} + \text{d}$ reaction.

Elab (keV)	Q (uC)	a0	da0	a1	da1	p0	dp0
169.5	11274	1257	47	1519	56	4649	93
160	6499	412	26	563	35	1865	62
150	11427	464	28	519	38	1702	60
140	14107	304	23	323	29	1244	51
130	20708	218	20	283	29	813	44
120	31265	132	15	174	27	503	35
110	37912	89	12	122	14	230	26
100	64892	73	10	93	15	170	25
90	59783	--	--	75	15	---	--

Original data for d+11B reaction
yield measurement 07/20/93 Tuesday
file-name = (D+11B-3):\ef\data-Z.txt

spectra measured at 130-degree lab angle
target = natural boron (purity > 99%), infinitely thick
detector solid angle = 0.02809